UNIVERSITÀ
DEGLI STUDI
DI PADOVA

Sede Amministrativa: Università degli Studi di Padova
Dipartimento di Ingegneria Industriale

SCUOLA DI DOTTORATO DI RICERCA IN: Ingegneria Industriale
INDIRIZZO: Ingegneria dell'Energia
CICLO: XXVII

Energy analysis of household devices and their modeling software

Direttore della Scuola: Ch.mo Prof. Paolo Colombo
Coordinatore d'indirizzo: Ch.ma Prof. Luisa Rossetto
Supervisore: Ch.mo Prof. Roberto Zecchin

Dottorando: Andrea Cervato

February 2015

"Sit down before fact as a little child,
be prepared to give up every conceived notion,
follow humbly wherever and whatever abysses nature leads,
or you will learn nothing."

Thomas Huxley

UNIVERSITY OF PADOVA

Abstract

DEPARTMENT OF INDUSTRIAL ENGINNERING
PhD School in Industrial Engineering

Doctor of Philosophy

Energy analysis of household devices and their modeling software

by Andrea Cervato

The purpose of this work was to develop three simulation models of tumble dryers: heat pump tumble dryer, air vented tumble dryer and condenser tumble dryer. In interests of competitiveness, manufactures of tumble dryers are seeking to reduce both their electricity consumption and the drying time. Nowadays, this challenge has led to use innovative work methodologies, especially in case of complex and non-linear dynamic systems as the drying process, where the development of a model plays a crucial role.

The heat pump tumble dryer system is divided into three parts: heat pump module, drum and air circuit. A model, for each of the previous components, was developed. The first part of this dissertation tries to develop a dynamic model of a vapor compression cycle system, and hence of the heat pump module, using a first-principles modeling framework. The mass and energy conservation principles were used to draw up the equation set, whereas collected experimental data was used to validate each component. The modeling of the heat exchanger is based on the moving-boundary scheme, the capillary tube was modeled through an analytical correlation found in literature and the dynamic behaviour of the compressor was considered. The characteristic of the aeraulic circuit of the heat pump tumble dryer was investigated using performance tests that allowed to characterize its aeraulic resistances as well as the characteristic curve of the process fan. A significant part of the work was focused on the analysis of the physical phenomena that take place inside the dryer drum due to the interaction between the air stream and the moistened laundry load. The features of this component determine the mass and energy flow through the complete unit. The analysis of experimental tests led to develop a correlation that gives the overall heat transfer coefficient between air and laundry load. The overall mass transfer is deduced invoking the heat and mass transfer analogy based on the Lewis number. An original model of the system laundry-content of water is presented. This model was validated through a series of drying tests.

The models of the heat pump, the air circuit and the drum were joined together to develop the entire model of the heat pump tumble dryer. The model predictions were compared with experimental data, and the result showed that the energy consumption is adequately predicted with maximum deviation of $\pm$ 10% if the drying time is properly predicted. Further some case studies are presented where the capabilities in prediction of the model, in cases where model's parameters were strongly varied, were checked.

The second dryer analyzed and modeled is the air vented tumble dryer that operates with an open-configuration. The modeling effort on this dryer platform was focused on the understanding of the fluid-dynamic aspects that govern its behaviour. Two sources of leakage, where the air can enter into the process circuit, were detected. These sources heavily affect the performances. The whole experimental aeraulic characterization of the air process circuit is presented together with the pressure drop correlation of each component. These correlations allowed to develop a simulation model where also the heat transfer dynamics concerning the heating element and the evaporation process were considered. Simulation results are in excellent agreement with experimental data.

The third dryer analyzed and modeled is the condenser tumble dryer. This kind of tumble dryer can be viewed as an extension of the air vented tumble dryer where the air leaving the drum is recirculated back. Before crossing the heater, the air stream is cooled and dehumidified by an air-to-air heat exchanger with cross flow arrangement. In order to develop the whole system a heat exchanger model was developed. The model is based on a 2D discretization of the metallic plate whose properties are considered as lumped. Furthermore, the model is able to catch both mass and energy phenomena. Also for this device the aeraulic circuit was first analyzed experimentally and then modeled for the purpose of predicting the process mass flow rate along the drying cycle. The model capabilities were checked by testing the model throughout the drying cycle and the results are presented. The different arrangement of the drum flange seems to reduce the active portion of the mass flow rate involved in heat and mass transfer exchanges with the laundry load. This leads a longer drying time compared with those derived by the relations developed for the heat pump and air vented tumble dryer that predict the mass and energy transfer between air and laundry.

Abstract in Italian

Lo scopo di questo lavoro è stato lo sviluppo di tre modelli numerici adatti alla simulazione dinamica di asciugatrici domestiche. In particolare modo è stata analizzata l'asciugabiancheria a pompa di calore, l'asciugabiancheria ad aria ventilata ed infine l'asciugabiancheria a condensa. Oggigiorno i produttori di asciugabiancheria, per ragioni di competitività, si stanno sfidando sul mercato con prodotti sempre più efficienti: ridotto consumo energetico e ridotta durata del ciclo. Questa sfida ha condotto all'uso di metodologie di lavoro innovative come il ″model-based-design‟ adatto all'analisi di sistemi complessi e non lineari come è il ciclo di asciugatura. In questo approccio riveste un ruolo fondamentale lo sviluppo di un modello matematico che spieghi il funzionamento del sistema.

L'asciugatrice a pompa di calore è costituita da tre componenti principali: modulo pompa di calore, cesto e circuito aeraulico. Per ognuno di essi è stato sviluppato un modello. La prima parte di questo lavoro è stata dedicata allo sviluppo di un modello dinamico del ciclo a compressione di vapore usando un approccio di primo principio in cui i principi di conservazione della massa e dell'energia vengono applicati per sviluppare le equazioni che ne descrivono il comportamento. Gli scambiatori di calore sono stati modellizzati attraverso l'approccio a frontiera mobile noto in letteratura con il nome: ″moving-boundary‟. Per la stima della portata di refrigerante elaborata dal tubo capillare è stata impiegata una relazione analitica disponibile in letteratura, coerente con i valori sperimentali. Infine il comportamento dinamico del compressore manifestatosi durante alcune fasi del ciclo di asciugatura, è stato considerato sviluppando un modello a due capacità termiche. Le caratteristiche del circuito aeraulico della pompa di calore sono state soggette prima ad analisi sperimentali, permettendo la derivazione delle correlazioni in grado di stimare le perdite di carico lato aria di processo, e successivamente alla loro modellizzazione utilizzando l'analogia elettrica. Una significativa parte del lavoro è stata concentrata sull'analisi del processo di evaporazione a cui è soggetta l'acqua contenuta nei panni. L'analisi sperimentale condotta ha permesso di sviluppare la correlazione che spiega come varia la trasmittanza media aria-panni durante il ciclo di asciugatura, inoltre sfruttando l'analogia di scambio di calore e di massa, basata sul numero di Lewis, è stato determinato il coefficiente medio di scambio di massa. Il sistema acqua-panni è stato modellizzato con un approccio originale che prevede di dividerlo in due zone: una zona secca ed una zona bagnata, l'estensione della zona bagnata è funzione del grado di asciugatura. La correlazione che spiega come varia l'estensione di tale zona è stata ricavata dai dati sperimentali. Il modello è stato validato e mostra una accuratezza del 5% nella predizione del tempo di asciugatura. I tre sotto-modelli sviluppati sono stati collegati tra di loro in modo da sviluppare il modello complessivo

dell'asciugabiancheria a pompa di calore. L'attendibilità del modello è stata verificata prima con confronti sperimentali e successivamente con più casi studio che hanno evidenziato, qualora il tempo ciclo fosse predetto, delle deviazioni di circa il 10% sulla stima del consumo energetico del compressore.

La seconda piattaforma di asciugabiancheria che è stata analizzata è il modello ad aria ventilata. Questo tipo di elettrodomestico opera con una configurazione di ciclo aperta in cui l'aria uscente dal cesto viene espulsa in ambiente. Lo sforzo modellistico è stato concentrato nella comprensione dei fenomeni fluidodinamici che ne regolano il funzionamento. Due tipi di sorgenti di perdita sono stati messi in luce, in questi punti, l'aria può entrare nel sistema. L'effetto della portata non riscaldata influenza notevolmente le prestazioni dell'asciugabiancheria. L'intera caratterizzazione sperimentale del circuito aeraulico ha permesso di dedurre delle correlazioni che stimano le perdite di carico attraverso i vari componenti. Ciò ha permesso la derivazione di un modello aeraulico, che accompagnato dalla descrizione dinamica dell'elemento riscaldante, ha permesso lo sviluppo del modello complessivo della macchina. Il modello è stato validato sperimentalmente ed il confronto tra risultati sperimentali e numerici ha indicato che esso è in grado di predire eccellentemente le prestazioni della macchina nel ciclo di aciugatura.

La terza piattaforma di asciugabiancheria che è stata analizzata è il tipo a condensa. Esso può essere visto come un'estensione del modello ad aria ventilata in cui il flusso d'aria proveniente del cesto viene ricircolato ma prima di passare attraverso l'elemento riscaldante il flusso d'aria transita in uno scambiatore compatto ad aria dove viene raffreddato e deumidificato. Pertanto lo sforzo modellistico si è concentrato non solo nello sviluppo del consueto modello aeraulico derivato dai dati sperimentali ma anche nello sviluppo di un modello bidimensionale dello scambiatore di calore. La piastra metallica dello scambiatore di calore è strata discretizzata bidimensionalmente. Il modello è in grado di cogliere fenomeni sia di scambio sensibile che di trasporto di massa. Le capacità di predizione del modello sono state testate confrontando i risultati su un intero ciclo di asciugatura. La diversa configurazione della flangia, che immette l'aria all'interno del cesto, riduce la porzione attiva di portata d'aria a contatto con i panni.

Preface

This thesis is the result of an industrially driven research in the field of household tumble dryer development with modern working methodology as the Model Based Design. The entire work was financed by Electrolux Italia SpA. The most part of the experimental activities presented in this thesis were carried out at the Electrolux laboratories located in Porcia, Pordenone, Italy.

Acknowledgements

Gran parte di questa tesi è stata sviluppata in collaborazione con Electrolux Italia Spa che ringrazio per avermi dato questa grande opportunità. In particolar modo però voglio ringraziare principalmente le persone che mi hanno accompagnato, guidato e supportato in questa esperienza:

- *Ing. Stefano Zandonà* (Electrolux Italia). Con lui ho condiviso momenti di grande soddisfazione ma anche situazioni di totale sconforto quando le cose sembravano non volere tornare per nessuna ragione. L'ho sempre sentito a mio fianco e questo mi ha dato la forza per superare anche i momenti più difficili di questa esperienza. Lo stimo molto come Uomo e come tecnico e spero che il nostro rapporto possa proseguire anche oltre il mondo del lavoro. Grazie.
- *Dott. Ing. Luca Cecchinato* (Everest). Lo ringrazio per avermi sempre indicato la strada giusta da percorrere e per avermi fatto vedere le cose con chiarezza e luciditá. È grazie a lui se ho iniziato questa esperienza ed è per merito suo se oggi mi sento molto migliorato sia come persona che come tecnico. Grazie.
- *Ing. Gianpiero Artico* (Electrolux Italia). Lo ringrazio per essere stato sempre premuroso nei miei confronti e per avermi fatto lavorare sempre nelle migliori condizioni possibili. Lo ringrazio per avermi dato la possibilità di lavorare a stretto contatto con tutto l'"Energy & Resources Team" e per aver avuto la possibilità di seguire da vicino lo sviluppo di nuovi prodotti. Grazie.
- *Ing. Francesco Cavarretta* (Electrolux Italia). Lo ringrazio per i preziosi consigli, per le molte discussioni tecniche che hanno sempre arricchito il mio bagaglio di conoscenze e per la disponibilità che mi ha sempre dimostrato. Grazie.
- Ringrazio il *Prof. Roberto Zecchin* per la disponibilità dimostratami soprattutto nell'ultimo periodo e per l'aiuto nella correzione di questo lavoro. Grazie.

Un ringraziamento particolare va inoltre all'*Ing. Davide Camata*, a *Massimo Castiglione*, all'*Ing. Lorenzo Corso*, ed a *Roberto Ragogna* per avermi permesso di lavorare a loro stretto contatto, per le conoscenze che mi hanno trasmesso ed anche per aver reso piacevoli le giornate passate con loro. Grazie.

Andrea Cervato

Contents

List of Figures

List of Tables

Abbreviations

COP	**C**oefficient **O**f **P**erformance
ER	**E**vaporation **R**ate
L	**L**iquid, subcooled zone
LWC	**L**oad **W**ater **C**ontent
R	**R**esistance (aeraulic)
RL	**R**atio **L**oad
SC	**S**ubcooling
SH	**S**uper**H**eated region
TP	**T**wo-**P**hase
NTC	**N**egative **T**emperature **C**oefficient
NTU	**N**umber of **T**ransport **U**nit

Symbols

A	flow area	[m^2]
c_p	specific heat	[J kg^{-1} K^{-1}]
D	diameter	[m]
FQ	compressor factor quality	[-]
h	enthalpy	[kJ Kg^{-1}]
h	heat transfer coefficient	[W $m^{-2}K^{-1}$]
h	hydraulic diameter	[m]
K	overall heat transfer coefficient	[W $m^{-2}K^{-1}$]
K	pressure drop loss factor	[m^{-4}]
L	length	[m]
Le	Lewis number	[-]
$\dot{m}$	mass flow rate	[kg s^{-1}]
M	refrigerant mass	[kg]
M	water mass	[kg]
Nu	Nusselt number	[-]
P	Power	[W]
P	air pressure	[Pa]
P	mass and thermal efficiency	[-]
p	pressure	[Pa]
q	heat flux	[W]
r	latent heat of vaporization	[kJ Kg^{-1}]
Re	Reynolds number	[-]
RH	relative humidity	[%]
S	cross section area	[m^2]
t	time	[s]

T	temperature	[℃]
u	internal energy	[J kg^{-1}]
V	volume	[m^3]
V	volumetric flow rate	[m^3 h^{-1}] or [Nm^3 h^{-1}]
v	velocity	[m s^{-1}]
x	refrigerant quality	[-]
x	specific humidity	[kgv/kga]
z	spatial coordinate	[m]
α	heat transfer coefficient	[W m^{-2}K^{-1}]
η	overall surface efficiency	[-]
η	efficiency	[-]
λ	thermal conductivity	[W m^{-1}K^{-1}]
γ	void fraction	[-]
$\bar{\gamma}$	void fraction mean	[-]
ρ	density	[kg m^{-3}]
ΔP	pressure drop	[Pa]
μ	dynamic viscosity	[Pa s]

Subscripts

a	air
c	condenser
cab	cabinet
can	canister
ch	channel
$coil$	electric filament
$conv$	convective
$c.c$	compression chamber
$cool-s$	cooling side
dry	load dry zone
e	evaporator
e	ambient
$evap$	evaporation
f	fluid
i	inlet or inner
in	input
in	inlet
is	isentropic
int	air node in the cabinet
int	interface refrigerant mass flow rate
l	saturated liquid
l	laundry
l	loss
m	mass transfer phenomenon
o	outlet

p	plate
$proc-s$	process side
r	refrigerant
s	sensible heat transfer
sat	saturation
suc	suction
v	saturated vapor
v	volumetric
w	tube wall
w	water
wb	wet bulb
wet	load wet zone
$zone$	zone

1	SH zone in condenser or TP zone in evaporator
2	TP zone in condenser or SH zone in evaporator
3	L zone in condenser

To my family and friends...

Chapter 1

Introduction

1.1 Introduction

The purpose of this work was the development of three models of tumble dryers: heat pump tumble dryer, air vented tumble dryer and condenser tumble dryer. Therefore, in this chapter the main features for each platform will be discussed although more details will be given in the chapters dedicated to specific models. Briefly, the current energy labelling of household tumble dryers will be presented, the real driving force for this work, for which many home appliance manufacturers compete to produce increasingly efficient appliances. Nowadays, this challenge has led to use different work methodologies, especially in case of complex dynamic systems, where the model based design approach allows to seek new area of improvements without passing through experimental tests. The model development requires a deep knowledge of the physical phenomena governing its operation, hence in this introductory chapter the thermodynamic transformations that the air stream undergoes during the drying process will be introduced. In addition, a section that briefly describes the features of a vapor compression cycle (VCC) is presented.

1.2 Household clothes dryers: models in the market

For adsorbing moisture from clothes it is necessary to heat an air flow stream (in order to increase its potential of humidity transport). Although there are several technological solutions and system designs, household tumble dryers could be divided into two categories based on the aeraulic circuit features: open-cycle and closed-cycle dryers. Based on the device used to heat the air stream could be founded two categories: electrical resistance and heat pump dryers. Air vented dryers are open-cycle devices and for heating

the flow stream an electrical resistance is used. In these dryers, the air is drawn from the ambient, heated to a suitable temperature before passing through the clothes inside the drum, and finally is rejected into the laundry room or outdoors (if a wall break is available). The air process fan is often placed after the drum as shown in Figure 6.1. One of the advantages of the venting tumble dryer is the simple construction, which makes it a low cost product, and most of the supplied energy is transported out from the laundry room as well as the water vapor from the clothes. Condenser dryers work according to a closed-loop air cycle and an electrical resistance is used to heat the air. The air flow is heated by the electrical resistance, driven through the drum and then is cooled and dehumidified inside an air-to-air heat exchanger before re-entering into the drum. The cold fluid is drawn from the room ambient air. The water that is removed from the textiles fills up a tank, which is manually emptied when the drying cycle is finished. As the room air is used as the cooling fluid, this air must not be too hot, since this would significantly reduce the dryer efficiency due to poor condensation of water vapor. This is one reason why this type of dryer is rarely found in warmer countries [2]. A schematic is reported in Figure 7.1. Heat pumps dryers work with a closed loop air circulation. The fan extracts the moistened air from the tumble drum and forces it through the evaporator, removing the moisture; then the air stream is driven through the condenser, before re-entering the drum. Thus, the heat pump refrigerating capacity is used to dehumidify the moistened air, whereas the heating capacity is used for warming up the cold air. A schematic is reported in Figure 2.1.

1.3 The energy labelling of household tumble dryers

Energy labelling for household appliances is mandatory and common to all countries in the EU. The purpose of the label is to guide the consumer to choose a product with low energy use in order to lower the costs and the environmental impact during use. Another purpose is to encourage the producers to develop more energy efficient products in order to be competitive on the market. The European Union (EU) has implemented a highly effective and internationally influential energy labelling programme for household appliances since 1995. In 2010 the energy labelling directive was recast (Directive 2010/30/EU of the European Parliament): its scope of applicability was broadened; many of the existing labels, specifically those applying to refrigerators and freezers, washing machines and dishwashers were redesigned. These new labels were implemented in November 2011. Much discussion preceded the adoption of the new labels. The discussion centred on whether it would be better to redraw the old A-to-G energy efficiency scale or to add new higher efficiency classes above class A. In the end a decision was made to add

higher efficiency classes for products where markets were concentrated in the highest label classes: the revised labels ranges from A+++ to D (see Figures 1.1 and 1.2), clearly the most energy efficient dryer is labelled with an A+++.

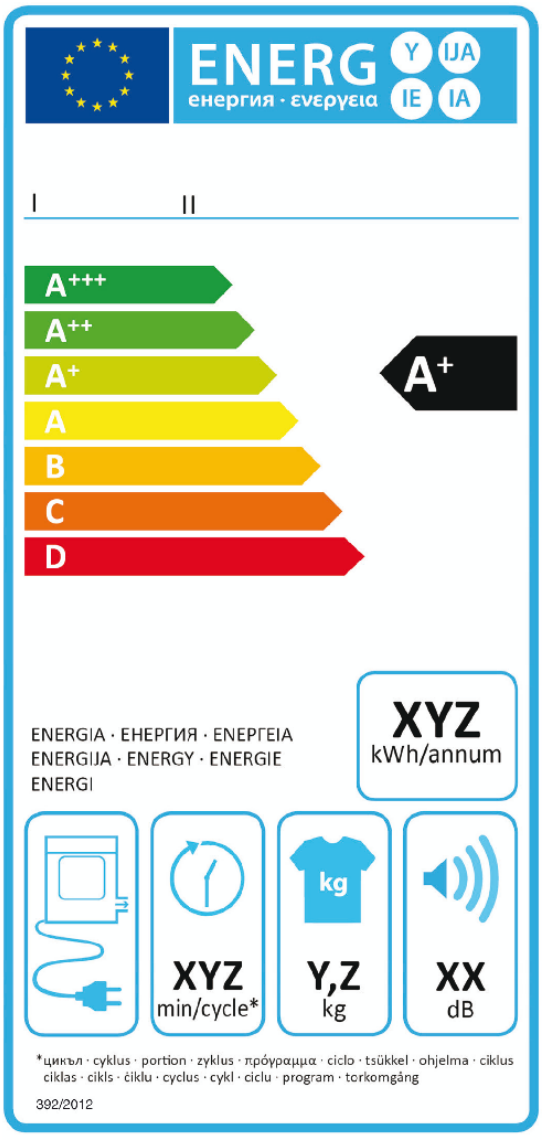

FIGURE 1.1: Label for air-vented household tumble dryer [3].

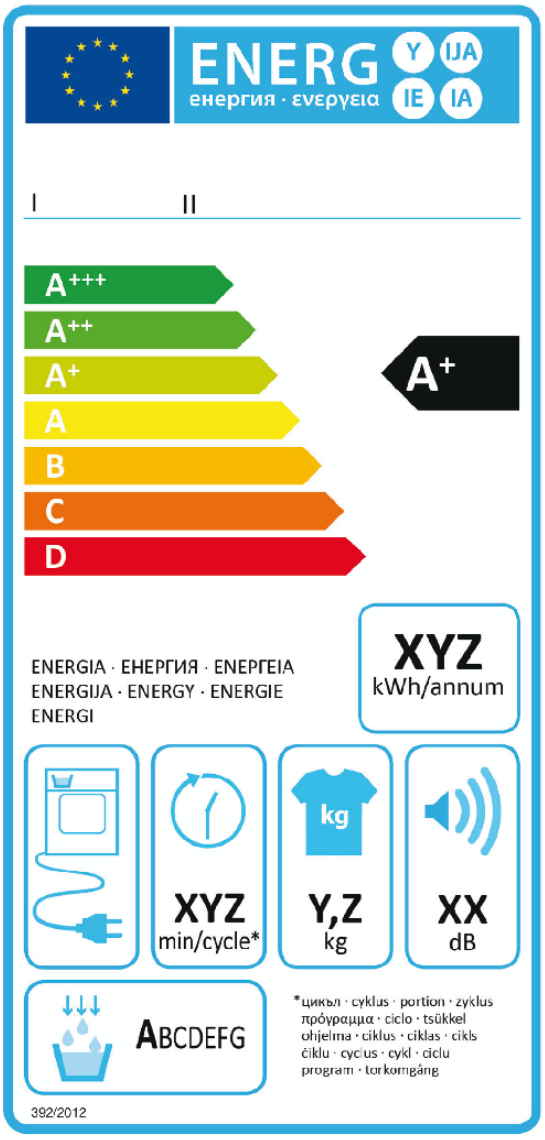

FIGURE 1.2: Label for condenser household tumble dryer [3].

The following informations are included in the label: energy efficiency class, weighted annual energy consumption in kWh/year, cycle time corresponding to the standard cotton programme at full load in minutes, rated capacity in kg, the sound power level during the draining phase for the standard cotton programme express in dB. In addition, for the condenser tumble dryer, is added the condensation (recovery) efficiency (C) that is defined as the ratio between the condensed and collected mass of moisture in the container of a condenser household tumble drier ($M_{w,collected}$) and the mass of moisture

removed from the load by the programme ($M_w(t=0) - M_w(t)$):

$$C = \frac{M_{w,collected}}{M_w(t=0) - M_w(t)} \cdot 100 \quad [\%] \tag{1.1}$$

The class position is defined through the calculation of the Energy Efficiency Index (EEI). The EEI is defined as the ratio between the weighted annual energy consumption for the standard cotton programme at full load and partial load and the standard annual energy consumption, the complete calculation procedure is defined in the supplementing of the Directive 2010/30/EU for energy labeling of household tumble driers [3]. The wighted is referred to the method for computing the drying time that is define as the weighted average for cycles at full (T_{dry}) and partial load ($T_{dry\,1/2}$):

$$T_t = \frac{3 \cdot T_{dry} + 4 \cdot T_{dry\,1/2}}{7} \tag{1.2}$$

tests at partial load strongly affect the weighted time programme since they have lower energy efficiencies, as proved in [2], in terms of SMER. The SMER signifies the electric energy consumed to remove 1 kg of moisture from load and its unit is kWh/kg. This index is a common basis for comparison, although its definition changes from one standard to another.

1.4 Vapor compression cycle system

This section is devoted to describe very briefly the features of a vapor compression cycle (VCC) with reference to the heat pump module installed in the heat pump tumble dryer. Essentially, a VCC system is a thermo-fluid system where the refrigerant fluid evolves changing its thermodynamic state. It has four primary components: an evaporator, a condenser, a compressor and an expansion device. In the evaporator the temperature of the refrigerant is lower than the temperature of the air flow therefore it absorbs energy from the air stream reaching the compressor inlet section near to a dry vapor state or, more common, with some degree of superheat. In the compressor, refrigerant increases its pressure and its temperature, then it is driven into the condenser where it is cooled and condensed into a liquid by rejecting heat to the air stream. The condensed liquid refrigerant is next routed through a capillary tube where it undergoes an abrupt pressure reduction and transitions from a liquid to a two-phase state. An ideal VCC system assumes an isentropic compression of the refrigerant across the compressor, an isenthalpic condition through the expansion device, and an isobaric process in the condenser and evaporator, as presented in the pressure-enthalpy (P-h) diagram in Figure 1.3. The following figure represents the typical conditions reached by a heat pump system equipped

with R134a. Condensation temperature near to 65 ℃ and evaporation temperature near to 25 ℃. The superheat is about 15 K and the subcooling is about 5 K. In addition, Figure 1.3 clarifies that the processes occurring in the heat exchanging components involve multiple phases of the refrigerant. The two-phase section of both the condenser and the evaporator provides the most heat transfer due to the large heat transfer coefficients that are associated with two-phase fluids. Therefore, most system designs maximize the two-phase length of the heat exchanger in order to achieve the most efficient heat transfer dynamics between the refrigerant and the ambient or conditioned space. This fact is useful for determining the dominant dynamics of each component of the system which is important in modeling.

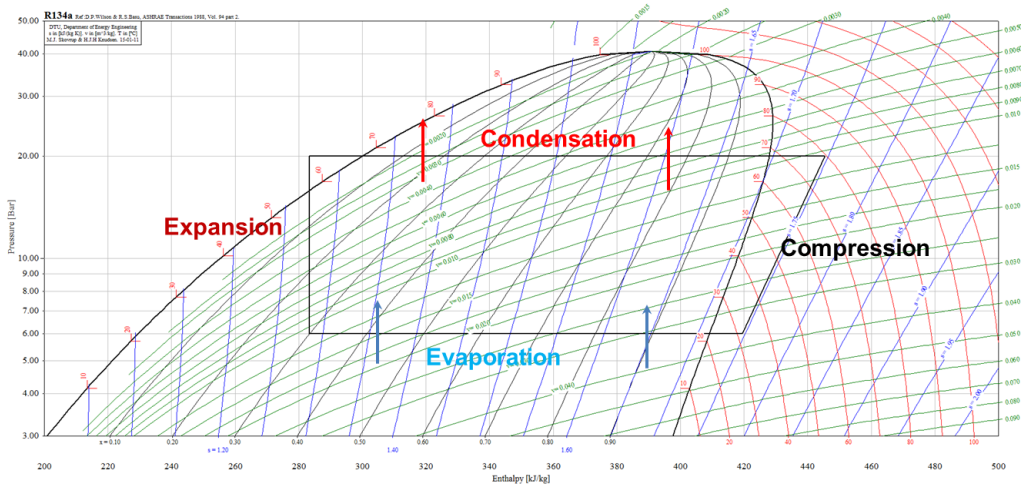

FIGURE 1.3: Refrigerant cycle.

1.5 Drying process: air cycle

Along the closed loop the air flow stream is subjected to temperature variations as shown in Figure 1.4. Humid air crosses the evaporator where is cooled down and dehumidified (A1-A2), then it crosses the condenser where is heated (A2-A3); finally enters into the drum where a nearly isenthalpic (but not strictly isenthalpic) process occurs (A3-A4) (clothes water evaporates and increases the air humidity ratio, while its temperature decreases as an effect of latent heat of vaporisation). The subsequent transformation (A4-A1) that closes the loop represents a further cooling due to heat dissipation: thermal balance is achieved when the dissipated heat corresponds to the work spent by the compressor and the fan. This transformation is represented by line A4-A1 for the sake of simplification, but actually can occur by thermal losses, for example through the structure walls of the cabinet, or by air leakage from the main path of the aeraulic circuit.

The temperature level of the closed profile, qualitatively represented in Figure 1.4, depends on the thermal balance between compression and fan work and heat dissipation; better the overall insulation of the dryer is, the higher the temperature level will be.

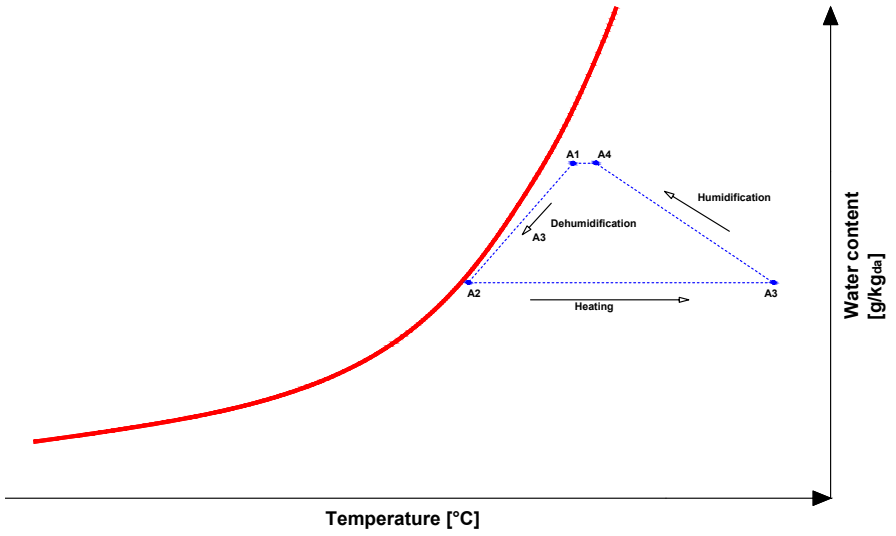

FIGURE 1.4: Drying process. Air cycle.

1.6 Air as drying medium

In ordinary tumble dryers, air is used as a drying medium. The air normally contains a certain amount of water vapor. In order to use the air as a drying medium, the air needs to evaporate water and improve its water vapor content. The humidity can be expressed in two ways, either as relative humidity or as specific humidity. The relative humidity (RH [%]) is defined as the ratio of the partial vapor pressure, (p_v [Pa]) to the saturated vapor pressure in the air at the same temperature (p_{sat} [Pa])

$$RH = \frac{p_v}{p_{sat}} \cdot 100 \tag{1.3}$$

The relative humidity describes the amount of water the air can take up. The lower the relative humidity of the air encountering the wet textiles, the larger the driving force for drying would be. The specific humidity (x [kg_v/kg]), or the amount of water in the air can be expressed as:

$$x = 0.622 \cdot \frac{RH \cdot p_{sat}}{p - RH \cdot p_{sat}} \tag{1.4}$$

The enthalpy (h [kJ/kg]) is used for describing the effects of the specific humidity and temperature (T [℃]) on the energy content of the air. To express the enthalpy of the

humid air, the latent heat of water vapor is also included. The reference temperature, T_0, is set at 0 ℃. The enthalpy for humid air is determined by the sum of the enthalpy of dry air and the enthalpy of water vapor in the air by:

$$h = cp_a \cdot T + x \cdot (cp_v \cdot T + r_0) \tag{1.5}$$

where cp_a is the specific heat fo dry air and cp_v is the specific heat for water vapor.

The thermophysical properties of the air used in this work are referred at the following work in literature [4] where the analytical correlations for the moist air in temperature range 0 - 100 ℃ and barometric pressure of 101.3 kPa are presented.

1.7 Testing procedure and experimental facility

All the drying tests shown in this work, concerning the heat pump tumble dryer, were performed with 8 or 9 kg of standard dry cotton clothes, subjected to preliminary wetting and spinning, according to the standard test procedure, thus assuring repeatability of the initial conditions of each test. The weight of the test load was immediately measured before and after the drying cycle; the mass of moisture condensed and accumulated inside the collecting canister was determined as well. The measured drying time and the total energy consumption were evaluated and corrected as stated up by international standards IEC 61121 (2010) [5]; IEC 61121 (2010) gives the rules to normalize the performance (energy consumption) to the nominal conditions of moisture content (i.e. 60% of initial moisture content and 0% of final moisture content for cotton textile).

In all the drying tests carried out in this work the aeraulic and the heat pump circuit were equipped with temperature and pressure sensors located as shown in Figure 1.5. Temperature and pressure measurements were acquired with a data logger equipped with minimum ten copper-constantan thermocouples (T type) that were used as temperature sensors. The estimated accuracy of the entire temperature measurement system is ± 1.5 ℃. Pressures were measured at the suction and discharge sides of the compressor. Two pressure sensors were used, with the following measuring ranges: 0-60 bar (discharge pressure) and 0-16 bar (suction pressure). The accuracy of the pressure transducers is ± 0.5% of the full range scale. The overall dryer prototype electrical consumption, compressor and auxiliary motors, was measured with a wattmeter with 0.1% accuracy. Occasionally, in some tests load weight was acquired with a precision balance with a repeatability of 0.1 g.

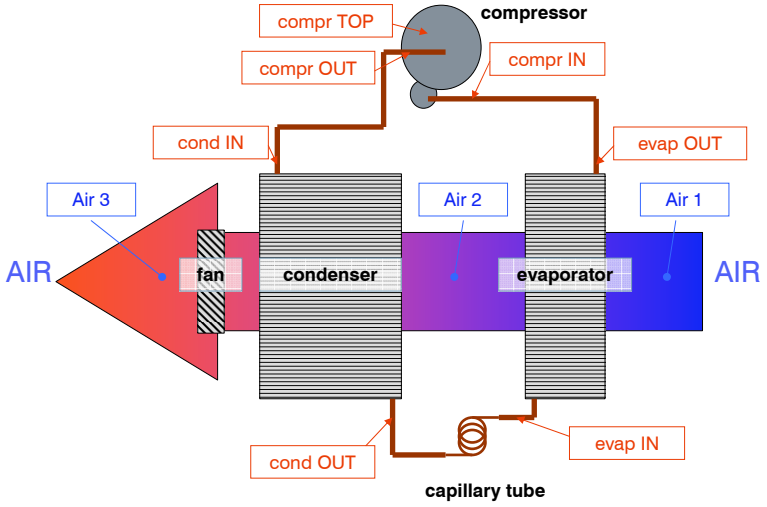

FIGURE 1.5: Thermocouple positions in experimental tests.

1.8 Organization of dissertation

The remainder of this dissertation is organized as follows. Chapter 2 presents all the steps doing in order to develop the heat pump model, the most challenging one. The chapter discusses the derivation of a first-principles model that captures the VCC system transient behavior under mode switch operations. The adopted method, for modeling the heat exchangers, is known in literature as moving boundary and it can be classified as a lumped parameter approach. Further, in this chapter, the model of the capillary tube and the dynamic model of the compressor are presented. Chapter 3 presents the heat pump tumble dryer aeraulic model and the results of the experimental analysis used for characterizing the components of the aeraulic circuit. Chapter 4 describes a theoretical model of the drying process drawn up from energy and mass balances. In addition, the validation of the model is presented using specific experimental tests. In Chapter 5 the previous three models are connected together in order to develop the whole heat pump tumble dryer model. The validation of the entire model is presented. Furthermore, two case studies are discussed to show the capabilities of the modeling approach in predicting scenarios where the boundary conditions and design parameters are heavily varied. Chapter 6 presents the dynamic model of the air vented tumble dryer, a different tumble dryer platform in which the process air circuit is opened and the air flow is heated through a heating element. The modeling effort is focused on the development of the aeraulic circuit since it is characterized by many sources of leakage where the air from the ambient and the cabinet can enter into the system. The thermal model is based on resistance-capacity (RC) approach. The validation of the model with experimental data is presented. Chapter 7 presents a condenser tumble dryer

dynamic model. This platform of dryer can be viewed as an extension of the air vented tumble dryer where the air leaving the drum is recirculated back passing first through a compact heat exchanger before being heated from the heater. The focus is on the aeraulic circuit and on the cross flow heat exchanger. The results of the aeraulic characterization is presented and discussed while for the heat exchanger its model is discussed. The experimental derivation of the mean heat transfer coefficient, used to predict the overall heat exchanger performance under conditions of heat and mass transfer, is presented and discussed. Chapter 8 provides a summary and conclusions of this work as well as some potential future directions for continuing this study.

1.9 Dissertation charts

Most of the charts reported in this dissertation were normalized for industrial secrecy reasons. Especially for the charts that plot the evolutions of the drying variables over the time.

Chapter 2

Dynamic modeling of a heat pump tumble dryer

2.1 Introduction

This chapter, the most extensive of this work, presents a detailed description of the fundamentals and methods used to derive a model for each component of the VCC system and hence of the heat pump module. First, the experimental features of the drying cycle will be discussed and, on the base of these, a suitable mathematical description will be presented. The heat exchanger will be described by a set of derivative equations for multiphase fluid flow keeping attention to guarantee high accuracy even with a low order model. The derivation method is known as the moving boundary, lumped parameter approach. The compressor will be described in a dynamic way in order to characterize the transients in some phases of the drying cycle. The adopted expansion device is a capillary tube. This component has a much faster dynamic than the dynamics of the previous components that regulate the heat transfer process in the system. Therefore, for this component a steady state approach is adopted and the best correlations available in literature matching the collected experimental data will be presented. The measurements prediction capabilities of each component model will be shown. In the last part of the chapter some crucial aspects will be emphasized.

2.2 Components description and features of the standard drying cycle

A heat pump tumble dryer involves a closed-loop air circulation, as shown in Figure 2.1, where the fan extracts the moistened air from the tumbler drum and forces it through the evaporator, removing the moisture; then the air stream is driven through the condenser, before re-entering into the drum again. Thus, the heat pump refrigerating capacity is used to dehumidify the moistened air, whereas the heating capacity is used for heating the cold air.

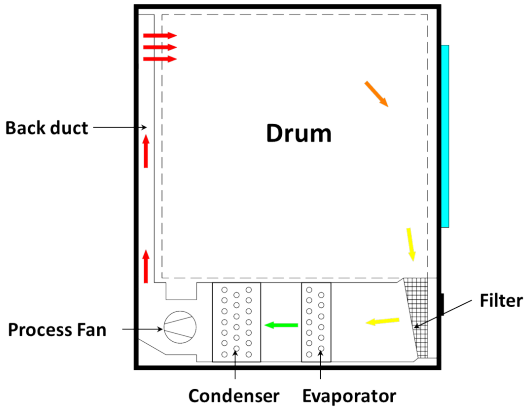

FIGURE 2.1: Heat pump tumble dryer schematic.

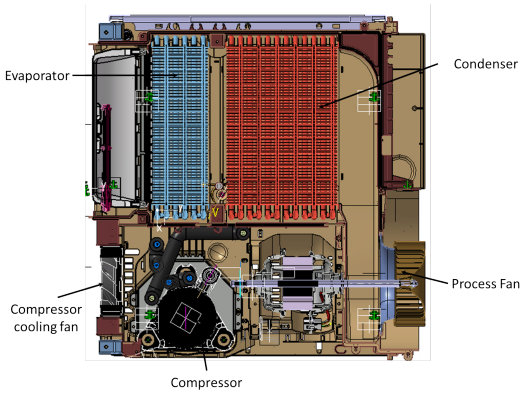

FIGURE 2.2: Heat pump basement.

The heat pump module is equipped with: condenser and evaporator finned tube heat exchangers with smooth copper or aluminum tube. They fit exactly the heat pump air ducts. At the drum outlet air duct is installed a lint filter that it is fully integrated inside the machine framework. The compressor used is a rolling piston type and the compression shell is at the condensation pressure, hence the refrigerant flow coming from the evaporator, enters the compression chamber where it is compressed, resides for a short time in the compression shell where it undergoes a heat transfer process and finally enters into the condenser through the discharge port of the compressor.

Drying process and heat pump are both complex thermodynamic systems, consequently the whole system is much more complex than each of these components taken separately. They should not be analyzed independently due to complex interactions between the air drying process and the heat pump (refrigerant) thermodynamic cycle. While the drying process fundamentals (i.e. heat and mass transfer theories) are well known, the interaction between these two thermodynamic systems requires a careful theoretical and experimental approach. In Figure 2.3 the variables that describe the drying process are plotted. As shown in figure, during the drying cycle the system does not reach a

steady state condition since at least one variable changes. The first phase of the cycle is characterized by a long transient where all the variables (pressure, refrigerant and air temperatures) rise. These variable indicate an energy system increment until the maximum allowable value of the compressor discharge temperature is reached. When this happens the compressor cooling fan is switched on: from this point the cooling fan is able to balance the power input to the system with the energy losses (sensible heat losses and enthalpic heat losses). Although this causes a level off of all system temperatures (refrigerant and air), the air humidity ratio never reaches a stationary condition since its value is determined by the drying process (load water content in the laundry) that is strongly dynamic and non-linear. The final part of the cycle, when the fabric load is almost dry, is indicated by the increment of the drum outlet air temperature (blue line in chart B of Figure 2.3) consequently this reduces the thermal load on the evaporator and hence the evaporation and condensation pressures slightly decrease. During the drying cycle other dynamics occur, that involve the refrigerant mass migration from a heat exchanger affecting the performance of the heat pump. The evolution of this behaviour is emphasized through the superheat at the evaporator, which value is a key variable in order to investigate how the charge inventory changes inside the heat exchanger during the cycle. High superheat indicates low refrigerant content. Hence, in the earliest phase of the drying cycle the evaporator is emptied (high superheat, see green line in graphs A of Figure 2.3) and the condenser is filled by the simultaneous action of the compressor and capillary tube. This phase shows the highest value of superheat during the whole drying cycle. The superheat trend is determined mainly by the design of the capillary tube that tries to balance the refrigerant circuit adapting to the compressor mass flow rate and thus changing the refrigerant charge inventory inside the heat exchangers. The end of the cycle is determined by an automatic system (conductivity probe), detecting when the textiles reach the desired moisture content, which signals the compressor (or the heater) to switch off and start a cooling period.

Approximately, since specific data cannot be reported for industrial secrecy reasons, during the pseudo steady state phase the temperature of the refrigerant at the compressor outlet is about 85 ℃, at the condenser outlet 55 ℃ (this temperature is also used as process variable for the cooling fan compressor relay strategy), at the suction of the compressor the temperature is 35 ℃. The condensation pressure is 26 bar and the evaporation pressure is near to 9 bar. The heat pump values shown in the following figures concern a device equipped with R-407C. The air temperature at the drum inlet is about 60 ℃ while the outlet drum temperature is near to 40 ℃. The drying time for a 8 kg dry moistened load at the 60% is nearly at 165 minutes, the compressor energy consumption is 1.3 kWh and the total energy consumption is about 2 kWh. The SMER index is about 0.4 kWh/kg.

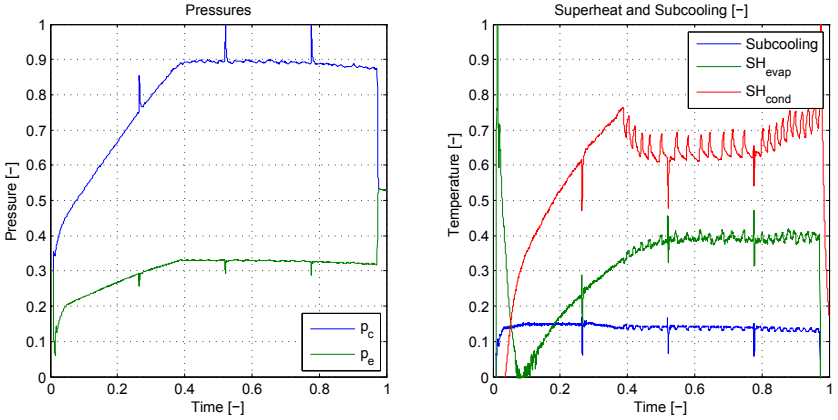

(A) Refrigerant pressures and Subcooling (blue line)-Superheat (Green line)-Condenser Overheating (red line).

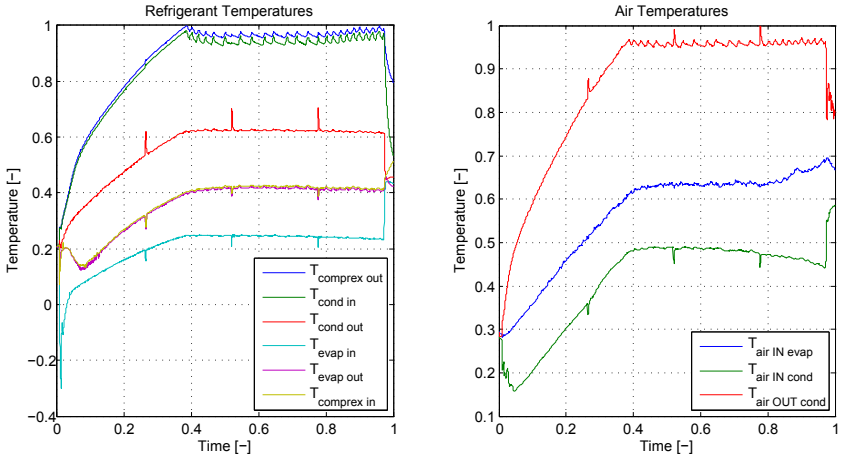

(B) Refrigerant temperatures and air temperatures.

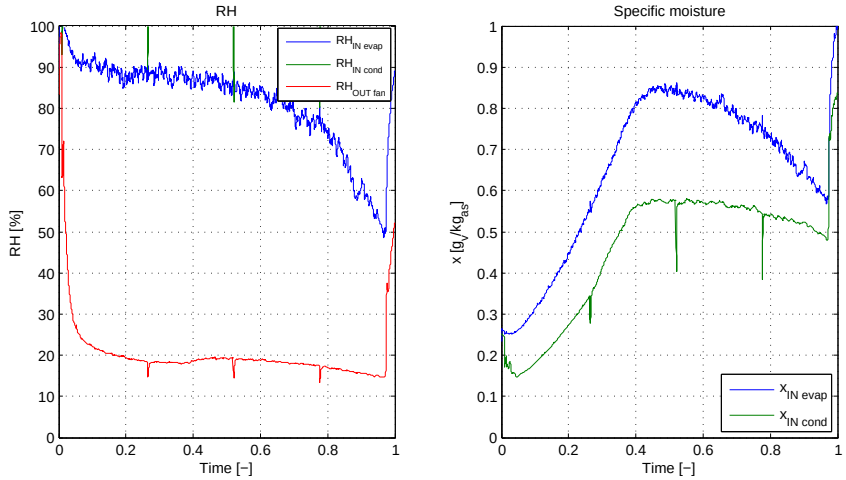

(C) Realtive and specific humidities

FIGURE 2.3: Standard drying cycle.

2.3 Vapor compression cycle (VCC) modeling

Vapor compression cycle (VCC) or vapor compression system (VCS) modeling has been studied extensively in literature using a wide variety of approaches. They are classified into physics based (white box models) or data driven dynamic modeling (gray and black box models). Physics models are described using physical laws, such as energy and mass conservation. Data driven models try to fit experimental results through simple reduced order dynamic models using the method known as identification or time-series analysis. However, due to the nature of this modeling procedure the models often are not robust and will not work outside of a very small range of operating conditions around where the data was collected. A detailed explanation of and a review of the current literature is given in [6].

A VCS system is characterized by thermal and mechanical dynamics, the goal of the modeling is to keep the slower dynamics neglecting the faster. As the lower dynamic involve heat exchange between refrigerant and the cooling/heating fluid special attention must be paid to the heat exchanger modeling. Several methods of heat exchangers dynamic modeling are present in literature ([7],[6],[8]). The research interest is on the development of models that are mathematically simple but without losing relevant details. The modeling approach should be sufficiently accurate to capture the essential dynamic behavior, while remaining simple enough to provide insight into the dynamics and adequately tractable to be useful as a control design tool. In terms of approaches, the most important differences are in the ways in which the refrigerant in the heat exchanger is treated. The heat exchangers models can be generally classified into three groups: discretized models, lumped parameter models, and moving boundary models that can be seen as a variation of the lumped parameter approach where parameters are again lumped in regions defined by fluid phase, but the transition point between fluid phases is allowed to be a dynamic variable. The discretized volumes or finite difference approach results in models that are very accurate. These models are appropriate mainly for dynamic simulations and not for developing control algorithm or for predicting extensive transient. The appeal of this approach is the ability to accurately predict the refrigerant behavior. With these approaches, each heat exchanger is divided into a number of fixed and equal-sized control volumes (zones or cells). The conservation equations are discretized and solved over the volumes and result in a system of ordinary differential equations. A lumped parameter approach results in less complex sets of equations but it is not accurate in the superheat/subcooling detection. It is unable to capture lower dynamics due to the complex heat exchanger behavior associated with the moving boundary between the two-phase zone and the single-phase flow regions.

For these reasons the use of this models is not recommended in advanced controls development. Therefore, a lumped parameter model with a moving interface boundary is seen as the best solution to capturing these important dynamics, while preserving the simplicity of lumped parameter models. Central to this modeling approach is the ability to predict the effective position of phase change in a heat exchanger. The moving boundary approach seeks to capture the dynamics of multiple fluid phase heat exchangers while preserving the simplicity of lumped parameter models. It is quite important to get the trade-off between the finite-volume and moving-boundary model formulations. A moving-boundary model should require significantly less computation than a finite-volume approach because it utilizes a much smaller differential equation set. However, this approach utilizes lumped characteristics for each of the control volumes, as a mean void fraction for the two-phase zone, and this could penalize its accuracy.

2.4 Moving-boundary approach

In the moving-boundary lumped-parameter modeling approach, as shown schematically in Figure 2.4, heat exchangers are divided into control volumes or zones based on the fluid phase, and the effective model parameters are lumped in each zone, leading to a model of low dynamic order. The location of the boundary between fluid phase zones is a dynamic variable and varies throughout the length of the heat exchanger. The lumped parameter approach assumes an average of the distribution of each of the thermodynamic properties within each fluid phase zone as a single value that is treated as constant throughout the zone. This allows the use of only one control volume per fluid phase zone. This approach differs from finite volume methods that attempt to approximate property distributions by defining multiple control volumes within each fluid phase zone. In this way the partial differential equations describing the heat exchanger dynamic behaviour (mass, energy and momentum conservation) are applied to each zone. This allows a simplification of the derivation of the state variables describing completely the state and dynamics of the heat exchanger.

The combination of the zones gives the heat exchanger working modes. For the condenser five modes are considered: a) SH and TP when the refrigerant is respectively in a superheated and in a two-phase state, b) SH-TP when the refrigerant flow is described by two zones in the first it is in a superheated state and in the second is a two-phase mixture, c) TP-L when the refrigerant flow is characterized by two regions the first is in two-phase condition and the second corresponds to subcooled state and finally, the most common, d) the three regions model SH-TP-L. The evaporator has two model representations: a) TP when all the refrigerant flow can be described as two-phase

mixture and b) TP-SH when the superheated region appears. The switching criteria is to manage the transition from one mode to another. Figure 2.4 shows a typical transition during the drying cycle, in the first minutes the condenser operates with a TP-L model (if the refrigerant charge is sufficient to guarantee the presence of the subcooled region) and evaporator with a TP representation due to both the capillary tube dynamics and low thermal load. First, the transition from TP-L to SH-TP-L mode occurs and, after 10-15 minutes from the beginning of the cycle, also the evaporator switches to a two zones representation (TP-SH). These latter configurations are maintained until the end of the cycle.

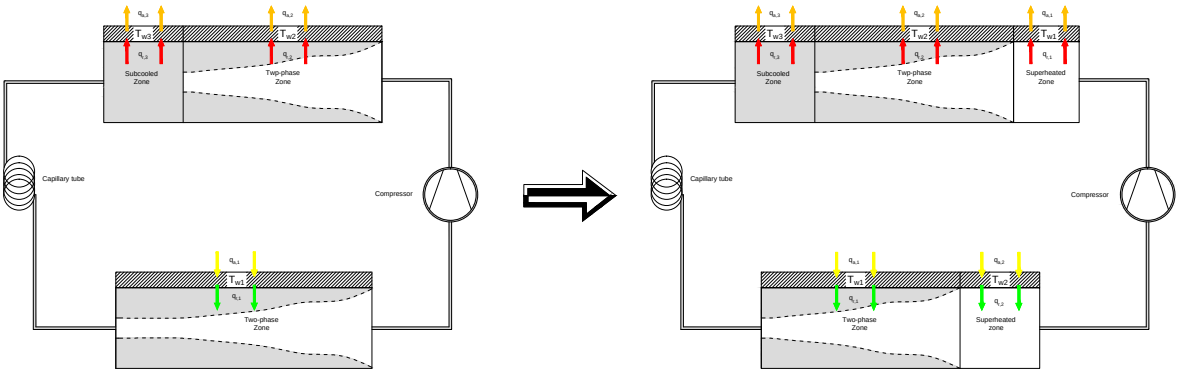

FIGURE 2.4: Transition from TP-L to SH-TP-L condenser mode and from TP to TP-SH evaporator mode.

The mathematical representation of the proposed model with moving-boundary approach is shown in Figure 2.5. Air mass flow rate, inlet temperature and specific humidity together with refrigerant inlet enthalpy and inlet and outlet mass flow rate are considered to be time dependent boundary conditions.

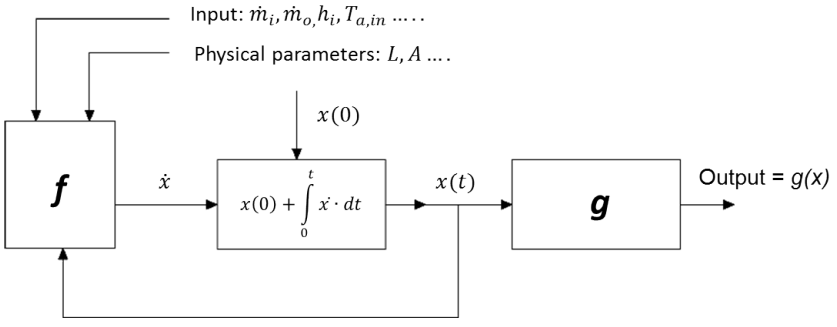

FIGURE 2.5: Mathematical solution scheme.

2.5 Condenser

The condenser heat exchanger is the component of the heat pump system that heats the air flow stream coming from the evaporator. As described in the previous section, the condenser is modeled using the moving boundary lumped parameter approach with mode switching capabilities. The condenser model has five possible operation modes (SH-TP-L, SH-TP, TP-L, TP and SH) depending on the boundary conditions. In this section details regarding the modeling assumptions, the governing conservation equations, the mean void fraction assumption, the derivation of each possible mode of the condenser with choice of state variables, and finally the switching criteria are provided.

2.5.1 Modeling assumptions

As usual in moving boundary lumped parameter approach ([9],[10],[11],[12],[13]), in order to reduce the overall order of the model and keep the model focused on the relevant dynamics of the described system, the following assumptions are made:

- the heat exchanger is modeled as a long circular tube whose length is many orders of magnitude larger than its diameter, in addition the cross sectional area is assumed to be constant;
- the refrigerant flows only in the longitudinal direction;
- axial heat conduction in the refrigerant is not considered;
- a linear profile of the refrigerant enthalpy on the single phases (subcooled and superheated regions) is assumed. This approach could be considered reliable if the length of the mono-phase zone is short: when the zone length is longer this approach can lead to impossible conditions at the outlet; for example, the outlet temperature associated with the enthalpy is colder than the wall temperature and/or the inlet air temperature (especially during the transient phase). To avoid this problem in [11] a log mean temperature profile is proposed. The approach fits an exponential temperature distribution across the zone assuming a saturated temperature condition at the inlet and that the outlet temperature is bounded by the wall temperature. The drawback of this method is that the outlet refrigerant temperature is determined by a non-linear equation, therefore, to solve for it an iterative solver must be used. The enthalpy distribution in the two phase region varies as function of the refrigerant quality (see Paragraph 2.5.3);
- a linear profile of the heat exchanger wall temperatures is assumed. The temperature at the boundary section is calculated as the weighted mean temperature

based on the length ratio of the neighboring regions [14] (see also Appendix A for other details);

- another common assumption is to neglect the pressure drop along the heat exchanger. In this work the pressure drops through the heat exchangers are not completely neglected since they reduce the heat transfer due to a reduction of the mean temperature between the air and the refrigerant. Furthermore they reduce the pressure at the capillary tube inlet section. The pressure drops through the heat exchangers are introduced in a static way therefore the equation of the momentum conservation is not considered (this reduce the complexity of the model). In other words the model assumes that pressure drop affects the heat transfer and the prediction of the mass flow rate through the capillary tube but it does not impact on the refrigerant dynamic;
- the heat exchanger walls have isotropic properties;
- the air is incompressible therefore no mass and energy accumulation occur.

2.5.2 Governing conservation equations

For each zone where the refrigerant can be assumed as: subcooled liquid, superheated vapor and two-phase flow the equation of the energy conservation and the equation of the mass conservation are written. On the hypothesis of one-dimensional flow and constant heat exchanger pipe section (as discussed in the above paragraph) the following equations can be written:

$$A \cdot \frac{\partial \rho}{\partial t} + \frac{\partial (\dot{m})}{\partial z} = 0 \tag{2.1}$$

$$A \cdot \frac{\partial (\rho \cdot u)}{\partial t} + \frac{\partial (\dot{m} \cdot h)}{\partial z} + \pi \cdot D_i \cdot \alpha_r \cdot (T_r - T_w) = 0 \tag{2.2}$$

hence Equation 2.1 expresses mass conservation instead Equation 2.2 expresses energy conservation applied at the refrigerant. In addition the term $\pi \cdot D_i \cdot \alpha_r \cdot (T_r - T_w)$ is the heat transfer between the refrigerant flow and wall. In the first term of Equation 2.2 appears the internal refrigerant energy, u, whose definition is:

$$\rho \cdot u = \rho \cdot h - p \tag{2.3}$$

Rearranging Equation 2.2 with the internal energy definition, the equation of the energy conservation becomes:

$$A \cdot \frac{\partial (\rho \cdot h - p)}{\partial t} + \frac{\partial (\dot{m} \cdot h)}{\partial z} + \pi \cdot D_i \cdot \alpha_r \cdot (T_r - T_w) = 0 \tag{2.4}$$

The wall dynamic behaviour is described by the equation of the energy conservation on the hypothesis of isotropic properties and constant cross-sectional area S:

$$(\rho \cdot c_p \cdot S)_w \frac{\partial T_w}{\partial t} = \pi \cdot D_i \cdot \alpha_r \cdot (T_w - T_r) + \pi \cdot D_i \cdot \alpha_a \cdot (T_a - T_w) \tag{2.5}$$

in the previous equation, in order to preserve the energy consistency, the first term of the numerator must be equal to the convective heat transfer that is added (e.g. evaporator) or removed (e.g. condenser) from the refrigerant. The second term: $\pi \cdot D_i \cdot \alpha_a \cdot (T_a - T_w)$ is the convective heat transfer from the heat exchanger tube wall to the air.

Equations 2.1, 2.2 and 2.5 are PDEs and are therefore unsuitable for numerical computation. In order to remove the spatial dependence completely, the equations are integrated along the length of the fluid phase zone that they describe. Within the current modeling framework some of the boundaries vary with time, hence in order to perform this integration, the general form of Leibniz's rule must be applied to the first term of the left hand side of the previous equations. By doing this the PDEs can be reduced to ordinary differential equations (ODEs) which are much more suitable for numerical computations [11].

$$\int_{z_1(t)}^{z_2(t)} \frac{\partial f(z,t)}{\partial t} \cdot dz = \frac{d}{dt}\left[\int_{z_1(t)}^{z_2(t)} f(z,t) \cdot dz\right] - f(z_2(t),t) \cdot \frac{d(z_2(t))}{dt} + f(z_1(t),t) \cdot \frac{d(z_1(t))}{dt} \tag{2.6}$$

2.5.3 Mean void fraction

All models in literature concerning moving-boundary use the assumption of the mean void fraction that leads to consider the two-phase region in lumped form [6]. A void fraction is the ratio between the vapor volume and the total volume and many correlations are available in literature for predicting void fraction under various conditions and fluids. One of the most used correlation is the Zivi's correlation [15] since is function only of the pressure and the refrigerant quality. Also in this work the correlation developed by Zivi is used and it is integrated along a quadratic relationship between the refrigerant quality and two-phase zone length L_{TP}, the quadratic relation is defined as follows:

$$x = \frac{x_i - x_o}{L_{TP}^2} \cdot z^2 + \frac{2}{L_{TP}} \cdot (x_o - x_i) \cdot z + x_i \tag{2.7}$$

where z is the spatial coordinate, x_i and x_o are respectively the inlet and the outlet refrigerant quality of the two-phase zone. The quadratic relation assumption derived from a stationary analysis with a finite volume software [16] in which the refrigerant

variables (subcooling, superheat, isentropic and volumetric compressor efficiencies) air temperatures and humidities values were imposed to the software model in addition to the geometric features of the heat exchangers. The values were experimentally deduced and related to the beginning of the drying cycle pseudo stationary phase (Paragraph 2.2). As shown in Figure 2.6 for the condenser the refrigerant quality trend along the heat exchanger (node) can be assumed quadratic whereas for the evaporator the assumption of linear profile can be used. Finally, the void fraction mean is defined as:

$$\bar{\gamma} = \frac{1}{L_{TP}} \cdot \int_0^{L_{TP}} \gamma(z) dz \tag{2.8}$$

γ is the Zivi's local void fraction correlation:

$$\gamma = \frac{1}{1 + \frac{1 - x(z)}{x(z)} \cdot \left(\frac{\rho_v}{\rho_l}\right)^{0.67}} \tag{2.9}$$

the void fraction mean is computed numerically.

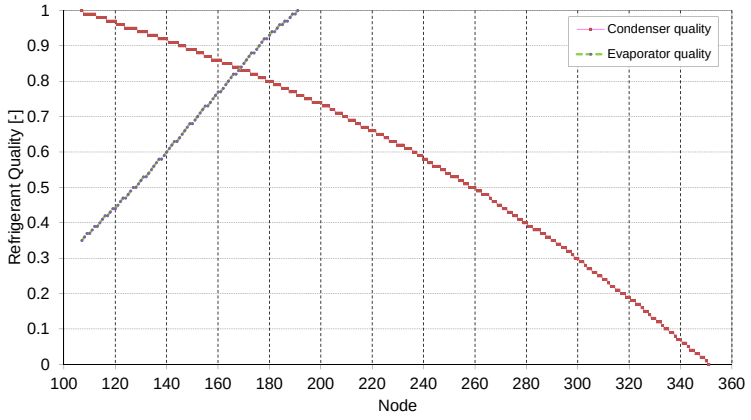

FIGURE 2.6: Refrigerant quality trends.

2.5.4 Condenser state variables

The state variables, with boundary known variables, are able to describe the overall state of the condenser. The choice of the state variables is a critical task since they affect the features of the model in terms of: computational robustness, energy and mass system integrity. In literature concerning moving boundary approach two methods are common: some models adopt the mean void fraction as a state variable, other models consider the outlet enthalpy as a state variable. Both approaches have advantages and drawbacks. In the models that use void fraction mean as state variable ([12],[17]) the mass is well conserved although not totally guaranteed during the switching of

some modes (e.g. from SH to SH-TP). In addition in order to predict the value of the outlet enthalpy as function of the outlet quality ($\bar{\gamma}(x_i, x_o, p) \implies x_o \implies h_o$) is necessary to solve a non-linear equation when the last zone is two-phase or to adopt a huge look-up tables correlating: mean void fraction, refrigerant pressure, inlet and outlet vapor quality. This increases the computational effort. If the outlet enthalpy is chosen as state variable the refrigerant mass conservation cannot be guaranteed as pointed out in [10] and [18]. In heat pump devices, especially when working with long transient (as in the drying cycle), the refrigerant mass strongly affects the performance of the devices, therefore in order to develop a model that is able to efficiently predict all the drying cycle and to compare different heat pump configurations (different heat exchangers and capillary tube geometries, and compressor displacement) the refrigerant mass conservation must be guaranteed. In this work a third solution is proposed in order to have an intrinsically mass conservative system. The average condenser density, ρ_c, is chosen as a state variable. The state variables vector chosen for representing the behaviour of the condenser heat exchanger is:

$$X = [p, \rho_c, \rho_3, L_2, T_{w1}, T_{w2}, T_{w3}]^T \tag{2.10}$$

where p is the condensation pressure, ρ_c is the mean condenser density, ρ_3 is the mean density of the subcooled zone and finally L_2 is the length of the two phase region. With these four variables the refrigerant in the condenser is completely described. All the condenser (seen as a system) is defined if three states are considered for the wall temperatures: T_{w1} is the wall mean temperature for the superheated zone, T_{w2} is the wall mean temperature for the two-phase zone and T_{w3} is the mean temperature of the liquid zone.

The boundary condition vector, X_{BC}, is defined as:

$$X_{BC} = [\dot{m}_{r,i}, \dot{m}_{r,o}, h_{r,i}, T_{a,i}, x_{a,i}, \dot{m}_{a,i}]^T \tag{2.11}$$

where: $\dot{m}_{r,i}$ is the inlet refrigerant mass flow rate, $\dot{m}_{r,o}$ is the outlet refrigerant mass flow rate, $h_{r,i}$ is the inlet enthalpy, $T_{a,i}$ is the air temperature at the condenser inlet section, $x_{a,i}$ is the air humidity ratio at the condenser inlet and $\dot{m}_{a,i}$ is the air mass flow rate crossing the condenser (no mass accumulations are taken into account therefore the inlet air mass flow rate is equal to the outlet mass flow rate).

2.5.5 SH-TP-L model

The first mode of the condenser assumes three distinct fluid phase zones within the heat exchanger with two moving boundaries at the phase transitions. This representations is the most common during the operation of the heat pump system during the drying cycle.

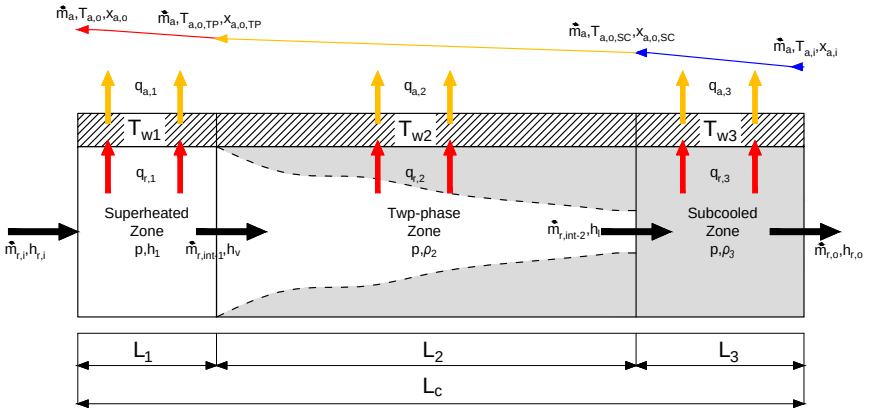

FIGURE 2.7: SH-TP-L model.

In the next sections refrigerant zone definition, with the choice of the state variables made in the previous paragraph, will be presented.

The **superheated zone** is described by pressure, p, and enthalpy h_1. The condensation pressure, p, is a state variable instead h_1 is computed knowing the inlet enthalpy $h_{r,i}$ (it is a boundary variable):

$$h_1 = \frac{h_{r,i} + h_v}{2} \tag{2.12}$$

where h_v is the vapor enthalpy. As discussed above, in this work, the effect of the pressure drop on the heat transfer is considered:

$$\Delta P_1 = 2 \cdot f \cdot \frac{G^2}{\rho} \cdot \frac{L_1}{D_i} + G^2 \cdot \left(\frac{1}{\rho_{o,1}} - \frac{1}{\rho_{i,1}} \right) \tag{2.13}$$

f is the friction factor and it is computed with the Haaland's approximation [19]. In addition G is the specific mass flow rate, $\rho_{o,1}$ and $\rho_{i,1}$ are respectively the refrigerant density at the inlet and outlet of the superheated zone. Therefore, considering the pressure drop, the mean pressure of the zone is:

$$p_1 = p - \frac{\Delta P_1}{2} \tag{2.14}$$

with the previous value of the pressure and the mean enthalpy, h_1, the mean temperature of the zone, $T_{r,1}$, is computed using the refrigerant properties and therefore the heat transfer from the refrigerant to the wall is evaluated as follows:

$$q_{r,1} = \pi \cdot D_i \cdot L_1 \cdot \alpha_{r,1} \cdot (T_{r,1} - T_{w1}) \tag{2.15}$$

where $\alpha_{r,1}$ is evaluated with the Gnielinski's correlation ([20]).

The **two phase zone** is described by pressure, p, and the mean density zone ρ_2:

$$\rho_2 = \rho_v \cdot \bar{\gamma} + \rho_l \cdot (1 - \bar{\gamma}) \tag{2.16}$$

$\bar{\gamma}$ is previously defined (see Paragraph 2.5.3).

The mean enthalpy of the zone, h_2, can be expressed as:

$$\begin{aligned} (\rho \cdot h)_2 = \frac{1}{L_2} \int_0^{L_2} \rho \cdot h \cdot dz &= \frac{1}{L_2} \int_0^{L_2} \left[\rho_v \cdot h_v \cdot \gamma + \rho_l \cdot h_l \cdot (1 - \gamma)\right] dz \\ &= \rho_v \cdot h_v \cdot \bar{\gamma} + \rho_l \cdot h_l \cdot (1 - \bar{\gamma}) \\ h_2 &= \frac{\rho_v \cdot h_v \cdot \bar{\gamma} + \rho_l \cdot h_l \cdot (1 - \bar{\gamma})}{\rho_2} \end{aligned} \tag{2.17}$$

In order to evaluate properly the pressure drop along the two-phase region and consequently the heat transfer from the refrigerant to the wall, the zone is divided into three elements since the refrigerant quality strongly affect both the convective heat flux and the estimation of the pressure drop. For each element the pressure drop with the Cavallini et al.'s procedure [21] (details [22]) is estimated and the convective heat transfer coefficient [23], for the the first element:

$$p_{2,1} = p - \Delta p_1 - \frac{\Delta p_{2,1}}{2} \tag{2.18}$$

with the corrected pressure is possible to evaluate the mean void fraction of the element with the Equation 2.8 and finally the mean enthalpy of the element, $h_{2,1}$, with Equation 2.17. With the refrigerant properties, knowing $p_{2,1}$ and $h_{2,1}$, is possible to evaluate the refrigerant temperature, $T_{r,2,1}$, in the two phase zone and consequently the heat transfer:

$$q_{r,2,1} = \pi \cdot D_i \cdot L_{2,1} \cdot \alpha_{r,1} \cdot (T_{r,2,1} - T_{w2}) \tag{2.19}$$

Therefore, the total pressure drop, the pressure at the outlet section of the TP zone and the total heat transfer may be evaluated as:

$$\Delta p_2 = \sum_{i=1}^{3} \Delta p_{2,i} \tag{2.20}$$

$$p_{2,o} = p - \Delta p_1 - \Delta p_2 \tag{2.21}$$

$$q_2 = \sum_{i=1}^{3} q_{r,2,i} \tag{2.22}$$

The **subcooled zone** is described by the pressure, p, and the mean density zone ρ_3. Both are state variables. In the same way of the superheated zone may be obtained the pressure drop along the liquid zone and hence the heat transfer, here only the following equations are reported:

$$p_3 = p - \Delta p_1 - \Delta p_2 - \frac{\Delta p_3}{2} \tag{2.23}$$

$$p \text{ and } \rho_3 \Longrightarrow h_3 \text{ and } p_3 \Longrightarrow T_{r,3} \tag{2.24}$$

$$q_3 = \pi \cdot D_i \cdot L_3 \cdot \alpha_{r,3} \cdot (T_{r,3} - T_{w3}) \tag{2.25}$$

where α_3 is evaluated, also in this case, with the Gnielinski's correlation [20].

Knowing the refrigerant mass inside the heat exchanger, at each time step, the lengths of the zones L_1 and L_3 can be obtained. The refrigerant mass inside the condenser, at each time step, may be evaluated as:

$$\rho_c \cdot L_c = \rho_1 \cdot L_1 + \rho_2 \cdot L_2 + \rho_3 \cdot L_3 \tag{2.26}$$

ρ_c and L_2 are state variables while ρ_1 and ρ_2 can be computed from the zone properties, therefore in the previous equation remaining only one unknown term: L_3 and hence:

$$L_3 = \frac{(\rho_c - \rho_1) \cdot L_c + (\rho_1 - \rho_2) \cdot L_2}{\rho_3 - \rho_1} \tag{2.27}$$

and L_1:

$$L_1 = L_c - L_2 - L_3 \tag{2.28}$$

Finally, with the assumption of enthalpy linear profile, the enthalpy at the condenser outlet can be computed:

$$h_o = 2 \cdot h_3 - h_l \tag{2.29}$$

2.5.6 SH-TP model

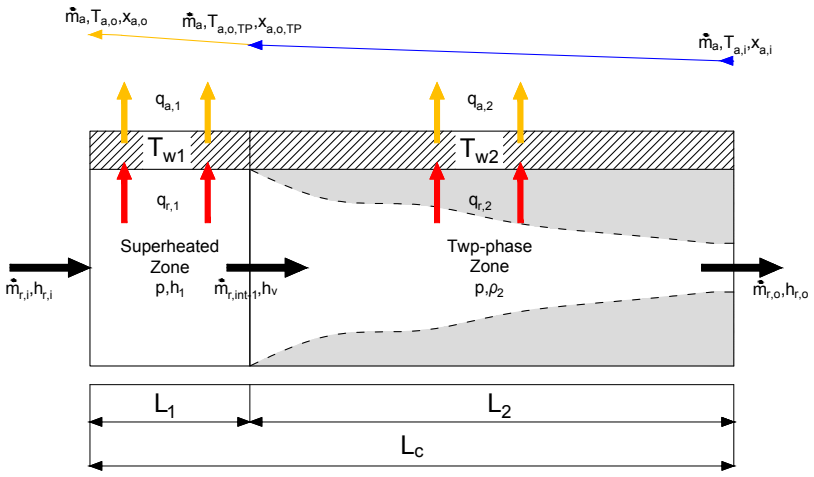

FIGURE 2.8: SH-TP model.

The second mode of the condenser assumes two distinct fluid phase zones, superheated (SH) and two-phase (TP), with one moving boundary at the phase transition (L1). In this model the subcooled zone is lost.

As in the SH-TP-L model the **superheated zone** is described by pressure p and $h1$.

The **two phase zone** is described by pressure p and the mean density zone ρ_2. Different from the SH-TP-L model in this condenser mode the density of the two-phase region is deduced from the refrigerant mass inside the condenser:

$$\rho_c \cdot L_c = \rho_1 \cdot L_1 + \rho_2 \cdot L_2 \tag{2.30}$$

where ρ_c and L_2 are state variables and the definition of the L_1 is trivial: $L_1 = L_c - L_2$, therefore the mean density of the two-phase region may be expressed as:

$$\rho_2 = \rho_1 + \frac{L_c}{L_2} \cdot (\rho_c - \rho_1) \tag{2.31}$$

Computing the value of the outlet enthalpy is less trivial, first a non-linear equation must be solved in order to predict the refrigerant outlet quality x_o and then, knowing the refrigerant pressure, the outlet enthalpy can be evaluated. The value of the void fraction mean can be computed since the mean density of the two phase zone (ρ_2) and

the refrigerant pressure are known:

$$\bar{\gamma} = \frac{\rho_2 - \rho_l}{\rho_g - \rho_l} \tag{2.32}$$

this value must be equal to the Zivi's void fraction mean (see Equation 2.8):

$$\bar{\gamma} - \bar{\gamma}_{Zivi}(x_i, x_o, p) = 0 \tag{2.33}$$

in this model $x_i = 1$. The previous equation is solved with a find-root algorithm (*Regula Falsi* algorithm is used in this work).

Also for this model, the heat transfer between the refrigerant node and the wall is reduced considering the refrigerant pressure drop in a static way, as discussed when the SH-TP-L mode has been presented (see Paragraph 2.5.5).

2.5.7 TP-L model

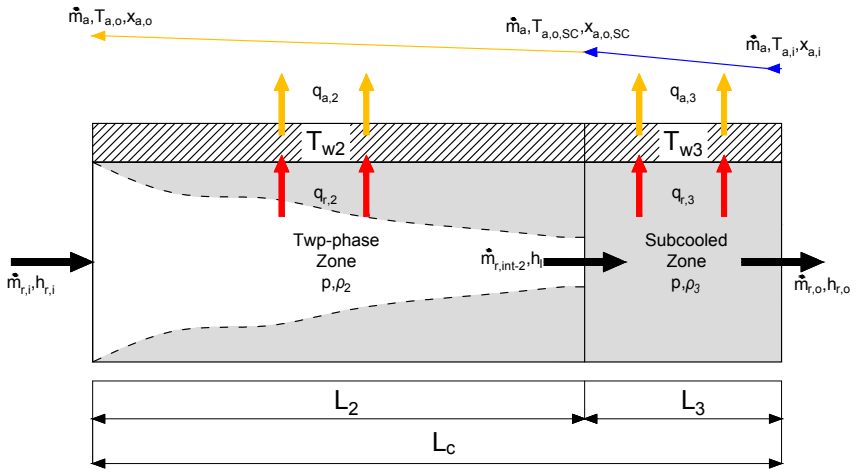

FIGURE 2.9: TP-L model.

The third mode of the condenser assumes two distinct fluid phase zones, the two-phase (TP) and the subcooled zone (L), with one moving boundary at the phase transition (L_2). In this model the superheated zone does not exist.

The **two phase zone** is described by pressure, p, and the mean density zone, ρ_2. The mean density of the two-phase zone is defined through the Zivi's void fraction mean. Knowing the inlet enthalpy (it is a boundary variable) and the condensation pressure from the refrigerant properties, the refrigerant inlet quality can be computed (the refrigerant outlet quality in this model is equal to 0), therefore also the mean void fraction

mean can be evaluated. The mean density of the zone is finally computed with the Equation 2.16.

The **subcooled zone** is described by the pressure, p, and the mean density zone, ρ_3.

The extension of the subcooled zone is deduced from the state variable: L_2. The outlet enthalpy is computed as in Equation 2.29.

2.5.8 TP model

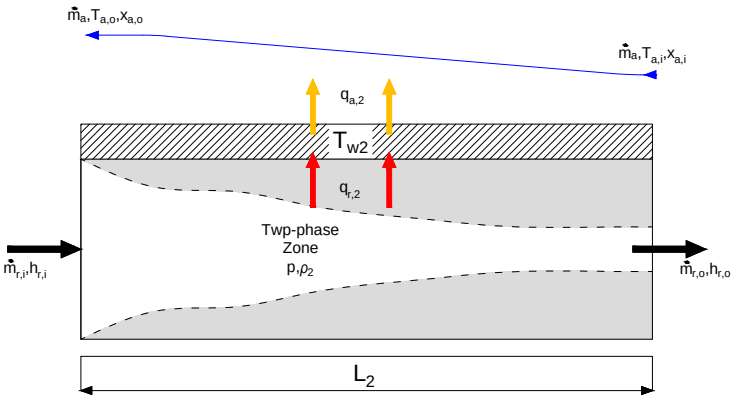

FIGURE 2.10: TP model.

The fourth mode of the condenser assumes one fluid two-phase zone throughout the heat exchanger. This mode typically occurs as a transitional mode during startup cycling operations with high value of the refrigerant charge and capillary tube not properly designed.

In this model, the mean density of the two phase zone is equal to the mean density of the heat exchanger: $\rho_c = \rho_2$. As in the SH-TP model, the quality at the outlet section is computed with the Equation 2.33.

2.5.9 SH model

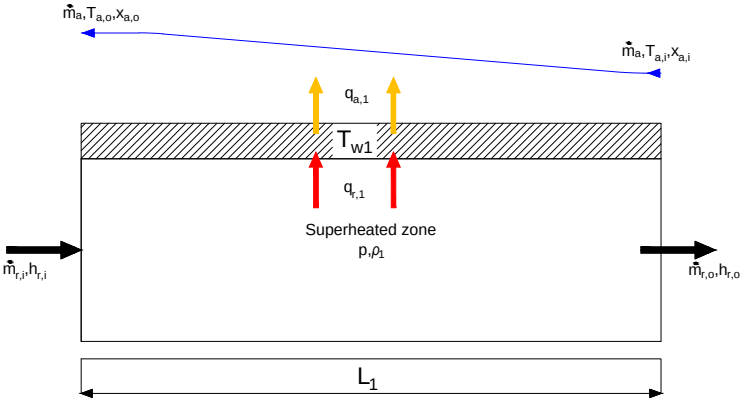

FIGURE 2.11: SH model.

The fifth mode of the condenser works with one superheated zone throughout the heat exchanger. In this model the zone mean density is equal to the mean density of the heat exchanger: $\rho_c = \rho_1$. The outlet enthalpy is assumed to be equal to the mean enthalpy h_1. This is computed since p and ρ_1 are known.

2.5.10 Governing equations SH-TP-L model

As already pointed out, for each zone where the refrigerant can be considered as superheated, subcooled and two-phase mix the equation of energy and mass conservation are written. In addition, each wall zone is described with a time dependent thermal capacity. Here, the final expression of the equations are reported (for a full derivation procedure the interested reader can see Appendix A).

Superheated zone

Conservation of refrigerant mass:

$$A \cdot L_1 \cdot \left.\frac{\partial \rho_1}{\partial p}\right|_{h_i} \cdot \frac{dp}{dt} + A \cdot (\rho_1 - \rho_v) \cdot \frac{dL_1}{dt} + \dot{m}_{int-1} = \dot{m}_i - A \cdot L_1 \cdot \left.\frac{\partial \rho_1}{\partial h_i}\right|_{p} \cdot \frac{dh_i}{dt} \tag{2.34}$$

Conservation of refrigerant energy:

$$\begin{aligned} A \cdot L_1 \cdot \left(\left.\frac{\partial (\rho \cdot h)_1}{\partial p}\right|_{h_i} - 1 \right) \cdot \frac{dp}{dt} + A \cdot ((\rho \cdot h)_1 - (\rho \cdot h)_v) \cdot \frac{dL_1}{dt} + \dot{m}_{int-1} \cdot h_v = \\ \dot{m}_i \cdot h_i - A \cdot L_1 \cdot \left.\frac{\partial (\rho \cdot h)_1}{\partial p}\right|_{p} \cdot \frac{dh_i}{dt} + q_{r,1} \end{aligned} \tag{2.35}$$

Conservation of wall energy:

$$\frac{dT_{w1}}{dt} = \frac{q_{r,1} + q_{a,1}}{(m \cdot c_p)_{w1}} - \frac{T_{w1} - T_{w2}}{L_1 + L_2} \cdot \frac{dL_1}{dt} \tag{2.36}$$

Two-phase zone

Conservation of refrigerant mass:

$$A \cdot L_2 \cdot \frac{d\rho_2}{dp} \cdot \frac{dp}{dt} + A \cdot (\rho_v - \rho_l) \cdot \frac{dL_1}{dt} + A \cdot (\rho_2 - \rho_l) \cdot \frac{dL_2}{dt} - \dot{m}_{int-1} + \dot{m}_{int-2} = 0 \tag{2.37}$$

Conservation of refrigerant energy:

$$\begin{aligned} &A \cdot L_2 \cdot \left(\frac{\partial (\rho \cdot h)_2}{\partial p} - 1 \right) \cdot \frac{dp}{dt} + A \cdot ((\rho \cdot h)_v - (\rho \cdot h)_l) \cdot \frac{dL_1}{dt} \\ &+ A \cdot ((\rho \cdot h)_2 - (\rho \cdot h)_l) \cdot \frac{dL_2}{dt} - \dot{m}_{int-1} \cdot h_v + \dot{m}_{int-2} \cdot h_l = q_{r2} \end{aligned} \tag{2.38}$$

Conservation of wall energy:

$$\begin{aligned} \frac{dT_{w2}}{dt} = \frac{q_{r,2} + q_{a,2}}{(m \cdot c_p)_{w2}} - \left[\frac{T_{w1}}{L_1 + L_2} + \frac{T_{w2}}{L_2} \cdot \left(\frac{L_1}{L_1 + L_2} - \frac{L_3}{L_1 + L_2} \right) - \frac{T_{w3}}{L_2 + L_3} \right] \cdot \frac{dL_1}{dt} - \\ - \frac{T_{w2} - T_{w3}}{L_2 + L_3} \cdot \frac{dL_2}{dt} \end{aligned} \tag{2.39}$$

Subcooled zone

Conservation of refrigerant mass:

$$A \cdot L_3 \cdot \frac{d\rho_3}{dt} + A \cdot (\rho_l - \rho_3) \cdot \frac{dL_1}{dt} + A \cdot (\rho_l - \rho_3) \cdot \frac{dL_2}{dt} - \dot{m}_{int-2} = -\dot{m}_o \tag{2.40}$$

Conservation of refrigerant energy:

$$\begin{aligned} &A \cdot L_3 \cdot \left(\rho_3 \cdot \left. \frac{\partial h_3}{\partial p} \right|_{\rho_3} - 1 \right) \cdot \frac{dp}{dt} + A \cdot L_3 \cdot \left(\rho_3 \cdot \left. \frac{\partial h_3}{\partial \rho_3} \right|_{p} + h_3 \right) \cdot \frac{d\rho_3}{dt} + \\ &A \cdot ((\rho \cdot h)_l - (\rho \cdot h)_l) \cdot \frac{dL_1}{dt} + A \cdot ((\rho \cdot h)_l - (\rho \cdot h)_3) \cdot \frac{dL_2}{dt} - \dot{m}_{int-2} \cdot h_l = -\dot{m}_o \cdot h_o + q_{r3} \end{aligned} \tag{2.41}$$

Conservation of wall energy:

$$\frac{dT_{w3}}{dt} = \frac{q_{r,3} + q_{a,3}}{(m \cdot c_p)_{w3}} - \frac{T_{w2} - T_{w3}}{L_2 + L_3} \cdot \left(\frac{dL_1}{dt} + \frac{dL_2}{dt} \right) \tag{2.42}$$

Condenser conservation of refrigerant mass

$$A \cdot L_c \cdot \frac{d\rho_c}{dt} = \dot{m}_i - \dot{m}_o \tag{2.43}$$

Equations from 2.34 to 2.42 describe the time evolution of the state variables when the mode of the condenser is SH-TP-L. Some derivatives of the state variables are already made explicit (wall temperatures and the condenser mean density ρ_c) for the other (p, L_2, ρ_3) must be solved, at each time step the algebraic system ($A \cdot y = b$), composed by Equations: 2.34, 2.35, 2.37, 2.38, 2.40 and 2.41 that are energy and mass conservation for each refrigerant zone. The unknown vector, y, is:

$$y = \left[\frac{dp}{dt}, \frac{d\rho_3}{dt}, \frac{dL_1}{dt}, \frac{dL_2}{dt}, \dot{m}_{int-1}, \dot{m}_{int-2} \right] \tag{2.44}$$

Some coefficients of the algebraic system (A) are the partial derivative of functions that express specific refrigerant properties. These coefficients are numerically computed (details in Appendix A.0.3 and [24]).

2.5.11 Governing equations SH-TP model

In this condenser mode the superheated zone is described by the same derived equations for the SH-TP-L model. Instead, the governing equations for the two-phase zone (TP) are the following.

Conservation of refrigerant mass:

$$A \cdot L_2 \cdot \frac{d\rho_2}{dt} + A \cdot (\rho_g - \rho_2) \cdot \frac{dL_1}{dt} - \dot{m}_{int-1} = -\dot{m}_o \tag{2.45}$$

Conservation of refrigerant energy:

$$\begin{aligned} &A \cdot L_2 \cdot \left(\rho_2 \cdot \left. \frac{\partial h_2}{\partial p} \right|_{\rho_2} - 1 \right) \cdot \frac{dp}{dt} + A \cdot L_2 \cdot \left(\rho_2 \cdot \left. \frac{\partial h_2}{\partial \rho_2} \right|_{p} + h_2 \right) \cdot \frac{d\rho_2}{dt} + \\ &+ A \cdot \left((\rho \cdot h)_v - (\rho \cdot h)_2 \right) \cdot \frac{dL_1}{dt} - \dot{m}_{int-1} \cdot h_g = -\dot{m}_o \cdot h_o + q_{r2} \end{aligned} \tag{2.46}$$

Conservation of wall energy:

$$\frac{dT_{w2}}{dt} = \frac{q_{r,2} + q_{a,2}}{(m \cdot c_p)_{w2}} - \frac{T_{w1} - T_{w2}}{L_c} \cdot \frac{dL_1}{dt} \tag{2.47}$$

in addition, in this model:

$$\frac{dT_{w1}}{dt} = \frac{q_{r,1} + q_{a,1}}{(m \cdot c_p)_{w1}} - \frac{T_{w1} - T_{w2}}{L_c} \cdot \frac{dL_1}{dt} \tag{2.48}$$

$$\frac{dL_2}{dt} = -\frac{dL_1}{dt} \tag{2.49}$$

In this condenser mode the subcooled zone does not exist, this zone implodes and the state variables (ρ_3 and T_{w3}), that describe it, need to be tracked to a suitable value adopting a pseudo-state equation as suggested by Pettit et al. [25] and Li and Alleyne [17]. Therefore, they were tracked as follows:

$$\frac{d\rho_3}{dt} = K_\rho \cdot (\rho_{l-track} - \rho_3) \tag{2.50}$$

$$\frac{dT_{w3}}{dt} = K_T \cdot (T_{w2} - T_{w3}) \tag{2.51}$$

where $\rho_{l-track}$ is computed as follows:

$$h_3 = \frac{h_o + h_l}{2} \implies \rho_{l-track} = \rho_3(p, h_3) \tag{2.52}$$

The K values, in the previous equations, are constant and are chosen appropriately to make tracking occur quickly compared to the system dynamics. Eqs. 2.34 2.35, 2.45, 2.46, form a set of four linear equations ($A \cdot y = b$) where y has some derivative of the state variables. The y vector is defined as:

$$y = \left[\frac{dp}{dt}, \frac{d\rho_2}{dt}, \frac{dL_1}{dt}, \dot{m}_{int-1}\right] \tag{2.53}$$

The y vector and Eqs. 2.47,2.48, 2.50, 2.51, 2.43 allow to define all the derivative states for this condenser mode.

2.5.12 Governing equations TP-L model

In this mode, the condenser has lost the superheated zone. The TP-L condenser mode proposed in this work is different from how pointed out in Cervato [24]. Due to the choice of the condenser state variables in this model there is a surplus of information, since ρ_c and ρ_3 are already able to describe completely the model, therefore expressing one of the state variables as function of the other is required. Here, the length of the two phase zone (L_2 is state variable) is made function of: p, ρ_c, ρ_3 and a boundary condition h_i as follows:

$$\frac{dL_2}{dt} = A_{L_2} \cdot \frac{d\rho_c}{dt} + B_{L_2} \cdot \frac{dp}{dt} + C_{L_2} \cdot \frac{d\rho_3}{dt} + D_{L_2} \cdot \frac{dh_i}{dt} \tag{2.54}$$

where A_{L_2}, B_{L_2}, C_{L_2} and D_{L_2} are appropriate coefficients (for the full derivation of the governing equations of the TP-L model see Appendix B).

Two-phase zone

Conservation of refrigerant mass:

$$\begin{aligned} &A \cdot \left[L_2 \cdot \left. \frac{\partial \rho_2}{\partial p} \right|_{h_i} + (\rho_2 - \rho_l) \cdot B_{L_2} \right] \cdot \frac{dp}{dt} + A \cdot (\rho_2 - \rho_l) \cdot C_{L_2} \cdot \frac{d\rho_3}{dt} + \\ &+ A \cdot (\rho_2 - \rho_l) \cdot A_{L_2} \cdot \frac{d\rho_c}{dt} + \dot{m}_{int-1} = \dot{m}_i - A \cdot \left[L_2 \cdot \left. \frac{\partial \rho_2}{\partial h_i} \right|_p + (\rho_2 - \rho_l) \cdot D_{L_2} \right] \cdot \frac{dh_i}{dt} \end{aligned} \tag{2.55}$$

Conservation of refrigerant energy:

$$\begin{aligned} &A \cdot \left[L_2 \cdot \left[\left. \frac{\partial (\rho h)_2}{\partial p} \right|_{h_i} - 1 \right] + [(\rho h)_2 - (\rho h)_l] \cdot B_{L_2} \right] \cdot \frac{dp}{dt} + [(\rho h)_2 - (\rho h)_l] \cdot C_{L_2} \cdot \frac{d\rho_3}{dt} + \\ &A \cdot [(\rho h)_2 - (\rho h)_l] \cdot A_{L_2} \cdot \frac{d\rho_c}{dt} + \dot{m}_{int-1} \cdot h_l = \dot{m}_i \cdot h_i + q_{r,2} - \\ &\left[A \cdot L_2 \cdot \left. \frac{\partial (\rho h)_2}{\partial h_i} \right|_p + A \cdot [(\rho h)_2 - (\rho h)_l] \cdot D_{L_2} \right] \cdot \frac{dh_i}{dt} \end{aligned} \tag{2.56}$$

Subcooled zone

Conservation of refrigerant energy:

$$\begin{aligned} &A \cdot \left[L_3 \cdot \left[\rho_3 \cdot \left. \frac{\partial h_3}{\partial p} \right|_{\rho_3} - 1 \right] + B_{L_2} \cdot [(\rho h)_l - (\rho h)_3] \right] \cdot \frac{dp}{dt} + A \cdot \left[L_3 \cdot \left[\rho_3 \cdot \left. \frac{\partial h_3}{\partial \rho_3} \right|_p + h_3 \right] \right. \\ &\left. + C_{L_2} \cdot [(\rho h)_l - (\rho h)_3] \right] \cdot \frac{d\rho_3}{dt} + A_{L_2} \cdot [(\rho h)_l - (\rho h)_3] \cdot \frac{d\rho_c}{dt} - \dot{m}_{int-1} \cdot h_l = \\ &= -\dot{m}_o \cdot h_o + q_{r,3} - A \cdot D_{L_2} \cdot [(\rho h)_l - (\rho h)_3] \cdot \frac{dh_i}{dt} \end{aligned} \tag{2.57}$$

The fourth equation, in order to define all the state variables needed for this mode, is the global equation of the mass conservation over the condenser:

$$A \cdot L_c \cdot \frac{d\rho_c}{dt} = \dot{m}_i - \dot{m}_o \tag{2.58}$$

With Equations: 2.55, 2.56, 2.57 and 2.58 the TP-L model is described and the unknown terms may be determined. In this model the unknown terms are the time derivatives of the condensation pressure (dp/dt), the mean density of the subcooled zone ($d\rho_3/dt$), the mean density of the condenser ($d\rho_c/dt$) and finally the boundary mass flow rate between TP ad L zone ($\dot{m}_{int-1}$). The time derivative of the two-phase zone length is computed with the definition given in: 2.54. To conclude, no refrigerant state variables are tracked since all are defined.

The wall derivatives have the identical form of Equation 2.47 and the wall of the superheated zone, T_{w1}, must be tracked to the two-phase wall temperature, T_{w2}.

2.5.13 Governing equations TP model

In this mode the condenser has lost two zones: the superheated and the subcooled zone. In order to define two thermodynamic variables that describe it (p and ρ_2) two equations must be introduced: the first is the equation of the mass conservation and the second is the conservation of refrigerant energy. Naturally, in this mode, the mean density of the two-phase zone is equal to the mean density of the condenser: $\rho_2 = \rho_c$. The wall state, T_{w2}, is defined applying the equation of the energy conservation.

Conservation of refrigerant mass:

$$A \cdot L_2 \cdot \frac{d\rho_2}{dt} = \dot{m}_i - \dot{m}_o \tag{2.59}$$

Conservation of refrigerant energy:

$$A \cdot L_c \cdot \left(\rho_2 \cdot \left.\frac{\partial h_2}{\partial p}\right|_{\rho_2} - 1 \right) \cdot \frac{dp}{dt} + A \cdot L_c \cdot \left(\rho_2 \cdot \left.\frac{\partial h_2}{\partial \rho_2}\right|_{p} + h_2 \right) \cdot \frac{d\rho_2}{dt} = \dot{m}_i \cdot h_i - \dot{m}_o \cdot h_o + q_{r,2} \tag{2.60}$$

Conservation of wall energy:

$$\frac{dT_{w2}}{dt} = \frac{q_{r,2} + q_{a,2}}{(m \cdot c_p)_{w2}} \tag{2.61}$$

The solution of the system of Equations (2.59 and 2.60) gives the following vector, y:

$$y = \left[\frac{dp}{dt}, \frac{d\rho_2}{dt} \right] \tag{2.62}$$

In addition for the refrigerant side, to define all the state variables, two pseudo state equations are introduced, the first tracks the length of the two-phase zone, L_2, at the condenser pipe length:

$$\frac{dL_2}{dt} = \begin{cases} K_L \cdot (L_c - \delta L - L_2) & h_o < h_l \text{ or } SH > 0.5\ ^\circ\text{C} \\ K_L \cdot (L_c - L_2) & \text{otherwise} \end{cases} \tag{2.63}$$

where: $\delta L = 10^{-3}$ and $SH = T_{r,i} - T_{r,v}$ (difference between the inlet refrigerant temperature and dew temperature at the condensation pressure). The second pseudo state equation tracks the mean density of the subcooled zone as shown in 2.51. Clearly, the

wall state variable of the superheated zone must be tracked to a suitable value:

$$\frac{dT_{w1}}{dt} = K_T \cdot (T_{w2} - T_{w1}) \tag{2.64}$$

as it is clear from the previous, the wall temperature of the superheated zone is tracked to the two-phase zone wall temperature. The wall states of the subcooled zone is tracked as follows:

$$\frac{dT_{w3}}{dt} = K_T \cdot (T_{w2} - T_{w3}) \tag{2.65}$$

2.5.14 Governing equations SH model

The fifth mode of the condenser assumes one superheated zone throughout the heat exchanger. As for the TP model, in order to define the two thermodynamic variables, that describe it (p and $\rho_1 = \rho_c$) two equations must be introduced: the first is the equation of the mass conservation and the second is the conservation of refrigerant energy. The wall state, T_{w1}, is defined applying the equation of the energy conservation.

Conservation of refrigerant mass:

$$A \cdot L_1 \cdot \frac{d\rho_1}{dt} = \dot{m}_i - \dot{m}_o \tag{2.66}$$

Conservation of refrigerant energy:

$$A \cdot L_c \cdot \left(\rho_1 \cdot \left.\frac{\partial h_1}{\partial p}\right|_{\rho_1} - 1 \right) \cdot \frac{dp}{dt} + A \cdot L_c \cdot \left(\rho_1 \cdot \left.\frac{\partial h_1}{\partial \rho_1}\right|_{p} + h_1 \right) \cdot \frac{d\rho_1}{dt} = \dot{m}_i \cdot h_i - \dot{m}_o \cdot h_o + q_{r,1} \tag{2.67}$$

Conservation of wall energy:

$$\frac{dT_{w1}}{dt} = \frac{q_{r,1} + q_{a,1}}{(m \cdot c_p)_{w1}} \tag{2.68}$$

The time derivate of the two-phase length is equal to zero since it does not exist, however, near to the switching phase, it is computed as follows:

$$\frac{dL_2}{dt} = \begin{cases} K_L \cdot (L_{2,track} - L_2) & \rho_c > \rho_1 \text{ and } h_i > h_g \Longrightarrow \text{SH-TP model} \\ K_L \cdot (L_c - L_2) & \rho_c > \rho_1 \text{ and } h_i < h_g \Longrightarrow \text{TP model} \\ K_L \cdot (0 - L_2) & \text{otherwise} \end{cases} \tag{2.69}$$

where $L_{2,track}$ is defined as:

$$L_{2,track} = L_c \cdot \frac{\rho_c - \rho_1}{\rho_{2,swt} - \rho_1} \tag{2.70}$$

and hence $\rho_{2,swt}$:

$$\rho_{2,swt} = \begin{cases} \rho_v & x_o > 1 \\ \rho_v \cdot \bar{\gamma} + \rho_l \cdot (1 - \bar{\gamma}) & \text{otherwise} \end{cases} \tag{2.71}$$

Hence, near to the transition from SH to TP model the length of the two phase zone is tracked to the condenser length, instead, near to the transition from SH to SH-TP model it is tracked to a value that is able to explain the refrigerant charge inventory in the condenser according to the choice of the void fraction mean correlation that has been made. The other state variables are tracked as follows:

$$\frac{dT_{w2}}{dt} = K_T \cdot (T_{dew} - 1 - T_{w2}) \tag{2.72}$$

$$\frac{dT_{w3}}{dt} = K_T \cdot (T_{w1} - T_{w3}) \tag{2.73}$$

$$\frac{d\rho_3}{dt} = K_\rho \cdot (\rho_l - \rho_3) \tag{2.74}$$

2.5.15 Switching criteria

In this section the criteria used to trigger the model to switch between the five modes will be shown. The model uses the state variables and boundary conditions, at each time step, to decide which mode is the best for describing the condenser in that point in time. The criteria are mainly based on the refrigerant mass integrity of the system: at each point in time, knowing the boundary conditions and the state variables, can be computed the length of the zones. These lengths are compared with constant values that indicate if a zone can occur. Hence, before to trigger the model switch, some variables are determined:

$$\rho_1 = \rho(p, h_1) \tag{2.75}$$

$$\rho_{2,TP-L} = \frac{\rho_c \cdot L_c - \rho_3 \cdot (L_c - L_2)}{L_2} \tag{2.76}$$

$$L_{3,TP-L} = L_c - L_2 \tag{2.77}$$

$$\rho_{2,SH-TP-L} = \rho_v \cdot \bar{\gamma}_{SH-TP-L} + \rho_l \cdot (1 - \bar{\gamma}_{SH-TP-L}) \tag{2.78}$$

$$\text{where: } \bar{\gamma}_{SH-TP-L} = \bar{\gamma}(p, x_i = 1, x_o = 0)$$

$$L_{3,SH-TP-L} = \frac{(\rho_c - \rho_1) \cdot L_c + (\rho_1 - \rho_{2,SH-TP-L}) \cdot L_2}{\rho_3 - \rho_1} \tag{2.79}$$

$$L_{1,SH-TP-L} = L_c - L_2 - L_{3,SH-TP-L} \tag{2.80}$$

$$L_{1,SH-TP} = L_c - L_2 \tag{2.81}$$

Therefore, using the previous definitions, the **SH-TP-L model** occurs if the following conditions are accomplished:

$$\rho_3 > \rho_l \qquad L_{1,SH-TP-L}/L_c > 10^{-3} \qquad L_{3,SH-TP-L}/L_c > 10^{-3} \qquad \rho_1 < \rho_g \tag{2.82}$$

These conditions state that the SH-TP-L mode occurs when the mean density of the subcooled zone is greater than the liquid (at the condensation pressure), when the mean density of the superheated zone is lower than the vapor, in addition, the lengths of the superheated and subcooled zone must be greater than a minimum value ($L_c \cdot 10^{-3}$).

The **SH-TP model** occurs if the following conditions are respected:

$$L_{1,SH-TP}/L_c > 10^{-3} \qquad L_{3,SH-TP-L}/L_c < 10^{-3} \qquad \rho_1 < \rho_g \tag{2.83}$$

These conditions say that the length of the superheated (SH) zone must be greater than a minimum value ($L_c \cdot 10^{-3}$) and the length of the subcooled zone (L) must be nearly to zero. Finally, the mean density of the superheated zone must be lower than the vapor density.

The **TP-L model** occurs if the following conditions are achieved:

$$L_{3,TP-L}/L_c > 10^{-3} \qquad \rho_c > \rho_{2,TP-L} \qquad \rho_3 > \rho_l \qquad h_i < h_v \tag{2.84}$$

The previous conditions indicate that the TP-L model can occur when the length of the subcooled zone is greater than a minimum value, when the mean density of the two-phase zone is lower than the mean density of the condenser: this condition says that the refrigerant charge inventory in the condenser is greater than the mass in two-phase zone. Therefore, the difference may be balanced from a subcooled zone if its density is greater than the liquid and its length is greater than zero. Additionally, the inlet enthalpy must be lower than the vapor value.

The **TP model** occurs if the following condition is achieved:

$$L_{3,TP-L}/L_c < 10^{-3} \tag{2.85}$$

hence, if the length of the subcooled zone is lower than a minimum value.

Finally, the **SH model** occurs if the following conditions are achieved:

$$\rho_c < \rho_v \qquad L_2/L_c < 10^{-3} \qquad h_i > h_v \tag{2.86}$$

in this condenser mode, the refrigerant inventory is explained only if the mean density is lower than the vapor value. Inlet enthalpy value and length of the two phase zone are also checked. To conclude: the above reported conditions are checked at each time step, however if no condition is fulfilled the model remains in the same model of the previous time step (this is implemented with a discrete variable).

2.5.16 Governing equations air side

With reference to the Figure 2.7 a counterflow arrangement is assumed, the air from the evaporator exchanges first with the subcooled zone, after with the two-phase region and finally with the superheated zone. Clearly, this assumption is made according with the layout of the heat pump. The air thermal inertia is negligible, therefore its dynamic behaviour was neglected. A mean air-side heat transfer coefficient along the heat exchanger is assumed. The heat exchange is realized between the air flow stream and the mean temperature of the wall (free tube area and fins area) of each zone that can be considered as a hot fluid that does not change its temperature, consequently the ε-NTU relation can be applied for heat exchangers where a fluid has infinity capacity:

$\varepsilon = 1 - e^{-NTU}$ where NTU is evaluated for each zone as follows:

$$NTU_{zone} = \frac{K_\alpha \cdot \alpha_{w,a} \cdot (\eta_0 + \Delta\eta_0) \cdot A_e \cdot \left(\frac{L_{zone}}{L_c}\right)}{\dot{m}_a \cdot \bar{c_{p_a}}} \tag{2.87}$$

where A_e is the total heat transfer area of the finned tube heat exchanger, the term η_0 is the overall surface efficiency (details in [26]). The mean heat transfer coefficient $\alpha_{w,a}$ is evaluated with different correlations depending on the fin pattern (plain [27], wavy [28] and louvered [29]). In practice, considering the air process circuit of the tumble dryer, the previous correlations cannot be considered totally reliable hence a gain, K_α,was introduced in order to tune the model. Additionally, some tested heat exchangers with this model had a not negligible contact resistance between tube and fins. To penalize the overall heat transfer coefficient another term, $\Delta\eta_0$, was introduced, that increases or decreases the surface efficiency.

Before computing the zone outlet conditions, the wall temperature is compared with the dew temperature of the air at the inlet conditions. If the wall temperature is higher than the dew temperature there is not mass transfer phenomenon and the outlet temperature is computed as:

$$T_{a,zone,o} = T_{w,zone} - (T_{w,zone} - T_{a,zone,i}) \cdot e^{-NTU} \tag{2.88}$$

in this case the outlet humidity ratio is equal to the inlet value (knowing the temperature and the specific humidity is trivial to define the outlet enthalpy). Instead, if the air temperature at the zone inlet section is less than the dew point, mass transfer phenomena occur on the finned surface. Assuming the humidity air enthalpy as the driving potential for total heat transfer, considering the lower value of the potential the air enthalpy in saturation condition at the temperature of the wall ($h_{w,s}$), therefore:

$$h_{a,zone,o} = h_{w,s} + (h_{a,zone,o} - h_{w,s}) \cdot e^{-NTU(zone)} \tag{2.89}$$

and the outlet specific humidity $x_{a,zone,o}$ can be calculated with the relation that links the enthalpy and the specific humidity for a generic section to the values of the enthalpy and specific humidity at the inlet conditions and the values defined in saturation condition at the temperature of the plate ($h_{w,s}$ and $x_{w,s}$). Therefore, obtained the outlet enthalpy from the Equation 2.89 with the following expression is possible to estimate the specific humidity:

$$x_{a,zone,o} = x_{a,zone,i} - (h_{a,zone,i} - h_{a,zone,i}) \cdot \frac{x_{a,zone,i} - x_{w,s}}{h_{a,zone,i} - h_{w,s}} \tag{2.90}$$

For both cases the heat transfer from the wall to the air is evaluated as:

$$q_{zone} = \dot{m}_a \cdot (h_{a,zone,i} - h_{a,zone,o}) \tag{2.91}$$

according to definition of the wall sate state given in 2.5.

2.5.17 Condenser model validation and simulation results

The condenser model was tested and the results was compared with experimental data. The evaporator was simulated with experimental data for the evaporation pressure p_e, for the outlet enthalpy $h_{r,o,evap}$ and for the evaporator outlet temperature $T_{a,o,evap}$. Additionally, in order to define all the boundary conditions vector, the compressor model and the capillary tube model, that give the value of the mass flow rate at the condenser inlet (compressor) and outlet (capillary tube), were connected to the condenser model and finally an appropriate value of the air volumetric flow rate ($\approx$ 160 Nm^3/h) was used to perform the simulation. In Figure 2.12 the comparison between the real and the simulated condensation pressure is reported: considering the low value of the subcooling, the model slightly over-predicts the condensation pressure although, to be more precise, a difference of 1.5 ℃ does not significantly affect the condensation pressure since the condensation surface is not greatly decreased.

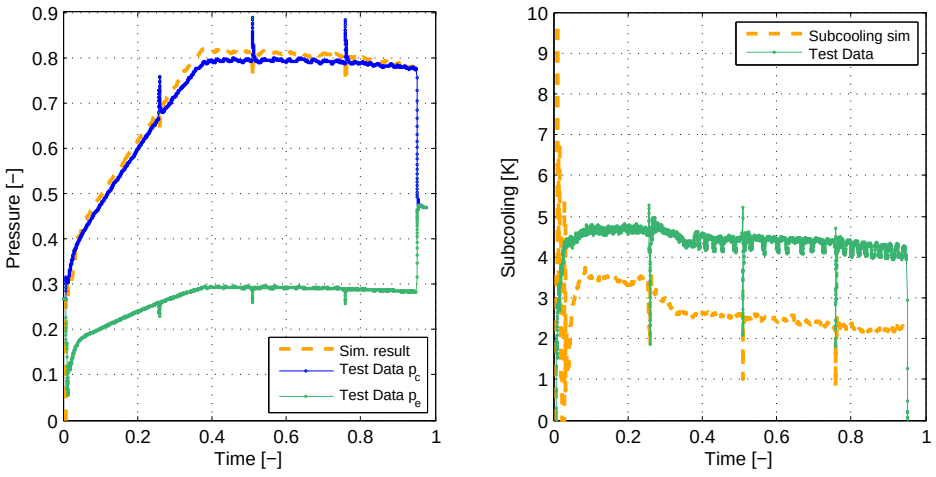

FIGURE 2.12: Condensation pressure and subcooling comparison.

In Figure 2.13 the comparison between the measured and the simulated air outlet temperature is plotted. Since the condensation pressure is quite well predicted, also the air temperature is properly predicted. Greater differences can be seen in the final part of

the cycle (in particular for the relative humidity) where the assumption of fixed volumetric flow rate does not match properly at phenomena that occur in the last stage of the drying cycle (see Chapter 3). To conclude, except for the first minutes of the cycle where there are a series of transitions from TP-L mode (initial conditions of the state variables were set up for starting with a TP-L mode) to TP, from TP to TP-L, the condenser model works with SH-TP-L mode for all the cycle.

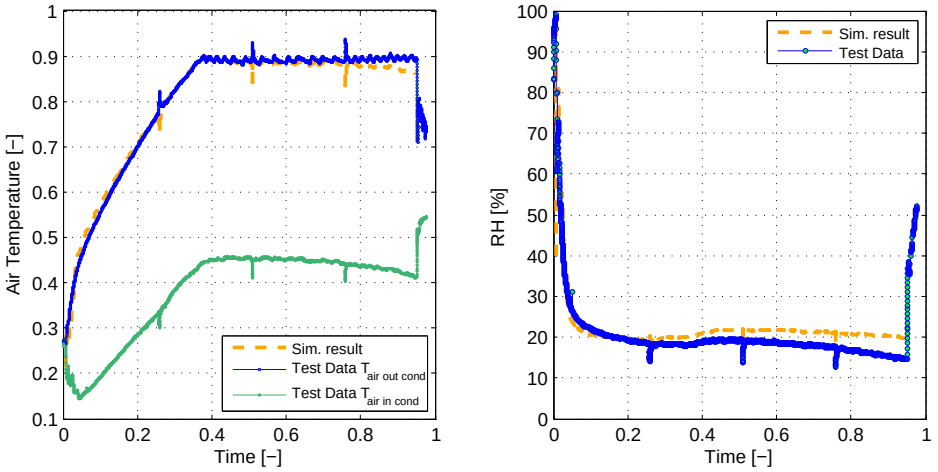

FIGURE 2.13: Condenser outlet air temperature and relative humidity.

The numerical stability of the model was checked with some test cases. In Figures 2.14, 2.16 and 2.15 the results of a test case are shown. In this test, both the inlet enthalpy and the outlet mass flow rate were varied with a sinusoidal function: this leads to force repeated switching between representation modes (all the condenser modes except the SH were tested: the SH mode can occur in the first phase of the start up transient and therefore in the final part of the shut-down for some configurations of the VCC cycle layout). The model is intrinsically mass conservative, this can be seen in Figure 2.15 where the condenser refrigerant charge inventory returns at its initial value ($\approx$ 240 g) every period (T = 5 min) of the sinusoidal function for the outlet mass flow rate. The inlet refrigerant enthalpy varies during this period. Although, the transition from one model to another occurs sometimes with some slightly discontinuities, these do not significantly affect the condensation pressure drop and the outlet enthalpy. Discontinuities are magnified in the length of the zones, producing other discontinuities on the values of the heat flux from the refrigerant to the wall. Obviously this impacts on the ″cleannesses‟ of the transition from one model to another, introducing chattering on the model. In Figure 2.16 the refrigerant pressure drops along the condenser zone are highlighted. As expected the pressure drop of the liquid zone does not significantly impact on the total pressure drop since it is inversely proportional to the refrigerant density.

Instead, pressure drops along the two phase and superheated zone strongly affect the total pressure drop.

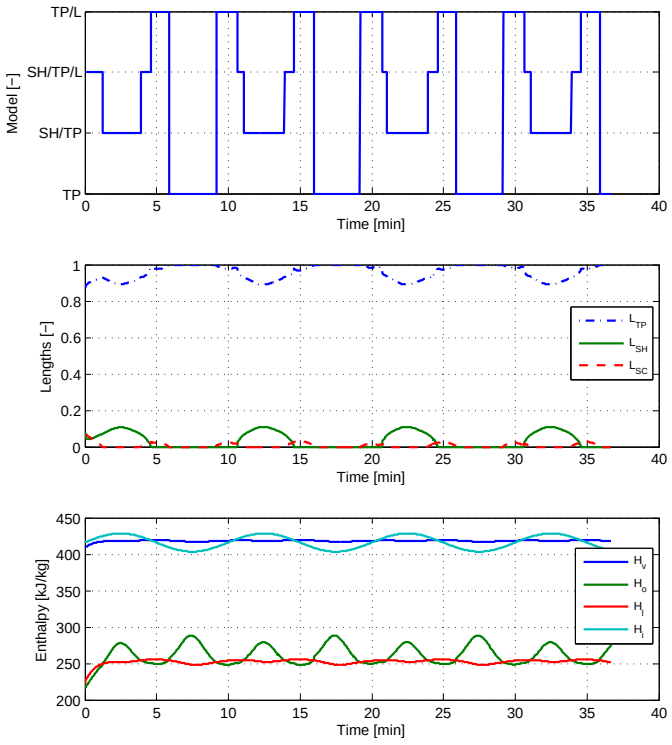

FIGURE 2.14: On the top the condenser modes during the test. On the middle, the length of the zones (SH, TP and L) evolution. Below the enthalpy evolution: H_v and H_l are respectively the vapor and the liquid enthalpy at the condensation pressure and H_i and H_o are respectively the inlet and outlet condenser enthalpy.

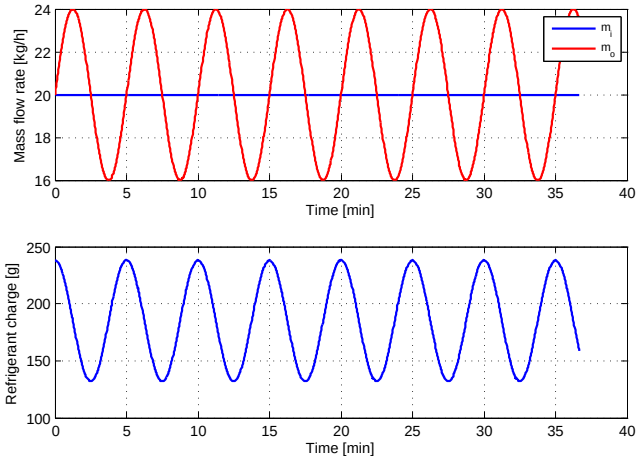

FIGURE 2.15: On the top, the refrigerant mass flow rate at the condenser inlet and outlet, below the refrigerant charge inventory of the condenser during the test.

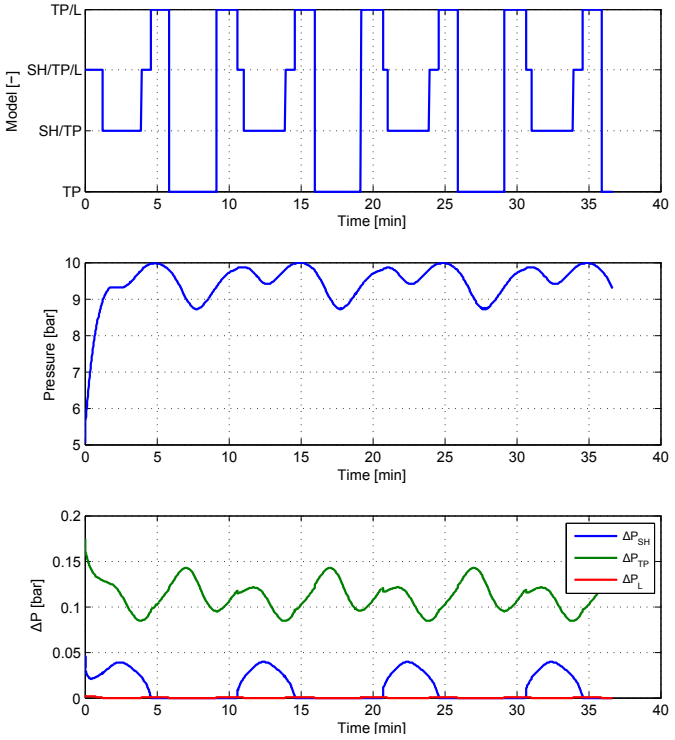

FIGURE 2.16: In the middle the condensation pressure, below the refrigerant pressure drop for each condenser zone.

2.6 Evaporator

In this section the evaporator model will be presented. As for the condenser, the evaporator is modeled using the moving boundary approach with mode switching capabilities. The evaporator model has two operating modes: TP mode when the heat exchanger is described by only one zone where the fluid can be considered in two-phase mixture conditions. The second is the TP-SH mode if the evaporator can be characterized with two zones where the refrigerant can be assumed as two-phase mixture (TP) in the first zone and in superheated state (SH) in the second zone. The framework of the evaporator model presented in this section derives heavily from the work of Cecchinato and Mancini [13] and Mancini [10] where the authors present an intrinsically mass conservative evaporator model. The main feature of this work is to introduce the evaporator mean density as a state variable (ρ_e) that guarantees the mass integrity of the system. The states variables, chosen for describing the behaviour of the heat exchanger, are:

$$X = [p, \rho_e, \rho_2, T_{w1}, T_{w2}]^T \tag{2.92}$$

where p is the evaporation pressure, ρ_e is the mean evaporator density, ρ_2 is the mean density of the superheated zone and finally the two temperature states of the wall zones (T_{w1}, T_{w2}). The modeling assumptions and the governing conservation equations are identical to those presented in the condenser model derivation. Differently from the condenser case the void fraction mean, here, is integrated assuming a linear relationship between refrigerant quality and two-phase length (see Figure 2.6). The final expression of the void fraction mean is given in the next equation:

$$\bar{\gamma} = \frac{1}{x_o - x_i} \cdot \left[\frac{C}{(C-1)^2} \cdot \ln \left(\frac{|x_i \cdot (C-1) - C|}{|x_o \cdot (C-1) - C|} \right) + \frac{x_i - x_o}{C-1} \right] \tag{2.93}$$

where $C = (\rho_g/\rho_l)^{0.67}$. The boundary condition vector is identical to the condenser one and it is defined as:

$$X_{BC} = [\dot{m}_{r,i}, \dot{m}_{r,o}, h_{r,i}, T_{a,i}, x_{a,i}, \dot{m}_{a,i}]^T \tag{2.94}$$

2.6.1 TP-SH model

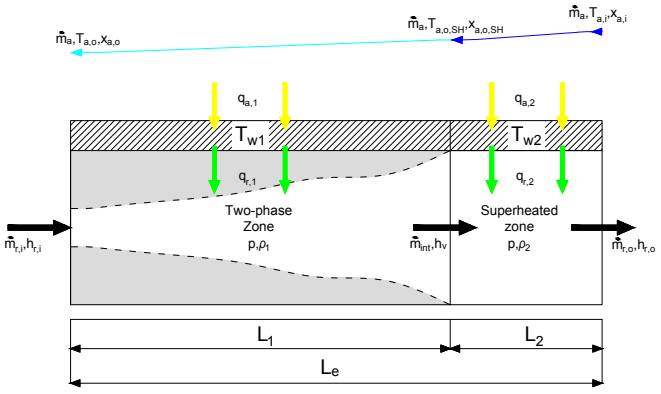

FIGURE 2.17: TP-SH model schematic.

The **two-phase zone** is described by pressure, p, and the mean density zone, ρ_1. The evaporation pressure is a state variable, whereas the mean density of the two phase zone is evaluated as follows:

$$\rho_1 = \rho_v \cdot \bar{\gamma} + \rho_l \cdot (1 - \bar{\gamma}) \tag{2.95}$$

the void fraction mean (evaluated with 2.93) is computed knowing the inlet refrigerant enthalpy $(x_i = x(p_e, h_i))$, the mean enthalpy of the zone is computed as shown in 2.17. Knowing the mean density of the evaporator can be computed the length of the two phase zone:

$$L_1 = \frac{\rho_e - \rho_2}{\rho_1 - \rho_2} \cdot L_e \tag{2.96}$$

the heat transfer from the refrigerant to the wall is evaluated as follows:

$$q_{r,1} = \pi \cdot D_i \cdot L_1 \cdot \alpha_{r,1} \cdot (T_{r,1} - T_{w1}) \tag{2.97}$$

the average heat transfer coefficient in the two-phase zone, $\alpha_{r,1}$, is obtained integrating over quality the Gungor and Winterton's correlation [30].

The **superheated zone** is described by pressure, p, and the mean density zone, ρ_2. Both of them are state variables. The length of the zone (L_2) is estimated as: $L_2 = L_e - L_1$. The outlet refrigerant enthalpy can be found with the linear assumption:

$$h_o = 2 \cdot h_2 - h_v \tag{2.98}$$

The heat transfer coefficient in the superheated zone, $\alpha_{r,2}$, is evaluated with the Gnielinski's correlation [20], the heat transfer expression has the same form of the Equation 2.97.

2.6.2 TP model

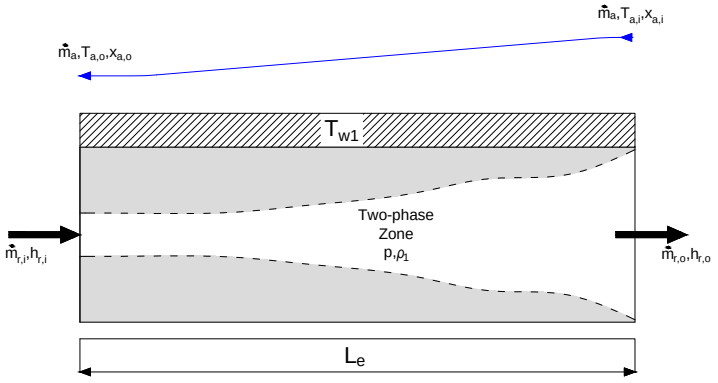

FIGURE 2.18: TP model schematic.

The **two-phase zone** is described by pressure, p, and the mean density zone, ρ_1. Clearly, in this evaporator mode, the mean density of the two-phase zone is equal to the evaporator density. The void fraction mean is computed as:

$$\bar{\gamma} = \frac{\rho_e - \rho_l}{\rho_v - \rho_l} \tag{2.99}$$

and hence may be expressed the mean enthalpy, h_1. The outlet refrigerant enthalpy is find out solving a non-linear equation that gives the outlet quality:

$$\bar{\gamma} - \bar{\gamma}_{Zivi}(x_i, x_o, p) = 0 \implies x_o \implies h_o = h(p, x_o) \tag{2.100}$$

In order to define all the state variables is necessary to introduce two pseudo-sate equations for tracking the mean density of the superheated zone and its wall temperature:

$$\frac{d\rho_2}{dt} = K_\rho \cdot (\rho_v - \rho_2) \tag{2.101}$$

$$\frac{dT_{w2}}{dt} = K_T \cdot (T_{w1-track} - T_{w2}) \tag{2.102}$$

$$\text{where:} \quad T_{w1-track} = T_{r,v} + \left[T_{w1} - \left(\frac{T_{r,i} + T_{r,o}}{2} \right) \right]$$

therefore, the mean density of the superheated zone is tracked to the vapor density at the evaporation pressure and the wall temperature is tracked to a value that is the sum of the dew temperature ($T_{r,v}$) and the ΔT of the two-phase zone respect to its wall temperature. Cecchinato and Mancini [13] track the density to the outlet density when the evaporator model works, for a limited amount of time, on the TP mode although the other state variables ρ_e and p would imply the presence of the superheated zone. No significant difference was observed using ρ_v as tracked variable.

2.6.3 Governing equations TP-SH model

In this paragraph the state equations for the refrigerant in the two-zone model (TP-SH) are reported in their final form, details about their derivation process can be found in Mancini [10]. For the two-phase zone, the mass and energy equations can be written as follows.

Two-phase zone

Conservation of refrigerant mass:

$$A \cdot L_1 \cdot \left.\frac{\partial \rho_1}{\partial p}\right|_{h_i} \frac{dp}{dt} + A \cdot (\rho_1 - \rho_v) \cdot \frac{dL_1}{dt} + \dot{m}_{int} = \dot{m}_i - A \cdot L_1 \cdot \left.\frac{\partial \rho_1}{\partial h_i}\right|_{p} \cdot \frac{dh_i}{dt} \tag{2.103}$$

Conservation of refrigerant energy:

$$\begin{aligned} A \cdot L_1 \cdot \left(\left.\frac{\partial (\rho h)_1}{\partial p}\right|_{h_i} - 1 \right) \cdot \frac{dp}{dt} + A \cdot [(\rho h)_1 - (\rho h)_v] \cdot \frac{dL_1}{dt} + \dot{m}_{int} \cdot h_v = \dot{m}_i \cdot h_i - \\ - \left.\frac{\partial (\rho h)_1}{\partial p}\right|_{h_i} \cdot \frac{dh_i}{dt} + q_{r,1} \end{aligned} \tag{2.104}$$

Conservation of wall energy:

$$\frac{dT_{w1}}{dt} = \frac{q_{r,1} + q_{a,1}}{(m \cdot c_p)_{w1}} + \frac{T_{w2} - T_{w1}}{L_e} \cdot \frac{dL_1}{dt} \tag{2.105}$$

For the superheated zone, the mass and energy conservation equations can be written as follows.

Superheated zone

Conservation of refrigerant mass:

$$A \cdot L_1 \cdot \frac{d\rho_2}{dt} + A \cdot \frac{dL_1}{dt} \cdot (\rho_v - \rho_2) - \dot{m}_{int} = \dot{m}_o \tag{2.106}$$

Conservation of refrigerant energy:

$$A \cdot L_2 \cdot \left(\rho_2 \cdot \left.\frac{\partial h_2}{\partial p}\right|_{\rho_2} - 1 \right) \cdot \frac{dp}{dt} + A \cdot L_2 \cdot \left(\rho_2 \cdot \left.\frac{\partial h_2}{\partial \rho_2}\right|_{p} + h_2 \right) \cdot \frac{d\rho_2}{dt} +$$
$$A \cdot \left((\rho \cdot h)_v - (\rho \cdot h)_v\right) \cdot \frac{dL_1}{dt} + A \cdot \left((\rho \cdot h)_v - (\rho \cdot h)_2\right) \cdot \frac{dL_2}{dt} - \dot{m}_{int} \cdot h_v = -\dot{m}_o \cdot h_o + q_{r2} \tag{2.107}$$

Conservation of wall energy:

$$\frac{dT_{w2}}{dt} = \frac{q_{r,2} + q_{a,2}}{(m \cdot c_p)_{w2}} + \frac{T_{w2} - T_{w1}}{L_e} \cdot \frac{dL_1}{dt} \tag{2.108}$$

Equations 2.103, 2.104, 2.106 and 2.107 form a set of four linear equations ($A \cdot y = b$) where y has some derivative of the state variables. The y vector is defined as:

$$y = \left[\frac{dp}{dt}, \frac{d\rho_2}{dt}, \frac{dL_1}{dt}, \dot{m}_{int} \right]^T \tag{2.109}$$

The derivative of the evaporator average density, ρ_e, can be calculated in a straightforward way as:

$$\frac{d\rho_e}{dt} = \frac{\dot{m}_i - \dot{m}_o}{A \cdot L_e} \tag{2.110}$$

The solution vector 2.109 and Equations 2.110, 2.108, 2.105 determine all the derivatives of the state variables when the evaporator operates in TP-SH mode.

2.6.4 Governing equations TP model

In some situations the superheated zone does not exist. This typically occurs after the first initial transient where the thermal load on the evaporator is low (since the evaporation process of the water inside the load is not yet totally activated) and the capillary tube tries to balance the refrigerant charge between the heat exchangers. Therefore, the TP model is used instead of the TP-SH model. The two-phase zone refrigerant mass and energy equations are:

Conservation of refrigerant mass:

$$A \cdot L_e \cdot \frac{d\rho_1}{dt} = \dot{m}_i - \dot{m}_o \tag{2.111}$$

Conservation of refrigerant energy:

$$A \cdot L_e \cdot \left(\rho_1 \cdot \left. \frac{\partial h_1}{\partial p} \right|_{\rho_1} - 1 \right) \cdot \frac{dp}{dt} + A \cdot L_e \cdot \left(\rho_1 \cdot \left. \frac{\partial h_1}{\partial \rho_1} \right|_{p} + h_1 \right) \cdot \frac{d\rho_1}{dt} = \dot{m}_i \cdot h_i - \dot{m}_o \cdot h_o + q_{r,1} \tag{2.112}$$

Conservation of wall energy:

$$\frac{dT_{w1}}{dt} = \frac{q_{r,1} + q_{a,1}}{(m \cdot c_p)_{w1}} \tag{2.113}$$

Eqs. 2.111 and 2.112 form a set of two linear equations ($A \cdot y = b$) where y has some derivative of the state variables. The y vector is defined as:

$$y = \left[\frac{dp}{dt}, \frac{d\rho_1}{dt} \right] \tag{2.114}$$

$\rho_1 = \rho_e$. As discussed above (Paragraph 2.6.2) some state variables, that describe the SH zone, need to be tracked with Equations 2.101 and 2.102. Therefore, all state derivatives are defined and the solution can be integrated over time.

2.6.5 Switching criteria

Switching from one (TP) to two-zone (TP-SH) representation occurs when the following conditions are satisfied:

$$\rho_2 < \rho_v \qquad\qquad L_2/L_e > 10^{-3} \tag{2.115}$$

the transition from TP mode to TP-SH mode happens when the mean density of the superheated zone becomes smaller than the vapor density at the evaporation pressure and the length of the superheated zone is greater than a minimum value ($L_e \cdot 10^{-3}$). The value of the superheated zone length L_2 is evaluated at each time step, before checking the previous conditions, with the Equation given in 2.96.

2.6.6 Governing equations air side

The procedure, in order to define the air outlet conditions, remains identical to that developed for the condenser in the Paragraph 2.5.16 however more attention must be kept to define the heat transfer to the wall zone. During the drying cycle the evaporator produces a dehumidification of the air that crosses it. Not all the removed energy from the air must be considered gained by the wall zone since a not negligible enthalpy flux ($\approx$ 40 W), associated with the condensed vapor, occurs.

$$H_{flux} = \dot{m}_a \cdot (x_{a,i,e} - x_{a,o,e}) \cdot c_{p,w}|_{T_{a,o,e}} \cdot T_{a,o,e} \tag{2.116}$$

and finally the heat flux to consider in the energy equation of the wall is:

$$q_{zone} = \dot{m}_a \cdot (h_{a,i,zone} - h_{a,o,zone}) - H_{flux} \tag{2.117}$$

If no mass transfer phenomena occur: $H_{flux} = 0$.

2.6.7 Evaporator model validation and simulation results

As for the condenser model also the evaporator model was tested and the results were compared with experimental data. For the test shown in Figures 2.19 and 2.20 experimental data was used: condensation pressure (p_c), inlet refrigerant enthalpy ($h_{r,i}$), air temperature ($T_{a,i,e}$) and relative humidity ($RH_{a,i,e}$). The capillary tube and compressor model were connected to the evaporator in order to define the mass flow rates at the evaporator inlet and outlet. Furthermore, the condenser was simulated with experimental data. The model properly predicts the evaporation pressure (the orange line is

almost superimposed at the green line, see chart on the left in Figure 2.19), also the superheat is efficiently predicted although the trend is decreasing whereas the actual value remains constant from half drying cycle to the end. In the final part of the cycle the evaporator thermal load decreases due to the reduction of the air humidity ratio from the drum outlet, since the laundry load is almost dry. This leads to a slight reduction of the evaporation pressure and also of superheat degree in the model.

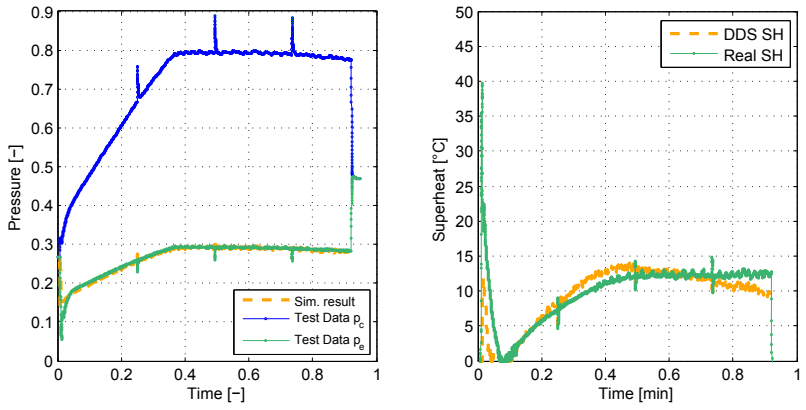

FIGURE 2.19: Evaporation pressure and superheat comparison.

The air temperature at the evaporator outlet is compared in Figure 2.20. Although during the initial transient the model efficiently predicts the actual value, in the middle part of the cycle there are differences of 5%. It is worth noting that the measurement between the evaporator and the condenser is not always representatives of the mean temperature of the section due to non-uniform distribution of the air flow.

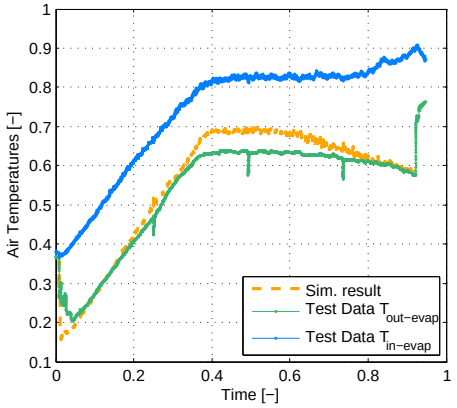

FIGURE 2.20: Outlet evaporator temperature.

The numerical stability of the model was checked forcing the model to switch between the two operational modes. Figures 2.21 and 2.22 show some variables during a test. In this test the inlet enthalpy was varied with a sinusoidal function (see red line in the chart below of Figure 2.21). Not significant discontinuities can be seen during the transition from modes although in some transitions, in particular from TP to TP-SH mode, the model shows chattering issue (see how the vertical lines from TP to TP-SH are thicker than the lines from TP-SH to TP).

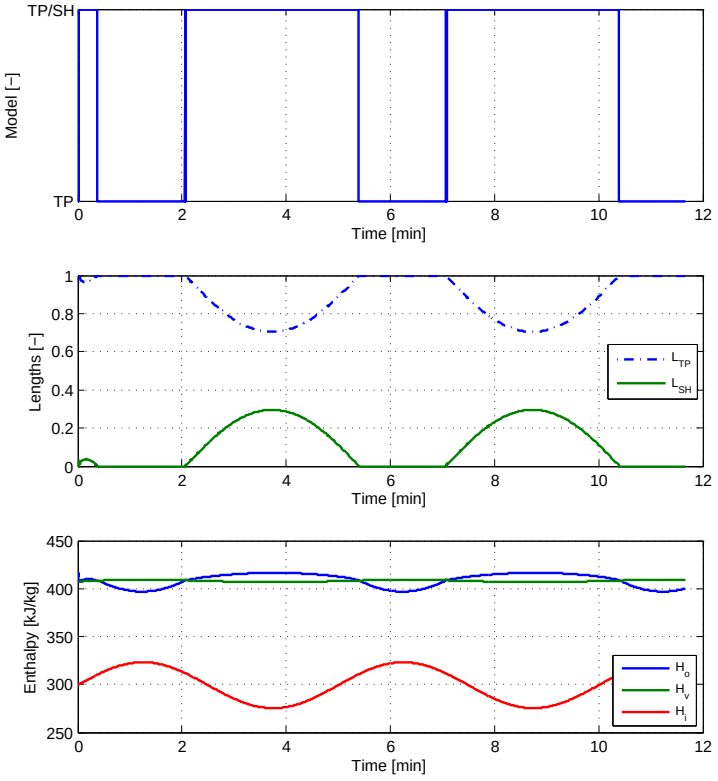

FIGURE 2.21: On the top evaporator mode during test. In the middle: length of the zones. Below: refrigerant enthalpies, H_v is the vapor enthalpy at the evaporation pressure while H_i and H_o are respectively the inlet and outlet enthalpy.

Figure (2.22) shows the evolution of the evaporation pressure and pressure drops along the refrigerant zones. As can be seen from the figure, values of the superheated length greater of 30% of the total evaporator length produce pressure drop values higher than those of two-phase zone.

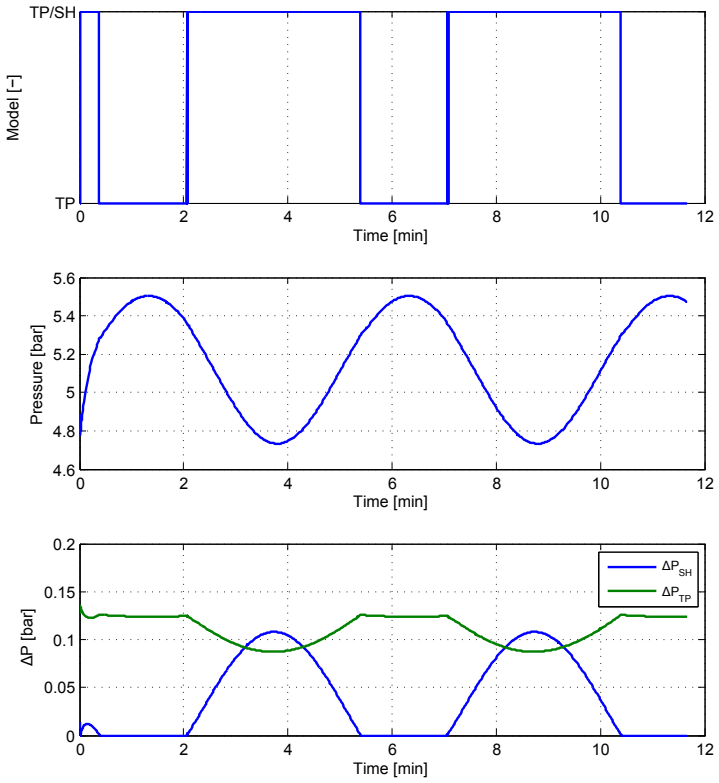

FIGURE 2.22: On the top: evaporator modes during test. In the middle: evaporation pressure. Below: pressure drop on the superheated zone and on the two-phase zone.

2.7 Capillary tube

The capillary tube is the most used expansion device in small domestic appliances such as fridge and freezer. A capillary tube is a long, narrow tube of constant diameter. The word ″capillary‶ is a misnomer since surface tension is not important in refrigeration application of capillary tubes. Typical diameters of refrigerant capillary tubes range from 0.5 mm to 3 mm and the length ranges from 1.0 m to 6 m. In the studied heat pump in this work the capillary tube connects the outlet of the condenser to the inlet of the evaporator, this configuration is called adiabatic capillary, however in other application (refrigerators and freezer) the capillary tube is soldered to the suction line and the combination is called capillary-tube/suction-line heat exchanger system or diabatic configurations.

Many investigator have studied the performance of capillary tubes using experimental data or theoretical models to predict the refrigerant flow rate. Essentially models in the literature could be divided in three categories:

1. numerical model: in this model the capillary tube is divided into a number of elements and the equations of continuity, energy conservation and momentum are evaluated and applied at each control element (examples in literature are Bansal and Wang [31] or Wang et al. [32]). The creation of the model and its implementation demand a certain degree of time and effort. Additionally the discretization of the equations and the system integration brings up numerical issues one has to handle;

2. empirical models: this model apply the Buckingham Π theorem, and charts to predict refrigerant mass flow rate through adiabatic capillary tubes. Some of these dimensionless correlations are generalized for different refrigerants considering the refrigerant properties in the dimensionless parameters (examples in literature are: American Society of Heating and Engineers [33], Yang and Wang [34] and Park et al. [35], the last one compares straight capillary tube against spirally coiled capillary tube);

3. analytical model: to balance generality of numerical models and simplicity of the empirical correlations, several scientists tried to develop an analytical description of the capillary tube flow by introducing simplifying assumptions for the calculation of the fluid properties along the capillary tube. In this way they were able to transform the governing differential equations into their integral form. They obtained an algebraic equation which can predict the mass flow rate or alternatively the geometry of the capillary tube for given boundary conditions. Although empirical parameters are included in these equations, too, they are based on a physical background. Zhang and Ding [14] presented an approximate analytic solutions of adiabatic capillary tubes. The authors showed that the correlation is in good agreement with the experimental data in open literature. Hermes et al.[36] presents a model of a capillary tube suction line heat exchanger with the same level of accuracy as found with more sophisticated first-principles models. The methodology treats the refrigerant flow and the heat transfer as independent phenomena, thus allowing the derivation of explicit algebraic expressions for the refrigerant mass flow rate and the heat exchanger effectiveness. Comparisons between the model predictions and the experimental data revealed that more than 90% and nearly 100% of all data can be predicted within ± 10% and ± 15% error bands, respectively.

In order to evaluate the reliability of the different found correlations in literature some tests were carried out (see Figure 2.23). Four correlations were tested: three empirical correlations: American Society of Heating and Engineers [33], Park et al. [35], Yang and Wang [34] and one analytical correlation: Zhang and Ding [14] against the experimental

data. The experimental data was acquired for a heat pump working with R-407C and the capillary tube was coiled. The refrigerant flow rate was measured by a mass flow meter using the Coriolis effect with an uncertainty of ± 0.2%. The pressures and the temperatures of the refrigerant at the inlet and outlet of capillary tube were acquired by using pressure transducers with an uncertainty of ± 0.2% of full scale (60 bar for the high pressure and 25 bar for the low pressure) and T-type thermocouples with an uncertainty of ± 0.2%. The measured data was recorded by using a data acquisition system. The mass flow meter was connected to the condenser outlet (upstream the capillary tube inlet section) and to produce accurate measurements of the mass flow rate increasing significantly the refrigerant charge was necessary in order to establish a subcooled section by the final part of the condenser until the entrance of the capillary tube. This led a high degree of subcooling as can be seen in Figure 2.23. Therefore the refrigerant mass flow rate measurement through the capillary tube was carried out during a standard drying cycle and not in dedicated tests that were able to fix the thermodynamic conditions at the capillary inlet section.

(A) Mass flow meter. (B) Capillary tube and micrometric valve.

FIGURE 2.23: Measurement of the mass flow rate through the capillary tube

In Figure 2.24 the comparison between predict mass flow rate and experimental data is shown. From the figure can be pointed out that for the first 30 min there is noticeable difference among the measured refrigerant mass flow rate and the predicted values by the correlations, however this difference in the last part of the test decreases. At the final stage of the test the deviation from the experimental value is: 9.7% for the ASHRAE's correlation, 16.13% for Zhang-Ding's equation, 24.7% for the Yang-Wang's correlation and -21.9% for the Park et al.'s correlation. It is worth noting that the capillary tube length in all the equations/correlations tested was modified with the equivalent length definition given in [35]. This length considers the coiled effect.

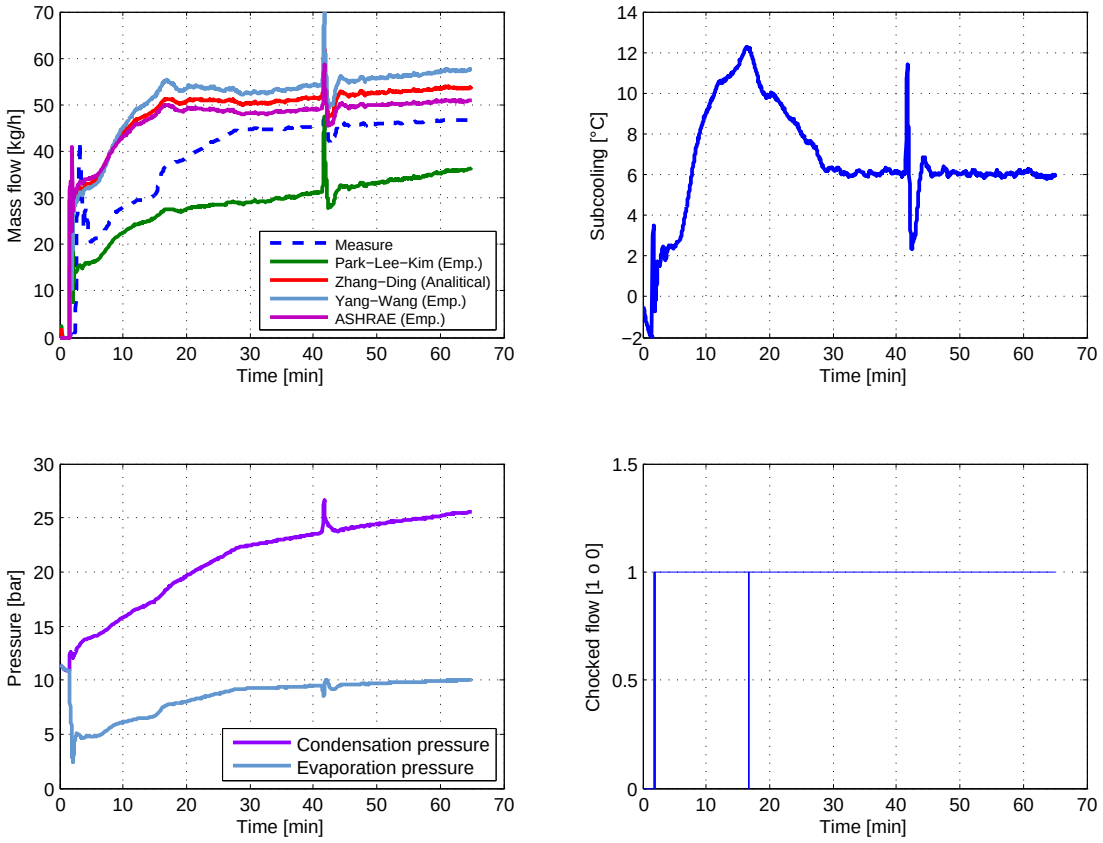

FIGURE 2.24: Comparison of different correlations for predicting the refrigerant flow rate through the capillary tube

In the first phase of the test all the correlations overestimate the value of the mass flow rate except the Park et al.'s correlation, however this correlation underestimates the mass flow rate for all the test (see green line in Figure 2.24). During this phase a high degree of subcooling is noted that could affect the friction factor along the subcooled region: this value could be underestimated and therefore leading to overestimate the value of the mass flow rate. For instance, in Zhang and Ding model the suggested friction factor correlation Bittle and Plate's correlation does not account for the tube roughness. Several attempts to modified the Zhang and Ding's correlations were made (Swamee and Jain's correlation, Romeo-Royo and Monzón's approximation, details are given [19]), however this did not solve the issue.

In this work the Zhang and Ding pure model is adopted since compared with the empirical correlations, the approximate analytic solution proposed is of better generalization. In addition the comparison between this model and the experimental data in open literature is satisfactory.

2.7.1 Capillary tube design considerations

The effect of the capillary tube length was analyzed using the heat pump model, performing some simulated cases where the heat module inlet conditions were fixed. The results of the refrigerant variables, in steady state condition, are plotted from Figure 2.25 to 2.28. A longer capillary tube determines:

- a higher flow resistance determining a higher pressure ratio balance point. The condensation temperature (T_c) is slightly affected whereas the evaporation temperature (T_e) is strongly affected;
- higher subcooling and superheat degree;
- condenser mass inventory increases;
- lower suction density determines lower mass flow rate;
- cooling capacity is lower (contrasting between the refrigerant mass flow and the specific cooling capacity effects);
- COP is slightly affected.

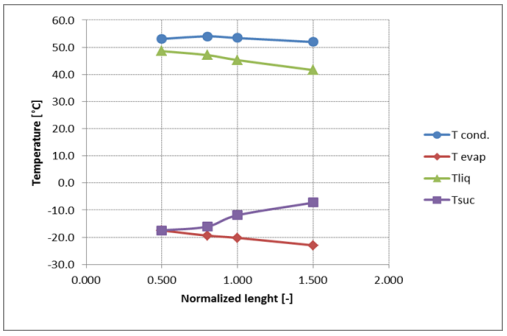

FIGURE 2.25: Refrigerant temperatures varying the capillary tube length.

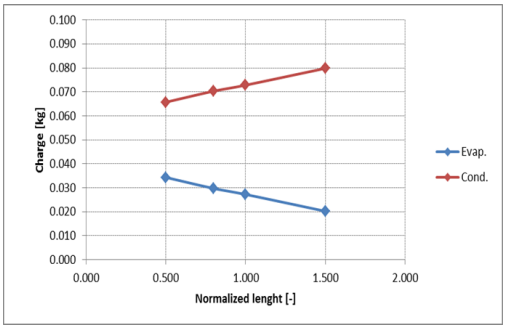

FIGURE 2.26: Heat exchanger refrigerant charge varying the capillary tube length.

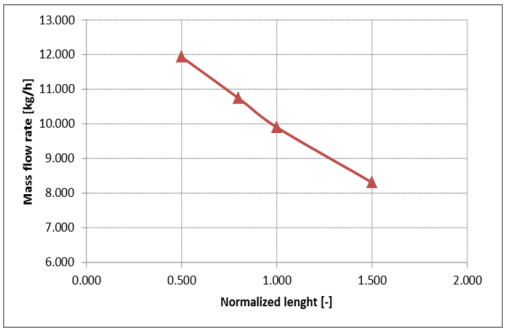

FIGURE 2.27: Mass flow rate varying the capillary tube length.

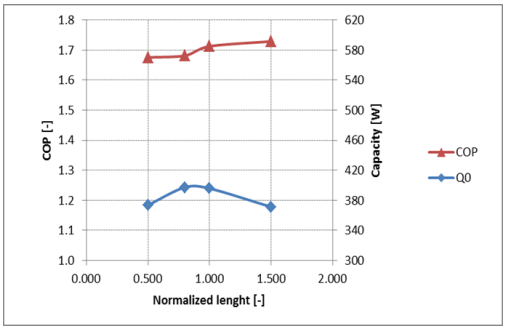

FIGURE 2.28: COP and Cooling capacity varying the capillary tube length.

In addition, also the effect of the refrigerant charge was analyzed. Charge inventory strongly affects the balance point (see Figures from 2.29 to 2.32), in particular charge increment causes:

- an increment of both pressures therefore the pressure ratio is slightly affected;
- higher subcooling and lower superheat degree;
- both condenser and evaporator mass inventory increase;
- higher suction density determines higher mass flow rate (density effect is dominant compared to the reduction of the superheat degree);
- cooling capacity is higher (both for mass flow and specific cooling capacity effects);
- COP is slightly affected.

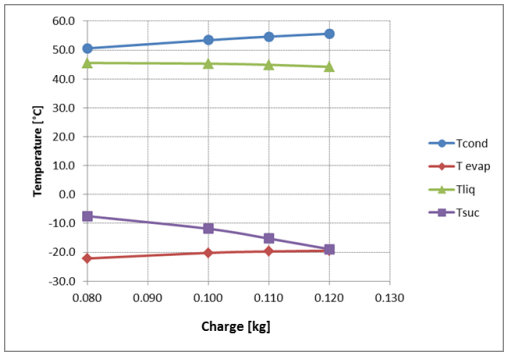

FIGURE 2.29: Refrigerant temperatures varying the charge inventory.

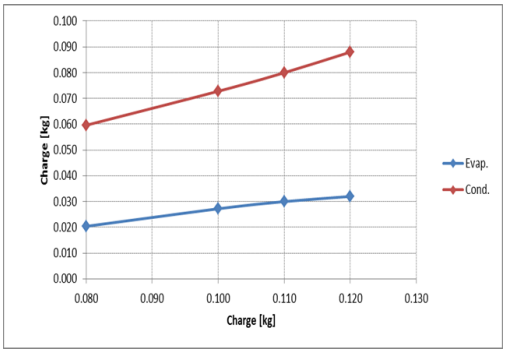

FIGURE 2.30: Heat exchanger refrigerant charge varying the charge inventory.

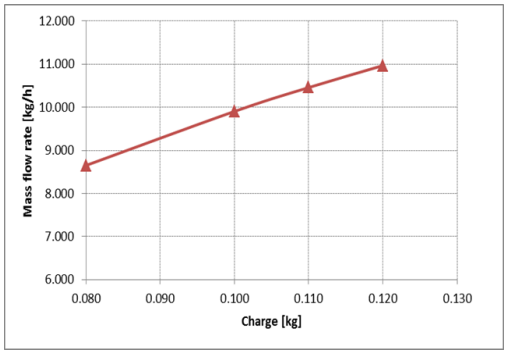

FIGURE 2.31: Mass flow rate varying the charge inventory.

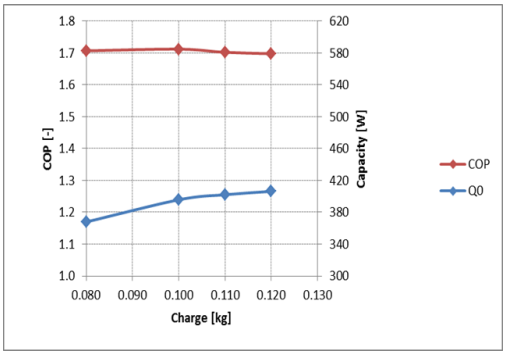

FIGURE 2.32: COP and Cooling capacity varying the charge inventory.

If the previous cases are analyzed together at the same degree of superheat (see Figures from 2.33 to 2.36) the following considerations can be observed:

- evaporation pressure, charge inventory and mass flow rates are very slightly affected;
- a longer capillary tubes determine higher condensation pressure and subcooling degree;
- a longer capillary tube increases condenser and overall charge contempt, hence the same superheat is obtained increasing the refrigerant charge;
- cooling capacity is higher for the longer capillary because of a higher specific cooling capacity effect at nearly constant mass flow rate. The higher specific cooling capacity is determined by lower liquid enthalpy determined in the condenser;
- for the considered length, the COP is higher for the longer capillary tube. This is determined by the cooling capacity increment which contrasts the input power increment associated to the higher pressure ratio balance point of the longer capillary.

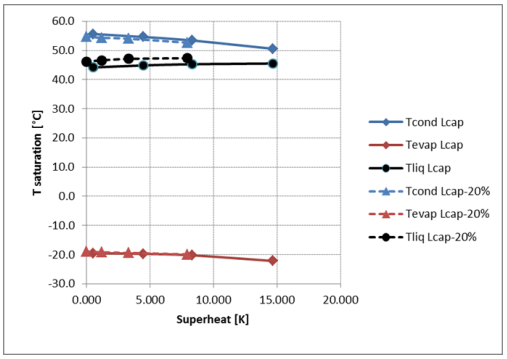

FIGURE 2.33: Refrigerant temperatures at the same degree of superheat.

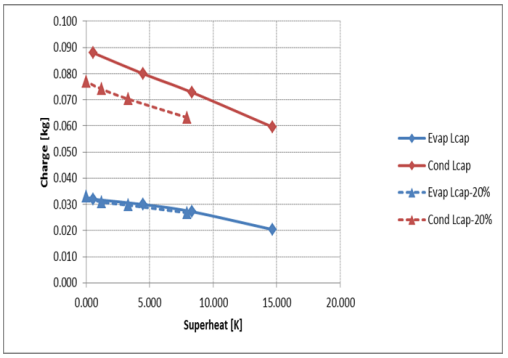

FIGURE 2.34: Heat exchanger refrigerant at the same degree of superheat.

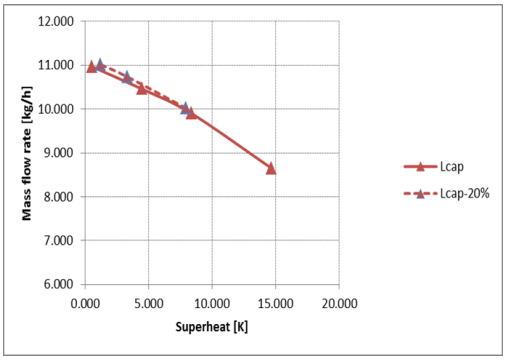

FIGURE 2.35: Mass flow rate at the same degree of superheat.

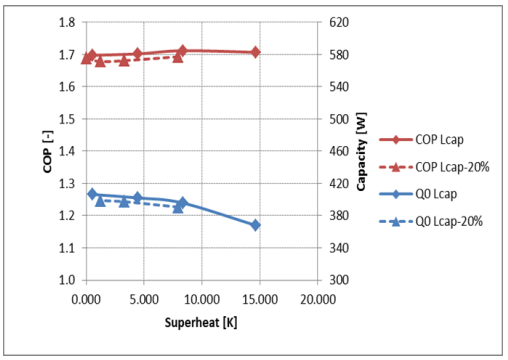

FIGURE 2.36: COP and Cooling capacity at the same degree of superheat.

2.8 Compressor model

The adopted rolling piston type rotary compressor in the heat pump module is shown in Figure 2.38. The compressor is consisted by an electric motor (rotor and stator), a crankshaft, a roller piston and a cylinder. Refrigerant enters in the compression chamber coming from a suction side accumulator. In the compression chamber, that has a cylindric shape, the refrigerant is compressed by the roller piston that rotates eccentrically respect to the center of the chamber. The motion of the piston creates two zone: compression and suction zone. The refrigerant leaves the cylinder passing trough the discharge valve, it resides for a short time in the compression shell where exchanges heat transfer with the shell walls and with the rotor and the stator. The compressor shell is exposed to the condensation pressure.

One of the best work in the literature where a dynamic model of a rolling piston type compressor is developed is: Park [1]; in this work all the different aspects concerning the compression process are considered: kinematics of the crankshaft and roller, mass flow due to leakages heat transfer between refrigerant and components. The overall analysis is carried out as function of the crankshaft rotation angle therefore, although the proposed model completely describes the compression process, cannot be applied in this work since it is focused on slow dynamic as those determined by the heat transfer. Another work where a rotatory compressor model is developed is: Padhy [37]. Here, heat transfer coefficients are calculated from the empirical/theoretical equations adapted from various sources.

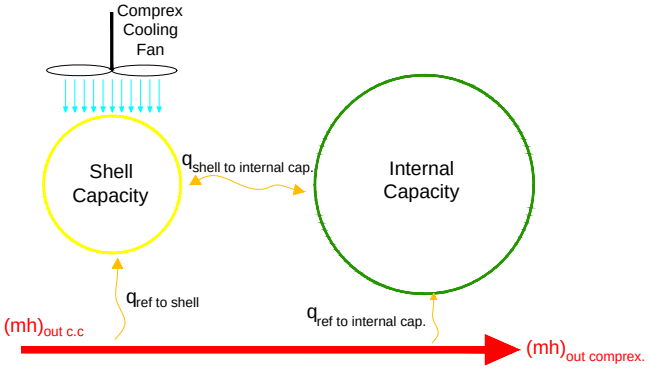

FIGURE 2.37: Compressor lumped model: thermal capacities.

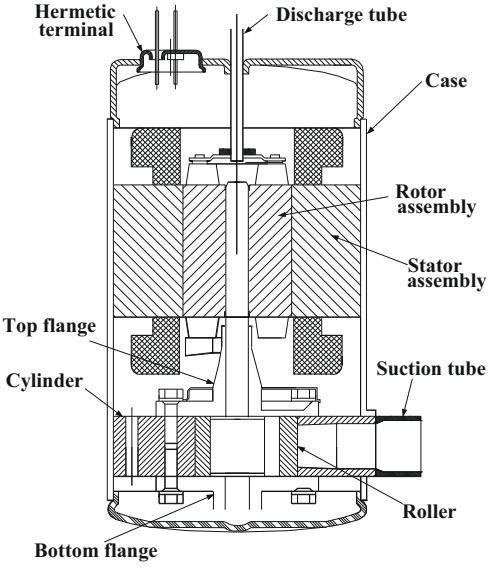

FIGURE 2.38: Schematic view of rolling piston type rotary compressor [1].

In this work the focus is to develop a dynamic compressor model that is capable to describe the dynamic behavior of the compressor in two phases of the cycle. The first is during the initial transient where some energy is used to increase the temperature of the metallic parts inside the compressor. A second phase occurs when the compressor cooling fan is switched on. In this phase the dynamic behaviour is faster than the initial transient where all the mass of the compressor is involved, consequently a second thermal capacity able to reproduce the experimental trends associated to the cooling fan must be included. The proposed model scheme is in Figure 2.37 where two thermal capacities are reported: the smaller is the capacity of the compressor shell and the bigger is the global capacity of the components inside the compressor. As shown in the scheme, when the cooling fan is switched on, it interacts only with the smaller thermal capacity. The compressor lumped model is developed in order to catch its dynamics therefore it does not describe all the heat transfer paths between components. For instance, the internal capacity is not heated by the electric energy losses and also the heat due to friction losses in the compression chamber is not considered. A more complicated model needs to split the power input in its components: power to fluid and losses (mechanical losses, rotor and stator losses, stray current losses) with the coefficients that define them: electrical and mechanical efficiencies (η_e and η_m), in addition the compression process should be simulated with a polytropic coefficient (n), since it cannot be considered adiabatic.

2.8.1 Experimental measurements

Experimental measurements were carried out with an R134a rolling piston type rotary compressor with 11.4 cm^3 displacement. The compressor was inserted in a calorimetry rig and the following parameters were measured: electric power input, refrigerating capacity, evaporation and condensation pressures, gas temperature at inlet and outlet of the compressor and cabinet temperature (that could be fixed). Additionally, the compressor was equipped with several thermocouples (type T) in order to measure the compressor wall temperatures in different positions, see Figure 2.39. The calorimetry rig is able to fix the value of the condensation and evaporation pressures and also the refrigerant suction temperature. Tests were developed for working conditions near to the pseudo-stable phase of the drying cycle: for a R134a tumble dryer: condensation pressure near to 21 bar, evaporation pressure near to 6 bar and superheat nearly to 15 K. Furthermore, when the compressor reached the steady state condition the compressor cooling fan was switched on in order to evaluate the overall thermal conductance between cooling air and refrigerant inside the compressor, see Figure 2.40.

FIGURE 2.39: Compressor measurements in a calorimetry rig.

FIGURE 2.40: Compressor measurements with cooling fan in a calorimetry rig.

An experimental test, with temperature of the air nearly to 35 °C and with the working conditions earlier reported, is shown in Figure 2.41. Near to 3500 seconds, the compressor cooling fan is switched on, as a result the mean temperature of the compressor shell decreases and consequently also the refrigerant discharge temperature reduces. However, the isentropic and volumetric efficiencies remain stable. This leads to assume that the increment of the heat flux does not significantly affect the performance of the electric motor and the definitions of isentropic and volumetric efficiencies can be used to describe the compressor. Generally, the compressor supplier provides data in accordance with UNI EN 12900 for the cooling capacity and for the power input that are used to compute the isentropic and volumetric efficiencies.

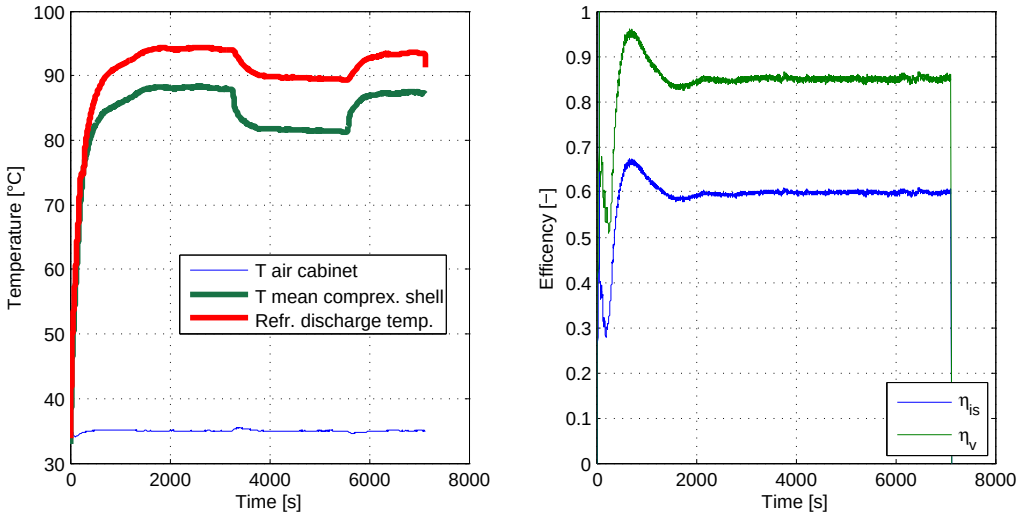

FIGURE 2.41: Temperatures and isentropic/volumetric efficiencies.

Figure 2.42 shows the evolution of other variables during the test. In the chart on the left the electric input power P_{in}, the power given at the refrigerant flow P_f and the loss $P_l = P_{in} - P_f$ are plotted. It can be pointed out that the evolution of the energy loss: in the first phase the input power is used to increase the energy content of the metallic body of the compressor since the computed power given to the fluid is nearly to zero. After this first transient, a steady state condition is reached, in this phase the losses are about 20% of the total input power and this power must be equal to the heat transfer flux with the surrounding air (this value was useful to predict the overall thermal conductance). When the compressor cooling fan is switched on the loss increases and reaches a value nearly to 30% of the total input power. The compressor quality factor (FQ), plotted in Figure 2.42, is defined as:

$$FQ = \frac{P_l}{P_{in}} \quad [\%] \tag{2.118}$$

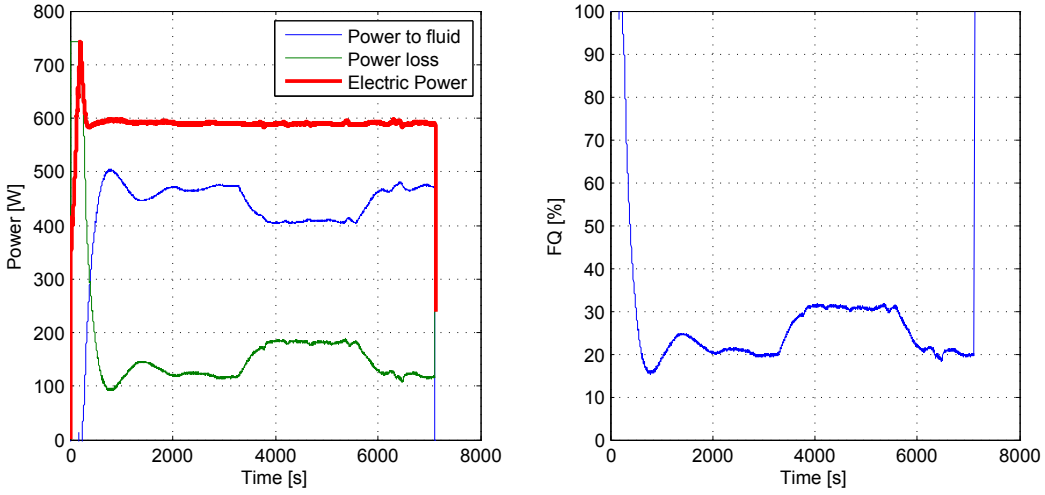

FIGURE 2.42: Powers and quality factor.

2.8.2 Compressor model

As discussed the compressor is described by static relations in order to predict the isentropic and volumetric efficiencies (η_{is} and η_v) in addition its dynamic behaviour is characterized with two thermal capacities. The shell capacity may be described with the conservation of energy equation in temperature formulation:

$$\frac{dT_{shell\,cap.}}{dt} = \frac{q_{ref.\,to\,shell} + q_{shell\,to\,int.\,cap} - q_{shell\,to\,air}}{(m \cdot c_p)_{shell\,cap.}} \tag{2.119}$$

and for the internal capacity:

$$\frac{dT_{int.\,cap.}}{dt} = \frac{q_{ref.\,to\,int.\,cap} - q_{shell\,to\,int.\,cap}}{(m \cdot c_p)_{int.\,cap.}} \tag{2.120}$$

where the heat transfer: $q_{ref.\,to\,shell}$ is evaluated with the P-NTU method [38] considering the exchange between the refrigerant mass flow rate coming from the compression chamber and the compressor wall. Therefore:

$$NTU = \frac{(K \cdot A)_{ref.\,to\,shell}}{(\dot{m} \cdot c_p)_r} \tag{2.121}$$

where $c_{p,r}$ is evaluated as:

$$c_{p,r} = \begin{cases} c_p(\bar{T}) & \text{if } T_{r,o,shell} > T_{dew}(p_c) \\ c_p(T_{r,v}(p_c)) & \text{if } T_{r,o,shell} < T_{dew}(p_c) \end{cases} \tag{2.122}$$

the previous equation indicates that in the event of condensation the heat transfer is dominated by the vapor phase (this could occur only in the first minutes of the start up) the term $(K \cdot A)_{ref.\,to\,shell}$ was evaluated with an identification method. The same approach is used to compute $q_{ref\,to\,int.\,cap}$, in this case the exchange is between the refrigerant stream at the temperature $T_{r,o,shell}$ and the internal capacity. Also $(K \cdot A)_{ref\,to\,int.\,cap}$ was found out with an identification method. The heat transfer between the two thermal capacities is expressed as:

$$q_{shell\,to\,int.\,cap} = (K \cdot A)_{shell\,int\,cap} \cdot (T_{shell\,cap.} - T_{int\,cap.}) \tag{2.123}$$

also in this case $(K \cdot A)_{shell\,int\,cap}$ was obtained from a numerical method. The heat flux $q_{shell\,to\,air}$ is obtained as:

$$q_{shell\,to\,air} = (K \cdot A)_{shell\,to\,air} \cdot (T_{shell} - T_{cab.}) \tag{2.124}$$

$(K \cdot A)_{shell\,to\,air}$ was evaluated from experimental measurements through the calorimetric test rig. As already discussed, in steady state conditions this heat flux must be equal to the heat loss from the compressor shell (see green line in Figure 2.42). It was computed in each of the working conditions with and without cooling fan.

The capacities $(m \cdot c_p)_{int.\,cap.}$ and $(m \cdot c_p)_{shell\,cap.}$ are computed with information of weight and material provided by the compressor supplier.

The refrigerant mass flow rate drawn by the compressor is computed as:

$$\dot{m}_{comprex} = \frac{rpm}{60} \cdot \eta_v \cdot \rho_{suc} \cdot V_{c.c} \tag{2.125}$$

the compressor outlet enthalpy is:

$$h_{o,c.c} = h_{suc} + \frac{h_{o,is} - h_{suc}}{\eta_{is}} \tag{2.126}$$

and finally, the power given at the refrigerant flow is:

$$P_f = \dot{m}_{comprex} \cdot (h_{o,c.c} - h_{suc}) \tag{2.127}$$

2.8.3 Compressor model validation

Tests on the calorimetric rig were used to compare the results from the model with experimental data. In Figure 2.43 the shell compressor temperature and the refrigerant outlet temperature are compared with the experimental measurements. The model slightly overestimates both, the reason can be found in low accuracy on the value of the isentropic efficiency, however the evolution is fairly in agreement with the experimental measurements. The compressor quality factor is plotted in Figure 2.44, also in this case the model properly predicts both the initial transient and the start up/shut down of the compressor cooling fan.

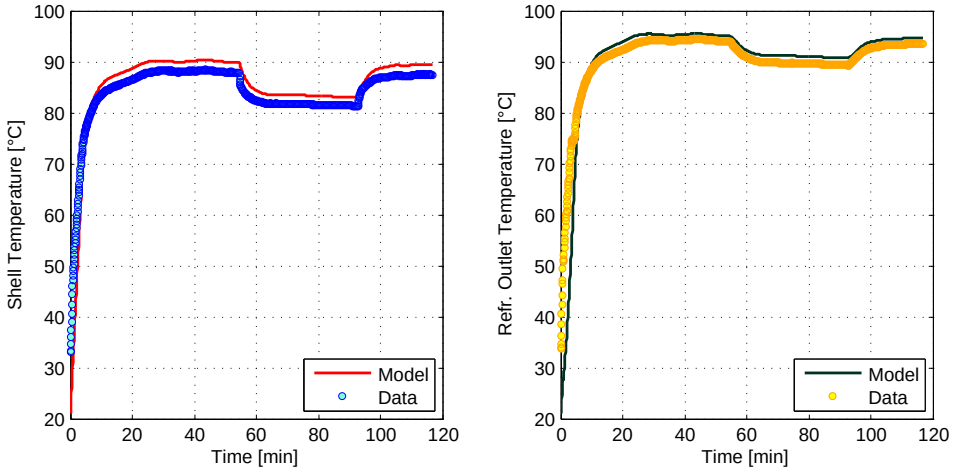

FIGURE 2.43: Shell temperature and compressor refrigerant outlet temperature comparison.

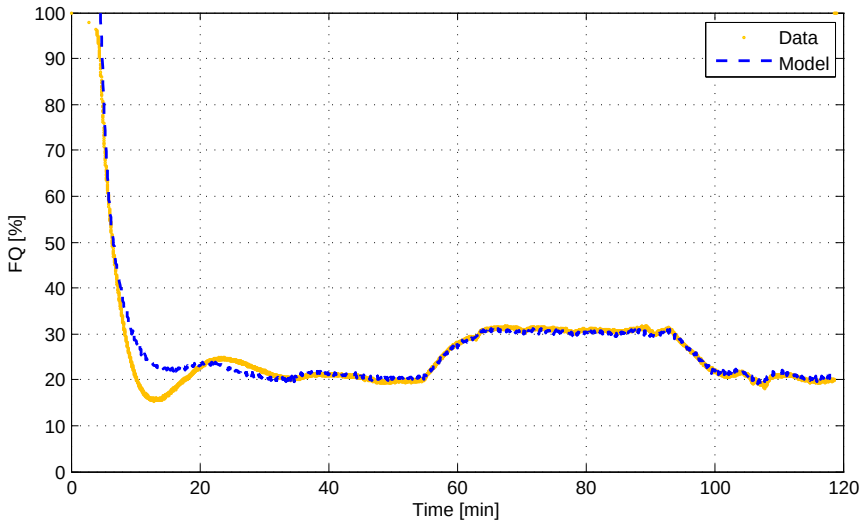

FIGURE 2.44: Compressor quality factor.

The model was tested also with different working conditions that are reported in the following table (see Table 2.1). These conditions identify three states during the drying cycle: the first is characterized by low condensation and evaporation pressure, although the pressure ratio is the highest of the entire cycle, and high degree of superheat (the evaporator is empty). The second point represents a condition in the middle between the first initial transient and the pseudo steady state phase, instead the last tested point represents a condition nearly to the pseudo steady state phase.

T_e	T_c	$rp = p_c/p_e$	SH
℃	℃	-	K
-7	32.5	3.60	25
6.5	42	2.90	11
20.5	69	3.57	15

TABLE 2.1: Test conditions.

The comparison between experimental data and simulated results is reported in Figures 2.45 and 2.46. The model was tested using the polynomial equations, expressed as function of the condensation and evaporation temperature, that give the cooling capacity and the power input of the compressor. The first point is the worst predicted (deviances greater than 6% could be noted for the shell temperature and for the power input, see Figure 2.45). The reason for this can be found on the low reliability of the correlations used for a domain very far from for which they are developed.

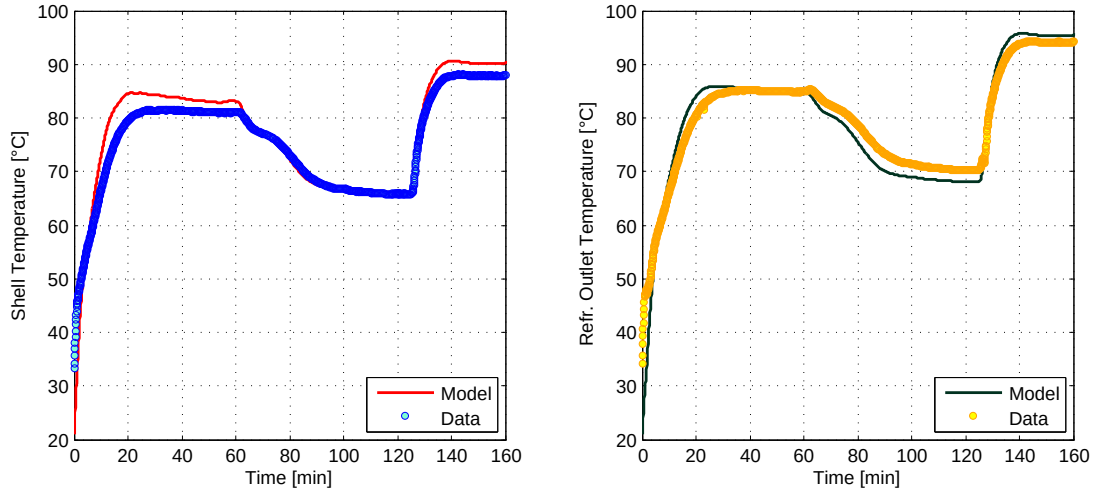

FIGURE 2.45: Shell temperature and compressor refrigerant outlet temperature comparison on different working conditions.

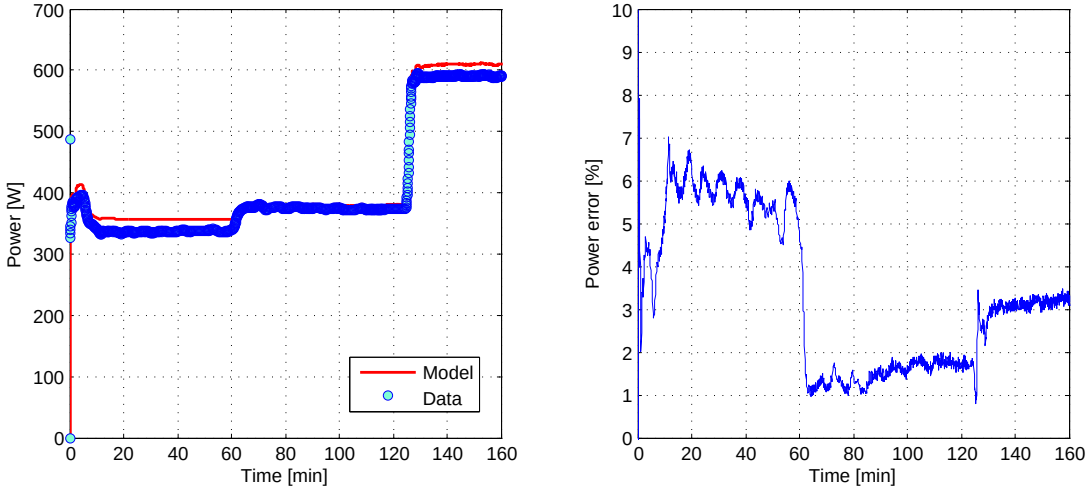

FIGURE 2.46: Compressor power input comparison during tests on different working conditions.

2.9 Refrigerant mass and void fraction mean

A significant difference on the prediction of the refrigerant mass was observed during the simulation tests. Trying to fix the superheat and subcooling degree the discrepancy that appears is about 50% of the true charge in the heat pump system. Similar results were founded in [39]. The difference between the model and the actual charge is mainly caused both by the choice of the void fraction correlation and its characteristics. The

total refrigerant mass in the heat pump system is described below as:

$$M_{total} = M_c + M_e + M_{liquid\,tube} + M_{compressor} + M_{other\,pipes} \tag{2.128}$$

where the M_c and M_e can be estimated as:

$$M_{exchanger} = \left((\bar{\gamma} \cdot \rho_v + (1 - \bar{\gamma}) \cdot \rho_l) \cdot L_{TP} + \sum_{i=1}^{n} \rho_{i\,single\,phase} \cdot L_{i\,single\,phase} \right) \cdot V_{exchanger} \tag{2.129}$$

where γ is the void fraction mean. As discussed in the Paragraph 2.5.3, Zivi's void fraction correlation is used in this work. At the condenser is assumed a quadratic relationship between length and quality whereas at the evaporator is integrated along a linear profile. Both the liquid pipe and the other pipes (compressor suction and discharge pipe) are not modeled and therefore their mass content is neglected. In addition also the refrigerant mass in the compressor is neglected.

The reliability of ten different void fraction correlations in the prediction of the actual refrigerant mass was tested on ten different heat pump modules (in Table 2.2 the heat exchangers internal volumes and the actual charge are reported). The analysis was made, in a static way, considering a refrigerant thermodynamic state near to the pseudo steady state condition in the drying cycle and the following assumptions were made:

1. the liquid length was estimated introducing a suitable value of the overall heat transfer coefficient (K_L) and assuming a reasonable value of the air mass flow rate ($\dot{m}_a$). The following procedure was developed:

$$q_L = \dot{m}_r \cdot (H_l - H_{o,c}) \tag{2.130}$$

$$T_{a,o,L} = T_{a,i,L} + \frac{q_L}{\dot{m}_a \cdot \bar{c_p}} \tag{2.131}$$

$$\Delta T_{m,log} = \frac{(T_l - T_{a,o,L}) - (T_l - SC - T_{a,o})}{\ln\left(\dfrac{T_l - T_{a,o,L}}{T_l - SC - T_{a,o}}\right)} \tag{2.132}$$

$$A_l = \frac{q_L}{K_L \cdot \Delta T_{m,log}} \tag{2.133}$$

$$L_l = \frac{A_l}{A_{tot}} \cdot L_c \tag{2.134}$$

where SC is the degree of subcooling measured experimentally. The refrigerant mass flow rate ($\dot{m}_r$) was estimated knowing the refrigerant conditions at the compressor suction inlet and assuming a value for the volumetric efficiency;

2. the length of the superheated zone (L_{SH}) at the condenser was assumed equal to:

$$L_{SH} = 0.10 \cdot L_c \tag{2.135}$$

therefore the length of the two-phase mix zone can be expressed trivially as $L_{TP} = L_c - L_{SH} - L_{TP}$;

3. the length of the two-phase mix zone at the evaporator was assumed equal to:

$$L_{TP} = 0.75 \cdot L_e \tag{2.136}$$

and hence the superheated zone as: $L_{SH} = L_e - L_{TP}$

The results of the analysis are reported in Figure 2.47 that shows the mean error and the standard deviation for all the correlations tested. The best correlation for this application is Winkler et al. [40] (in the bar chart is called W/K/G from the initial letters of the authors). It presents a mean error of 1.5% although its standard deviation is significant ($\approx 16\%$) and greater than other correlations. It is a drift-flux correlation with constant parameters and results from a wide experimental investigation for condensing flows of refrigerant R134a in minichannel geometries (square, rectangular and circular) with 2 $< D_h <$ 4.91 mm. The worst correlation, for this application, is Zivi's correlation integrated assuming a quadric profile for the refrigerant quality with error about 40% of the actual charge. Zivi assumes homogeneous flow, i.e. treating the two phase mixture as a single fluid (homogeneous mixture) with representative mean thermophysical properties. The assumption of equal velocities of the two phase limits its applicability to only a few two-phase flow situations, for instance at pressure close to the critical pressure, when vapor and liquid density approach at the same value. The approximation is emphasized in case of quadratic quality profile.

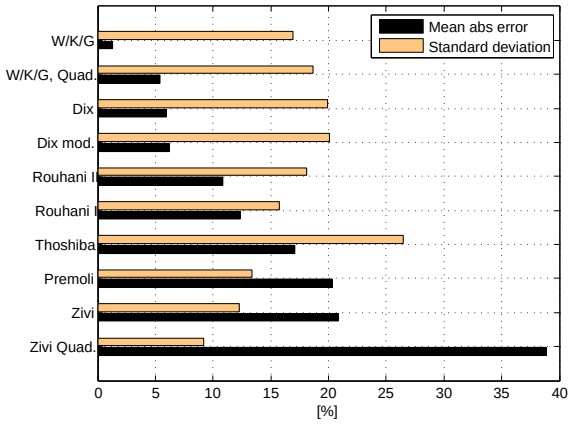

FIGURE 2.47: Mean error and standard deviation for all the correlations tested.

Figure 2.48 shows the refrigerant charge distribution for dryer n°4 working with R407c and where the Winkler et al.'s correlation [40] excellently predicts the actual refrigerant charge (mean error lower than 1%). The figure allows to recognize how the charge is distributed on the components: the charge inventory of the condenser is the greatest ($> 60\%$), follow to the evaporator with 38% and the other pipes with 2% (due to the arrangement of the heat pump module).

As the Winkler et al.'s correlation is depended from the refrigerant pressure (p), the inlet enthalpy (h_i) and the refrigerant mass flow ($\dot{m}_r$) and due to the made choice of the state variables (the void fraction mean is not a state variable) this leads to introduce complexity in the analytical development of the governing equations. For example, in the derivation of the equations for the TP-L (see Appendix B) the mean density of the two-phase zone (ρ_2) must be depended also from refrigerant mass flow time derivative as follows:

$$\frac{d\rho}{dt} = \left.\frac{\partial \rho_2}{\partial p}\right|_{h_i,\dot{m}} \cdot \frac{dp}{dt} + \left.\frac{\partial \rho_2}{\partial h_i}\right|_{p,\dot{m}} \cdot \frac{dh_i}{dt} + \left.\frac{\partial \rho_2}{\partial \dot{m}}\right|_{p,h_i} \cdot \frac{d\dot{m}}{dt} \tag{2.137}$$

In the SH-TP-L condenser mode since the inlet quality is equal to one the dependency is only both by the refrigerant pressure and the refrigerant mass flow. The time derivative of the refrigerant mass flow rate must not be neglected since all the drying cycle can be considered as a transient. However the signal noise generated by the time derivative of inlet enthalpy can have unintended side effects upon the dynamics of the simulation as well as cause many solvers to fail to converge to a solution. In general, it is not recommended to numerically differentiate input signals as any noise in the original signal is amplified through differentiation. For this reason the previous correlation is not adopted in this work, however if in the future improvements the void fraction mean is used as state variable then it could be used.

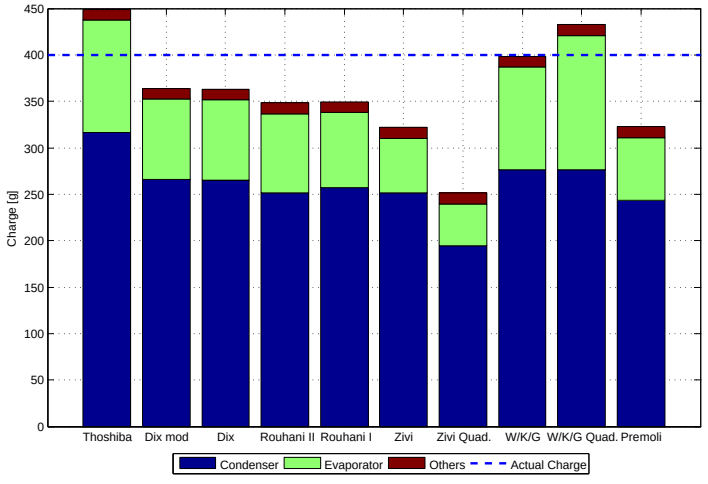

FIGURE 2.48: Refrigerant charge distribution for Dryer n°4.

Other correlations used for the analyses were deduced from the following work [41] where the performance of 68 void fraction correlations are tested on a wide dataset. From this assessment, four drift flux correlations: Rouhani I, Rouhani II, Toshiba, Dix and two slip ratio correlations with homogeneous flux assumption: Zivi and Premoli et al. were chosen.

Dryer	Refrigerant	V_c	V_e	V_{tot}	Actual charge
n°		[cm^3]	[cm^3]	[cm^3]	[g]
n°1	R407c	1389.4	692.19	2081.59	610
n°2	R407c	940.75	692.19	1632.94	520
n°3	R407c	701.88	545.69	1247.54	400
n°4	R407c	701.88	545.69	1247.54	400
n°5	R134a	1389.4	692.19	2081.59	590
n°6	R407c	1389.4	692.19	2081.59	635
n°7	R407c	940.75	692.19	1632.94	460
n°8	R134a	632.37	313.24	945.61	370
n°9	R134a	472.24	313.24	785.48	380
n°10	R134a	313.24	153.68	466.92	200

TABLE 2.2: Geometric features and actual charge of the tested dryers.

Chapter 3

Heat pump tumble dryer air circuit model

3.1 Introduction

This chapter is focused on the aeraulic circuit of the heat pump tumble dryer model. The chapter is divided into three parts: in the first part the developed model will be presented with the assumptions made in order to simplify the matter. In the second part the elements that characterize the aeraulic circuit will be discussed, analyzed and modeled with the experimental data acquired during specific tests developed for the aeraulic characterization. In the third part the comparison between experimental data and simulated results will be discussed in order to evaluate the model reliability.

3.2 Aeraulic circuit model

As the air is the working fluid in the dryer, Figures 3.1, 3.3, 3.4 can be used for following its flow path through various components of the machine. Starting from the fan outlet section, the air flows through the dryer back towards the drum, before entering into the drum, it crosses a perforated flange (R_{flange}) characterized by a large number of small holes. Inside the drum the clothes are dried by the air flow with the tumbling motion, the temperature of the air decreases, humidity increases and the air flow stream is affected by a low pressure drop (R_{load}) (due to a low velocity inside the drum because of large volume). The air leaving the drum is ducted through a lint filter before entering the heat pump module. The clogging effect of the filter increases progressively during the cycle because of the drying process generates lint ($R_{filter+door}$). In the heat pump

module the air flow first crosses the evaporator finned coil heat exchanger (R_{evap}) and then the condenser (R_{cond}). Leaving the heat pump the air flow stream is bended two times at 90° and is accelerated since the cross section is reduced in this part of the air circuit ($R_{air\ duct}$). Crossing the process fan the static pressure of the air flow stream rises.

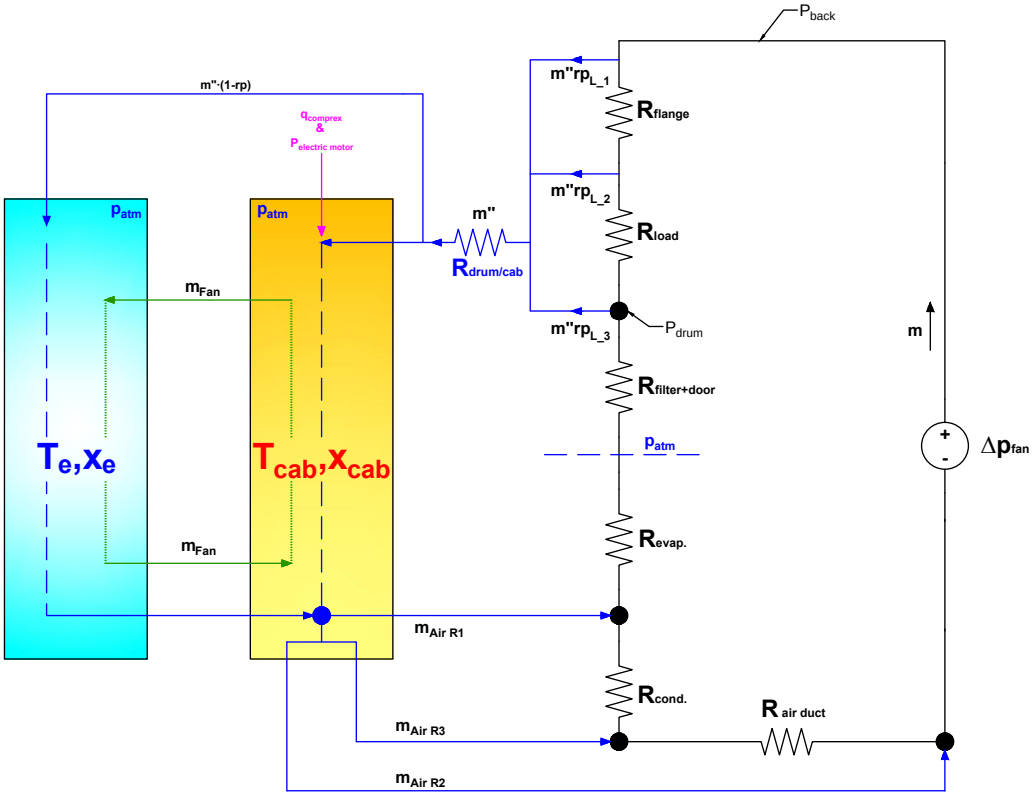

FIGURE 3.1: Air circuit model heat pump tumble dryer.

The air flow path discussed above is the main one. However, in order to evaluate properly the performances of the device, secondary flow paths must be accounted for. In particular, the air flow stream path, governed by the aeraulic resistance of the drum front and rear seals ($R_{drum/cab}$), that leaves the drum ($\dot{m}''$) must be described since it strongly affects the performance of the heat pump module (it increases or reduces the thermal load on the evaporator). Therefore, in order to efficiently model the air circuit a complete experimental characterization of the air circuit was carried out. With the experimental information a simple model for each aeraulic circuit component was developed.

Analytically, for estimating the mass flow rate drawn by the fan ($\dot{m}$), the mass flow rate exiting the system ($\dot{m}''$) and the temperature of the air inside the cabinet T_{cab}, the

following non-linear system has to be solved:

$$\begin{cases} \Delta P_{fan}(\dot{m}, T_{i,fan}) = \Delta P_{flange}(\dot{m} - \dot{m}^{''} \cdot rp_{L_1}, T_{i,drum}) + \\ \quad + \Delta P_{load}(\dot{m} - \dot{m}^{''} \cdot (rp_{L_1} + rp_{L_2}), T_{i,drum}, LWC) + \\ \quad + \Delta P_{filter+door}(\dot{m} - \dot{m}^{''}, T_{o,drum}, LWC) + \\ \quad + \Delta P_{e}(\dot{m} - \dot{m}^{''}, T_{o,drum}) + \\ \quad + \Delta P_{c}(\dot{m} - \dot{m}^{''} \cdot (1 - R_1), T_{i,c}) + \Delta P_{a,circuit}(\dot{m}_{HE}, \bar{T}_{HE}) \end{cases} \tag{3.1}$$

$$\Delta P_{filter+door}(\dot{m} - \dot{m}^{''}, T_{o,drum}, LWC) = \Delta P_{drum-cab.}(\dot{m}^{''}, T_{i,drum}) \tag{3.1,a}$$

$$\begin{aligned} \dot{m}_{cool.\,fan} \cdot c_{p,e} \cdot T_e + \dot{m}^{''} \cdot rp \cdot c_p|_{o,dryer} \cdot T_{o,dryer} + \dot{m}^{''} \cdot (1 - rp) \cdot c_{p,e} \cdot T_e + q_{comprex} - \\ - (\dot{m}_{cool.\,fan} + \dot{m}^{''}) \cdot c_{p,cab} \cdot T_{cab} - q_{cab-e} = 0 \end{aligned} \tag{3.1,b}$$

The first equation (3.1) in the system states up the static pressure balance of the aeraulic circuit, the second expresses the balance between the pressure drop across the filter and the difference in pressure between the cabinet and the drum. Finally the third equation indicates the conservation of the energy applied at the cabinet air volume.

In addition, the following assumptions are made:

- the air is incompressible therefore non mass and energy accumulation occurs along the air process circuit;
- the ambient pressure value inside the circuit is a fixed value and is located between the filter and the evaporator;
- theoretically, in order to predict the amount of mass flow rate that exits the drum ($\dot{m}^{''}$), two aeraulic resistances should be considered: one describing the resistance created by the rear seal and the other describing the aeraulic resistance of the front seal. Experimentally this was not possible and only one resistance $R_{drum-cab}$, that sums up the two effects is considered. For this reason the constant terms rp_{L2}, rp_{L3} are introduced: experimentally evidences indicate a greater value for the constant rp_{L3}, this means that the drum main leakage is located on the front seal although in some arrangement, between the rear drum flange and the drum, also the term rp_{L1} must be considered (see the following point);
- the constant term rp_{L1} is introduced in order to contemplate different flange and drum configurations as reported in Figure 3.2. In case of drum with fixed flange the term rp_{L2} is equal to zero since the back flange is installed before the air flowing into the drum, in other configurations the term rp_{L1} can assume a value not equal to zero;

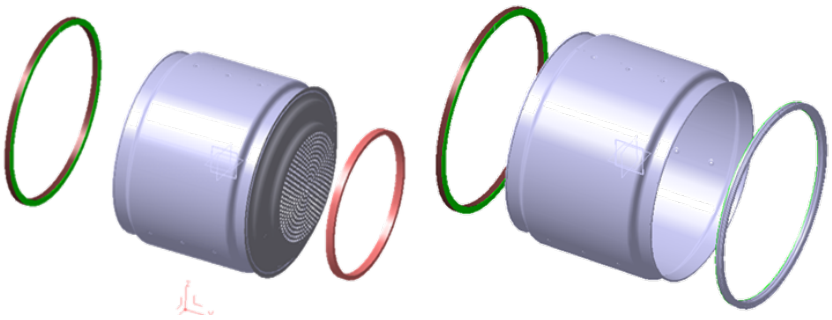

(A) Drum with flange. (B) Drum without flange.

FIGURE 3.2: Different configurations of the system flange and load

- also the assessment of the points where the mass flow rate enters the process circuit is an issue and this was not characterized. Experimentally evidences show that more points where the air enters into the system could exist. A first point is located between the evaporator and the condenser heat exchanger: this is caused by the not perfect sealing of the evaporator pipes with the basement (inlet and outlet evaporator pipes: the inlet pipe connects the heat exchanger to the capillary tube that is installed inside the cabinet, the outlet tube connects the evaporator to the compressor). A second point where the air enters the process circuit is placed after the condenser heat exchanger because, as for the evaporator pipes, the condenser inlet and outlet pipes are not properly isolated from the cabinet (the inlet pipe comes from the compressor and the outlet pipe is connected to the capillary tube). A third point, and experimentally it seems to be the greatest source of fresh air, is located at the fan inlet section due to a not perfect sealing of the impeller shaft with the cabinet. Therefore the parameters R_1, R_2 and R_3 representing air flow resistances associated to the leakage points are arbitrarily chosen and are not calibrated with experimental tests;

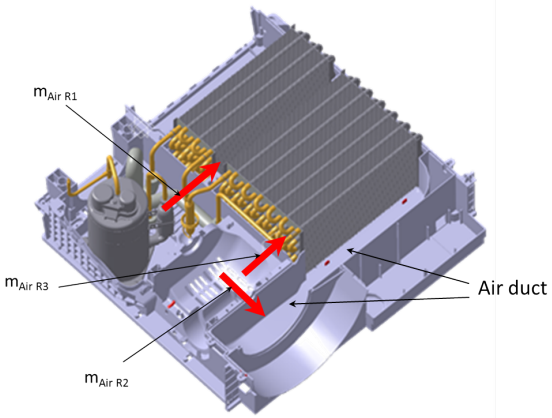

FIGURE 3.3: Heat pump module air circuit.

- not all the mass flow rate that goes out form the drum zone remains into the cabinet, a certain amount leaves the cabinet from the top part (see Figure 3.4). This quantity is defined by the constant rp that is arbitrarily chosen;

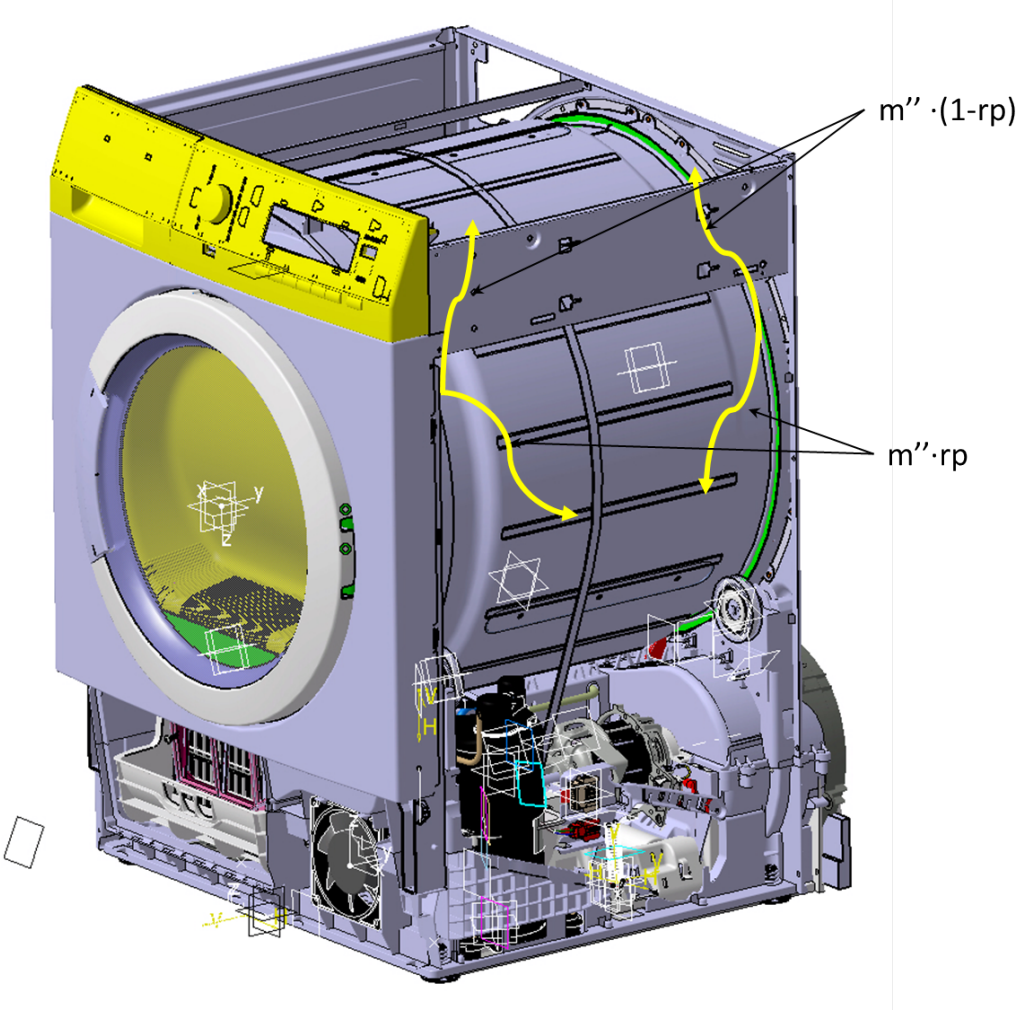

FIGURE 3.4: Mass flow rate exiting the drum.

- the thermohygrometric properties of the ambient (T_e , x_e and p_{atm}), where the device is placed, are constant;

- $\dot{m}_{cool.\,fan}$ is not an unknown term. This term is the mass flow rate that the compressor cooling fan draws. It sucks air from the ambient and blows it towards the compressor shell in order to increase the energy losses of the system. This value was measured experimentally as shown in Figure 3.5. The compressor cooling fan is switched on when the measured refrigerant temperature at the condenser outlet by a NTC probe exceeds a set-point value. This latter value is chosen in order to avoid working conditions outside the envelope of the compressor;

FIGURE 3.5: Measurement of the cooling fan mass flow rate.

- as discussed in [42] the pressure inside the cabinet is at the ambient pressure and therefore does not affect the value of the mass flow rate leakage.

3.3 Experimental characterization of the aeraulic circuit

In order to evaluate the pressure drops through the drum with and without load and the resistance that defines the amount of leakages through the drum seals a dedicated test rig was designed [42]; the scheme of the test rig is reported in Figure 3.6. The test rig allows the air flow stream to flow only in the drum air circuit: fan volute, back duct, drum and filter. The value of the volumetric flow rate that flows in the circuit (Q_{in}) is set before entering the system, the inlet temperature (T_{in}) and the static pressure ($P_{abs\,back\,flage}$) are also controlled. The outlet mass flow rate measurement allows to estimate the leakages as $\Delta Q = Q_{in} - Q_{out}$. The push-pull double fan configuration is necessary in order to control both the inlet mass flow rate and the pressure inside the drum. The experimental conditions tested in [42] were: volumetric flow rate in the range of 100-200 Nm^3/h, the drum inlet temperature from the ambient value to 60 °C and the drum inlet static pressure from 0 to 500 Pa. The normalized weight of the dry fabric load was 8 kg.

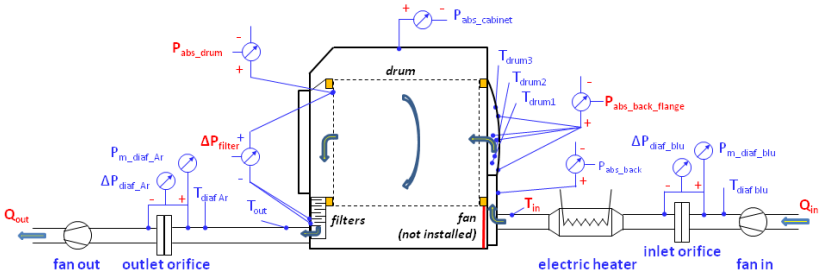

FIGURE 3.6: Test rig for characterization of the drum aeraulic circuit.

3.3.1 Drum flow leakages

In Figure 3.7 on the left chart the mass flow rate leakage is plotted as function of the static drum pressure ($P_{abs\,drum}$). In this chart the measurements of all tests (variable inlet flow rate, temperature and load conditions: wet, dry and without load) are plotted. The trend indicates that leakages increase if the pressure inside the drum rises (as expected). It is worth noting that negative values of ΔQ exists for low values of the pressure inside the drum: this means that there must be a region located downstream of the filter where a certain amount of mass flow rate enters the circuit.

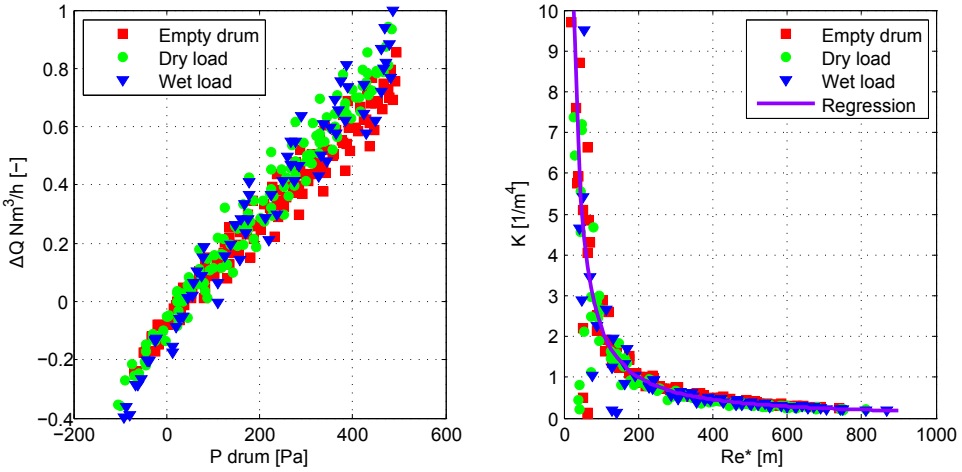

FIGURE 3.7: Drum flow leakages and loss coefficient at variable conditions of load, temperature and inlet flow rate. Re^* is defined by Equation 3.3

As described in [42] a data normalization process was made in order to develop a unique correlation for predicting the mass flow rate leakage. A pressure loss factor coefficient was introduced as:

$$K_{drum/cab.} = \frac{\Delta P}{\rho^* \cdot V^{*2}} \quad \left[\frac{1}{m^4}\right] \tag{3.2}$$

where: ΔP is equal to the static drum pressure ($P_{abs\,drum}$) since the cabinet is always at the ambient pressure and therefore does not affect the value of the mass flow rate leakage. The subscript (*) indicates the air reference conditions at which the thermodynamic properties of the air are evaluated. They were defined as: T^* and $p_{amb.}$ where T^* is the drum inlet temperature. Additionally, a linked parameter with the Reynolds number was expressed as:

$$Re^* = \frac{\rho^* \cdot V}{\mu^*} \tag{3.3}$$

where the dependency from a characteristic length is not significant in order to predict the trend of the loss factor, therefore it was neglected.

The result of the normalization is shown in Figure 3.7 on the right chart. The loss factor decreases when the Reynolds number increases as expected for low value of the Reynolds number. This loss factor defines the aeraulic resistance $R_{drum/cab.}$.

3.3.2 Flange pressure drop

The pressure drop across the drum inlet flange was measured as the difference between the static pressure $P_{abs\,back\,flage}$ and $P_{abs\,drum}$ without load. In [42] a constant value of the loss coefficient (K_{flange}) was obtained. Therefore, this value is used to compute the flange pressure drop ΔP_{flange}.

3.3.3 Load pressure drop

During tests with load, the difference between $P_{abs\,back\,flage}$ and $P_{abs\,drum}$ (see the scheme in Figure 3.6) is the sum of two pressure drops: the first is the flange pressure drop and the second is the pressure drop due to the fabric load. This latter can be expressed as follows:

$$\Delta P_{load} = (P_{abs\,back\,flage} - P_{abs\,drum}) - \Delta P_{flange} \tag{3.4}$$

The data normalization leads to the chart in the following figure.

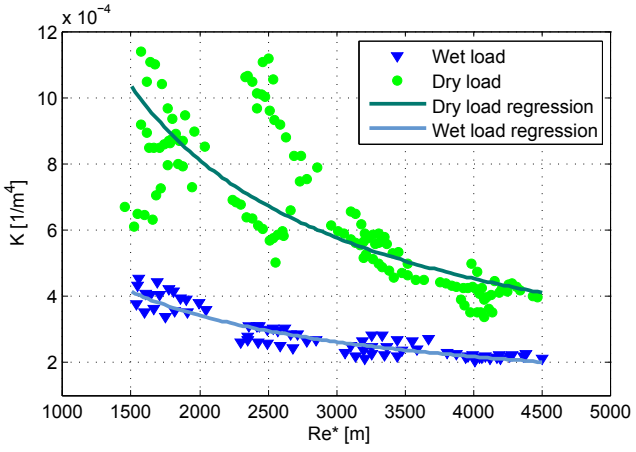

FIGURE 3.8: Load loss coefficient. Re^* is expressed by the Equation 3.3.

The two data regression correlations have this form:

$$K_{load\,wet/dry} = a \cdot (Re^*)^b \tag{3.5}$$

where a and b are two constants and cannot be here reported for industrial secrecy reasons. In the model the transition between wet and dry condition is made linearly with the LWC (load water content, definition given in 4.1). Therefore, K_{load} may expressed as:

$$K_{load} = K_{dry\,load} - \frac{K_{dry\,load} - K_{dry\,wet}}{100} \cdot LWC \tag{3.6}$$

3.3.4 Filter pressure drop

The filter pressure drop was evaluated as the difference between the static drum pressure ($P_{abs\,drum}$) and the measured pressure downstream of the filter (see the scheme in Figure 3.6).

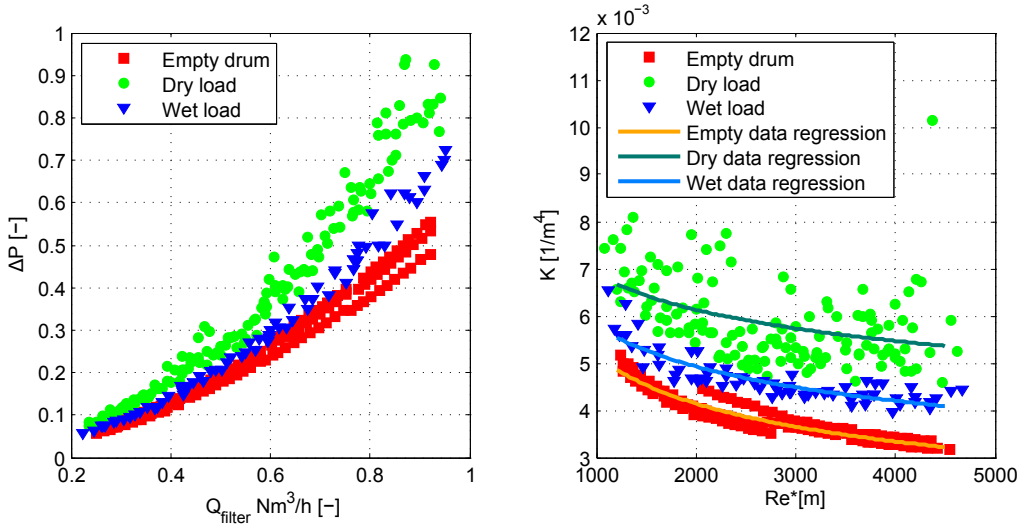

FIGURE 3.9: Filter pressure drop and loss factor. The Reynolds number in the chart follows the definition given in 3.3.

Similarly to the static pressure across the load, the transition of the filter loss coefficient (K_{filter}) between wet and dry condition is made linearly with the LWC definition given in 4.1. In all tests the filter has to be considered as clean as possible, although during the dry load tests it got dirty quickly (the drying process generates lint). During the test carried out for characterizing the evaporation process of the moisture content from the laundry (see Chapter 4), the pressure drop from the drum back panel and the downstream section of the filter was measured. This pressure drop is the sum of three effects: the pressure drop across the flange, the load and the filter. The sum of the previous pressure drops, for different tests conditions, as function of the LWC is reported in Figure 3.10. From the figure it can be clearly pointed out that the mass flow rate strongly affects the value of the pressure drop. Tests show that passing from 100 Nm^3/h

to 140 Nm^3/h determine a pressure drop increment of about 12% while passing from 140 Nm^3/h to 180 Nm^3/h show a 20% pressure drop increment. The air temperature affects the pressure drop about 2-3%, this effect is greater for high values of the mass flow rate than lower values. The effect of the humidity is not significant. The final part of the drying process, when the laundry load is almost dry, is strongly affected by the load quantity. In Figure 3.11 data for tests at full load and tests at half load are plotted and a noticeable pressure drop difference at the end of the cycle (for value greater than 60% of LWC) can been pointed out. Nearly to 0% of LWC value the difference is almost 20%. Therefore, in order to develop a unique correlation expressing the pressure drop as a function of the mass flow rate, temperature, load water content (LWC) and load quantity a regression analysis was carried out and the resulting correlation form is:

$$\Delta P_{flange+load+filter} = (a \cdot LWC^3 + b \cdot LWC^2 + c \cdot LWC + d) \cdot RL^e + f \cdot \left(\frac{\dot{m}_{i,drum}}{\rho_{i,drum}} \right)^2 \tag{3.7}$$

where: a, b, c, d, e and f are constants deducted from the regression process and cannot be here reported for secrecy industrial reasons. RL is called ratio load and is equal to the weight of the normalized dry load over the weight test load. For this correlation, the coefficient of determination (r^2) is equal to 0.92.

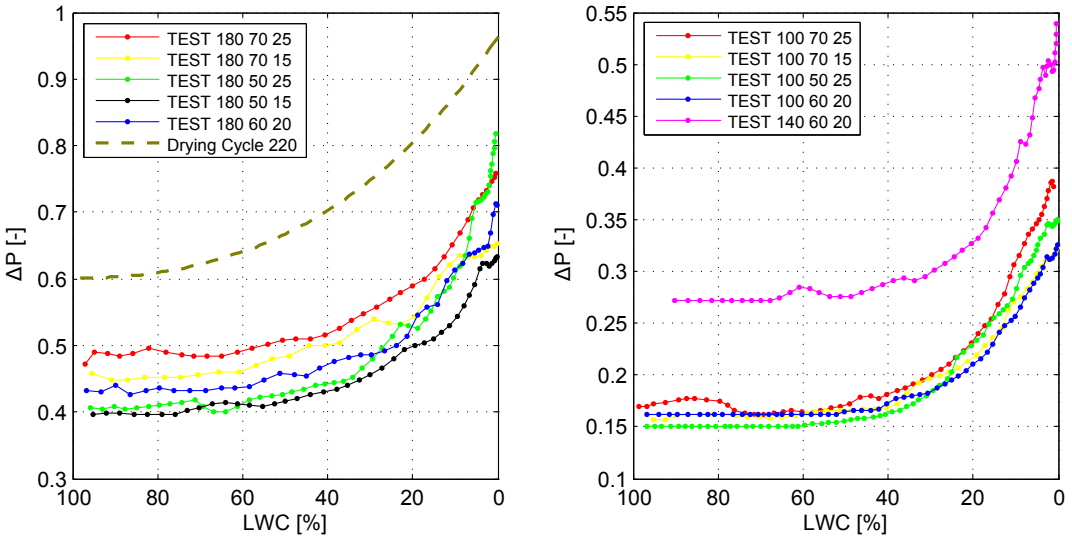

FIGURE 3.10: Flange+load+filter pressure drop. The label on the legend must be read in this way: the first value is the volumetric flow rate (Nm^3/h), the second value is the inlet temperature (°C) and the third value is the relative humidity (%).

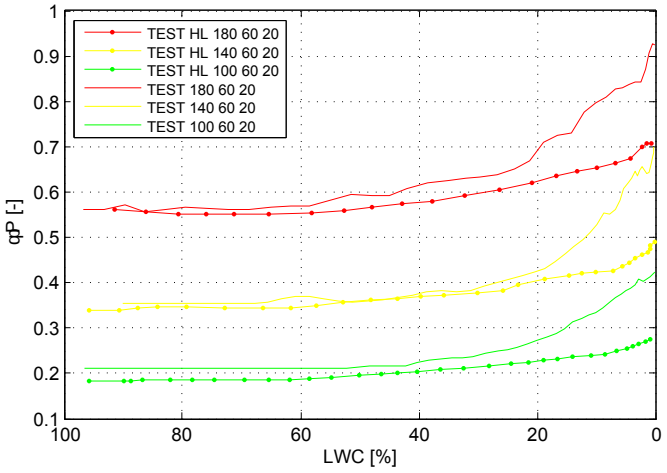

FIGURE 3.11: Flange+load+filter pressure drop for full and half load tests.

Considering Equation 3.7 the clogging effect of the filter can be expressed as:

$$\Delta P_{clog.\,filter} = \Delta P_{flange+load+filter} - \Delta P_{flange} - \Delta P_{load} - \Delta P_{filter} \tag{3.8}$$

the result is plotted in the next Figure 3.12. ΔP_{flange} is calculated as discussed in the Paragraph 3.3.2, ΔP_{load} is computed as shown in Paragraph 3.3.3, ΔP_{filter} is determined as described in Paragraph 3.3.4 and finally $\Delta P_{flange+load+filter}$ with the correlation given in 3.7.

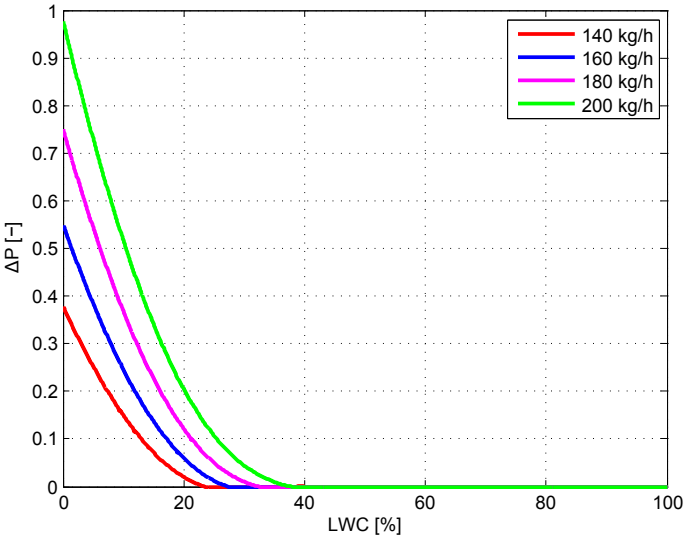

FIGURE 3.12: Clogging effect of the filter.

To sum up, in the aeraulic model of the heat pump tumble dryer, the pressure drop across the filter is evaluated as:

$$\Delta P_{filter} = K_{filter} \cdot \rho_{a,i,filter} \cdot V_{i,filter}^2 + \Delta P_{clog.\,filter} \tag{3.9}$$

3.3.5 Evaporator and condenser pressure drop

The pressure drops across the evaporator and the condenser finned coil heat exchanger are evaluated via software [16]. This software uses a finite volume approach and allows steady-state analysis. From a series of tests, where the volumetric flow rate was varied and the thermohygrometric properties of the air were fixed, the pressure drop correlation is deduced as follows:

$$\Delta P_{HX}^* = a \cdot V^{*2} + b \cdot V^* + c \tag{3.10}$$

where V is the volumetric flow rate respect to the air properties at the conditions indicate with the superscript (*), and a, b, c are constants that change for different heat exchanger arrangement. The correlation, as set out above, is obtained for fixed thermohygrometric properties of the air. Therefore, in order to contemplate different working conditions during the drying cycle (e.g. the temperature at the condenser inlet varies more than 20 ℃ during the drying cycle) the actual value of the pressure drop is computed as follows:

$$\Delta P_{HX} = \Delta P_{HX}^* \cdot \frac{\rho^*}{\rho_{i,HX}} \tag{3.11}$$

3.3.6 Air duct pressure drop

The heat pump air duct connects the condenser outlet to the fan inlet section, see Figure 3.3. In [43] an experimental procedure is developed in order to quantify the process mass flow rate that flows in the main aeraulic path to characterize the aeraulic circuit of the heat pump module. The procedure is based on two steps: first the pressure rise across the fan (ΔP_{fan}) is measured during tests in which the tumble dryer operates on an open cycle. The air circuit is opened in a suitable point where the device is connected to a duct where heater and booster fan are installed (see Figure 3.13). In addition, the duct is instrumented with a mass flow meter (orifice flow meter). Tests at different constants temperature and volumetric flow rate values can be performed with the heater and the booster fan configuration. Furthermore, the pressure drop across the heat exchangers is acquired (ΔP_{HE}). The second step is to restore the real operating cycle (closed loop) and use the fan pressure rise signal to predict the fan mass flow rate during a standard drying cycle.

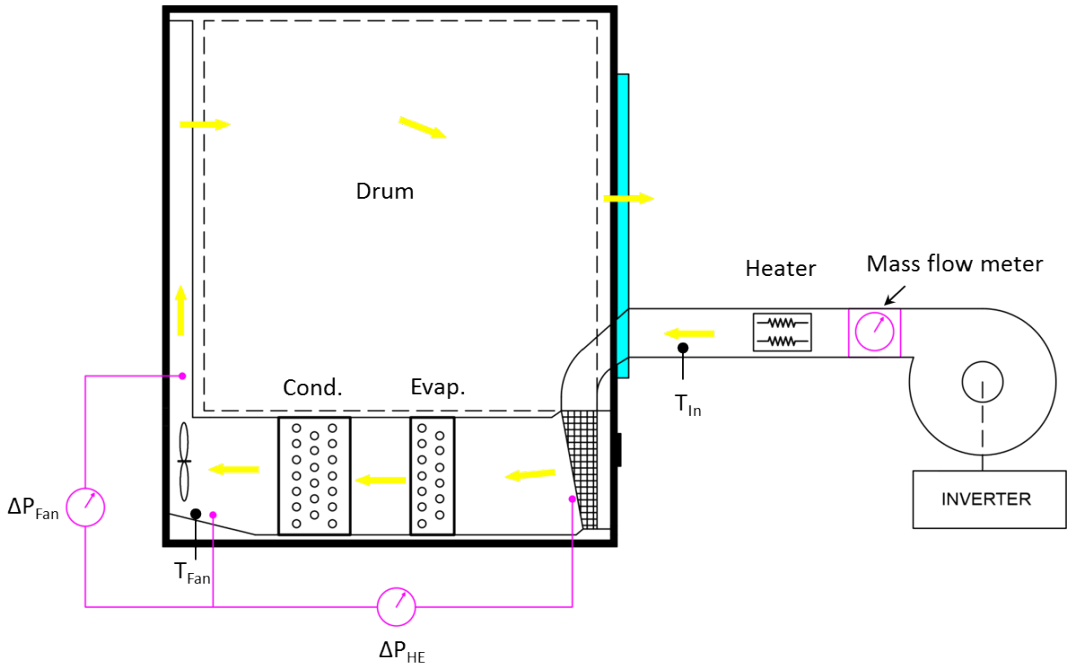

FIGURE 3.13: Schematic of the test rig for the characterization of the heat pump aeraulic circuit.

The signal of the pressure drop across the heat exchangers is used to compute the pressure drop along the air duct since the heat exchanger downstream pressure tap is located nearly to the inlet fan section. In the model the following equation is implemented:

$$\Delta P_{air\,duct} = \Delta P_{HE} - \Delta P_e - \Delta P_c \tag{3.12}$$

In Figure 3.14 on the left chart is plotted the pressure drop (ΔP_{HE}) as function of the standard volumetric flow rate. A slight dependency on the fan speed can be observed. This suggests that the pressure filed across the heat exchangers is affected by the fan working conditions. In order to develop a unique correlation two parameters were defined:

$$\phi_{HE} = \frac{\dot{m}}{\rho \cdot \Omega} \quad [m^3] \tag{3.13}$$

$$\psi_{HE} = \frac{\Delta P_{HE}}{\rho \cdot \Omega^2} \quad [m^2] \tag{3.14}$$

where the air density was computed with reference to the mean flow temperature across the heat exchangers and Ω is the fan angular velocity. The parameters ϕ_{HE} and ψ_{HE} are able to describe the process since all data collapses on a single curve.

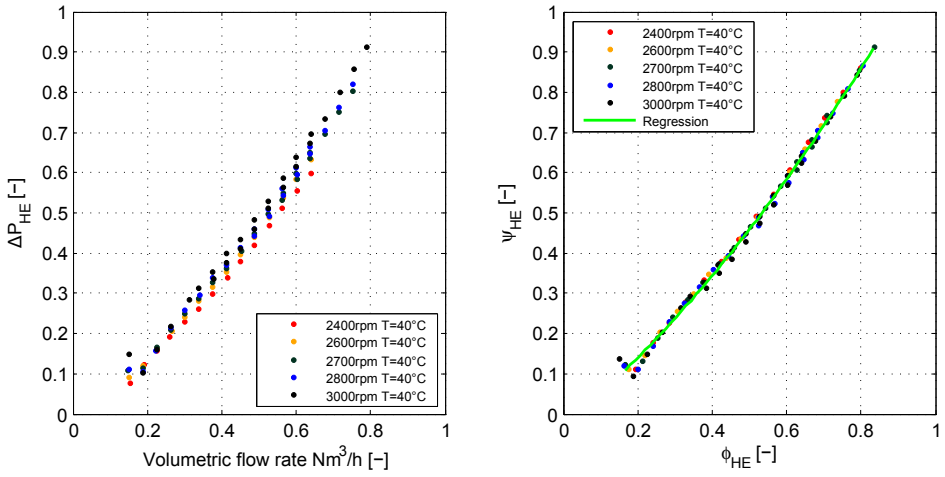

FIGURE 3.14: ΔP_{HE} on the left and non-dimensional data on the right.

3.3.7 Fan pressure rise

With the procedure mentioned in the previous paragraph, it was possible to estimate the fan characteristic curve. The curve is plotted in terms of dimensionless parameters, defined accordingly to the fan theory as:

$$\phi = \frac{\dot{m}}{\rho \cdot \Omega \cdot D^3} \quad \psi = \frac{\Delta P_{Fan}}{\rho \cdot \Omega^2 \cdot D^2} \tag{3.15}$$

where Ω is the fan angular velocity and D is the impeller diameter. They are respectively the flow and the pressure coefficient. The fan model accepts different fan curves allowing a comparison on the same aeraulic circuit.

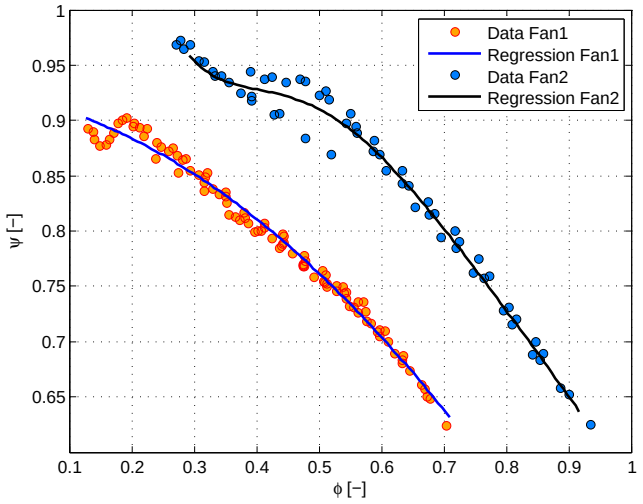

FIGURE 3.15: Two fans characteristic curves.

3.4 Aeraulic model validation and simulation results

The discussed correlations in the previous paragraphs were implemented in Matlab and Simulink environment and they define the non-linear system given in 3.1 that describes the behaviour of the aeraulic circuit model depicted in Figure 3.1. The comparison between simulation and experimental results was carried out setting on the model to experimental test conditions. The experimental values were obtained from closed circuit tests where the dryer was first warmed up to 40 ℃ and then tests were performed with the fabric load dried in closed loop configuration. These experimental choices allow to estimate the volumetric flow rate in the last part of the drying cycle. These conditions were applied at the model (air circuit temperature near to 40 ℃ and LWC equal to 1%). The comparison is shown in the Figure 3.16. For all the experimental points the difference is lower than 10%, the greatest discrepancies are obtained for values of the volumetric flow rate, that enters into the heat pump module, relating to conditions of 3000 rpm and 2400 rpm. It should be pointed out that all the component pressure drop correlations were obtained in an open circuit configuration whereas the comparison is made on data from a close circuit configuration. Therefore, due to the modification of the flow field passing from open to close circuit, the relations cannot be consider totally reliable. Finally, the experimental trend shows a plateau on the 2700-2800 rpm range that does not occur in the simulation results.

The difference from the two curves is the mass flow rate that leaves the drum from the rear and the front seal ($\dot{m}''$). In the model this quantity is significantly greater than the experimental value.

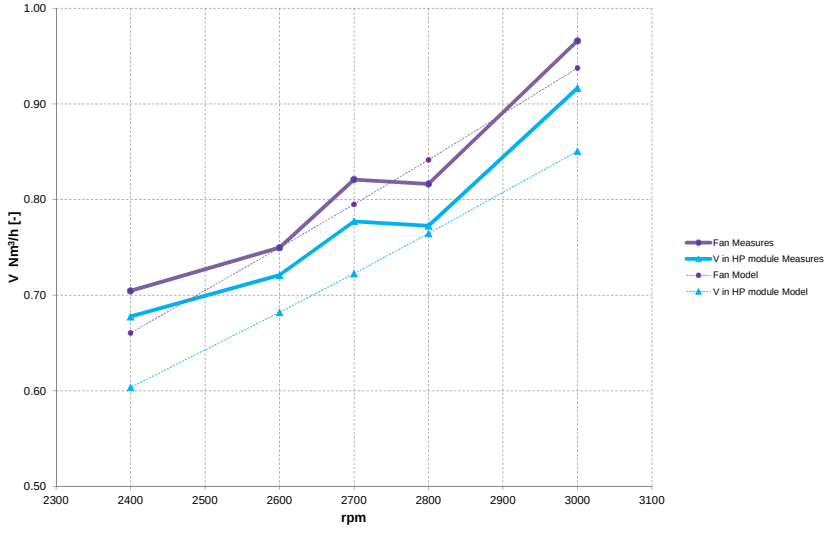

FIGURE 3.16: Volumetric flow rate: comparison between experimental data and simulation results.

3.4.1 Simulation results

In Figures 3.17 and 3.18 the evolutions of temperatures, relative humidities, volumetric flow rates and pressure drops are reported. Furthermore, the comparison (for some variables) between experimental data and simulation results is plotted. In these charts a complete drying cycle is simulated using as input variables the experimental measurements of temperature and relative humidity at the drum inlet and at the evaporator outlet (the compressor shell temperature was fixed at 90 °C). A sensible heat loss was introduced in order to predict the energy loss from the air flow stream leaving the heat pump module before entering into the drum. This loss increases the energy of the tumble dryer structure and it is described by a slow dynamic behaviour, without introducing another thermal capacity, its dynamic was connected to the LWC dynamic as follows:

$$q_{structure} = P_{comprex} \cdot \frac{100 - LWC}{100} \cdot \frac{\%P_{comprex}|_{LWC=0}}{100} \tag{3.16}$$

where $P_{comprex}$ is the compressor power, LWC is the load water content defined in Equation 4.1 and $\%P_{comprex}|_{LWC=0}$ is a percentage of the compressor power when the laundry is dry (LWC = 0). In other words, the heat losses varies with the dynamic of LWC and its maximum value is equal to a percentage of the compressor power that is reached at the end of the drying cycle.

As depicted in Figure 3.17 the model is able to properly predict the drum outlet temperature and the relative humidity (therefore also the humidity ratio is efficiently predicted). Also the volumetric flow rate drawn by the process fan is efficiently predicted although in the final part of the cycle there is a difference greater than 15%. The last part of the cycle characterization is a tricky task due to the stochasticity of the drying process where many effects start to affect the system, for instance: clogging filter effect and increment of the laundry pressure drop. These two effects can be seen on the right chart in Figure 3.18 where the evolution of the pressure drops is plotted. In the last part of the cycle the filter pressure drop rises sharply due to the progressive clogging effect and also the load pressure drop increases although more gradually than the drop on the filter. Consequently, the fan pressure rises and the volumetric flow rate decreases and hence the pressure drop of the other components is reduced progressively. Similarly, the mass flow rate leakage from the process circuit tends to increase since it is governed by the static pressure inside the drum. The air duct pressure drop value is particularly high. This is not totally caused by the frictional effect along the duct wall, since the shape of this component is convergent and therefore the variation of the dynamic term of the total pressure has to be equal to the static term (the flow stream velocity increases more than five times from the condenser outlet section to the fan inlet section).

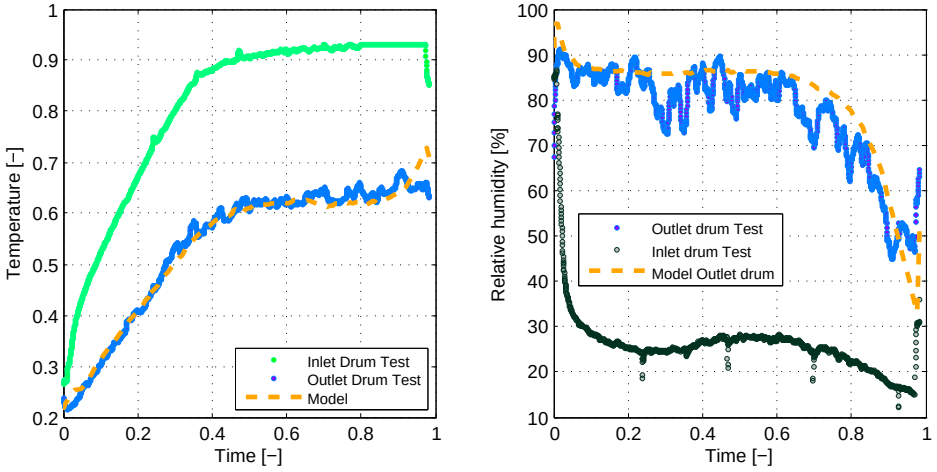

FIGURE 3.17: Air temperatures on the left and on the right relative humidities.

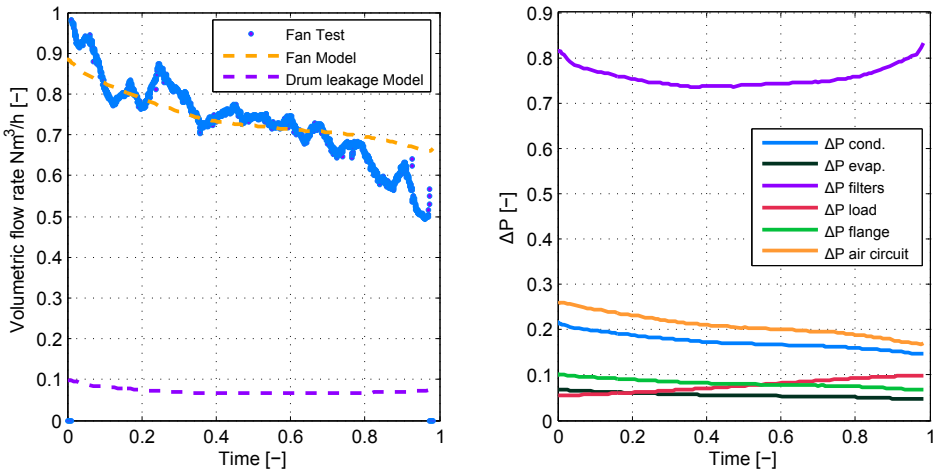

FIGURE 3.18: Volumetric flow rates (on the left): comparison between experimental data and simulation results. Pressure drops on different positions of the aeraulic circuit (on the right).

Chapter 4

Drum model

4.1 Introduction

This chapter is focused on the key element of any model of household tumble dryer: the drum. Its description affects the mass and energy flows thought the complete unit. In order to study and analyze the evaporation process that takes place from the laundry to the air some experimental tests were carried out. Two kinds of tests were developed: keeping the drum inlet conditions constants (mass flow rate, temperature and specific humidity ratio) therefore the heat pump system was deactivated, and tests setting only the mass flow rate at the drum inlet, holding the heat pump activated. Test results allowed to develop a correlation that explains the overall heat transfer coefficient between laundry load and air; the overall mass transfer coefficient was obtained applying the *heat and mass transfer analogy* based on the Lewis number. These correlations were used to develop a dynamic model of the system laundry-moisture content. The proposed model divides the system into two zones: a wet and a dry zone. The extension of the dry zone varies as function of the load moisture content and affects only the final part of the cycle. The comparison that will be shown between experimental data and model results indicates that the developed model is able to predict properly the air drum outlet thermohygrometric properties and the drying time. Finally, the results of the energy consistency tests will be proposed and discussed.

4.2 Experimental facility and system

The experimental facility used for studying the evaporation phenomenon and for developing the functions that describe how the water evaporates from the laundry is described in this section. As shown from the schematic in Figure 4.1, the heat pump system was disconnected from the drum. The drum inlet was connected to an external system that was able to fix the thermohygrometric properties of the air at the drum inlet section. This system is composed by:

1. fan. The fan was equipped with an inverter and hence it was possible to fix a set point value for the volumetric flow rate. The volumetric flow rate was measured by an orifice flow meter;
2. orifice flow meter; the orifice was realized in agreement with the directive UNI EN ISO 5167-21;
3. heater. The heater was equipped by an electronic device that was able to fix the value of the air temperature at drum inlet (see point 1 in Figure 4.1). The enthalpy of the ambient air is increased by heat input from the electrical heater;
4. humidifier. The humidifier was equipped by an electronic device that was able to fix the value of the relative humidity at drum inlet (see point 1 in Figure 4.1);
5. cell load. The heat pump dryer was mounted on load cells to record changes in its total mass.

Photographs of the experimental facility are shown in Figure 4.2

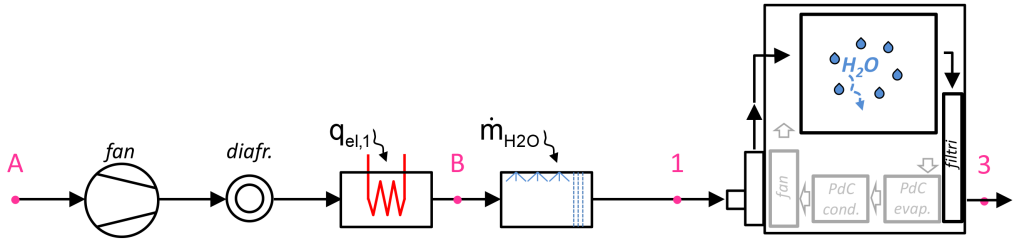

FIGURE 4.1: Experimental facility for drum analysis.

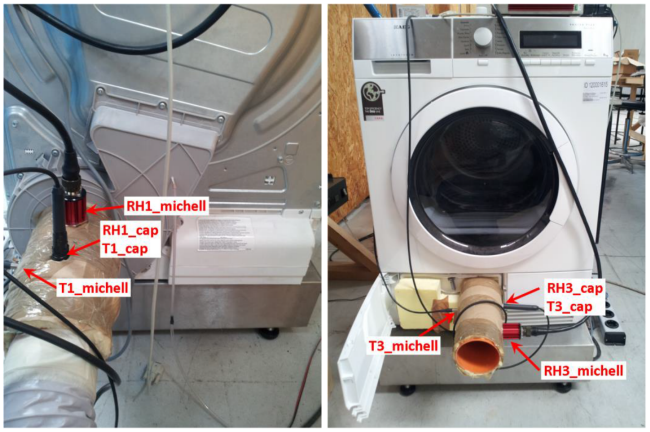

FIGURE 4.2: Measurements points.

The experimental system, as shown in Figure 4.2, was instrumented with a capacitive RH probe with integrated a temperature sensor. The accuracy is ± 0.8% RH (T=17 ℃) ± 2.5% RH (T=70 ℃) and also with an optical probe that measures the dew point temperature and its accuracy is lower than 1% on the range -40 to 90 ℃, and 0.5 to 100% RH.

4.3 Experimental data analysis

In order to investigate the process of the evaporation water from the laundry, a test plan was built. The variables that affect the evaporation process are: volumetric flow rate, air temperature and humidity at the drum inlet, weight and material of the load and finally the geometric features of the drum (the drum has a designated maximum dry load of 8 kg). In test plan in Table 4.1 the fabric material (only cotton load was considered) and the geometric features of the drum were set constants whereas the other variables were varied. The range of the variables, that affect the evaporation process, was chosen on the base of the experimental values measured in a standard drying cycle with a heat pump tumble dryer device. As observed by Deans in [44] the fabric material affects the last part of the drying cycle. In this phase significant differences in the fabric temperatures and in the exit air (drum outlet temperature) can be observed, therefore in order to develop a more general correlation different fabrics load should be tested. Typical results from a test are given in Figures 4.3a, 4.3b and 4.3c where the temperatures, humidities and evaporation rates of three tests at the same thermohygrometric conditions at the drum inlet (T = 140 ℃, RH = 20%) but different values of the volumetric flow rate (tests with higher volumetric flow rate are shorter) are reported. The variation over the time shows the main features of the drying cycle although cannot compare clearly tests with

different conditions. As shown in the figures during a complete drying cycle separate drying periods can be detected. First there is a heating phase during which the textiles and the dryer are heated. Thereafter a constant drying rate period is detected where the difference over time in the temperature leaving the dryer is small and finally the falling drying rate period where the rate of drying is descending and the drum outlet temperature is increasing.

Volumetric flow rate Nm^3/h	**T Drum Inlet** ℃	**RH Drum Inlet** %	**Load** Kg
100	60	20	full half
140	60	20	full half
180	60	20	full half
100	50	15 25	full
	70	15 25	
180	50	15 25	full
	70	15 25	

TABLE 4.1: Experiments table.

It is useful to introduce a dimensionless parameter to compare different tests. This parameter is called load water content LWC and is defined as:

$$LWC = \frac{M_w(t)}{M_w(0)} \cdot 100 \quad [\%] \tag{4.1}$$

where: $M_w(t)$ is the mass of water inside the laundry at the time t and $M_w(0)$ is the mass of water at the initial time $t = 0$. With this definition, for each test, the parameter LWC is equal to 100% at the beginning of the test, instead it is equal to 0% at the end.

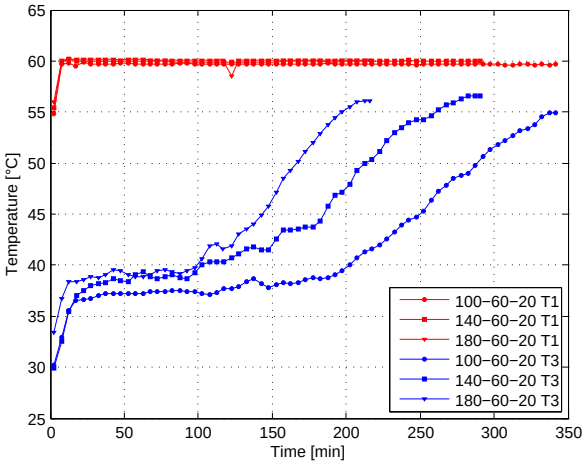

(A) Drum inlet and outlet temperatures.

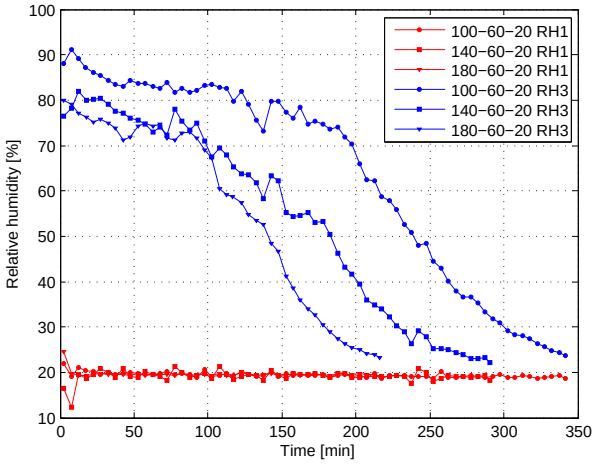

(B) Drum inlet and outlet humidities.

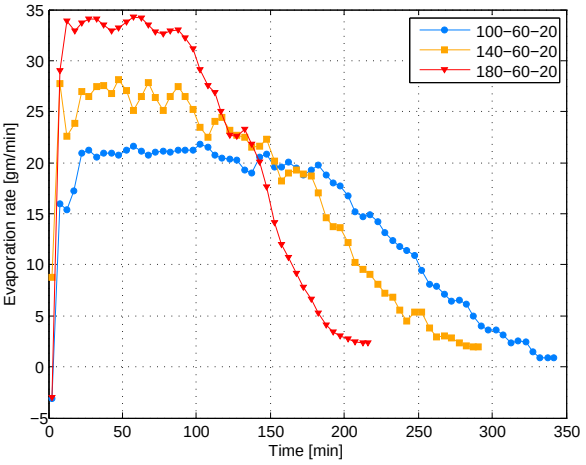

(C) Evaporation rates.

FIGURE 4.3: Temperatures (a) and relative humidities (b) at the drum inlet and at the drum outlet. Evaporation rate trends (c). The point values are the mean on five minutes. The label must be read in this way: volumetric flow rate [Nm^3/h]-temperature [℃]-relative humidity [%]

With the definition of LWC, as defined in 4.1, is possible to compare tests at different drum inlet conditions. All tests at full load condition are summarized in Figure 4.4 where the laundry temperature is shown. Some aspects could be observed from this chart:

1. in the $100 - 180$ Nm^3/h range the volumetric flow rate does not affect the temperature of the laundry. This temperature is close to the wet bulb temperature and it is determined only by the thermohygrometric conditions of the air at the drum inlet section in the 20%< LWC < 90% range (see Table 4.2, the maximum value of the deviation is lower than 2.5%);

2. the drying process could be divided into three phases as discussed earlier. A first phase where the laundry and the water inside are heated, a second phase where the water inside the laundry evaporates and a third phase where all the water is evaporated and therefore the temperature of the laundry increases.

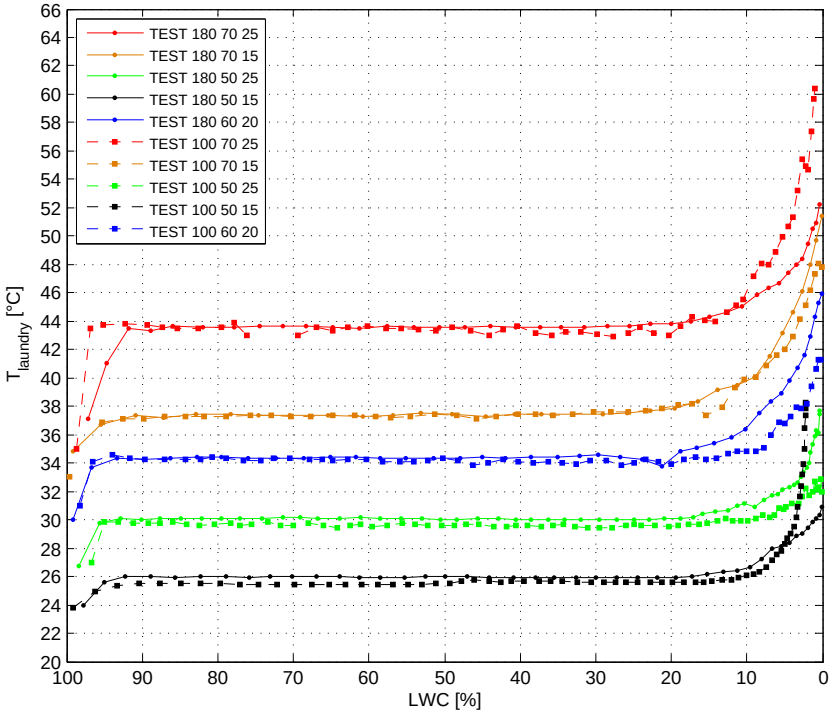

FIGURE 4.4: Laundry temperatures for all tests at full load conditions.The label must be read in this way: volumetric flow rate [Nm^3/h]-temperature [°C]-relative humidity [%]

In the first phase (90% < LWC < 100% range) the air yields heat at the laundry ($T_{air\,node} > T_{laundry}$, see Figure 4.5) and some vapor in air could condense if the temperature of the laundry is lower than the dew point temperature at drum inlet conditions.

In this phase, the convective heat flux is greater then the evaporation flux: $q_{conv} > q_{evap}$. In other words, during this stage the energy input is used to increase the temperature of the clothes and the structure of the dryer. In the second phase (20% < LWC < 90% range) the air yields heat at the laundry ($T_{air\,node} > T_{laundry}$) and water vapor evaporates from the laundry to the air. In this phase there is a balance between the convective heat flux and the evaporative heat flux ($q_{conv} = q_{evap}$). The temperature of the laundry is close to the wet bulb temperature of the air at the drum entrance condition. During this phase the surface of the laundry could be considered in saturated conditions. In the third phase (0% < LWC < 30% range) air yields heat at the laundry ($T_{air\,node} > T_{laundry}$) and water vapor evaporates from the laundry to the air, however, in this phase, the evaporative heat flux is not able to sustain the convective heat flux due to a reduction of the evaporation rate. Consequently, there is not a balance between the convective heat flux and the evaporative heat flux: $q_{conv} > q_{evap}$ and hence the laundry temperature increases.

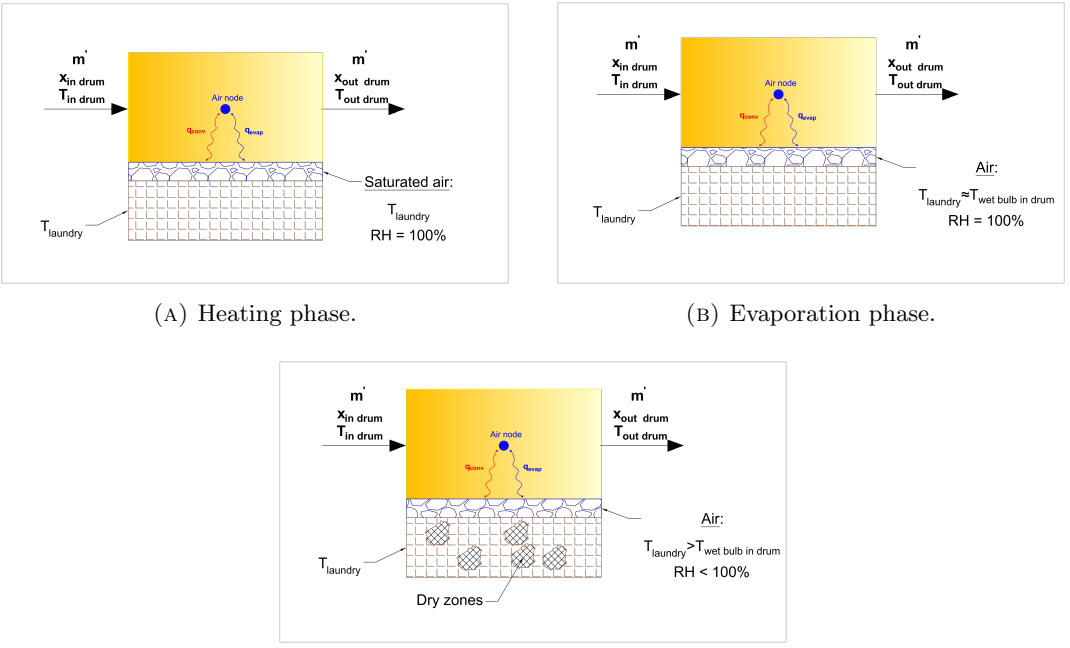

(A) Heating phase.

(B) Evaporation phase.

(C) Drying phase.

FIGURE 4.5: Drying process phases.

In addition to constant inlet conditions tests, other tests were carried out fixing only the drum inlet volumetric rate and keeping the heat pump activated. All the data was used to develop the correlations for the heat and mass transfer coefficient. Another result is presented in Figure 4.6 where, for each test, the maximum value of the evaporation rate over the difference between the wet bulb humidity ratio (at the drum inlet conditions) and the inlet are plotted. This difference can be considered as the governing force

of the mass transfer phenomena. The chart proves this assumption and shows how the measurements are arranged with a linear trend (on the considered domain) for equal mass flow rate tests. The mass flow rate moves to the top the evaporation rate maximum values and also changes the slop of the lines.

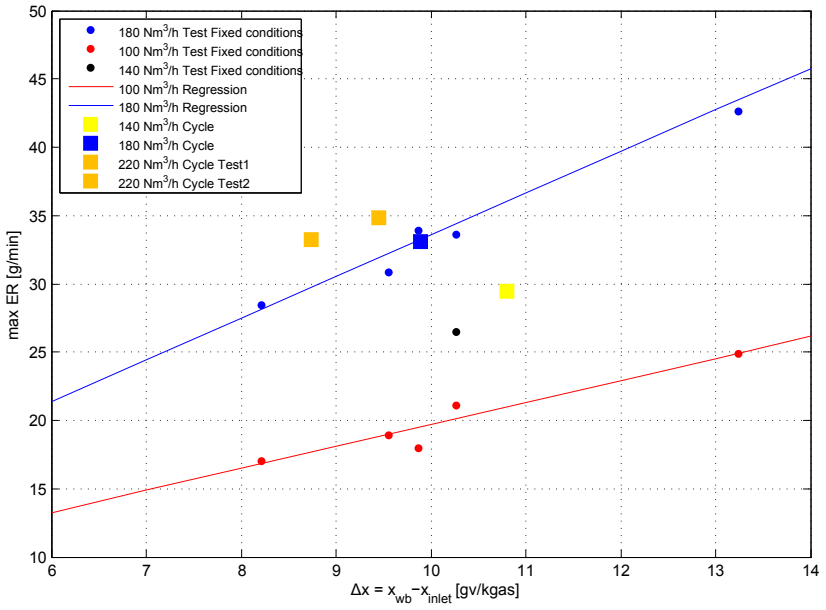

FIGURE 4.6: Evaporation rate over the difference between the wet bulb specific humidity and the inlet.

Conditions	$T_{wb,i}$	T_l	Deviation
℃-%	℃	℃	%
70-25	44.25	43.56	1.58
70-15	38.18	37.38	2.1
60-20	34.89	34.31	1.66
50-25	30.42	29.73	2.27
50-15	26.17	25.55	2.37

TABLE 4.2: Table wet bulb temperature comparison. $T_{wb,i}$ is calculated and T_l is the mean on $20\% < \text{LWC} < 90\%$ range.

4.4 Evaporation model

In this section the model of the system laundry-load will be presented starting from theoretically considerations of mass and heat transfer.

4.4.1 Theoretical considerations

The air flow stream that leaves the heat pump module interacts with the wet laundry inside the drum. Due to this interaction the air is cooled and humidified and the water in the laundry evaporates. Evaporations occurs from the surface of the laundry, and the energy associated with the phase change is the latent heat of vaporization of the liquid. The energy required to sustain the evaporation comes from the internal energy of the system laundry-water that adsorbs energy from the air that surrounds it. For a log period of the drying process the balance between the energy lost by the system laundry-water and energy form the convective heat transfer is maintained. At the end of the cycle the convective heat transfer is greater than the evaporative flux.
To sum up, the thermal process occurring inside the drum, involves air and the system laundry-water. It could be described by two processes that are linked together: a convection heat transfer process and a mass transfer process.

The convective heat transfer occurs due to a difference in temperature between the air and the laundry surface. Considering the generic portion of the laundry surface dA, the local heat flux may be expressed as:

$$q'' = h \cdot dA \cdot (T_a - T_l) \tag{4.2}$$

where h is the local convective coefficient between air and laundry surface, T_a is the air local temperature and T_l is the laundry surface local temperature.
Because flow conditions vary from point to point on the surface, both q'' and h vary on the surface. The total heat transfer, q, may be obtained by integrating the local flux over the entire surface. Hence:

$$q = (T_a - T_l) \int_A h \, dA \tag{4.3}$$

Defining an average convective coefficient, $\bar{h}$, for the entire surface, the total heat transfer rate may also be expressed as:

$$q = \bar{h} \cdot A \cdot (T_a - T_l) \tag{4.4}$$

Similar results may be obtained for the convective mass transfer. The mass transfer occurs due to a difference in molar concentration of the water vapor from the laundry surface and the air flow stream. Species transfer may also be expressed as a mass flow as follows:

$$d\dot{m}_v = h_m \cdot (\rho_{V,l} - \rho_{V,a}) dA_m \tag{4.5}$$

where h_m is the convective mass transfer coefficient, $\rho_{V,l}$ is the vapor mass density at the laundry surface (dry saturated vapor), $\rho_{V,a}$ is the vapor mass density in the air flow and dA_m is the generic wet zone surface. The evaporation rate on the overall wet surface may be expressed as:

$$\dot{m}_v = \int_{A_m} h_m \cdot (\rho_{V,l} - \rho_{V,a})|_{dA_m} \cdot dA_m = \int_{A_m} h_m \cdot \rho_a \cdot (x_l - x_a)|_{dA_m} \cdot dA_m = \\ = \int_{A_m} h_m^* \cdot (x_l - x_a)|_{dA_m} \cdot dA_m \tag{4.6}$$

where x_l and x_a are the local specific humidity and h_m^* is equal to $h_m \cdot \rho_a$. Hence, defining an average mass transfer coefficient $\bar{h}_m$ for the entire wet surface, the evaporation rate may also be expressed as:

$$\dot{m}_v = \bar{h}_m^* \cdot A_m \cdot (x_l - x_a) \tag{4.7}$$

The subscript a, in Equations 4.4 and 4.7 would describe the air in the mean conditions inside the drum. However these two equations (4.4 and 4.7) may be expressed also in terms of heat transfer efficiency and mass transfer efficiency:

$$q = \dot{m}_a \cdot \bar{c_{p}}_{i,o} \cdot P_s \cdot (T_{a_{i,drum}} - T_l) \tag{4.8}$$

$$\dot{m}_v = \dot{m}_a \cdot P_m \cdot (x_l - x_{a_{i,drum}}) \tag{4.9}$$

where the heat transfer efficiency, P_s, is defined as:

$$P_s = 1 - e^{-NTU} \qquad NTU = \frac{\bar{h}A}{\dot{m}_a \cdot \bar{c_{p}}_{i,o}} \tag{4.10}$$

the term P_s represents the thermal efficiency for an hypothetical heat exchanger where the hot fluid is the air that interacts with the laundry and the cold fluid is a constant temperature represented by the surface of the laundry. The mean specific heat, $\bar{c_{p}}_{i,o}$, is evaluated with reference to the mean air temperature from inlet to the outlet section and the mass transfer efficiency, P_m, is expressed as:

$$P_m = 1 - e^{-NTU_m} \qquad NTU_m = \frac{\bar{h}_m^* A_m}{\dot{m}_a} \tag{4.11}$$

The two previous relations (4.10 and 4.11) require the definitions of two coefficients: the overall heat transfer conductance $\bar{h}A$ since the actual transfer area could not be determined and the overall mass transfer conductance $\bar{h}_m^* A_m$. Considering the *heat and mass transfer analogy* [26], based on the Lewis number (Le), is possible to define the overall mass transfer conductance knowing the overall heat transfer conductance. The

Lewis analogy is defined as:

$$\frac{\bar{h}}{\bar{h}_m^*} = \bar{c_p}_f \cdot L_e^{2/3} \tag{4.12}$$

where the $\bar{c_p}_f$ is evaluated at the film temperature. Multiplying the previous equation by the ratio between the heat transfer area (A) and the mass transfer area (A_m) Equation 4.12 becomes:

$$\frac{\bar{h}}{\bar{h}_m^*} \cdot \frac{A}{A_m} = \frac{A}{A_m} \cdot \bar{c_p}_f \cdot L_e^{2/3} \tag{4.13}$$

rearranging the previous, if the term $\bar{h}_m^* A_m$ is made explicit :

$$\bar{h}_m^* A_m = \frac{\bar{h}A}{\frac{A}{A_m} \cdot \bar{c_p}_f \cdot Le^{2/3}} \tag{4.14}$$

substituting in 4.11 where the definition of NTU_m is given:

$$NTU_m = NTU \cdot \frac{A_m}{A} \cdot Le^{-2/3} \tag{4.15}$$

It is worth noting that is assumed that the $\bar{c_p}_f$ is equal to $\bar{c_p}_{i,o}$ although they describe different phenomena. As a result, to define the evaporation process is needed to determine two parameters: the overall heat transfer coefficient ($\bar{h}A$) and the ratio between the mass and heat transfer area (A_m/A) therefore the mass transfer coefficient is deduced through these two parameters. Hence, the model proposed in this work tries to characterize the evaporation process defining two phenomena that identify it: mass and heat transfer.

4.4.2 Drum model

In this section the model of the evaporation process will be presented. The system laundry and water is divided into two zones: a wet zone and a dry zone. The extension of this two zones is not fixed but changes during the drying cycle as function of the load water content (LWC). The temperature and the specific humidity of the laundry are described as:

$$T_l = R_0 \cdot T_{wet} + (1 - R_0) \cdot T_{dry} \tag{4.16}$$

$$x_l = R_0 \cdot x_{wet} + (1 - R_0) \cdot x_{dry} \tag{4.17}$$

where: $R_0 = A_{wet}/A$ is the ratio between the surface area of the wet zone and the heat transfer area (it will better discuss below), $T_{dry} = T_{a,drum,i}$ is the dry zone that it is assumed being equal to the air inlet temperature, identical considerations for the

humidity ratio: $x_{dry} = x_{a,drum,i}$. Finally, the wet zone is assumed being in saturated conditions, therefore $x_{wet} = x_{sat}(T_{wet})$. A schematic of the model is given in Figure 4.7.

Whereas the dry zone is modeled as static with the previous definitions, the equations of the mass conservation and energy conservation applied at the wet zone allow to define two states that characterize it:

$$\frac{dM_w}{dt} = \dot{m}_a \cdot P_m \cdot R_0 \cdot (x_l - x_{a,drum,i}) \tag{4.18}$$

where M_w is the water laundry content, clearly, its rate of change with time is equal to the water evaporation rate (ER) from the laundry. The dime derivative of the laundry wet zone is:

$$\frac{dT_{wet}}{dt} = \frac{q - T_{wet} \cdot \left(\frac{dM_w}{dt} \cdot c_{p,w} + M_l \cdot c_{p,l} \cdot \frac{1}{M_w(0)} \cdot \frac{dR_0}{dLWC} \cdot \frac{dM_w}{dt} \cdot 100 \right)}{(M_w \cdot c_{p,w} + M_l \cdot R_0 \cdot c_{p,l})} \tag{4.19}$$

for references see Appendix E, in addition q is equal to:

$$q = \dot{m}_a \cdot R_0 \cdot \bar{c_p} \cdot P_s \cdot (T_{a,drum,i} - T_{wet}) - \dot{m}_a \cdot R_0 \cdot P_m \cdot (x_{a,drum,i} - x_{wet}) \cdot r_{T_{wet}} \tag{4.20}$$

the first term is the convective heat flux (q_{conv}) from the air to the laundry and the second is the evaporative heat flux (q_{evap}) from the laundry to the air. In addition, $c_{p,w}$, $c_{p,l}$ and M_l are respectively the water specific heat, the fabric load specific heat and the laundry weight.

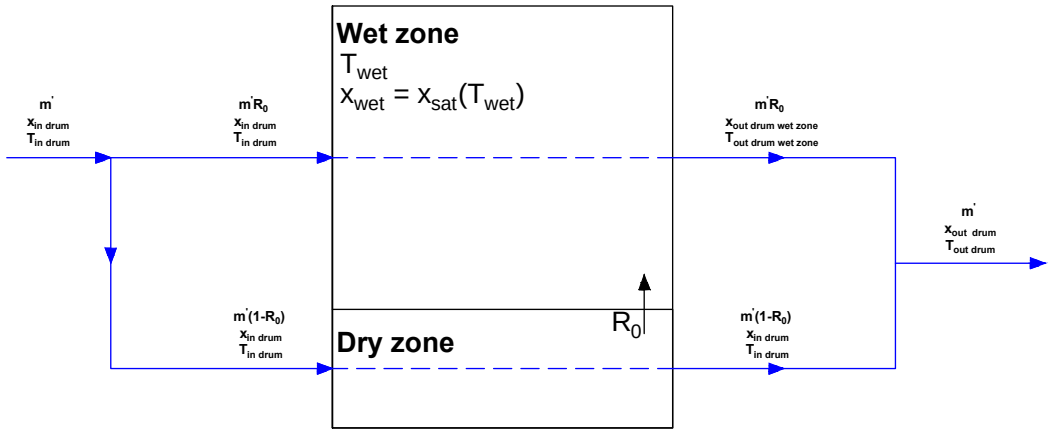

FIGURE 4.7: Evaporation model schematic.

The temperature and the specific humidity at the outlet section of the wet zone may be calculated as:

$$T_{a,wet-zone,o} = T_{a,drum,i} - P_s \cdot \ (T_{a,drum,i} - T_{wet}) \tag{4.21}$$

and:

$$ER = \dot{m}_a \cdot P_m \cdot R_0 \cdot (x_{a,drum,i} - x_{wet}) \tag{4.22}$$

$$x_{a,wet-zone,o} = x_{a,drum,i} + \frac{ER}{\dot{m}_a \cdot R_0} \tag{4.23}$$

clearly the enthalpy at the outlet section of the wet zone may be calculated with the air properties: $h_{a,wet-zone,o} = h(T_{a,wet-zone,o}, x_{a,wet-zone,o})$. The outlet enthalpy may be calculated considering an adiabatic mixing between the wet and the dry air flux, and finally the outlet temperature can be evaluated knowing the enthalpy and the humidity ratio.

As stated in the previous paragraph, in order to describe the evaporation process two parameters are necessary: the overall heat transfer coefficient ($\bar{h}A$) and the ratio between the mass and heat transfer area (A_m/A). From the experimental tests the NuA and hence $\bar{h}A$ values were deduced with the following definitions:

$$q_{conv.} = \dot{m}_a \cdot \bar{c_p} \cdot (T_{a,drum,i} - T_{a,drum,o}) \tag{4.24}$$

$$P_s = \frac{q_{conv}}{\dot{m}_a \cdot \bar{c_p} \cdot (T_{a,drum,i} - T_l)} \tag{4.25}$$

$$\bar{h}A = -\dot{m}_a \cdot \bar{c_p} \cdot \ln(1 - P_s) \tag{4.26}$$

$$NuA = \frac{\bar{h}A \cdot D_{drum}}{\bar{\lambda}} \tag{4.27}$$

where T_l follows the definition of the laundry temperature given in 4.16 and considering, that the load measured temperature, is not representative of the remaining wet zone when the laundry is almost dry (the outlet temperature starts to rise), it was imposed that:

$$T_{wet} = \begin{cases} T_{l,measured} & \text{if } T_{l,measured} \leqslant T_{wb,i} \\ T_{wb,inlet} & \text{if } T_{l,measured} > T_{wb,i} \end{cases} \tag{4.28}$$

where $T_{l,measured}$ is the measured laundry temperature during tests. The dry zone temperature is imposed being the inlet temperature according to its definition. In Figure 4.8 the trend of the NuA term for three tests with inlet air properties equal to: $T_{a_{drum,in}} = 60$ °C and $RH_{a_{i,drum}} = 20\%$, full load (≈ 9 kg) varying the volumetric flow rate: $140 - 160 - 180$ Nm^3/h is shown. The figure shows that the volumetric flow rate significantly affects the NuA value. Additionally, the dependency from the LWC is noticeable and can be split in three zones: a first zone where the NuA value is at its maximum value, a middle zone (40-50% < LWC < 80-90% range) where it remains

constant and the final zone where it collapses. The reason for this trend in the latter part could be the reducing of the air channels due to the tumbling action when the laundry is almost dry.

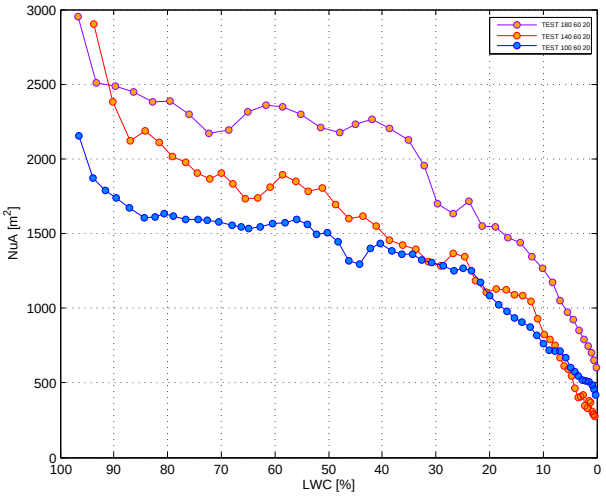

FIGURE 4.8: Nu·A, tests at: $T_{a,drum,i} = 60$ °C and $RH_{a,drum,i} = 20\%$, full load varying the mass flow rate.

The other term necessary to complete the description of the drying process is the term A_m/A. It is calculated indirectly finding the value that fulfills the *heat and mass transfer analogy*. From the experimental data the evaporation rate was calculated as follows:

$$ER = \dot{m}_a \cdot (x_{a,drum,o} - x_{a,drum,i}) \tag{4.29}$$

and hence the mass transfer efficiency and the overall mass transfer coefficient:

$$P_m = \frac{ER}{\dot{m}_a \cdot (x_{wet} - x_{a,drum,i})} \tag{4.30}$$

$$\bar{h}^*_m A_m = -\dot{m}_a \cdot \bar{c_p} \cdot \ln(1 - P_m) \tag{4.31}$$

where x_{wet} becomes, for identical considerations discussed earlier:

$$x_{wet} = \begin{cases} x_{sat}(T_{l,measured}) & \text{if } T_{l,measured} \leqslant T_{wb,i} \\ x_{wb,i} & \text{if } T_{l,measured} > T_{wb,i} \end{cases} \tag{4.32}$$

rearranging 4.14:

$$R_{Lewis} = \frac{A_m}{A} = \frac{\bar{h}^*_m A_m}{\bar{h} A} \cdot \bar{c_p} \cdot Le^{2/3} \tag{4.33}$$

since this latter equation is function of R_0 (see Equations 4.16 and 4.17) (for now R_0 can be considered equal to R_{Lewis}) then the task is to find the solution that fulfills the

following non-liner equation:

$$R_{Lewis} - \frac{A_m}{A} = 0 \tag{4.34}$$

the result for all tests at full load is reported in Figure 4.9

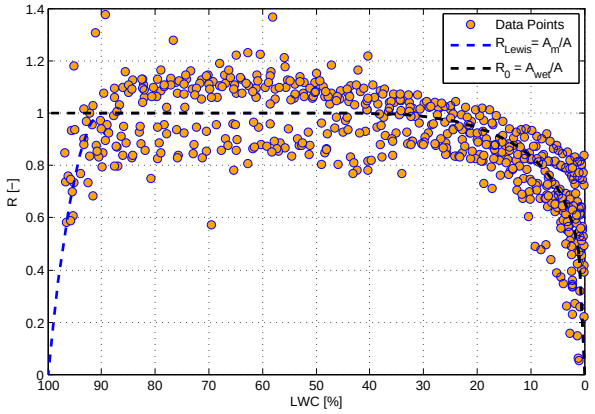

FIGURE 4.9: $\frac{A_m}{A}$ and $\frac{A_{wet}}{A}$

The figure shows first that the ratio between mass transfer surface area and heat transfer area is averagely equal to one in $40\% < \text{LWC} < 90\%$ range, this proves the reliability of the *heat and mass transfer analogy* for describing the drying process. Two sided zones appear: the zone in $90\% < \text{LWC} < 100\%$ range describes the heated phase where the heat transfer process is more active than the mass transfer, what is more, this phase is strongly affected by the dynamic of the heater and the dehumidifier to fix the inlet air properties conditions. The second zone, in $40\% < \text{LWC} < 0\%$ range, describes the final part of the drying process. Near to 40% of LWC the load starts to be dried as a results the active surface area for the mass transfer process decreases and hence some dried zone grow inside the clothes. Can be observed that, in this stage, not all tests finish with a ratio between areas nearly to zero: this indicates, that for these tests, the drying process was not complete. The relation used in the model neglects the first zone since, as pointed out above, it is affected by external dynamics. In the model, the implemented relation of R_0 is described as follows:

$$R_0 = \begin{cases} 1 & \text{if LWC} > 40\% \\ a \cdot LWC^K + b \cdot LWC + R_0 & \text{if LWC} \leqslant 40\% \end{cases} \tag{4.35}$$

where a and b are used to guarantee the continuity and derivability at LWC = 40%. The term K sets the slope of the curve.

In order to develop a correlation that explains the trend of the NuA values, first, a dimensionless procedure was used: the values of the NuA, for each test, are referred to their NuA mean value in the 70% < LWC < 90% range ($NuA_{70-90\%}$), in this way all the values become dimensionless and collapse in a unique curve although they are highly dispersed. The regression procedure gives the reported correlation in 4.36 and shown in Figure 4.10a. The coefficient of determination for this correlation is $r^2 = 0.844$. The variable $NuA_{70-90\%}$ is explained by the Reynolds and Prandtl number, the developed correlation is given in 4.37 and shown in 4.10b. For this correlation, the coefficient of determination is $r^2 = 0.9130$. The Reynolds and the Prandtl number are evaluated respect to the air drum inlet properties conditions.

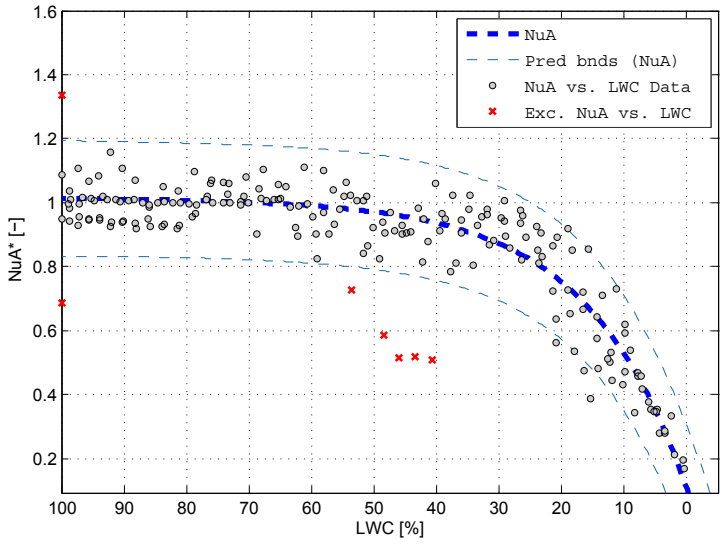

(A) Trend of NuA^* dimensionless.

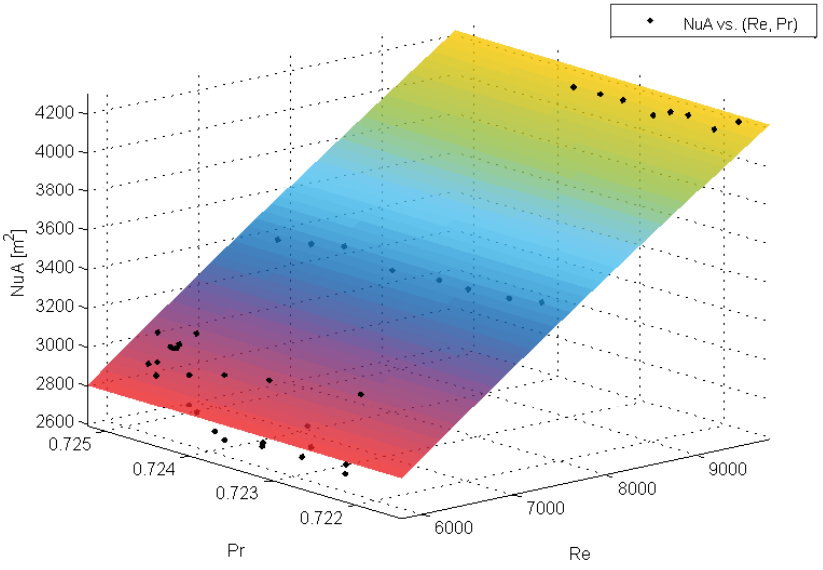

(B) Trend of NuA, in 70% < LWC < 90% range.

FIGURE 4.10: NuA correlation.

$$NuA^* = a \cdot e^{b \cdot LWC} + c \cdot e^{d \cdot LWC} \tag{4.36}$$

$$NuA_{70-90\%} = e \cdot Pr^f \cdot Re^g \tag{4.37}$$

$$NuA = NuA^* \cdot NuA_{70-90\%} \tag{4.38}$$

a, b, c, d, e, f and g are all constants. Their values cannot be transmitted for industrial secrecy reasons.

As shown in chart in Figure 4.10b the NuA term is strongly dependent from the Reynolds number (the dependency is almost linear) whereas can be observed only a slightly dependency on the Prandtl number.

4.4.3 Comparison of simulated and experimental results

The developed model was checked and the results generated are shown in Figure 4.11 where they are compared with experimental data. These latter data was obtained from a real drying test (the heat pump system was activated) where the volumetric flow rate was fixed (test in Figure 4.11 is referred to a volumetric flow rate equal to 140 Nm^3/h). The measurements of temperature and humidity at the condenser outlet were acquired and used as boundary condition variables for the model. The comparison shows that the simulation results predict a smaller difference for the drum outlet air temperature (the greatest error is nearly to 3%), the specific humidity is properly predict (the greatest error is lower than 1%). The evolution of the water content is in agreement with experimental results although the final water content of the model is greater than 2.5% of the initial value, this leads to a significant deviation (12.5%) on the prediction of the drying time (see Test n°1 in Table 4.3).

The model was also checked comparing it with six drying tests at identical conditions discussed above (tests with activated heat pump module). The deviations in terms of drying time are reported in Table 4.3. Tests times were corrected in order to compare tests with different final moisture content, in agreement with the international standard for measuring the dryer performance [5]. Table 4.3 shows that the results are in agreement with the experimental tests, except for a test (n°1), all the deviations are lower than 5%, the largest error is 12.5%.

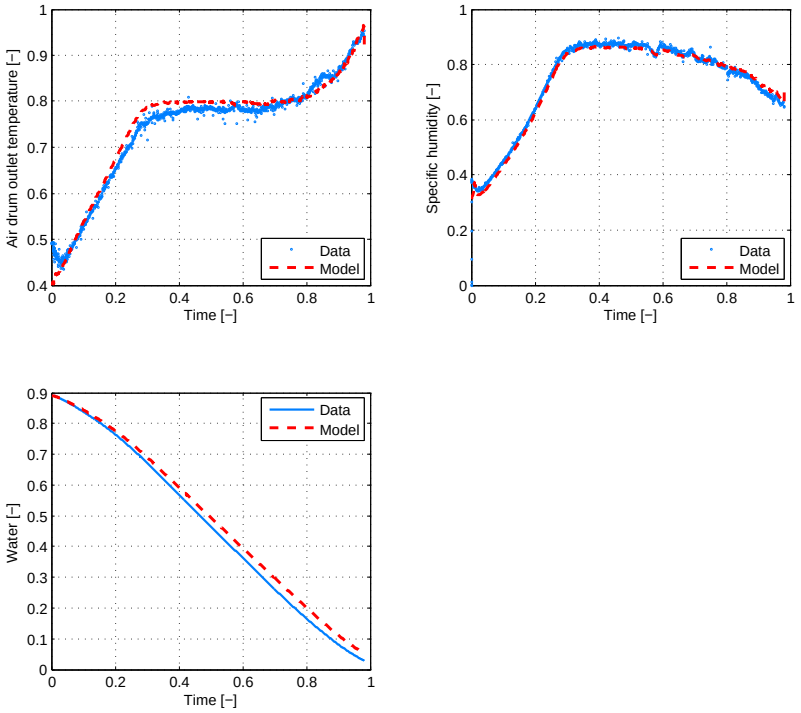

FIGURE 4.11: Drum model: comparison between experimental and simulated results.

Test	$V_{i,drum}$	ΔDrying Time
n°	Nm^3/h	%
n°1	140	12.45
n°2	140	2.84
n°3	180	2.50
n°4	180	-4.86
n°5	220	2.58
n°6	220	-2.67

TABLE 4.3: Drying time: comparison between tests and simulation results.

4.4.4 Model integrity check

The integrity is the consistency between the computer simulation and the governing equations. The model error is non-zero for several reasons: integration errors, round off, mathematical development of the differential equations. The model integrity was checked considering the consistency of the simulation results with the integral forms of

the energy equation (see Equation 4.39). Several test cases are presented in Table 4.4.

$$E_{wet}(t=0) + \int_0^t q_{a,drum} \cdot dt = E_{wet} \tag{4.39}$$

where E_{wet} is the internal energy of the wet capacity and is equal to:

$$E_{wet} = (M_w \cdot c_{p,w} + M_l \cdot R_0 \cdot c_{p,l}) \cdot T_{wet} \tag{4.40}$$

and $q_{a,drum}$ is the drum heat flux relating to the overall enthalpy change across the drum:

$$q_{a,drum} = \dot{m}_a \cdot (h_{a,drum,i} - h_{a,drum,o}) \tag{4.41}$$

relative error (related to the initial energy $E_{wet}(t=0)$) may be expressed as:

$$\varepsilon = \frac{\left| \int_0^t q_{a,drum} \cdot dt - (E_{wet} - E_{wet}(t=0)) \right|}{E_{wet}(t=0)} \cdot 100 \tag{4.42}$$

Test	$V_{i,drum}$	$\varepsilon_{(peak)}$	$E_{wet}(t=0)$
n°	Nm^3/h	%	kJ
n°1	140	0.126	631.76
n°2	140	0.125	619.52
n°3	180	0.121	627.08
n°4	180	0.123	626.27
n°5	220	0.120	631.38
n°6	220	0.119	626.91

TABLE 4.4: Table model integrity check.

Peak-errors, expressed as percentage of the initial energy values, are reported in the previous table. Recorded errors are always less than 0.126%. This proves that the model is energetically consistent.

4.4.5 Other considerations

This section is devoted to show a result from the computer model. The overall enthalpy change across the drum cannot be considered isenthalpic since the drying process is

strictly dynamic. In the first part of the cycle the power relating to the overall enthalpy change across the drum ($q_{a,drum}$) shows a positive value (see Figure 4.12), in this phase the evaporative heat flux does not sustain the convective heat flux that is greater, therefore the laundry load can be considered as an accumulator of thermal energy and its internal energy increases. Progressively the evaporation rate rises, this increases the energy ($ER \cdot h_v$) absorbed by the air flow stream leading to an overall enthalpy change:

$$h_{a,drum,o} = h_{a,drum,i} + \frac{ER}{\dot{m}_a} \cdot h_v \tag{4.43}$$

that reduces the internal energy of the system laundry-water. In the previous h_v is the saturated vapor enthalpy at the load temperature. Due to the choice of modeling the dry-zone as static, in the final part of the cycle is neglected the increment of energy of the load when the convective heat flux becomes greater than the evaporative heat flux, this would lead to a values of the power ($q_{a,drum}$) positive. In a better description of the drum model a dynamic behaviour of the drying zone should be considered as follows:

$$\frac{dT_{dry}}{dt} = \frac{q - T_{dry} \cdot \left(M_l \cdot c_{p,l} \cdot \frac{1}{M_w(0)} \cdot \frac{dR_0}{dLWC} \cdot \frac{dM_w}{dt} \cdot 100 \right)}{M_l \cdot (1 - R_0) \cdot c_{p,l}} \tag{4.44}$$

see the derivation in Appendix E, where q is equal to:

$$q = \dot{m}_a \cdot (1 - R_0) \cdot P_s \cdot \bar{cp} \cdot (T_{a,drum,i} - T_{dry}) \tag{4.45}$$

Equation 4.44 must be managed carefully since the denominator is zero when the dry zone starts to grow. Furthermore, during all the first part of the drying cycle it must be tracked to the wet zone temperature:

$$\frac{dT_{dry}}{dt} = K \cdot (T_{wet} - T_{dry}) \tag{4.46}$$

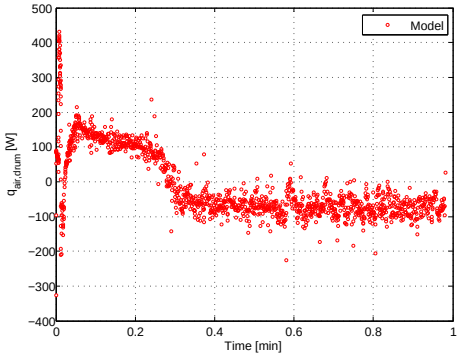

FIGURE 4.12: Drum heat flux.

Chapter 5

Heat pump tumble dryer model validation and simulation results

5.1 Introduction

This chapter is divided mainly into two parts. In the first part, the results from the overall heat pump tumble dryer model will be compared with experimental data. The whole model is the sum of three main sub-models: the heat pump model (developed in Chapter 2), the air circuit model (developed in Chapter 3) and the drum model (developed in Chapter 4). All these sub-models are developed in Matlab-Simulink environment and they were connected in a logic manner. Since the process air circuit is closed and the aeraulic model is developed with static relations it was essential to broke the data flow in order to avoid algebraic loop: the process air circuit is broken at the drum outlet section with a ″Memory block‟ that holds and delays its input by one integration time step.

The second part of the chapter will present two simulation case studies. The first one is related to the changing of the compressor features (displacement and efficiencies are varied). The second one is related to the changing of the condenser geometric features (fin pitch is varied). These cases and the model validation section would demonstrate the modeling accuracy and reliability in predicting system behavior under changing of its characteristic parameters. In the final section the heat pump dryer energy flows govern its operation mode will be presented. All experimental measurements about the heat pump tumble dryer, presented in this chapter, were collected at the Electrolux laboratories located in Porcia, Pordenone.

5.2 Model validation

In this section the comparison between simulation results and experimental data will show and discussed. The comparison was made setting the model with the same geometrical characteristics and features of the real heat pump tumble dryer. The aeraulic circuit model was tuned in order to obtain the measured mass flow rate with specific tests discussed in Paragraph 3.4. The refrigerant charge and the length of the capillary tube were determined with a series of simulations to obtain a degree of subcooling and superheat comparable with the actual values. All the geometric parameters of the finned coiled heat exchanger and the features of the compressor were introduced in the model. Figure 5.1 shows the comparison between experimental and simulated pressures. The start-up transient is fairly in agreement with the experimental measurements although some phenomena are not properly caught. In the beginning phase of the real test the evaporator is drained out, this is empathized from the value of the evaporation pressure that plummets and the superheat degree reaching 50 K (this value cannot be considered totally reliable since the first initial transient is very fast consequently the thermal inertia of the pipe wall, where the thermocouple is placed, strongly affects the measurement). This difference, in the first stage of the drying cycle, is due to the choice of the initial conditions of the heat exchanger states, in particular the refrigerant charge distribution plays a crucial role. In order to obtain the same experimental results the evaporator must be initialized with a low value of the total refrigerant charge (simulations show that a suitable value could be 20% of the total charge, and consequently about 80% resides in the condenser). However this affects also the numerical robustness of the model. Since the initial transient lasts for maximum of 5-6 min, it was decided to start with a refrigerant charge distribution that assures numerical stability: 35% of the total refrigerant charge on the evaporator and hence 75% on the condenser. Furthermore, the pressures trend shape is quite different from the measurements, this can be explained considering some aspects. First, the relations that give the isentropic and volumetric efficiency are not reliable for the whole transient domain (clearly, this affects the prediction of the inlet condenser enthalpy, refrigerant mass flow rate and consequently the compressor power input, see Figure 5.5). Second, also the adopted void fraction mean relation in this work (Zivi's correlation) could not be sufficiently accurate to describe the first initial transient since it is function only by the refrigerant pressure. The third aspect is associated to the energy losses, the shape of the transient is also modeled (in addition to the refrigerant mass migration phenomenon: Appendix C) by the ratio between compressor power input and energy losses, this is emphasized near to the 40% of the drying cycle (reported from Figure 5.1 to Figure 5.13) where the condensation pressure levels off gradually whereas the simulated sharply increases: this indicates that the energy losses are not efficiently predicted. Indeed, during the pseudo steady state phase, the overall

heat transfer coefficient from the cabinet air to the compressor shell (see Paragraph 2.8) was overestimated in order to stabilize the process. This leads to produce stiff variations of the condensation pressure and the condenser air outlet temperature (see Figure 5.1 and Figure 5.2). Nevertheless, the prediction of the drying variables can be considered in agreement with the experimental data: the greatest deviation is about 7%.

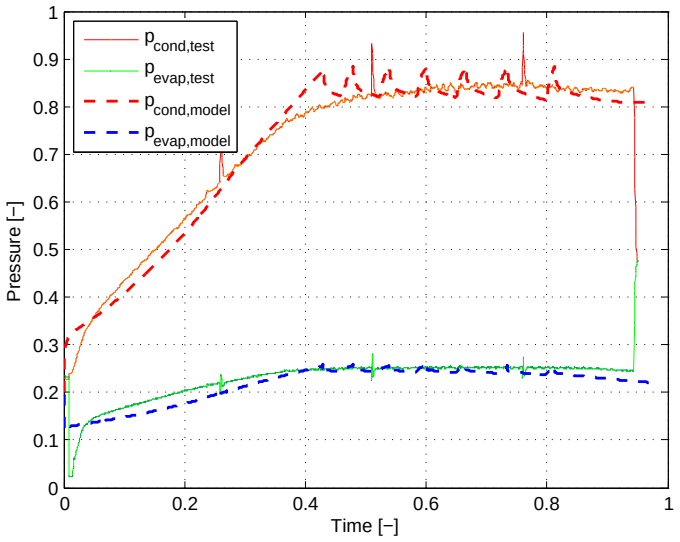

FIGURE 5.1: Refrigerant pressures comparison.

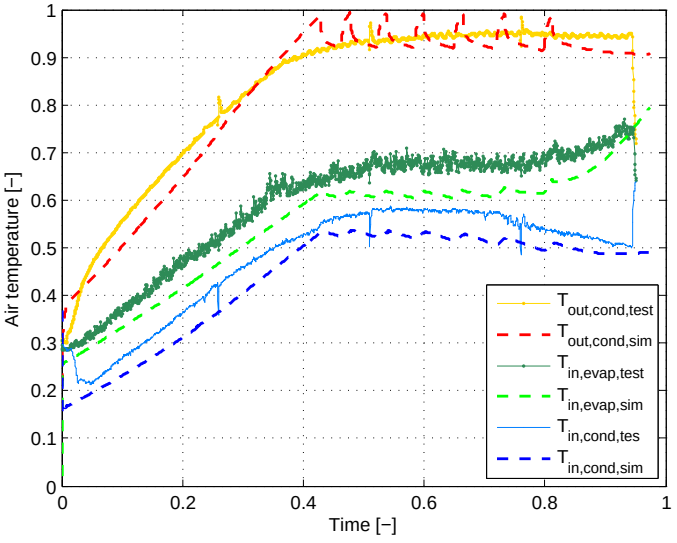

FIGURE 5.2: Air temperatures comparison.

Figure 5.3 shows the comparison between measured and simulated subcooling. The stationary value is properly predict although the simulated initial transient does not

match the actual trend. As stated earlier, this is the result of the choice of the state variables. In addition, a discontinuity can be seen near the 20% of the total drying cycle point, here there is a transition from TP-L to SH-TP-L condenser mode. Also the superheat trend is affected by the choice of the initial values of the state variables: the superheated zone starts later with respect to the experimental results. This causes the evaporator to operate for a longer period flooded, and can reduce accuracy in drying time prediction since the evaporation capacity is reduced because of the superheated region low internal heat transfer coefficient.

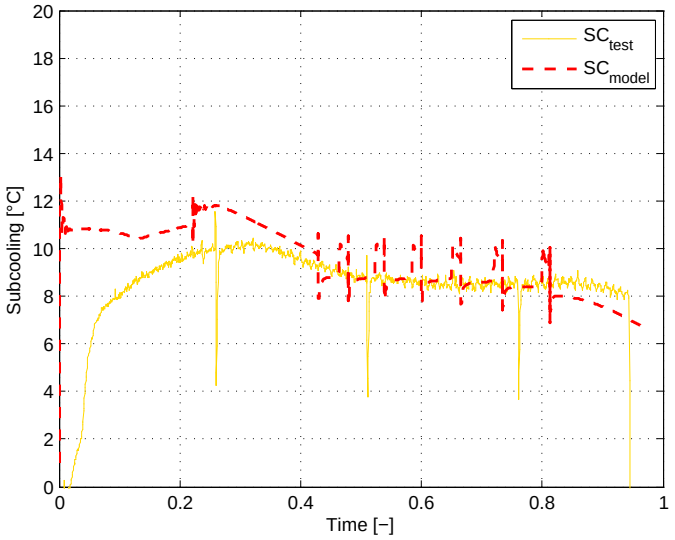

FIGURE 5.3: Subcooling comparison.

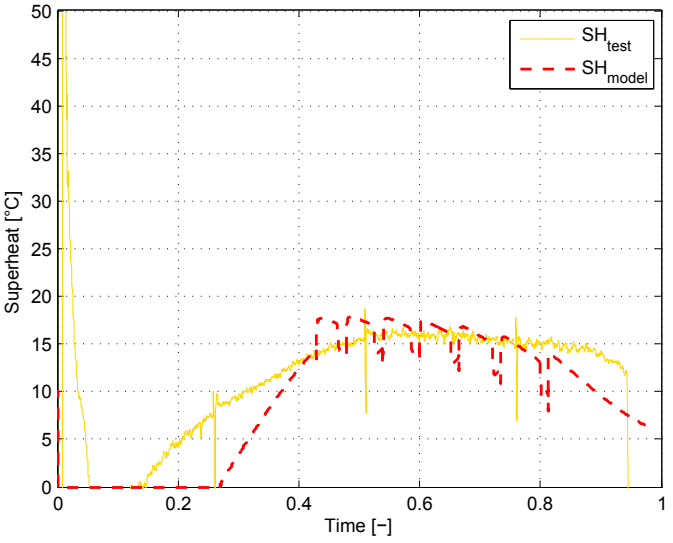

FIGURE 5.4: Superheat comparison.

The compressor power comparison is reported in Figure 5.5. The compressor power input is properly predicted when the pseudo stable phase is reached, earlier the simulated underestimates the real power and deviances greater than 15% can be seen. The area between the two curves represents the model accuracy to predict the compressor energy consumption, the accuracy, when the drying time is properly estimated, is near to 10%.

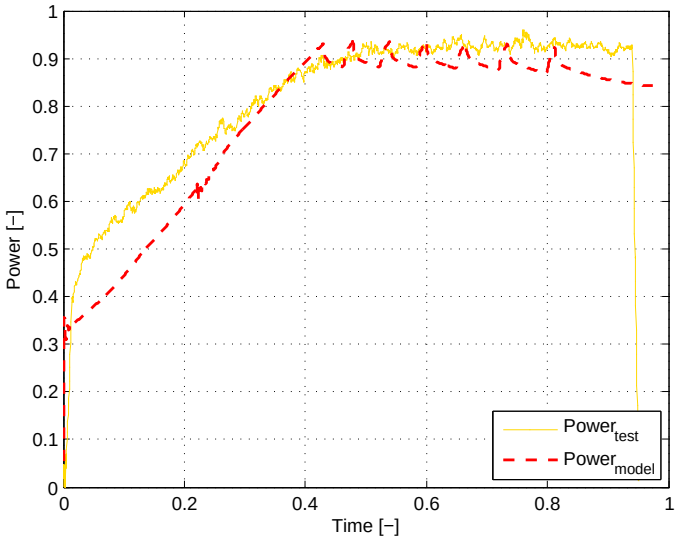

FIGURE 5.5: Compressor power comparison.

5.3 Simulation case studies

In this section two case studies will be presented. The first one is related to the changing of the compressor features (displacement and efficiencies are varied). The second one is related to the changing of the condenser geometric features (fin pitch is varied). This section would increase the confidence in the model fidelity through various scenarios.

5.3.1 Increasing of the compressor displacement

The heat pump tumble dryer model was used to compare different solutions that, with *a-priori* considerations, can lead to not proper decisions. For example, in this case an increment of 15% of the compressor displacement was evaluated. With *a-priori* knowledge one could argue that the drying time is reduced, however in terms of energy consumption the prediction could not be so trivial. Reported tests from Figure 5.6 to 5.8 show the comparison between two identical heat pump tumble dryers, except for the compressor displacement, for the length of the capillary tube and the refrigerant

charge that were adjusted to obtain the same superheat and subcooling between the two cases. The greater displacement increases both the condensation and evaporator pressure (the condensation pressure increment is higher than the evaporation pressure one, the latter is most affected by its degree of filling). The refrigerant mass flow rate drawn by the compressor (greater value for the displacement) rises and hence the cooling and condensing capacity increases. All the air temperatures move on the top, the condenser air outlet temperature increases about 7% consequently this rises the evaporation rate (see Figure 5.7) although a slightly lower volumetric flow rate (due to the effect of the air density at the inlet section of the process fan). As expected, the drying time decreases of 15% (of the total drying time with smaller compressor), however the total energy consumption rises of 3%: the surface area between the two power curves in Figure 5.8 is greater than the energy adsorbed, in case of smaller compressor, during the extra time period.

Therefore, to sum up, the following conclusion can be drawn: when the cylinder volume of the compressor increases by 15% the simulation model shows a 15% reduction of the drying time with unchanged or a slightly increment of the electrical use. The comparison was made adjusting the refrigerant charge in order to obtain the same degree of superheat and subcooling between the two cases. This was necessary because these two parameters, especially the superheat remarkably affects the heat pump module performances.

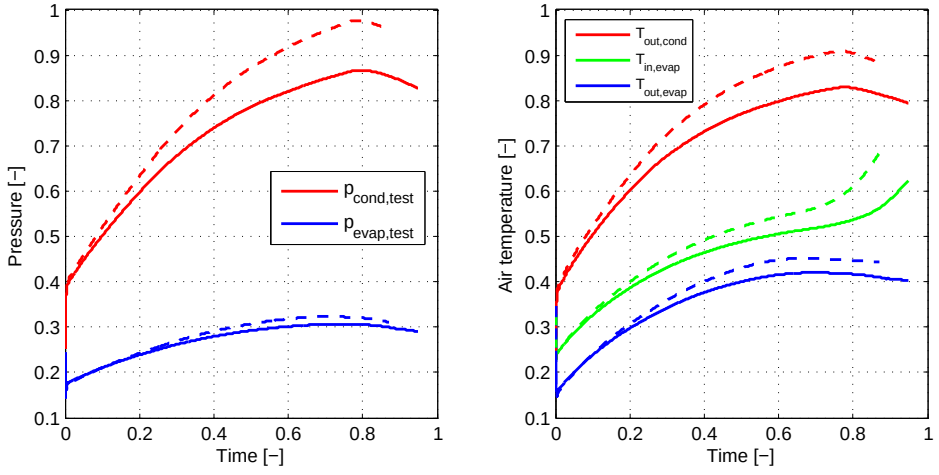

FIGURE 5.6: Refrigerant pressure drops and air temperatures, test case n°1. Dashed lines are in case of greater compressor.

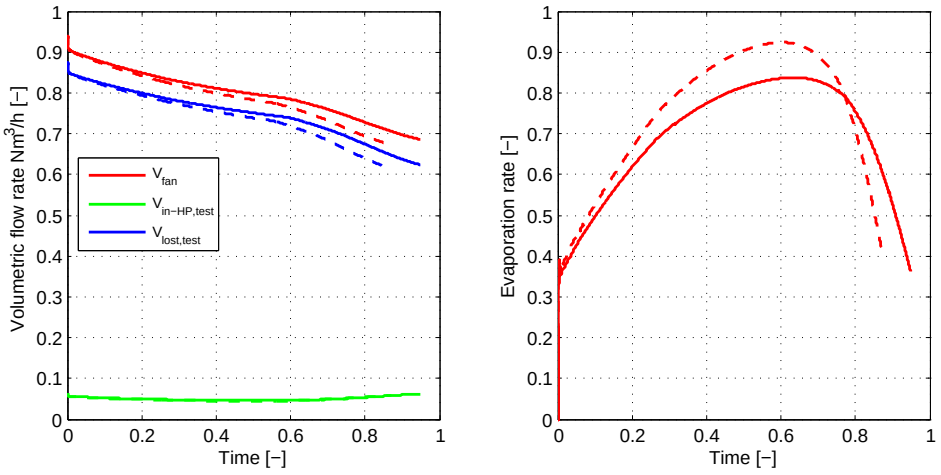

FIGURE 5.7: Volumetric flow rates and evaporation rates, test case n°1. Dashed lines are in case of greater compressor.

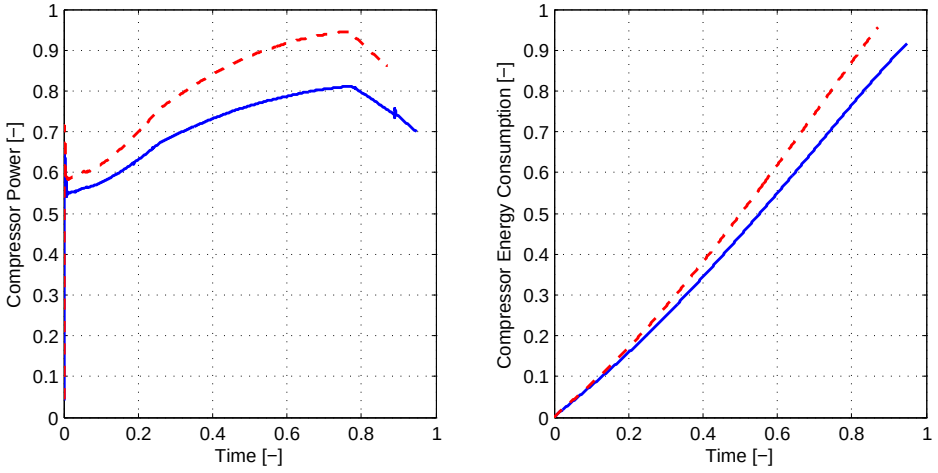

FIGURE 5.8: Compressor power and energy consumption, test case n°1. Dashed lines are in case of greater compressor.

5.3.2 Decreasing of the condenser finned coil surface area

The second reported test case, concerns the reduction of the condenser finned coils surface area. On the one hand, reducing the finned coils surface could seem not a proper decision from the the energy consumption reduction point of view. On the other hand reducing the finned coil surface by increasing fin pitch, could reduce the pressure drops of the air circuit and hence increasing the volumetric flow rate drawn by the fan. As a result, also the evaporation rate could be affected, therefore predicting if a reduction of the area could be convenient, to decrease the HP energy consumption,

is not a trivial matter. Figures from 5.9 to 5.12 show a test where the fin pitch of the condenser was increased by 30% (from 1.5 to 2 mm), therefore also the finned coil surface is decreased by the same amount. As expected, the volumetric flow rate increases (about 5% compared with the case with smaller fin pitch), in addition all the air temperatures decrease (average deviation of 3%) because of the surface area reduction and the increment of the volumetric flow rate. The lower temperature keeps the refrigerant pressure also lower (the high pressure is most affected than the low pressure) although the reduction of the area should be lead to increase the condensation pressure in order to allow the heat exchange from a higher temperature level. The analysis of the cooling and condensing capacity show that the higher values are reached by the case with smaller fin pitch in contrast with the increment of the air mass flow rate but according to the increment of the refrigerant mass flow rate. The evaporation rate trend indicates that the effect of temperature is more prevalent than the volumetric flow rate, consequently the evaporation rate, in case of smaller fin pitch, is greater.

Therefore, to sum up, the following conclusion can be drawn: when the condenser finned coils surface is reduced by 30% by increasing the fin pitch, the simulation model shows only a 3% increment of the drying time with unchanged electrical use. This result could be observed if the goal of the manufacturer is reducing the cost without impacting on the dryer performances.

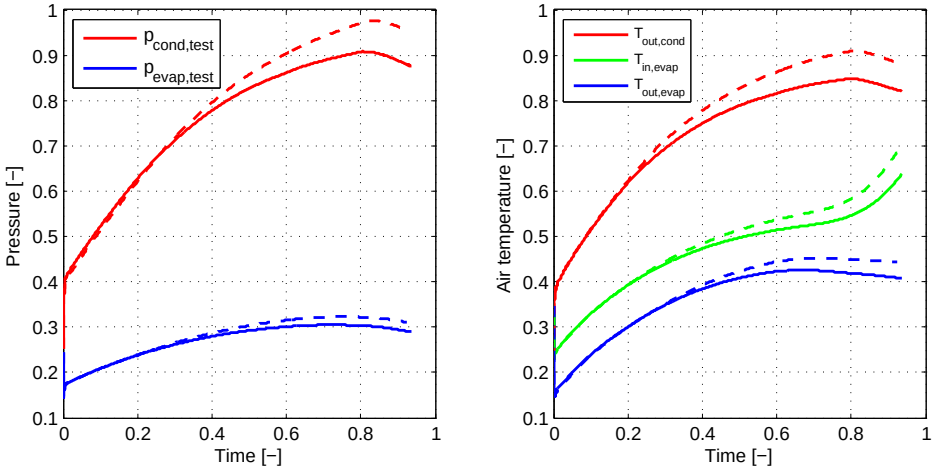

FIGURE 5.9: Refrigerant pressure drops and air temperatures, test case n°2. Dashed lines are in case of smaller fin pitch.

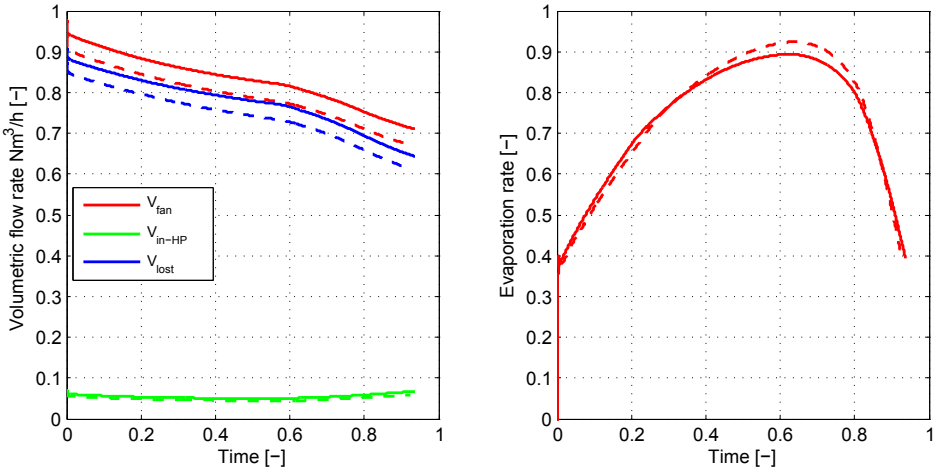

FIGURE 5.10: Volumetric flow rates and air pressure drops, test case n°2. Dashed lines are in case of smaller fin pitch.

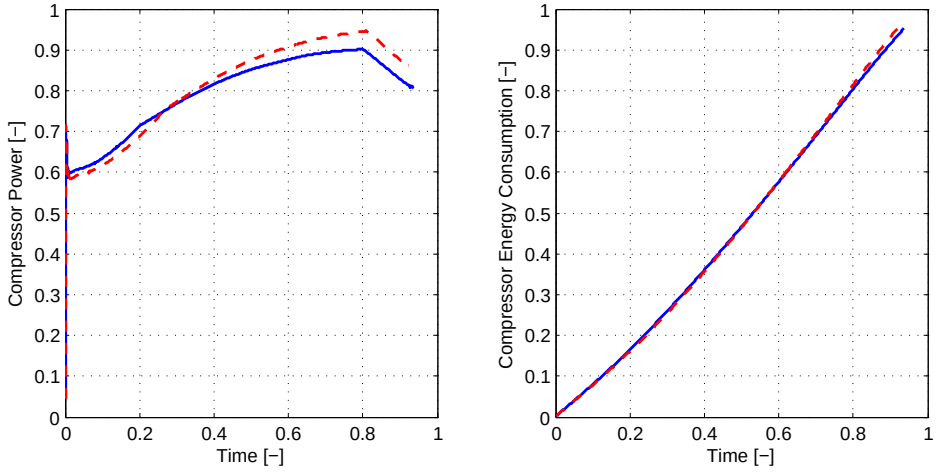

FIGURE 5.11: Compressor power and energy consumption, test case n°2. Dashed lines are in case of smaller fin pitch.

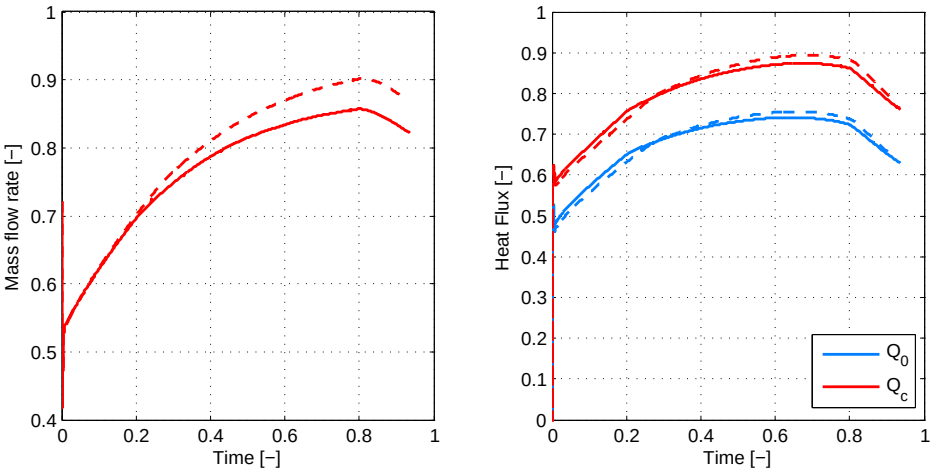

FIGURE 5.12: Refrigerant mass flow rate and cooling/condensing capacity, test case n°2. Dashed lines are in case of smaller fin pitch.

5.4 Energy losses and power input

This paragraph is devoted to clarify the energy paths in the heat pump tumble dryer. From a point of view the compressor absorbs a certain amount of electric power from the electrical grid depending on the features of the heat pump system (compressor displacement and efficiencies, finned coil heat exchanger design, capillary tube geometric features refrigerant charge). The compressor input power also depends on the air circuit design that affects the volumetric flow rate drawn by the fan and finally on the weight and the moisture content of the load. From another point of view, that characterizes better the energy paths, the absorbed electric power must be equal to the sum of the energy losses (near to a quasi steady state condition although the drying process is strictly dynamic). Five sources of energy losses can be identified:

1. heat flux related to the condensed vapor on the evaporator finned coil (see the blue line in Figure 5.14). This enthalpy flux may be expressed as:

$$q_w = \dot{m}_a \cdot (x_{a,i,e} - x_{a,o,e}) \cdot c_{p,w} \cdot T_{a,o,e} \tag{5.1}$$

   where: $\dot{m}_a \cdot (x_{a,i,e} - x_{a,o,e})$ is the condensed water mass flow rate and its enthalpy is $h_l = c_{p,w} \cdot T_{a,o,e}$. It is assumed that the condensed water temperature is near to the air temperature at the evaporator outlet;

2. sensible heat flux related to the energy loss from the back of the device (see the red line in Figure 5.14). Its definition is given in Equation 3.16;

3. sensible heat flux concerning the energy loss from the cabinet to the ambient (see the orange line in Figure 5.14). It is defined as:

$$q_{cab-amb} = (KA)_{cab-amb} \cdot (T_{cab} - T_e) \tag{5.2}$$

4. heat enthalpy flux related to the cooling compressor fan. When it is switched on, it produces the following energy loss:

$$q_{colling\,fan} = \dot{m}_{colling\,fan} \cdot (h_{cab} - h_e) \tag{5.3}$$

   where the $\dot{m}_{colling\,fan}$ is the cooling fan mass flow rate, h_{cab} is the enthalpy of the air in the cabinet evaluated knowing the cabinet temperature, T_{cab}, and humidity ratio, x_{cab}, and finally, h_e, is the ambient air enthalpy. In Figure 5.14 this leakage is not reported since during the simulation test it never switches on;

5. the enthalpy flux related to the leakage mass flow rate $\dot{m}''$ (see the green line in Figure 5.14). This mass flow rate, as discussed in Chapter 3, leaves the drum due to a not perfect sealing of the front and rear gaskets. The air, that leaves the drum, is characterized by a high humidity ratio content, clearly this affects the value of the enthalpy, instead, the air enthalpy returning in the process circuit is evaluated at the cabinet thermohygrometric conditions. As a result, the loss is expressed as:

$$q_{leakage} = \dot{m}'' \cdot (h_{o,dryer} - h_{cab}) \tag{5.4}$$

   where the $h_{o,dryer}$ is computed as:

$$h_{o,dryer} = \frac{\dot{m}'' \cdot (rp_{L1} + rp_{L2}) \cdot h_{i,drum} + \dot{m}'' \cdot rp_{L3} \cdot h_{o,drum}}{\dot{m}''} \tag{5.5}$$

   clearly: $h_{i,drum} = h(T_{i,drum}, x_{i,drum})$ and $h_{o,drum} = h(T_{o,drum}, x_{o,drum})$

The heat transfer between the air inside the cabinet and the compressor shell ($FQ \cdot P_{el.}$) cannot be considered as a source of leakage since it flows on the cabinet node increasing its temperature. In Figure 5.13 a schematic of the air process (see for details Figure 3.1) is reported. The energy losses are emphasized in purple.

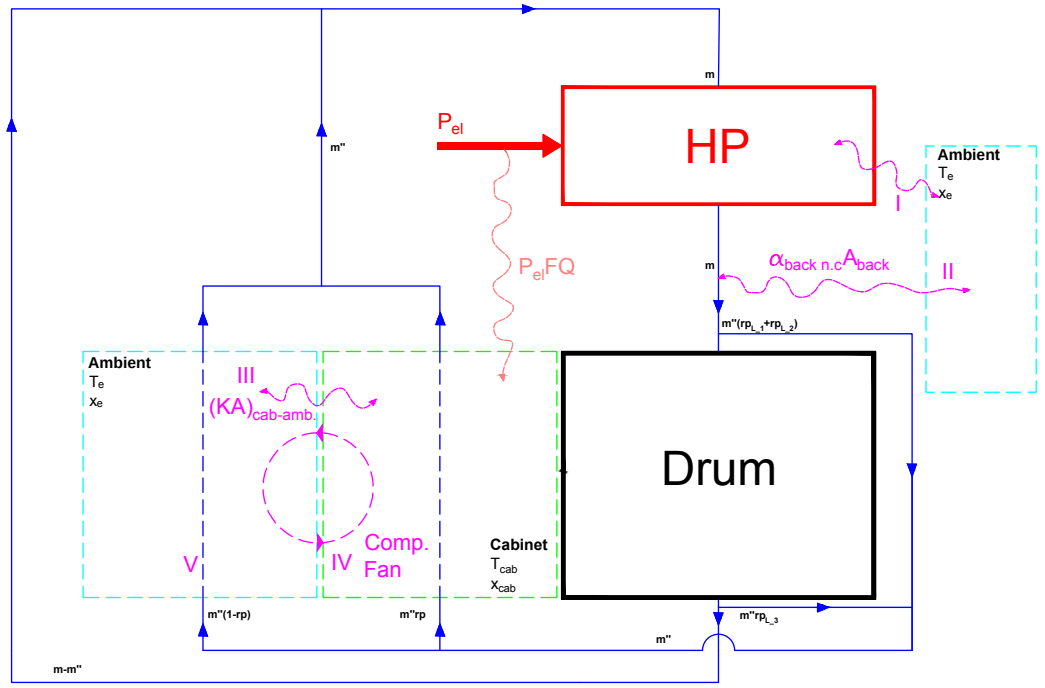

FIGURE 5.13: Energy losses and aeraulic circuit.

Figure 5.14 shows the trend of the heat fluxes discussed earlier during a simulation drying cycle without switching on the compressor cooling fan. Due to the highly non-linear features of the system a steady state conditions phase cannot be identified although the final part of the cycle shows values for the system balance nearly to zero. As discussed in the Paragraph 4.4.5, the trend of the power relating to the overall enthalpy change across the drum must be considered since in some phases of the cycle is positive (the laundry absorbs energy, first stage of the cycle) and in other is negative (the laundry returns energy) (see black line in Figure 5.14). The main energy loss is the enthalpy flux related to the leakage mass flow rate from the drum, its dependency is mainly given by the outlet drum temperature and humidity ratio and further by the trend of the mass flow rate. The heat flux concerning the condensed vapor cannot be neglected since its value is nearly to 10% of the compressor electric power. The sensible heat fluxes (cabinet-ambient and structure) is approximately to 15% of the compressor electric power. The overall energy balance (see chart below in Figure 5.14) shows, that for an extended phase, the energy balance is positive therefore the system increases its internal energy, whereas in the final stage the balance is close to zero (reach a steady state condition). This latter chart suggests that the power value, that the cooling fan should remove in order to stabilize the system, if it were activated, is lower than 50 W.

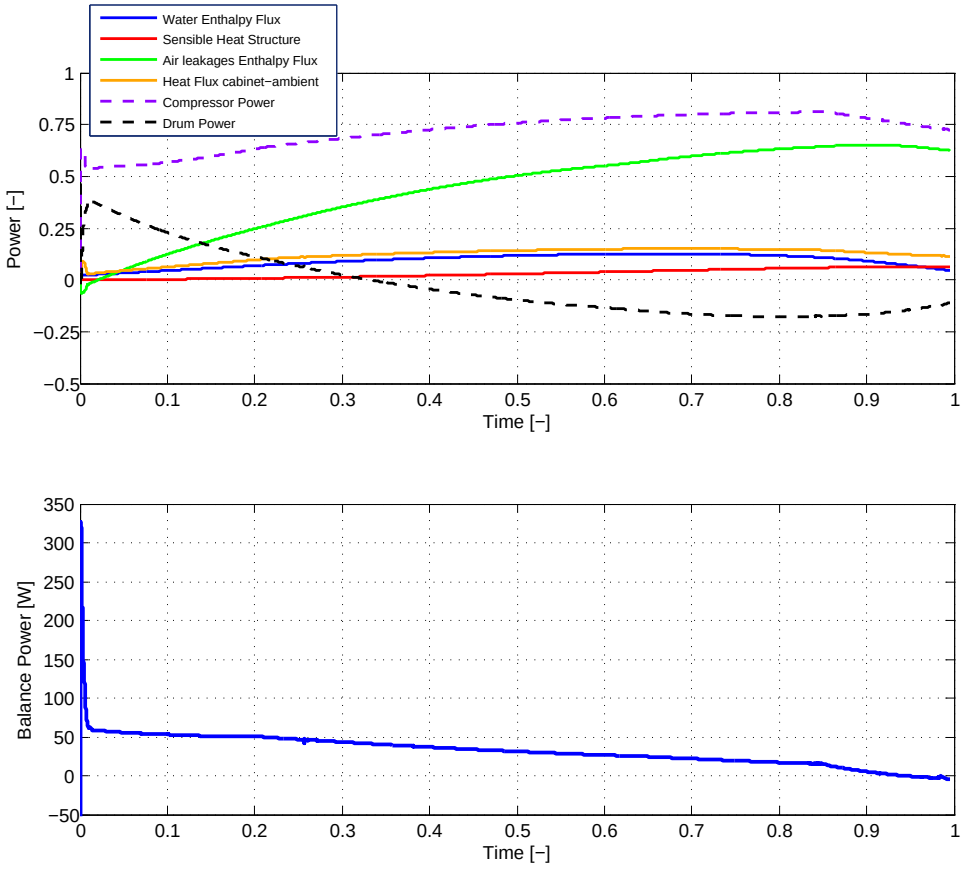

FIGURE 5.14: Energy losses during a simulated drying cycle.

The power balance on the above chart in Figure 5.14 is evaluated as:

$$P_{comprex} - q_{drum} = q_w + q_{structure} + q_{cab-amb} + q_{colling\,fan} + q_{leakage} \tag{5.6}$$

Chapter 6

Air vented tumble dryer model

6.1 Introduction

In this chapter the air vented tumble dryer model will be presented. To start with, the main features of the device will be shown, after that both the aeraulic and the thermal model will be discussed, more details about the heater model will be given. Lastly, the comparison between experimental and simulated results will be analyzed and discussed.

The aim of this chapter will be to develop an air vented tumble dryer dynamic model. The model will be able to effectively predict the performance of the device in terms of energy consumption and drying time varying the features of its components, in addition it will be used to design, evaluate and compare different control strategies (for instance, different strategies of the electric resistance duty-cycle).

In scientific literature there are not many references in dynamic modeling air vented tumble dryer systems. Yadav and Moon [45] developed a simplified model to study the factors affecting the energy consumption of the machine in term of SMER (electric-energy consumed to remove 1 kg of moisture from load, its unit is kWh/kg, for details see Paragraph 1.3). The only dynamics that they considered are those of the drying process and the features of the aeraulic circuit are not considered. Also Deans [44] modeled a vented tumble dryer to determine the overall energy efficiency and found that approximately 16% of the input energy leaves the dryer as sensible heat. The model was also used to investigate possible methods that could be used to recover part of this loss, for instance Deans demonstrated that the partial recirculation of the exhaust air caused an increment of the energy consumption: the exhaust loss decreases with recirculation, but the loss from the cabinet surface increases, because recirculation leads to a rise in the dryer temperatures.

6.2 Components description and features of the standard drying cycle

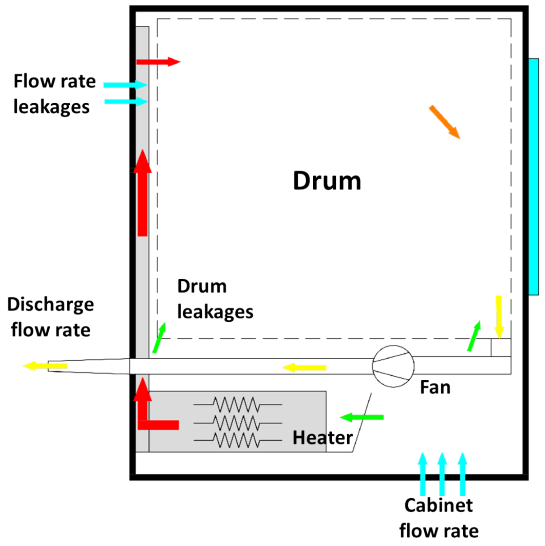

FIGURE 6.1: Air vented dryer scheme.

An air vented tumble dryer scheme is shown in Figures 6.1 and 6.5. The main components of this device are: heater (heating element), drum and process fan. The air circuit is opened: the air stream is drawn from the ambient (where the device is placed) through the ways between the ambient and cabinet (cabinet flow rate), than it is forced to across the heating element where is heated before entering into the drum where is humidified and cooled and finally is rejected to the laundry room or outdoors (if a wall break-through is available). The fan process is installed after the tumble drum and consequently all the aeraulic circuit from the cabinet to the inlet section of the process fan is below the atmospheric pressure (see Figure 6.2, the value zero is considered to be at the atmospheric pressure). For this reason the flows rate leakages could not be neglected (flow rate leakages from the dryer back and from the cabinet to the drum). This mass flow rate enters from different leakage sources and does not across the heating element (hence, it is not heated) therefore it has a remarkable effect on the performance of the system. Figure 6.3 shows one of the leakage source positions: the back panel leakage source. Indeed, this source is not concentrate in a fixed position since the air can enter from the three holes (that are used to contain the fire inside the drum in the event of burning of the fabric load) and also form the conjunction zone between the rear drum flange and the back panel. From experimental measurements, the amount of mass flow rate that enters due to this source is near to 10% of the total mass flow rate drawn by the fan. Another zone where the air stream can enter into the process circuit is from the

gap that occurs, due to high dimensional and geometric tolerances of the components forming the main aeraulic circuit, between the front and back rear gaskets and the front and back drum panel. From experimental measurements this quantity is near to 50% of the total mass flow rate.

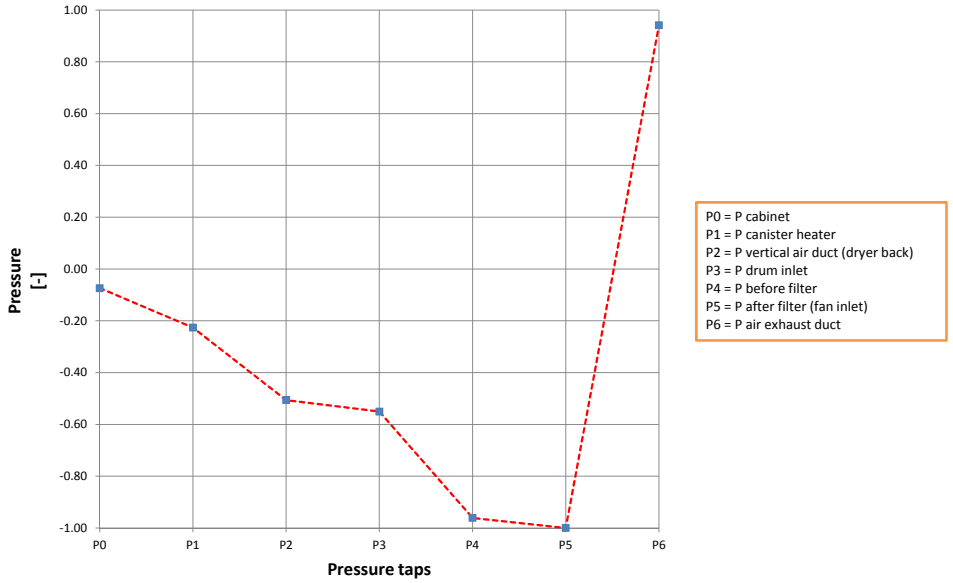

FIGURE 6.2: Air pressures distribution into the aeraulic circuit.

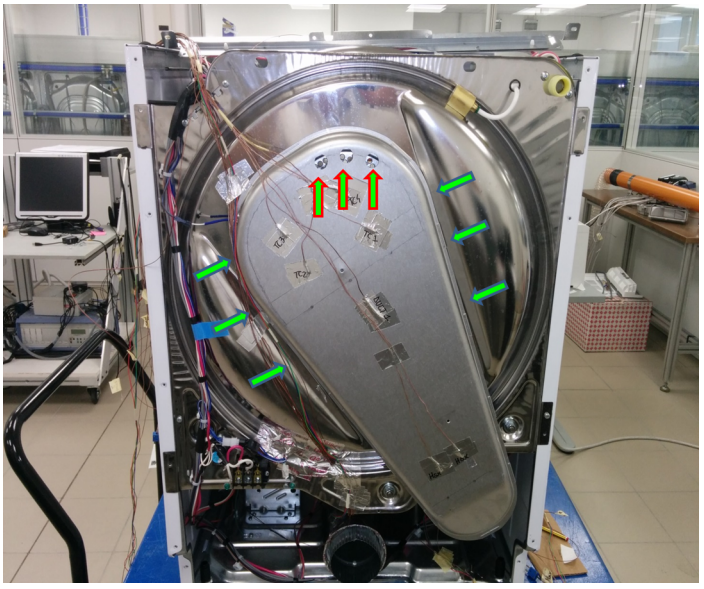

FIGURE 6.3: Back panel leakages.

The evolutions of temperatures, humidities and weight during a standard drying cycle are plotted in Figure 6.4. The evolution of temperatures shows that the steady thermal

conditions are reached after 20% of the total drying time from the beginning of the cycle. Indeed, the temperatures increase slowly for all the drying phase as a consequence of a reduction of the mass flow rate drawn by the fan, due to both an increment of the pressure drops inside the drum and also an increasing of the clogging effect on the filter (see Paragraphs 3.3.3 and 3.3.4). Despite the maximum value of the heater outlet temperature is near to 250 ℃ the drum inlet temperature is about 170 ℃, crossing the drum the air is cooled until a temperature near to 50 ℃. When the drying phase is near to be completed the drum outlet temperature increases (see the green line in Figure 6.4) consequently the fan pressure rise decreases. This reduces further the mass flow rate drawn by the fan and also the mass flow rate passing the heating element. Therefore the heater outlet temperature increases up to a fixed value (measured by a NTC probe before entering into the drum) for which the electrical resistances are switched off. This is caused by some protection criteria of the heating element control system. As shown in the chart in Figure 6.4 this occurred three times during the drying test. The evolution of the specific humidities indicates that the specific humidity of the air inside the cabinet remains constant for all the drying cycle (as expected) and is near to the ambient specific humidity. This value is reached also by the air stream that exits the drum during the last phase of the cycle (from 80% of the total drying time). The cabinet specific humidity is also the humidity of the mass flow rate that enters the drum and produces the evaporation of the water from the laundry load.

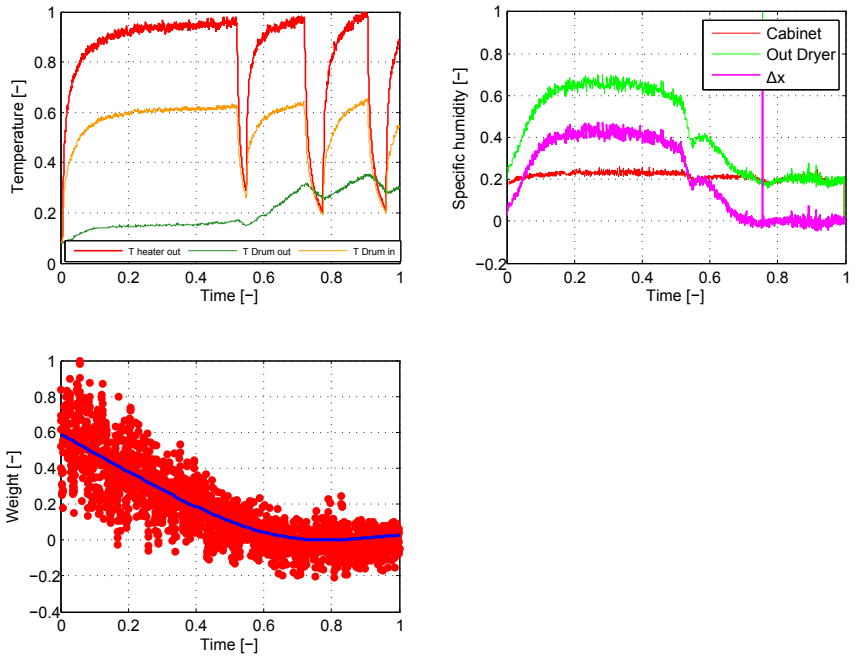

FIGURE 6.4: Temperatures, humidities and load water content during a standard drying cycle.

The drying time for a 3.8 kg dry moistened load at the 60% is nearly at 35 minutes, the maximum heater electric power is 5400 kW and the total energy consumption is about 2.5 kWh. The SMER index is about 1.13 kWh/kg.

6.3 Air circuit model

In this section the vented tumble dryer aeraulic model will be presented (see Figure 6.5). The model must be able to contemplate the physical phenomena that involve the aeraulic circuit as the flow rate leakages, as discussed in the previous paragraph. As done for the heat pump tumble dryer aeraulic circuit some assumptions are made:

- from the cabinet to the drum the air can enter through the front and the rear gasket. Characterized experimentally the two independent aeraulic resistances that govern the phenomenon is a difficult task and it was preferred to introduce a parameter (r_p) based on experimental evidence. For instance, during the drum spin motion more gap can be observed from the drum back flange and the rear gasket. As consequence, a value of r_p equals to 0.9 is adopted.

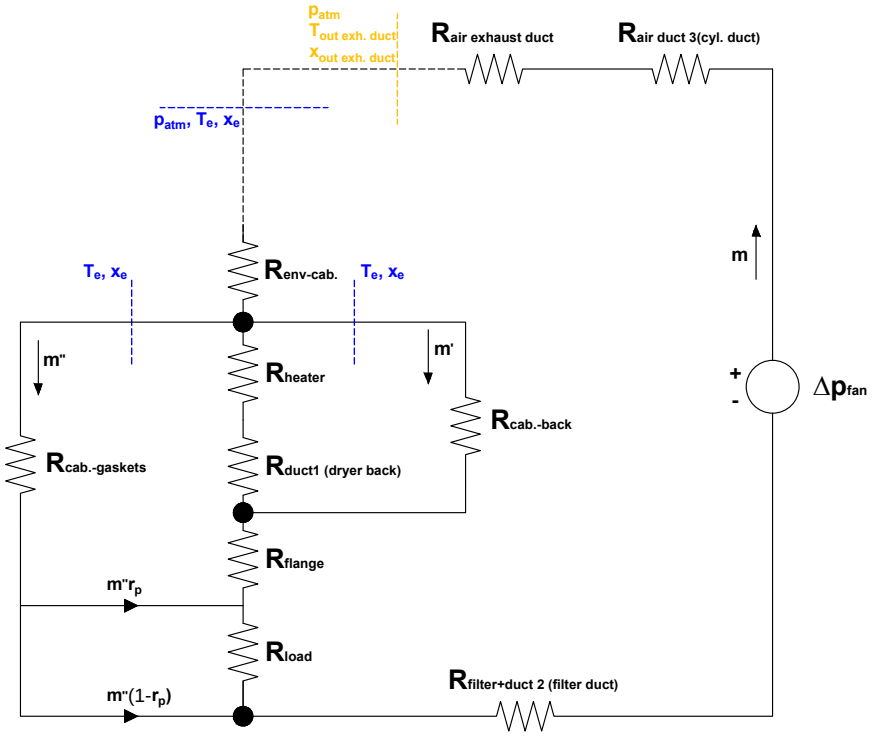

FIGURE 6.5: Vented dryer air circuit model. $R_{air\,duct\,3}$ is the aeraulic resistance of the cylindric duct between the fan and the exhaust duct. $R_{filter+duct\,2}$ is the sum of the aeraulic resistance of the filter and the shape of the duct containing the filter.

$$\dot{m}_{a,heater} = \dot{m} - \dot{m}^{'} - \dot{m}^{''}$$

- the thermodynamic properties of the air that enters into the system are equal to the ambient properties, therefore during the simulations are kept constants;
- every component or specific part of the aeraulic circuit is characterized by an aeraulic resistance which pressure loss factor was deduced from experimental measurements. For details of the components arrangement inside the cabinet see Figure 6.14b.
- the thermodynamic properties of the air entering the process circuit from the two main sources of leakages (front and rear gaskets and drum back panel) are at the ambient conditions;

In order to predict the mass flow rate drawn by the fan ($\dot{m}$), the mass flow rates entering the system as sources of leakage ($\dot{m}^{'}$ and $\dot{m}^{''}$) is necessary to solve the non-linear system 6.1, when the aeraulic circuit temperatures are known. The equations of the system express the static pressure balance between different aeraulic paths. The first equation (6.1) expresses the balance of static pressure considering the whole circuit. The second (6.1,a) considers the balance between the cabinet-gaskets pressure drop and the sum of four pressure drops: heater, duct1, flange and load (the duct1 pressure drop is absorbed by the heater). The third (6.1,b) considers the balance between the heater and duct1 pressure drop and the cabinet-back flange.

$$
\begin{cases}
\begin{aligned}
\Delta P_{fan}(\dot{m}, T_{i,fan}) = \Delta P_{a,duct\,3}(\dot{m}, \bar{T}_{a,duct\,3}) + \Delta P_{a,exh.\,duct}(\dot{m}, T_{i,exh.\,duct}) + \\
+ \Delta P_{e-cab}(\dot{m}, T_e) + \Delta P_{cab.\,gaskets}(\dot{m}^{''}, \Delta P_{cab.-drum}, T_{i,drum}) \\
+ \Delta P_{filter+duct2}(\dot{m}, T_{i,filter}, T_{i,drum})
\end{aligned} & (6.1) \\
\begin{aligned}
\Delta P_{cab.\,gaskets}(\dot{m}^{''}, \Delta P_{cab.-drum}, T_{i,drum}) = \Delta P_{heater}(\dot{m} - \dot{m}^{'} - \dot{m}^{''}, T_{i,heater}, T_{o,heater}) \\
+ \Delta P_{flange+load}(\dot{m}, T_{i,filter})
\end{aligned} & (6.1,a) \\
\Delta P_{heater}(\dot{m} - \dot{m}^{'} - \dot{m}^{''}, T_{i,heater}, T_{o,heater}) = \Delta P_{cab-back}(\dot{m}^{'}, T_e) & (6.1,b) \\
\Delta P_{cab-drum} = \Delta P_{heater+duct1} + \Delta P_{flange+load} & (6.1,c)
\end{cases}
$$

6.4 Experimental characterization of the aeraulic circuit

In order to evaluate the pressure drops through the aeraulic circuit elements some tests and analyses were carried out and in this section the results will be presented.

6.4.1 Fan pressure rise and cabinet pressure drop

In Figure 6.6 the characteristic curve of the fan in terms of non-dimensional parameters (ψ, ϕ) accordingly to the fan theory is plotted on the left chart. The pressure rise of the fan was measured for different values of temperatures at the fan inlet section (29-50-63 ℃) [46]. The chart on the right of Figure 6.1 shows the loss factor coefficient (introducing with Equation 3.2) as function of the mass flow rate entering from the ambient to the cabinet. The term $K_{env-cab}$ is defined as:

$$K_{env-cab} = \frac{\Delta P}{\rho_e \cdot V^2} \quad \left[\frac{1}{m^4}\right] \tag{6.2}$$

where: ΔP is the flow stream pressure drop from the ambient to the cabinet, ρ_e is the air density at the ambient conditions and V is the volumetric flow rate related also at the ambient conditions.

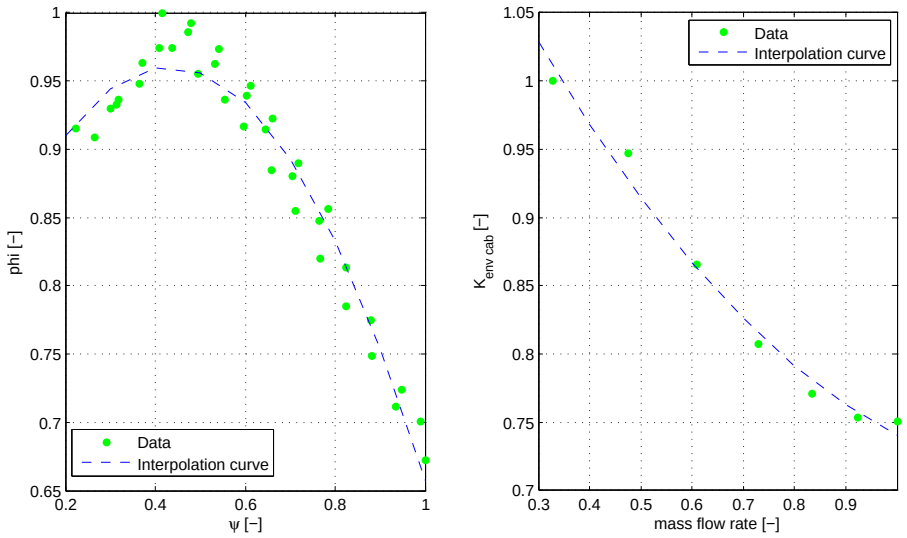

FIGURE 6.6: On the left: fan performance in terms of ψ and ϕ. On the right: loss factor coefficient for the ambient-cabinet aeraulic resistance.

6.4.2 Heater and back duct pressure drop

Experimentally, the total pressure drop from the cabinet to the drum flange inlet section was measured ($R_{heater} + R_{duct1}$, see Figure 6.5). The experimental setup required to install the heating element and the back duct (R_{duct1}) on a dedicated test rig [47] that allows a known mass flow rate to flow through the heating element and the back duct (for details see Figure 6.7). Tests were conducted for different values of the mass flow rate. In [47] data for ″hot‟ conditions (the heating element was switched on at full

power $\approx$ 5400 W) and for "cold" conditions (hence with air at ambient conditions) are reported. The computation of the mass flow rate was obtained by the readings of three signals: T_{diaf}, $P_{m,diaf.}$, $\Delta P_{diaf.}$, respectively temperature and static pressure upstream of the orifice and pressure drop across the orifice (see the test rig in Figure 6.7).

The data was fitted in a single polynomial curve ($\frac{\Delta P}{\rho^*}$ as function of the volumetric flow rate V^*), where the superscript (*) is to refer at the temperature T^* that is able to produce an effective non-dimensionalization of the data (loss factor K over the Reynolds number). T^* is defined in [47] as follows:

$$T^* = \lambda \cdot T_{a,heater,o} + (1 - \lambda) \cdot T_{a,heater,i} \tag{6.3}$$

where $0 < \lambda < 1$. The value of λ is not here reported for industrial secrecy reasons.

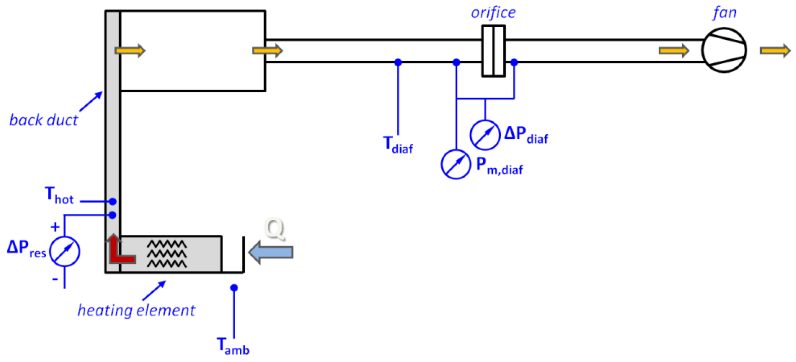

FIGURE 6.7: Heater and dryer back pressure drop: experimental setup [47].

6.4.3 Drum leakages

Also, the evaluation of the drum leakages (therefore the aeraulic resistance $K_{cab.-gaskets}$, see Figure 6.5) required a dedicated test rig that is shown in Figure 6.8. With this setup was possible to define the correlation that explains how mass flow rate enters into the drum (without passing the heating element) for different working conditions ($Q_{in}, T_{drum\,in}, p_{abs\,drum}$) (for more details see [46]). The air enters into the drum due to a poor contact between the drum gaskets (front and rear gaskets) and the rear/front drum flange that produces some gap, used by the air for entering in the process circuit because of high dimensional and geometric tolerances of the components.

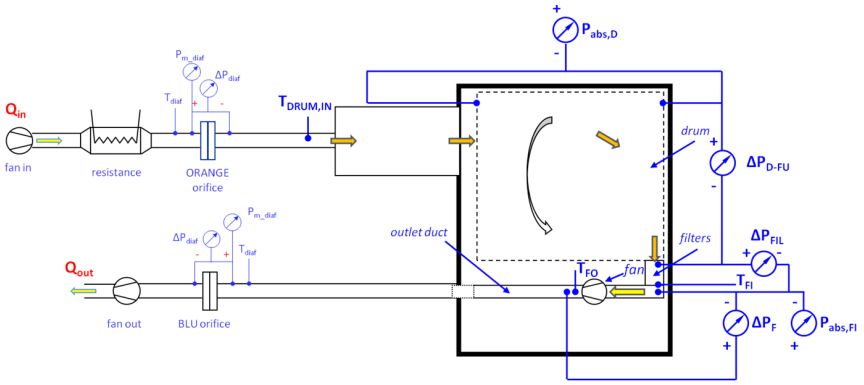

FIGURE 6.8: Drum leakages experimental setup.

As already done, a loss factor (K) was introduced in order to provide more general results. K is defined by the Equation 6.2 and the temperature reference condition is still the ambient temperature (T_e) since the thermohygrometric properties of the air that enters into the drum are nearer to the ambient thermohygrometric properties than the cabinet air properties. In Figure 6.9 the $K_{cab-gaskets}$ value is reported as function of the drum inlet temperature and the pressure inside the drum. As depicted in figure the loss factor increases gradually when the pressure inside the drum decreases, in addition the K value increases sharply when the drum temperature inlet rises. The reason for this trend can be explained if thermal expansion of the drum material is considered.

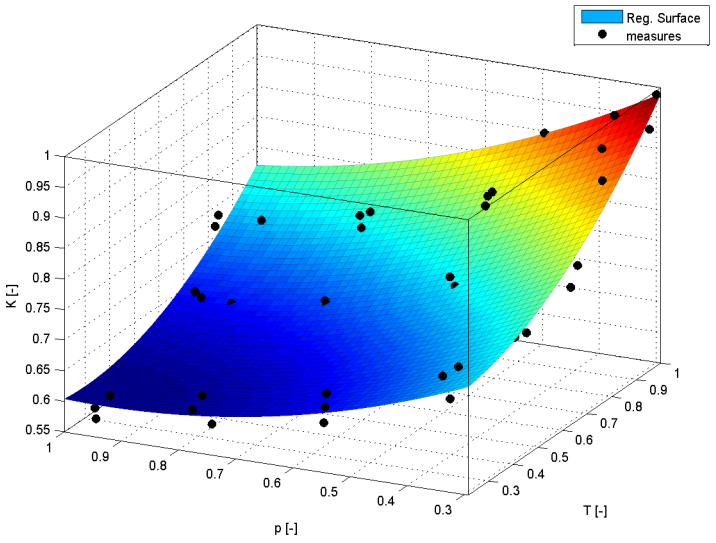

FIGURE 6.9: $K_{cab-gaskets}$.

6.4.4 Filter pressure drop

Filter pressure drop was evaluated with the setup shown in Figure 6.8. Here, a first attempt of generalization of the data was made with the following definition of loss factor $K_{filter} = \frac{\Delta P_{filter}}{\rho_{i,filter} \cdot V_{i,filter}^2}$. The results are shown in Figure 6.10. However, the chart demonstrates that all points do not fall on the same trend line, hence highlighting a not perfect generalization of the results; despite a decreasing monotonic trend of K is found. This is in agreement with the most common behavior of a general loss coefficient factor for low Reynolds number flows. From the trends in figure it is clear that the K value is dependent not by the overall mass flow rate crossing the filter but by the mass flow rate entering the drum (this explains the offset that appears between curves at the same drum inlet temperature) and also is dependent by the drum inlet temperature (this explains the distance between curves at different temperatures but identical mass flow rate). For these reasons it was decided to develop a correlation (see Figure 6.11) that explains the K value as function of the inlet drum mass flow rate and temperature, $K = f(Q_{i,drum}, T_{i,drum})$. The reasons of this behaviour could reside on the non-uniform distribution of the air velocity crossing the filter.

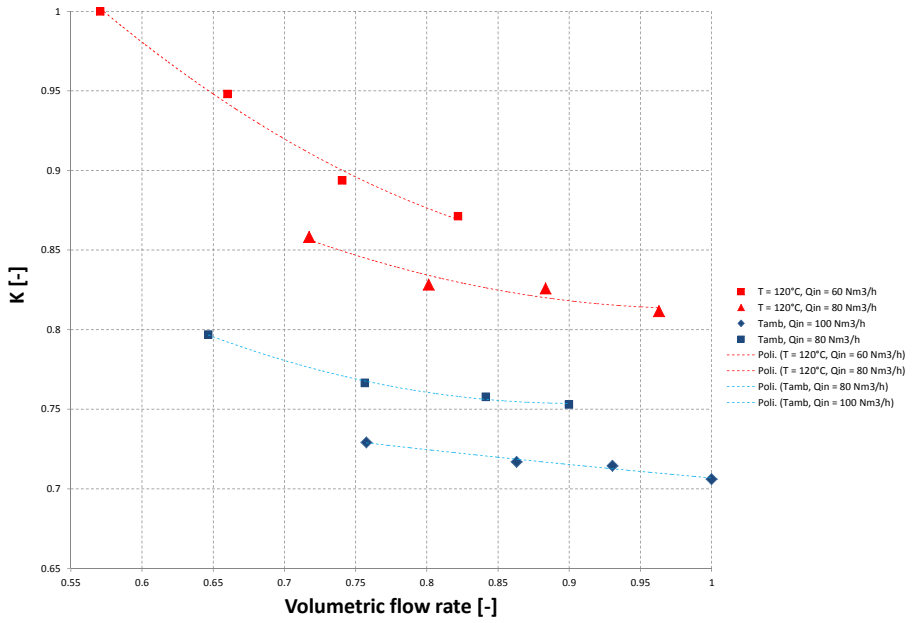

FIGURE 6.10: $K_{filter+duct2}$.

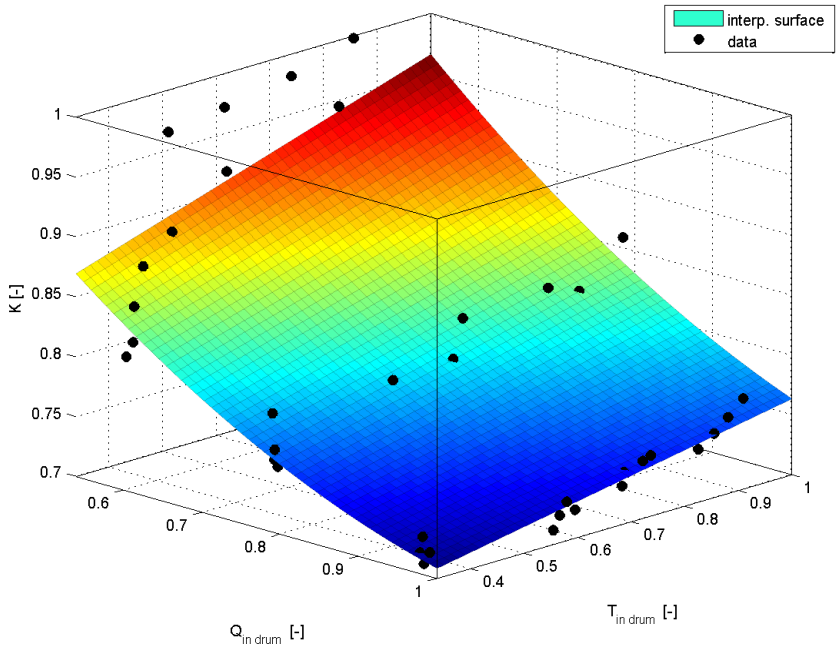

FIGURE 6.11: $K_{filter+duct2}$ as function of $Q_{i,drum}$ and $T_{i,drum}$.

6.4.5 Exhaust duct pressure drop

The exhaust duct is installed in order to simulate additional pressure drops during the development of new products. It could be viewed as a cone (see Figure 6.12) where the air flow stream is accelerated. In these conditions, for an incompressible fluid, as the air in the present case, and neglecting the surface friction may be written:

$$p_{i,cone} + \frac{1}{2} \cdot \rho_{i,cone} \cdot v_{i,cone}^2 = p_{o,cone} + \frac{1}{2} \cdot \rho_{o,cone} \cdot v_{o,cone}^2 \tag{6.4}$$

and hence, if the thermal losses are neglected:

$$\Delta P_{static} = p_{i,cone} - p_{o,cone} = \frac{1}{2} \cdot \rho_{i,cone} \left(v_{o,cone}^2 - v_{i,cone}^2 \right) \tag{6.5}$$

where $p_{o,cone} = p_{atm.}$, $v_{o,cone}$ is the cone outlet flow stream velocity and $v_{i,cone}$ is the cone inlet flow stream velocity and finally $\rho_{i,cone}$ is the air density at the cone inlet thermohygrometric conditions. Measured data in experimental tests (with a dedicated test rig 6.12) did not exactly match Equation 6.5, therefore the following relation was developed adding a concentrated pressure drop:

$$\Delta P_{exhaust\,duct} = \frac{1}{2} \cdot \rho_{i,cone} \left(v_{o,cone}^2 - v_{i,cone}^2 \right) + K_{exhaust\,duct} \cdot \rho_{i,cone} \cdot V_{i,cone}^2 \tag{6.6}$$

where $V_{i,cone}$ is the volumetric flow rate at the cone inlet thermohygrometric conditions and $K_{exhaust\,duct}$ is a constant evaluated from experimental data.

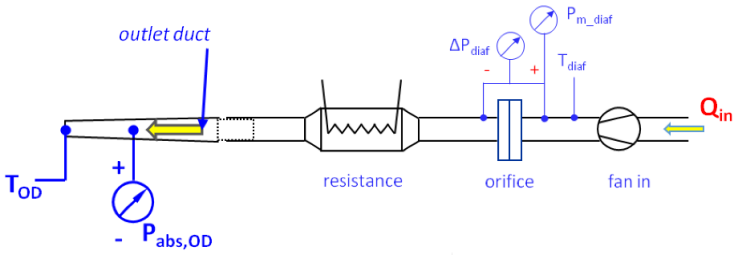

FIGURE 6.12: Exhaust duct measurement.

6.4.6 Flange and load pressure drop

The pressure drop due to the load was evaluated together with the flange. The value of $K_{flange+load}$ was estimated and defined as $K_{flange+load} = \frac{\Delta P_{flange+load}}{\rho_{i,filter} \cdot V^2_{filter\,in}}$. In Figure 6.13 the comparison between experimental data and pressure drop prediction using a constant value of $K_{flange+load}$ for both tests (empty and full load tests) is reported. The constant value is able to correctly predict the actual measurements (see the triangular points in Figure 6.13). Notice how, in this restrict domain, the trend of the measurements seems to be linear and not quadratic. The pressure drop, in case without load, can be considered near to the wet conditions that occur during the first stage of the dying cycle, since the large volume of the drum (greater than 87% respect to the one installed in the heat pump tumble dryer) reduces the load effect. The transition between wet and dry is managed linearly with the LWC definition.

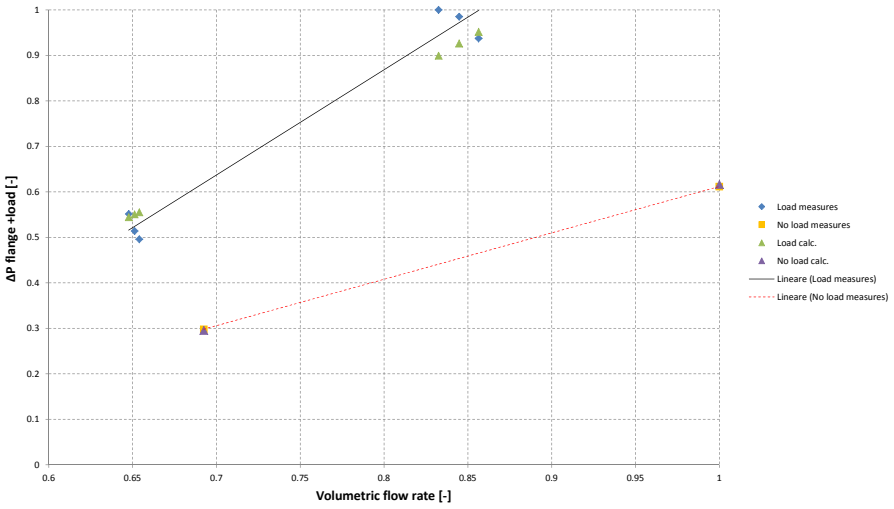

FIGURE 6.13: $K_{flange+load}$.

6.5 Cabinet thermal model

In this section the cabinet thermal model will be presented. It can be described by a number of temperature states with heat transfer interactions between them. A schematic representation of the heat flux paths is given in Figure 6.14. Convective and radiant heat fluxes are considered, these latter are introduce since the mean temperature of the wall canister reaches value higher than 300 °C and hence the radiative heat flux cannot be neglected.

The air volume inside the cabinet is not model with a thermal capacity. Its value is deducted applying the equation of energy conservation in a static way. This equation is reported in 6.7.

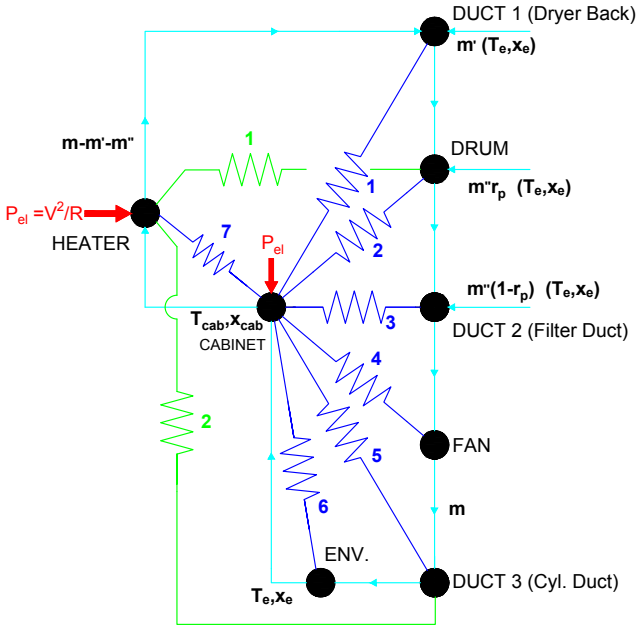

(A) Vented dryer thermal model.

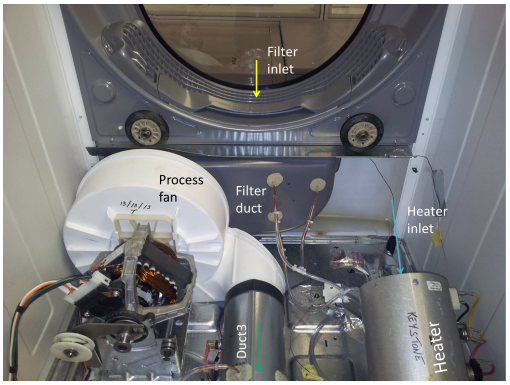

(B) Cabinet components.

FIGURE 6.14: Vented dryer thermal model and cabinet components. In the network representation the green lines describe a radiative exchange while the blue lines describe a convective heat exchange.

As shown in Table 6.1, that indicates the value of the thermal resistances, the convective heat transfer coefficient (α_{cab}) is unique for all the components. In addition the free convective heat transfer ($\alpha_{env\,cab}$) is introduced. It would describe the free convective heat transfer phenomenon between the external cabinet surface and the ambient.

Res.	Value
1	$1/(\alpha_{cab} \cdot A_{duct1})$
2	$1/(\alpha_{cab} \cdot A_{drum})$
3	$1/(\alpha_{cab} \cdot A_{duct2})$
4	$1/(\alpha_{cab} \cdot A_{fan})$
5	$1/(\alpha_{cab} \cdot A_{duct3})$
6	$1/(\alpha_{env\,cab} \cdot A_{cab.})$
7	$1/(\alpha_{cab} \cdot A_{heater})$
1	$\frac{1}{(\epsilon \cdot A)_{heater}} \cdot \frac{A_{drum}}{A_{drum}+A_{duct_3}}$
2	$\frac{1}{(\epsilon \cdot A)_{heater}} \cdot \frac{A_{duct_3}}{A_{drum}+A_{duct_3}}$

TABLE 6.1: Thermal resistances.

The equation of the energy conservation applied at the air volume inside the cabinet may be written as:

$$\begin{aligned} q_{heater-cab} + q_{duct1-cab} + q_{drum-cab} + q_{duct2-cab} + q_{fan-cab} + q_{duct3-cab} \\ - q_{cab-env} - \dot{m} \cdot (h_{cab} - h_e) + P_{el.\,motor} = 0 \end{aligned} \tag{6.7}$$

where: $q_{heater-cab} = \alpha_{cab} \cdot A_{heater} \cdot (T_{wall\,heater} - T_{cab})$, $q_{duct1-cab} = \alpha_{cab} \cdot A_{duct1} \cdot (T_{duct1} - T_{cab})$, $q_{drum-cab} = \alpha_{cab} \cdot A_{drum} \cdot (T_{drum} - T_{cab})$, $q_{duct2-cab} = \alpha_{cab} \cdot A_{duct2} \cdot (T_{duct2} - T_{cab})$, $q_{fan-cab} = \alpha_{fan} \cdot A_{fan} \cdot (T_{fan} - T_{cab})$, $q_{duct3-cab} = \alpha_{cab} \cdot A_{duct3} \cdot (T_{duct3} - T_{cab})$, $q_{cab-env.} = \alpha_{cab-env.} \cdot A_{cabinet} \cdot (T_{cab} - T_e)$ and $P_{el.\,motor} = (1 - \eta_{el.\,motor}) \cdot P_i$.

In addition: h_{cab} is the air enthalpy at the cabinet thermohygrometric conditions and h_e is the ambient air enthalpy. The solution of the previous equations, knowing the values of the state temperatures, the total mass flow rate drawn by the fan ($\dot{m}$), and the heat losses from the electric motor gives the air cabinet temperature (T_{cab}).

To explain the heat transfer interactions between all the parts of the model, the conservation of energy equation in temperature formulation is applied to each temperature state ($T_{wall\,heater}$, T_{duct1}, T_{drum}, T_{duct2}, T_{fan} and T_{duct3}). Starting with the ″duct1‶, the conservation of energy equation may be expressed as:

$$\frac{dT_{duct1}}{dt} = \frac{q_{a-duct1} - q_{duct1-cab}}{(m \cdot c_p)_{duct1}} \tag{6.8}$$

where $q_{duct1-cab}$ is already defined by Equation 6.7, the heat transfer $q_{a-duct1}$ is calculated applying the P-NTU method [38]:

$$T_{a,duct1,o} = T_{duct1} + (T_{a,duct1,i} - T_{duct1}) \cdot e^{-NTU} \tag{6.9}$$

$$NTU = \frac{\alpha_{a-duct1} \cdot A_{duct1}}{\dot{m}_{a,heater} \cdot \bar{c_p}} \tag{6.9,a}$$

$$q_{a-duct1} = \dot{m}_{a,heater} \cdot \bar{c_p} \cdot (T_{a,duct1,i} - T_{a,duct1,o}) \tag{6.9,b}$$

where $\alpha_{a-duct1}$ is evaluated with the Dittus-Boelter's equation [26]. For the ″duct2‟ the conservation of energy equation is given in the next equation:

$$\frac{dT_{duct2}}{dt} = \frac{q_{a-duct2} - q_{duct2-cab}}{(m \cdot c_p)_{duct2}} \tag{6.10}$$

where $q_{duct2-cab}$ is already defined Equation 6.7, the heat transfer $q_{a-duct2}$ is calculated as in 6.9. For the fan may be written:

$$\frac{dT_{fan}}{dt} = \frac{q_{a-fan} - q_{fan-cab}}{(m \cdot c_p)_{fan}} \tag{6.11}$$

where $q_{fan-cab}$ is already defined by Equation 6.7, the heat transfer q_{a-fan} is calculated as in 6.9. For the ″duct3‟ the conservation of energy equation is given in the next equation:

$$\frac{dT_{duct3}}{dt} = \frac{q_{a-duct3} + q_{rad.\,duct3} - q_{duct3-cab}}{(m \cdot c_p)_{duct3}} \tag{6.12}$$

where $q_{duct3-cab}$ is already defined by Equation 6.7, the heat transfer $q_{a-duct3}$ is calculated as in 6.9. Instead, $q_{rad.\,duct3}$ is the fraction of the radiation leaving the heater surface and it will be defined in Paragraph 6.6 (also $T_{wall\,heater}$ will be defined in this paragraph).

T_{drum} will be defined in the Paragraph 6.7.

6.6 Heater model

In this section the model of the heater will be proposed. The model will be able to predict the temperature of the heater components (canister wall and electric filament) and also the heater outlet air temperature under different working conditions, as well as the transient behavior during the start-up and shut-down of the heater. The heating element may be described with two states: one state for the canister wall and another state for the electric filament. A schematic representation with a frontal picture of the heater is given in Figure 6.15.

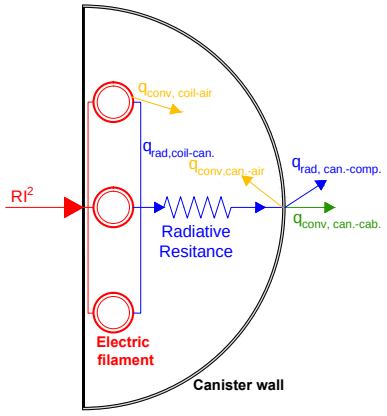

(A) Heater model.

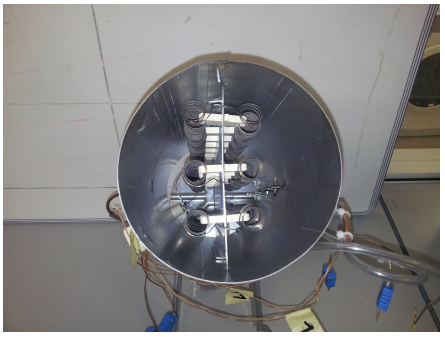

(B) Heater picture.

FIGURE 6.15: Heater model and picture.

Due to the geometric symmetry of the heater only half part is considered. The heater is described by two states and hence two thermal capacities: electric filament and the canister wall capacity. The equation of energy conservation applied at only one electric filament is given in the next equation:

$$\frac{dT_{coil}}{dt} = \frac{P_{el.\,one\,coil} - q_{rad,coil-can} - q_{conv,coil-air}}{(m \cdot c_p)_{coil}} \tag{6.13}$$

where: $P_{el.\,one\,coil} = \frac{V \cdot I^2}{3}$ in which V is the electric voltage and I is the electric current. The net radiation exchange $q_{rad,coil-can}$ between the filament surface and the internal surface of the canister (assuming gray surface behavior) may be expressed as [26]:

$$q_{rad,coil-can} = \frac{\sigma \cdot (T_{coil}^4 - T_{can}^4)}{\frac{1-\epsilon_{coil}}{\epsilon_{coil} \cdot A_{coil}} + \frac{1}{A_{coil} \cdot F_{coil-can}} + \frac{1-\epsilon_{can}}{\epsilon_{can} \cdot A_{can}}} \tag{6.14}$$

where: σ is the Stefan Boltzmann constant, ϵ_{coil} and ϵ_{can} are respectively the total, hemispherical emissivity of the electric filament surface and the total, hemispherical emissivity of the wall canister. Since the canister wall surface is orders in magnitude greater than the electric filament surface, Equation 6.14 may be changed with the radiation exchanged equation for a small convex object in a large cavity [26]. The heat flux $q_{conv,coil-air}$ is equal to:

$$q_{conv,coil-air} = P_{coil-air} \cdot \dot{m}_{a,heater} \cdot \bar{c_p} \cdot (T_{coil} - T_{a,heater,i}) \tag{6.15}$$

where $P_{coil-air}$ is the thermal efficiency according to P-NTU method [38]. This heat flux may be neglected since $A_{can} >> A_{coil}$.

The equation of energy conservation applied at only half side of the wall canister is given in the next equation:

$$\frac{dT_{can.}}{dt} = \frac{q_{rad,coil-can} \cdot n_{coils} - q_{conv,can-air} - q_{conv,can-cab.} - q_{rad,can-comp.}}{(m \cdot c_p)_{can}} \tag{6.16}$$

the heat flux $q_{rad,coil-can}$ is already defined above, in this equation it is only multiplied by the number of electric filaments. Instead, the term $q_{conv,can-air}$ is evaluated as the term $q_{conv,coil-air}$ in Equation 6.15. The term $q_{conv,can-cab}$ indicates the convective heat flux between the canister and the air inside the cabinet, hence may be expressed as: $q_{conv,can-cab} = \alpha_{cab} \cdot \frac{A_{can}}{2} \cdot (T_{wall,can} - T_{cab})$. The radiative heat flux $q_{rad,can-comp}$ indicates the radiant exchange between the canister surface and some cabinet components. As a consequence of the components arrangement only the surface of the drum and the surface of the ″duct3‟ exchange with the canister wall surface. Therefore, if the canister is considered as a small object inside a large cavity, $q_{rad,can-comp}$ may be written as:

$$q_{rad,can-comp} = \sigma \cdot \epsilon_{can} \cdot \frac{A_{can}}{2} \cdot (T_{can}^4 - \bar{T}_{comp}^4) \tag{6.17}$$

where: $\bar{T}_{comp.} = \frac{T_{duct3}+T_{drum}}{2}$, the value of A_{can} is divided by two because only half canister surface is considered in 6.14. Hence $q_{rad.\,duct3}$ in Equation 6.12 may be expressed as:

$$q_{rad.\,duct3} = 2 \cdot q_{rad,can-comp} \cdot \frac{A_{duct3}}{A_{duct3} + A_{drum}} \tag{6.18}$$

finally:

$$q_{rad.\,drum} = 2 \cdot q_{rad,can-comp} \cdot \frac{A_{drum}}{A_{duct3} + A_{drum}} \tag{6.19}$$

The heater outlet air temperature is estimated as:

$$T_{a,heater,o} = T_{a,heater,i} + \frac{q_{conv,can-air} + q_{conv,coil-air}}{\dot{m}_{a,heater} \cdot \bar{c_p}} \tag{6.20}$$

the specific heat ($\bar{c_p}$) is evaluated at the mean temperature between the inlet and outlet section of the heating element.

6.7 Drum model

The developed model in Chapter 4 was modified in order to contemplate the air energy losses from the air flow stream and the drum. In this tumble dryer the drum inlet temperature (about 120 ℃) is higher than the heat pump tumble dryer one (max 70 ℃). Therefore the losses, in this model, cannot be neglected.

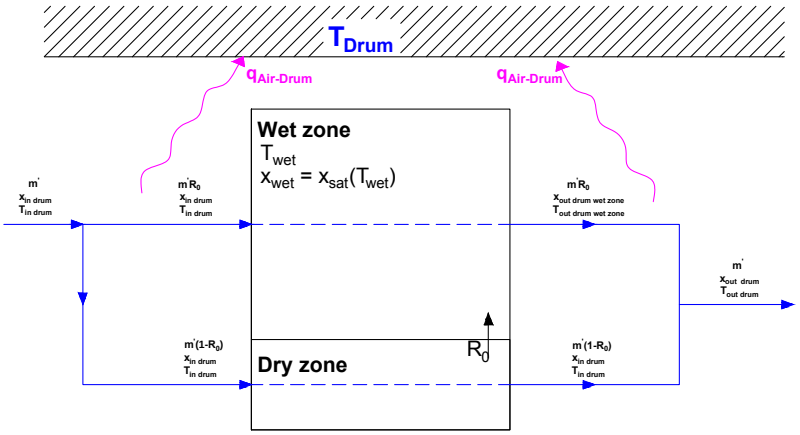

FIGURE 6.16: Drum model with energy losses from the air stream to the drum.

The drum is described by a thermal capacity, applying the equation of the energy conservation:

$$\frac{dT_{drum}}{dt} = \frac{q_{a-drum} + q_{rad.drum} - q_{drum-cab}}{(m \cdot c_p)_{drum}} \tag{6.21}$$

where: $q_{rad.drum}$ is already defined Equation 6.19 and $q_{drum-cab}$ in Equation 6.7. Additionally a heat transfer between the mean air crossing drum temperature, $\bar{T}_a$, and the drum metallic plate temperature, T_{drum}, is defined as:

$$q_{a-drum} = \alpha_{a-drum} \cdot A_{drum} \cdot (\bar{T}_a - T_{drum}) \tag{6.22}$$

$$q_{a-drum}|_{wet\,zone} = q_{a-drum} \cdot R_0 \tag{6.22,a}$$

$$q_{a-drum}|_{dry\,zone} = q_{a-drum} \cdot (1 - R_0) \tag{6.22,b}$$

Because of the introduction of the heat flux q_{a-drum} the enthalpy at the outlet section of the wet zone becomes:

$$h_{a,wet-zone,o} = h_{a,drum,i} - \frac{q_{a-wet\,zone} + q_{a-drum}|_{wet\,zone}}{\dot{m}_{a,drum} \cdot R_0} \tag{6.23}$$

and for the dry-zone becomes:

$$h_{a,dry-zone,o} = \begin{cases} h_{a,drum,i} & \text{if } R_0 = 1 \\ h_{a,drum,i} - \dfrac{q_{a-drum}|_{dry\,zone}}{\dot{m}_{a,drum} \cdot (1 - R_0)} & \text{if } R_0 < 1 \end{cases} \tag{6.24}$$

For the wet zone, when the outlet enthalpy and the specific humidity are known, the dry bulb temperature can be calculated.

6.8 Model validation and simulation results

In this section will be discussed the comparison between model results and experimental measurements (see Figure 6.17). The model correctly predicts the drum inlet and the drum outlet temperatures and it is also able to efficiently predict the drying time. Significant difference can be observed during the transient due to the shut-down of the electric resistance (near to 70% of the total drying time), however this difference does not affect in a relevant way the reliability of the simulation results. In Figure 6.18 the evolution of the mass flows rate during the drying cycle is plotted. The mass flow rate that flows through the heater is about 40% of the total volumetric flow rate drawn by the fan, the remaining part is composed for the 45% by the volumetric flow rate entering the system as a consequence of some gap that occurs from the front/rear gaskets and the front/rear drum vertical plate and for the 15% by the volumetric flow rate coming from the back panel. This distribution of the total mass flow rate drawn by the fan, along the three paths of the volumetric air circuit, matches experimental measurements: see the first chart in Figure 6.19. However, this flow rate distribution does not correctly match for all configurations: for instance, if the exhaust duct in the final part of the aeraulic circuit is removed noticeable differences appear (see the chart below in Figure 6.19). To conclude, it is worth noting how the total volumetric flow rate decreases sightly during the drying cycle. This is a consequence of the two factors: the first is the increment of the pressure drop due to the laundry and second appears at the last phase of the drying cycle when the temperature at the drum outlet section increases: this reduces the fan pressure rise (see Figure 6.18).

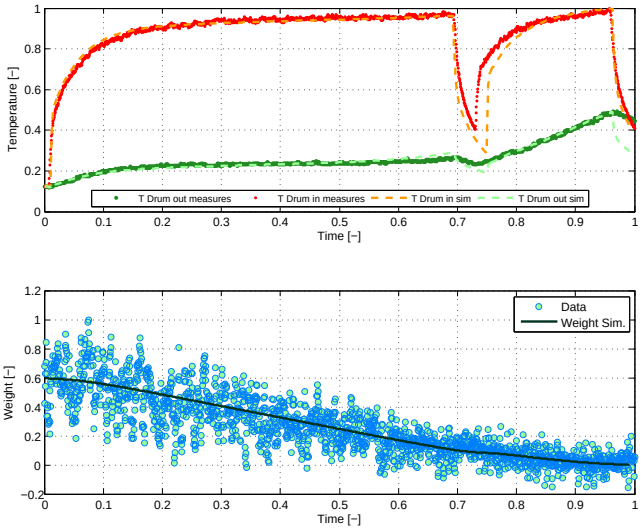

FIGURE 6.17: Temperatures comparison on the top and moisture content comparison below.

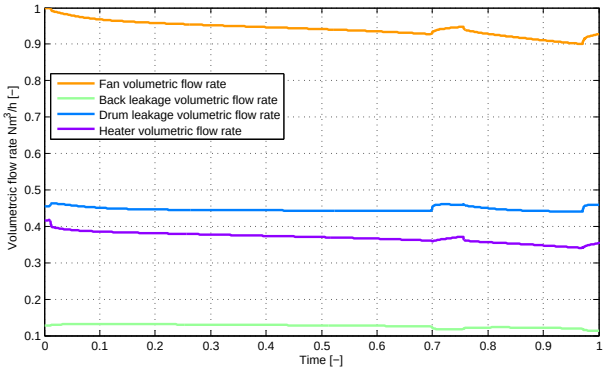

FIGURE 6.18: Volumetric flow rate trends.

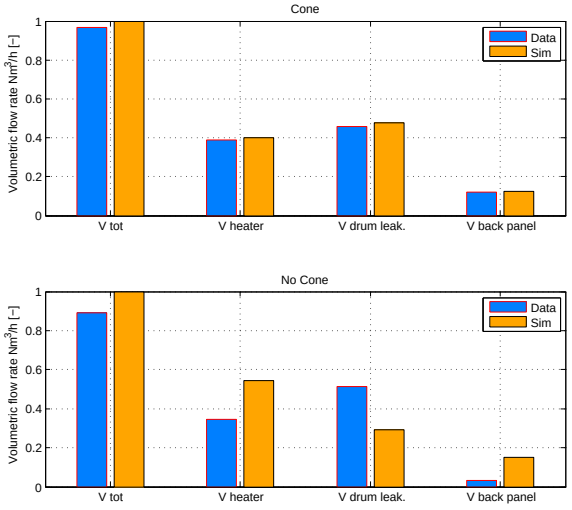

FIGURE 6.19: Volumetric flow rate distributions.

Chapter 7

Condenser tumble dryer model

7.1 Introduction

In this chapter a condenser tumble dryer for home application will be analyzed and modeled. This platform of dryer can be viewed as an extension of the air vented tumble drier where the air leaving the drum is recirculated back, first is driven through a heat exchanger and then to the heater creating a closed loop. A dynamic model will proposed: the focus will be on the aeraulic circuit and on the cross flow heat exchanger that, as stated earlier, is used to dehumidified the air coming from the drum (in a condenser dryer, the moisture removal process is governed by the condenser heat exchanger since the air circuit is closed). The heating element consists in two electrical resistances arranged in series: the model of this component is not detailed how the heater of the air vented tumble dryer, however, its dynamic behavior is considered (although it is faster than the dynamics of the heat transfer between other components).

7.2 Components description and features of the standard drying cycle

A scheme of the condenser tumble dryer machine is shown in Figure 7.1. The main components of this device are: heater, drum, process fan, condenser heat exchanger and cooling fan. The process fan draws air from the drum and blows it towards a compact heat exchanger where the air is cooled and dehumidified. After the heat exchanger, the air goes through the heater where is heated and finally enters into the drum where is cooled and humidified. The cold fluid, in the heat exchanger, is air that is drawn by another fan (cooling fan) from the ambient where the device is installed.

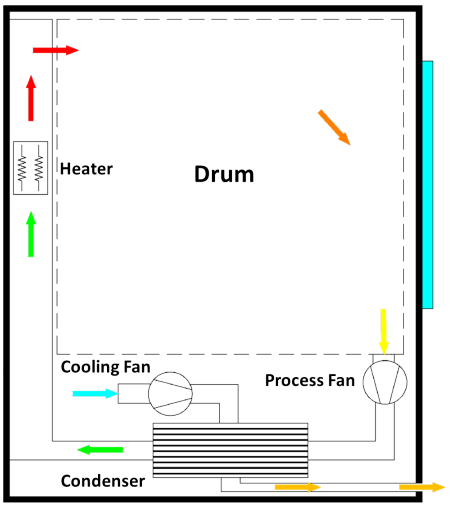

FIGURE 7.1: Condenser dryer scheme.

The drying cycle can be divided into four phases (during a normal cycle), in Figures 7.2 and 7.3 a typical drying cycle for the condenser dryer is shown. A first phase where all the temperatures of the systems increase. In this phase the power input at the system ($\approx$ 2600 W) is greater than the energy losses, however when the drum inlet temperature reaches a fixed value (measured by a NTC probe) the electric power is decremented with a relay strategy and a long drying phase begins. During this phase, although all the aeraulic circuit temperatures remain constant, the air specific humidity decreases progressively. This decrement is due to the evaporation rate from the laundry that decreases with lower levels of water in the laundry (LWC becomes smaller). A third phase begins when the drum outlet temperature reaches a fixed value, this indicates that the drying process is almost completed, therefore the electric power is decremented to a lower value (only the smaller electric resistance is activated, $\approx$ 900 W). The last phase starts when the conductivity probe indicates that the minimum water content is reached. In this phase, that is called cooling phase, the heating system is switched off, however both the process and the cooling fan remain activated. The drying cycle is completed when the drum outlet temperature decreases below 40 ℃. Figure 7.3 shows that the difference of specific humidity between the heat exchanger inlet section and outlet section reaches its maximum value near to the initial stage of the second phase, when the drum inlet temperature achieves its highest value. Notice that, during all the second phase, the difference of humidity ratio is maintained at a constant value, therefore also the condensation rate remains stable since, in this tumble dryer model, the fabric load does not significantly affect the total mass flow rate drawn by the process fan. As discussed in [48], the volumetric flow rate in the process air circuit is high in the first part of the drying cycle, that corresponds to the condition of low temperature at

the fan inlet section. The mass flow rate lower limit is reached with high temperature (at the fan inlet section) and fully dry load (conditions representative of the final stage of the drying cycle). However, the difference between the maximum and the lower value is less than 10%. This behaviour is due to the low value of the process volumetric flow rate that is about half of the one that flows in the heat pump tumble dryer.

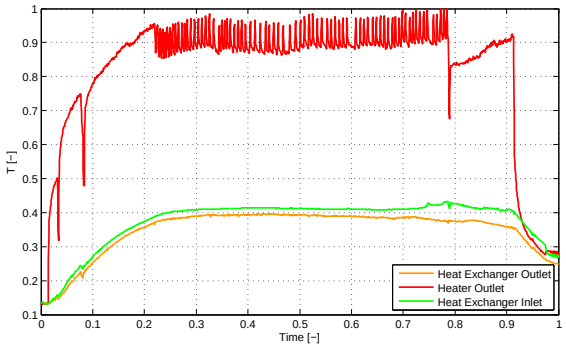

FIGURE 7.2: Condenser dryer air temperatures.

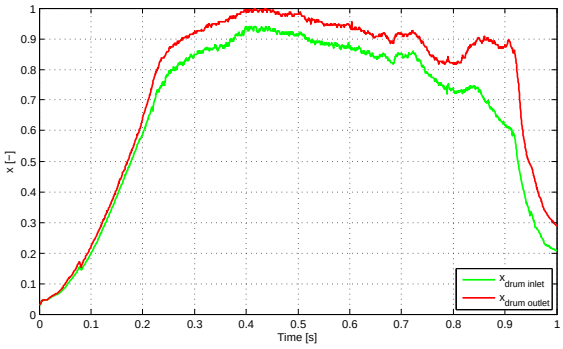

FIGURE 7.3: Condenser dryer specific humidities.

Approximately, since specific data cannot be here reported, for industrial secrecy reasons, during the pseudo steady state phase the temperature of the air at the heater outlet is about 150 ℃, the drum outlet temperature is near to 70 ℃, the heat exchanger outlet temperature is lower only than 1-2 ℃ compared to the inlet. From the cold side of the heat exchanger the air inlet temperature is higher than 2-3 ℃ compared to the fan inlet due to the heat flux from the air duct. The outlet temperature is near to 60 ℃. The drying time for a 8 kg dry moistened load at the 60% is nearly at 140 minutes and the energy consumption is about 5 kWh. The maximum electric power of the heating element, when both the electric resistances are switched on, is 2900 W. The SMER index is about 1 kWh/kg.

7.3 Condenser tumble dryer air circuit model

In this section the condenser tumble dryer air circuit model will be presented. The air circuit is modeled following an electric analogy ($\Delta P = \Delta V$ and Volumetric flow rate = I) as done for the heat pump and air vented tumble dryer. With this analogy the fan is the electric generator and the aeraulic resistances are the electric resistances. Every aeraulic resistance is defined by a pressure loss factor coefficient (K) that was determined by experimental data. In Figure 7.4 and in Figure 7.5 the schemes that sum up how the air circuit model is developed are shown.

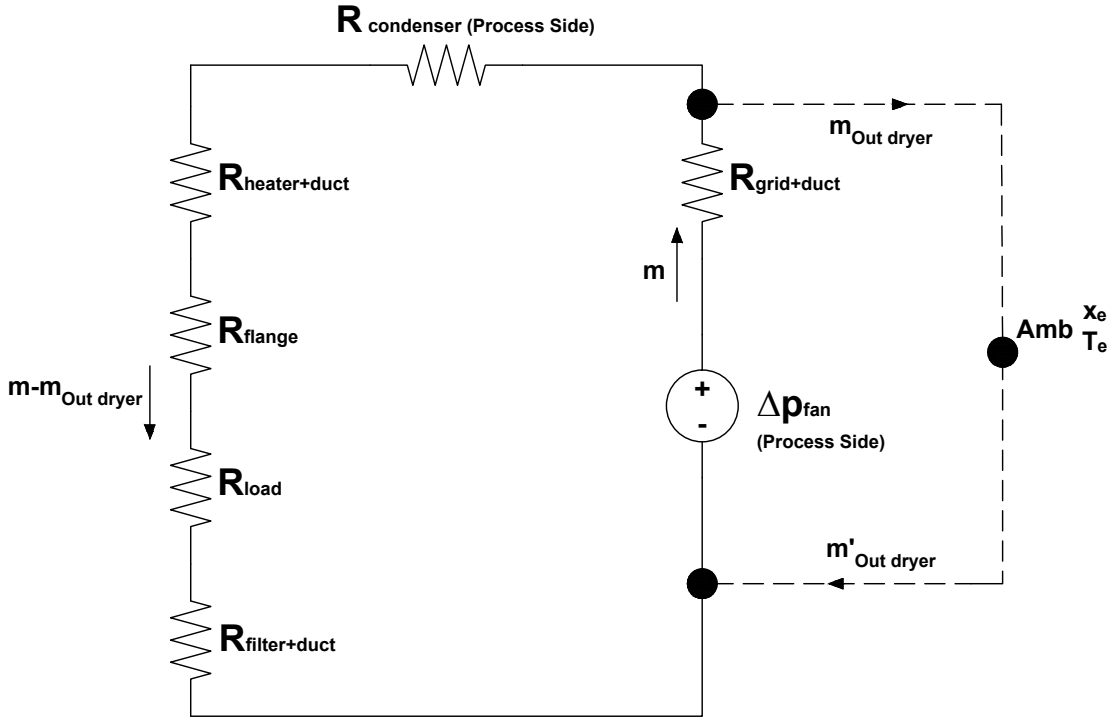

FIGURE 7.4: Process air circuit model.

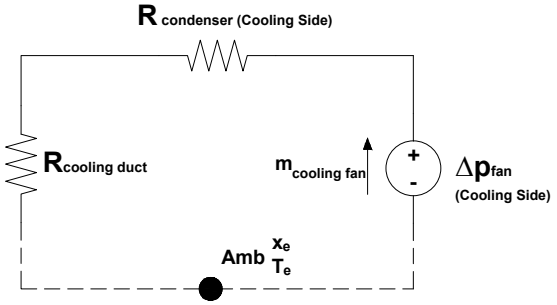

FIGURE 7.5: Cooling air circuit model.

For the process side circuit may be written the balance equation of the static pressure drops. The fan pressure rise must be equal to the sum of the components pressure drops:

$$\Delta P_{fan}\left(\dot{m}, T_{i,fan}\right) = \Delta P_{HX}\left(\dot{m}^{'}, \bar{T}_{HX\,proc.}\right) + \Delta P_{Heater+Flange}\left(\dot{m}^{'}, \bar{T}_{Drum}\right) + \\ + \Delta P_{load}\left(\dot{m}^{'}, T_{i,drum}, LWC\right) + \Delta P_{load}\left(\dot{m}^{'}, T_{o,drum}\right) \tag{7.1}$$

where:

- $\bar{T}_{HX\,proc.} = \dfrac{T_{i,HX} + T_{o,HX}}{2}$
- $\bar{T}_{Drum} = \dfrac{T_{o,HX} + T_{i,fan}}{2}$
- $\dot{m}^{'} = \dot{m} - \dot{m}_{o,dryer}$

In the previous equation the terms in brackets indicate the variables that change during the drying cycle.

The unknown term in Equation 7.1 is only the term $\dot{m}$, since the term $\dot{m}_{out\,dryer}$ is a fixed term. This value was chosen in order to predict the dryer water recovery efficiency. To solve Equation 7.1 the aeraulic circuit temperatures must be known, moreover terms that indicate how the pressure drops changing are nonlinear (typically a quadratic relation) therefore, to solve it is necessary to use a root-finding algorithm (secant method is adopted in this work).

For the cooling side circuit the static pressure drops balance equation may be written as:

$$\Delta P_{fan}\left(\dot{m}_{coolingfan}, T_{i,fan}\right) = \Delta P_{HX}\left(\dot{m}_{coolingfan}, \bar{T}_{HX\,cooling.}\right) + \Delta P_{air\,circuit}(\dot{m}_{coolingfan}) \tag{7.2}$$

where:

- $\bar{T}_{HX\,cooling.} = \left.\dfrac{T_{i,HX} + T_{o,HX}}{2}\right|_{cooling\,side}$
- $T_{i,fan} = T_e$. It is the ambient temperature where the device is installed.

In Equation 7.2 the term $\dot{m}_{coolingfan}$ is the only one unknown term if the temperatures of the cooling air circuit are known.

7.4 Experimental characterization of the air process circuit

The process circuit was characterized experimentally. The characterization led to obtain the correlations that explain how the static pressure drops vary as function of the mass flow rate and the thermohygrometric properties of the air at the component inlet section (or the mean thermohygrometric conditions in some components). The methodology used is identical to the procedure discussed in Paragraph 3.3.6 for the heat pump tumble dryer and consists in to interrupt the air circuit in a suitable point (the drum filter intake) and leading heated air into the process circuit. The air is heated with a set of electrical resistances, the mass flow rate is measured with an orifice flow meter and it is varied using a push-booster fan. The measured data of pressure, in these tests, was used to develop the pressure drop correlations. This methodology does not allow to characterize the pressure drop of the filter region. For measuring it, it was necessary to restore the standard configuration of the machine and running some tests in closed circuit configuration.

7.4.1 Process fan pressure rise

The static pressure produced by the fan (ΔP_{fan}) was measured for different working conditions (volumetric flow rate and fan inlet temperature different values). All the data was normalized and expressed accordingly to fan theory (ϕ and ψ) (Figure 7.6).

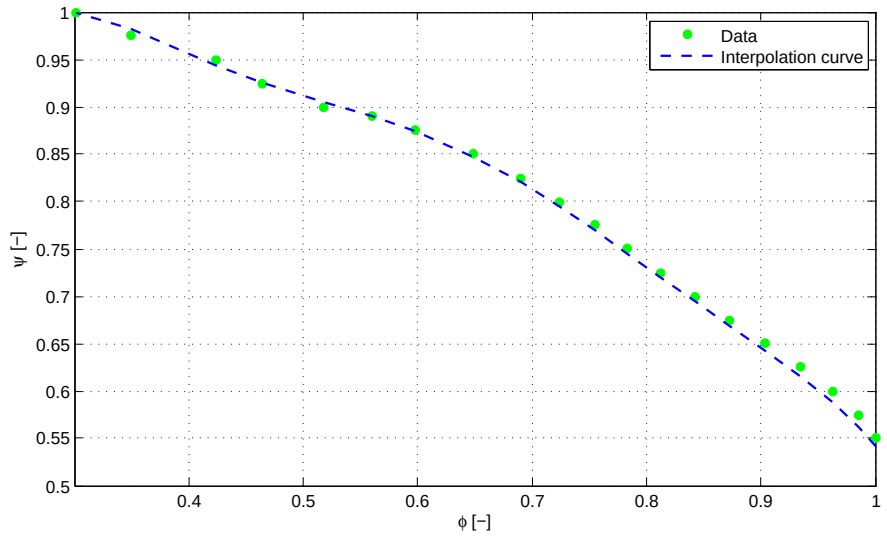

FIGURE 7.6: Process fan characteristic curve.

7.4.2 Heat exchanger pressure drop

During the fan performance tests, the pressure drop measurements across the condenser heat exchanger were performed. The air-to-air plate heat exchanger installed in the device has a cross flow configuration (Figure 7.7), and heat is transfered from the hot fluid to the cold fluid through thin aluminum plates. Inside the channels between plates there are not fins. The drying fluid entering in the heat exchanger is typically around 70 ℃ and 100% RH and the room air temperature, that is blows as clod fluid, it is significantly below the dew point temperature of the process air. Thus the humidity in the air exiting the drum is able to condense onto the heat exchanger. As room air is used as a cooling medium, this air must not be too hot, since this would significantly reduce the dryer efficiency due to poor condensation of water vapor. If different working conditions are considered by dividing the heat exchanger pressures drop by the air density at the actual temperature of each test, measurement values collapse on a single curve (Figure 7.8). The air density is calculated at the mean temperature: $\bar{T}_{HX\,proc.} = \frac{T_{HX\,in}+T_{HX\,out}|_{proc}}{2}$ for the process side and for the cooling side: $\bar{T}_{HX\,cooling.} = \frac{T_{i,HX}+T_{o,HX}\big|_{cool.}}{2}$.

(A) Cooling Side (B) Process Side

FIGURE 7.7: Cross flow heat exchanger.

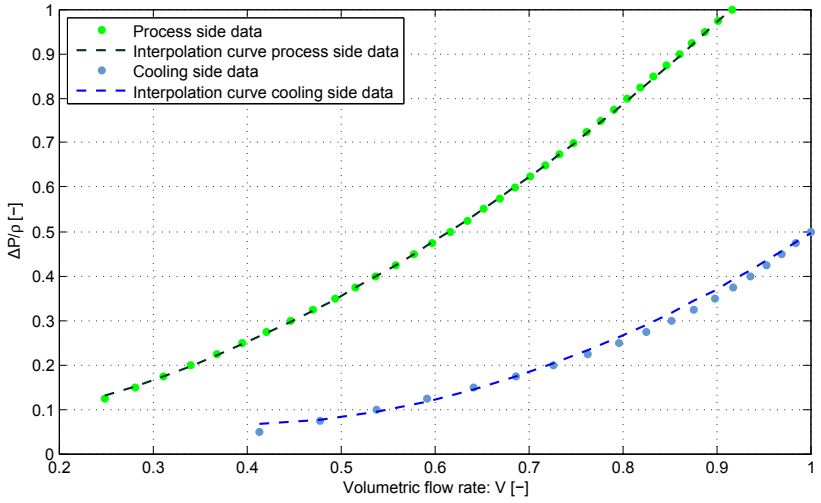

FIGURE 7.8: Heat exchanger pressure drops process and cooling side.

7.4.3 Back duct, heater and flange pressure drop

Also, from the data measured during the fan performance tests, the pressure drop between the heat exchanger outlet section and the drum was acquired and analyzed. This pressure drop is the sum of other pressure drops that the air undergoes from different components or due to the aeraulic duct geometry. From the heat exchanger outlet section the air flows through the drum and it crosses the heater and the rear flange, in addition, after the heat exchanger, the flow is bended by 90°. In order to generalize the pressure data, the pressure loss factor coefficient was introduced:

$$K_{air\,circuit+heater+flange} = \frac{\Delta P_{air\,circuit+heater+flange}}{\rho \cdot V^2} \quad \left[\frac{1}{m^4}\right] \tag{7.3}$$

This loss factor is able to define the following aeraulic resistance: $R_{heater+duct} + R_{flange}$. The reference temperature to calculate the air density is: $\bar{T}_{Drum} = \frac{T_{o,HX}+T_{i,fan}}{2}$. The results are shown in Figure 7.9. What is worth noting is the K behavior as function of the volumetric flow rate: the loss factor decreases progressively with the increment of the volumetric flow rate as depicted in Figure 7.9. The reason for this trend could be that for low values of the volumetric flow rate the flux is laminar and then, when the volumetric flow rate increases, the flow regime becomes gradually turbulent. For fully developed turbulent flow the friction factor is a constant and is a function only of the surface conditions [26].

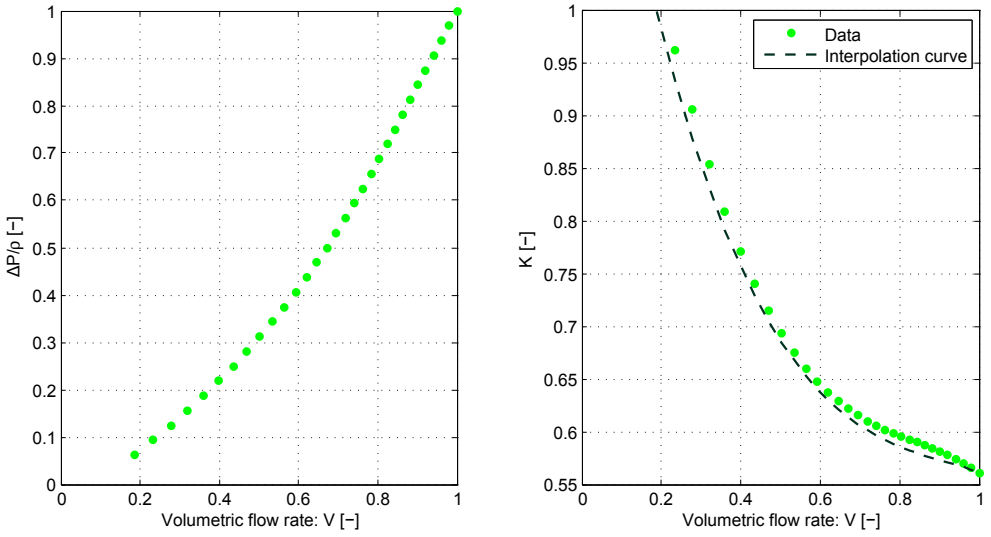

FIGURE 7.9: Heater, flange and air circuit total pressure drop.

7.4.4 Filter pressure drop

The pressure drop across the filter, $R_{filter+duct}$, (installed earlier of the process fan) was evaluated indirectly during the close circuit tests. In fact, as discussed earlier, in the open circuit tests, the pressure drop measurement across the filter was not possible. From the data acquired in these tests an estimation of the loss factor was possible. The definition is the same of Equation 7.3 and the reference temperature is the drum outlet temperature. The analysis showed a constant value.

7.4.5 Aeraulic model validation

The validation of the model was conducted with the data collected from the closed air circuit test. The model discussed in the Paragraph 7.3 was implemented in Matlab-Simulink with the correlations obtained for the static pressures drops in the previous paragraphs. The comparison between the experimental value of the volumetric flow rate drawn by the process fan and the model value is shown in Figure 7.10 for different working conditions. For empty tests (without load inside the drum), the difference between the values predicted by the model (purple dotted line) and the experimental data (red dotted line) is slightly (the error is smaller of 2%) and in addition the trend is identical for both curves (volumetric flow rate decreases as flow rate temperature raises). For full load tests, the behavior between the values predicted by the model (green solid line) and experimental measurements (light blue solid line) is different. The experimental values seem to be independent from the fan inlet temperature. Measurements with load are affected by a greater error than measurements without load due to the stochasticity of the drying process. For this reason the results from the model can be considered reliable.

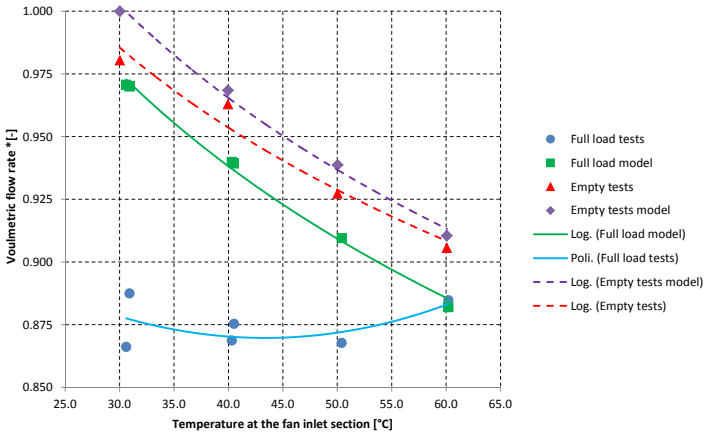

FIGURE 7.10: Aeraulic model validation. * standard conditions for air temperature and pressure (0 ℃ and 1 atm)

7.5 Heat exchanger model

This section shows how the cross flow heat exchanger, installed in this kind of tumble dryer machine, is modeled. The air-to-air plate heat exchanger is the key component of the machine, it has to be able to dehumidify the air coming from the drum. The heat exchanger model is based on a 2D finite volume discretization of the metallic plate. In Figure 7.11 is shown a 2x2 discretization, however the model is able to assume a generic mxn division.

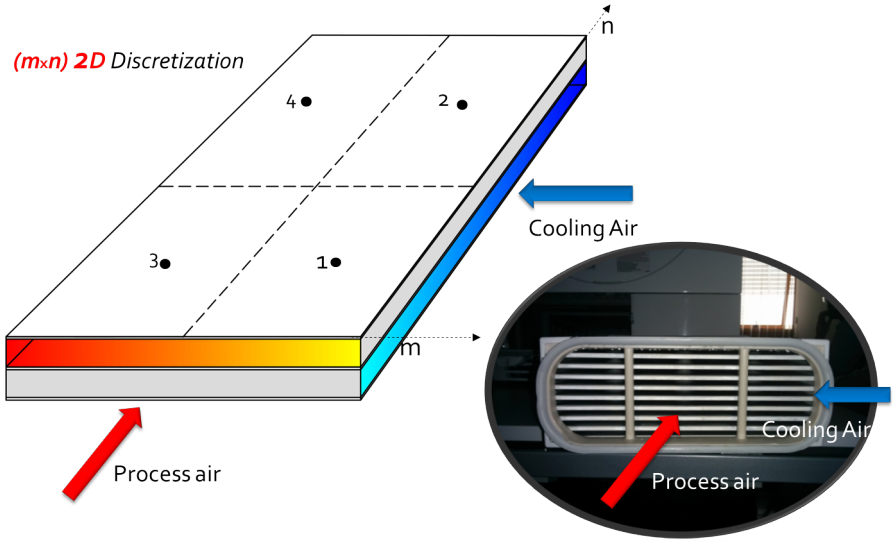

FIGURE 7.11: HX condenser dryer model.

The thermal behavior of the first element is described applying the equation of the energy conservation:

$$\frac{dT_1}{dt} = \frac{q_{hot} - q_{cold} - q_{12}|_{Cond} - q_{13}|_{Cond}}{(m \cdot c_p)_1} \tag{7.4}$$

the conductive heat fluxes may evaluated as:

$$q_{13}|_{Cond} = -\, q_{31}|_{Cond} = \frac{T_1 - T_3}{\frac{d}{S_{trans} \cdot \lambda}} \tag{7.5}$$

$$q_{12}|_{Cond} = -\, q_{21}|_{Cond} = \frac{T_1 - T_2}{\frac{w}{S_{long} \cdot \lambda}} \tag{7.6}$$

Where:

- S_{trans} and S_{long}: are the transversal and longitudinal section of the plate;

- d: is the distance between two central points of the elements along the longitudinal direction;
- w: is the distance between two central points of the elements along the transversal direction;
- λ: is the plate thermal conductivity;
- $(m \cdot c_p)_1$: is the plate capacity.

q_{hot} and q_{cold} will be defined in the next paragraph.

7.5.1 Governing equations air side

The air flow is assumed to be incompressible and unmixed. The air thermal inertia is negligible, and it was neglected. The air temperature profile can be derived analytically from the equations of one-dimensional steady state flow. Considering unmixed flow and uniform air-side heat transfer coefficient along the heat exchanger, the air temperature difference from the inlet to the outlet section for each element is obtained applying P-NTU solution [38]. The following expression may be written for the (i, j) heat exchanger element:

$$T_{a,o}(i,j) = T_w(i,j) + (T_{a,i}(i,j) - T_w(i,j)) \cdot e^{-NTU(i,j)} \tag{7.7}$$

$$NTU(i,j) = \frac{2 \cdot \alpha_s \cdot A_{i,j}}{\dot{m} \cdot \bar{c_p}} \tag{7.8}$$

In the NTU definition the area $A_{i,j}$ is multiply by two since the process air flow stream exchanges with a metallic plates below and above itself. Hence, the heat transfer rate from the air to the wall structure for each element is calculated with the following expression:

$$q(i,j) = \dot{m} \cdot \bar{c_p} \cdot (T_{a,i}(i,j) - T_{a,o}(i,j)) \tag{7.9}$$

With the previous equation can be calculated the hot ($q_{hot} = q(i,j)/2$) and cold ($q_{cold} = q(i,j)/2$) heat fluxes that appear in Equation 7.4. If the air temperature at the element inlet section is less than the dew point temperature, mass transfer phenomena occur on the plate surface. Assuming the humidity air enthalpy as the driving potential for total heat transfer considering the lower value of the potential the air enthalpy in saturation condition at the temperature of the plate $h_{w,s}(i,j)$, therefore:

$$h_{a,o}(i,j) = h_{w,s}(i,j) + (h_{a,i}(i,j) - h_{w,s}(i,j)) \cdot e^{-NTU(i,j)} \tag{7.10}$$

and the outlet specific humidity $x_{a,o}(i,j)$ can be calculated with the relation that links the enthalpy and the specif humidity for a generic section to the values of the enthalpy

and specific humidity at the inlet conditions and the defined values in saturation condition at the plate temperature ($h_{w,s}$ and $x_{w,s}$). Therefore, obtained the outlet enthalpy from Equation 7.10 with the following expression is possible to estimate the specific humidity:

$$x_{a,o}(i,j) = x_{a,i}(i,j) - (h_{a,i}(i,j) - h_{a,o}(i,j)) \cdot \frac{x_{a,i}(i,j) - x_{w,s}}{h_{a,i}(i,j) - h_{w,s}(i,j)} \tag{7.11}$$

and the total heat transfer is calculated with:

$$q(i,j) = \dot{m} \cdot (h_{a,i}(i,j) - h_{a,o}(i,j)) \tag{7.12}$$

Based on the calibration tests for the aeraulic circuit was possible to provide an estimation of the overall thermal conductance of the heat exchanger (KA). The mean heat transfer coefficient was evaluated experimentally as function of the cooling volumetric flow rate and the heat exchanger inlet temperature (process side) (30 and 50 ℃), whereas the air process volumetric flow rate was kept constant. In Figure 7.12 the values are reported. The following expressions were used to determinate the overall thermal conductance:

$$\Delta T_{proc-s} = (T_{a,i,HX} - T_{a,o,HX})_{proc-s} \tag{7.13}$$

$$\Delta T_{cool-s} = (T_{a,o,HX} - T_{a,i,HX})_{cool-s} \tag{7.13a}$$

$$\Delta T_{mean} = F \cdot \frac{\Delta T_{proc-s} - \Delta T_{cool-s}}{\ln \dfrac{\Delta T_{proc-s}}{\Delta T_{cool-s}}} \tag{7.13b}$$

$$q_m = \frac{q_{proc-s} + q_{cool-s}}{2} \tag{7.13c}$$

$$KA = \frac{q_m}{\Delta T_{mean}} \tag{7.13d}$$

Where F is the correction factor and ΔT_{mean} was obtained by applying the correction factor to the value of the log mean temperature difference that is computed under the assumption of counterflow conditions. In addition, the thermal flux is averaged because the two values for process and cooling side did not correspond exactly (due to experimental approximations). Because of the thermal and velocity gradients at the heat exchanger outlet sections, the experimental measurements showed differences on the values of the cold and hot heat fluxes greater than 20% in some tests.

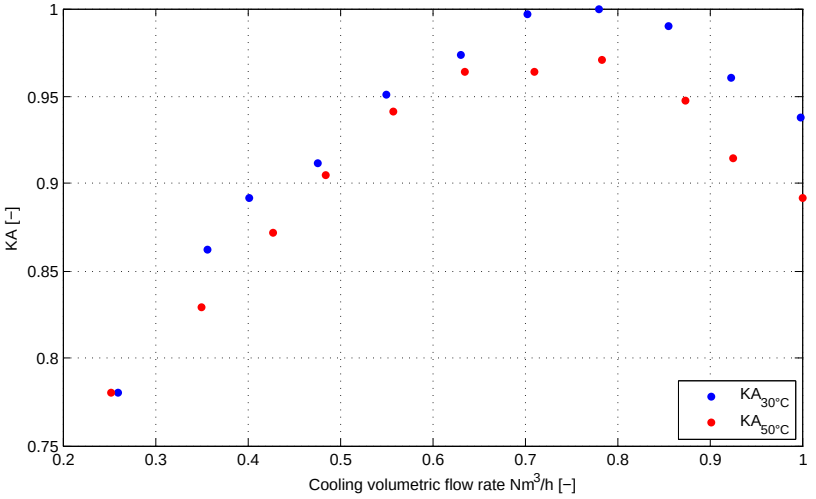

FIGURE 7.12: Heat exchanger overall thermal conductance.

The results were generalized in order to obtain the heat transfer coefficient values. In this heat exchanger geometric configuration, neglecting the conductive resistance, the overall heat transfer coefficient may be expressed as:

$$K = \frac{A_p}{\frac{1}{\alpha_{proc-s}} + \frac{1}{\alpha_{cool-s}}} \tag{7.14}$$

further, between the cooling and the process side heat transfer coefficients may be expressed the following relation:

$$\frac{\alpha_{proc-s}}{\alpha_{cool-s}} = \frac{Nu_{proc-s}}{Nu_{cool-s}} \tag{7.15}$$

$$\alpha_{proc-s} = \frac{Nu_{proc-s}}{Nu_{cool-s}} \cdot \alpha_{cool-s} \tag{7.15a}$$

$$\alpha_{proc-s} = r^{1/3} \cdot \frac{D_{h,proc-s}}{D_{h,cooling\,side}} \cdot \alpha_{cool-s} \tag{7.15b}$$

where r is the ratio between the air velocity inside the process and the cooling channel $r = \frac{v_{ch,proc-s}}{v_{ch,cool-s}}$. Rearranging Equation 7.14 with the definition 7.15b, the heat transfer coefficient inside the cooling channel becomes:

$$\alpha_{cool-s} = \frac{KA \cdot \left(1 + \frac{1}{r^{1/3} \cdot \frac{D_{h,proc-s}}{D_{h,cool-s}}}\right)}{A_p} \tag{7.16}$$

and the $Nu_{cool-s} = \dfrac{\alpha_{cool-s} \cdot D_{h,cool-s}}{\bar{\lambda}_a}$. The Nusselt values as function of the Reynolds numbers are show in Figure 7.13

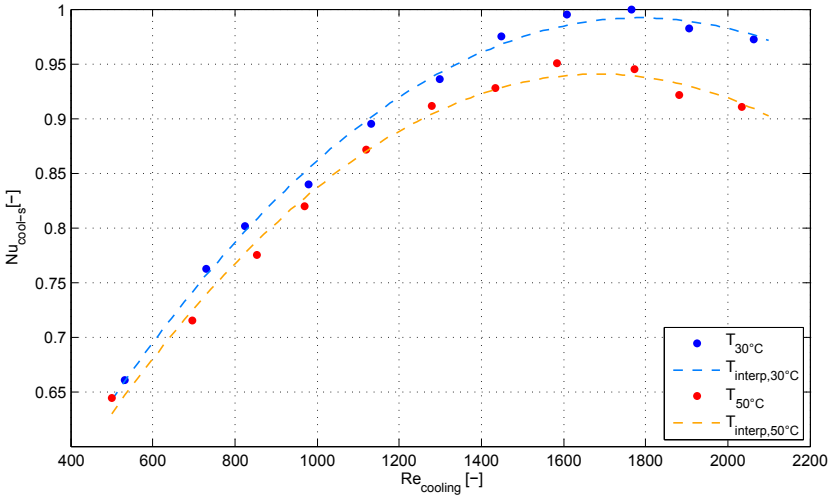

FIGURE 7.13: Nusselt number.

As shown in Figure 7.13 the Reynolds number inside the channel indicates that the flow regime is laminar. In the range 600 to 1400 of the Reynolds number the Nusselt number seems to be function only of the Reynolds number as can be seen in Figure 7.13. The values shown in the chart were correlated in a unique correlation that has the same form of the Sieder and Tate's correlation given in 7.17 [26]. This correlation is able to predict the mean heat transfer coefficient in cases in which the temperature and velocity profiles develop simultaneously for laminar flow.

$$Nu = 1.86 \cdot Re^{1/3} \cdot Pr^{1/3} \cdot \left(\frac{D_h}{L_{HX}}\right) \cdot \left(\frac{\mu}{\mu_p}\right)^{0.14} \tag{7.17}$$

The first constant term of the Sieder and Tate's correlation was changed in order to match the experimental data reported in Figure 7.13. The original form of the Sieder and Tate's correlation presents an exponent equals to 1/3 for the Reynolds number. This justifies the assumption to use the same exponent in Equation 7.15b where the ratio (r) of the air velocities has been introduced.

7.5.2 Heat exchanger model validation

The plots in Figures 7.14 and 7.15 compare the experimental measurements (heat exchanger outlet temperatures were measured) with the model results. The comparison is based on two values of the inlet heat exchanger temperature on the process side (30

and 50 ℃) varying the cooling volumetric flow rate. Both of cases show that the model is able to predict the temperatures at the heat exchanger outlet sections (process and cooling side) with deviations less than 6%.

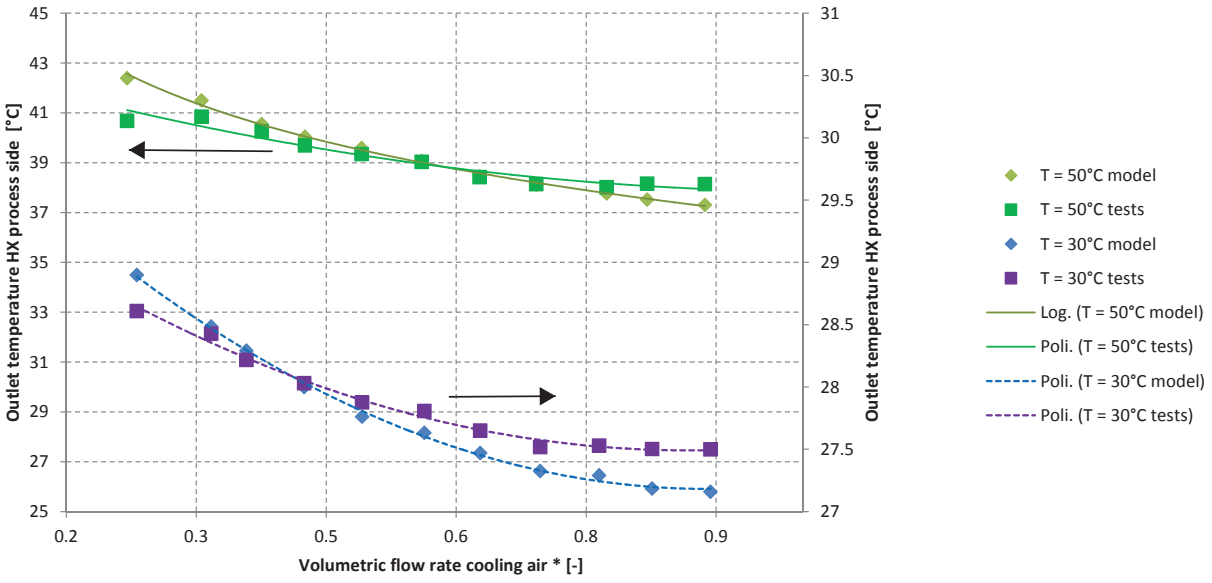

FIGURE 7.14: Comparison between experimental data and model results $T_{a,o,HX,process}$. * standard conditions for air temperature and pressure (0 ℃ and 1 atm)

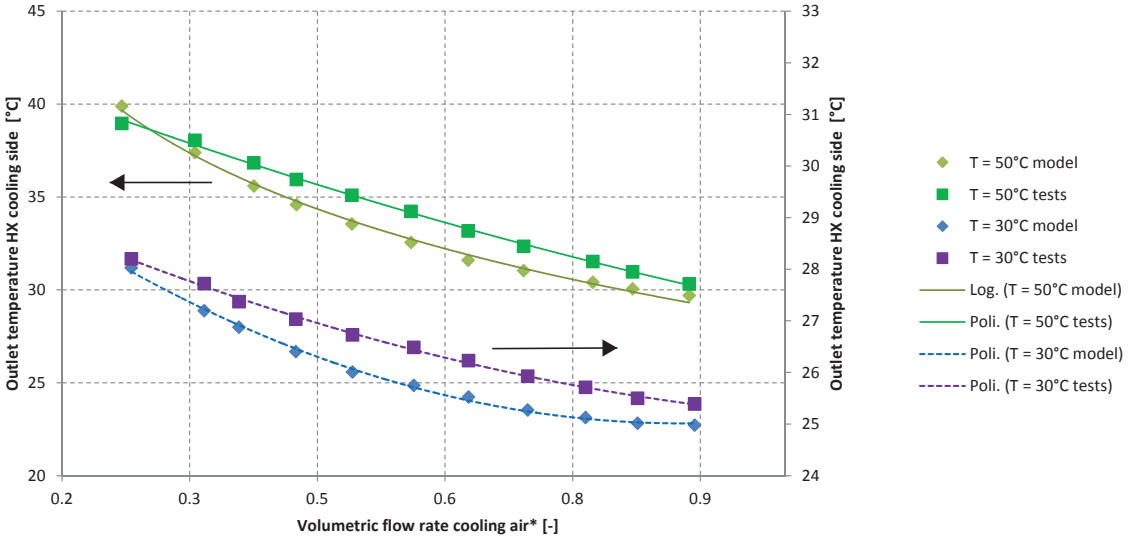

FIGURE 7.15: Comparison between experimental data and model results $T_{a,o,HX,cooling}$. * standard conditions for air temperature and pressure (0 ℃ and 1 atm)

7.6 Model validation and simulation results

This section is devoted to show the performance of simulations of the condenser tumble dryer model. This section will show the results coming from the simulation of the whole drying cycle. The model of the evaporation process from the laundry, discussed in Chapter 4, was added to both the model of the aeraulic circuit, presented earlier, and the air-to-air plate heat exchanger model developed in the previous paragraphs. All the models were connected between each other inside a unique Matlab function, see Figure 7.16. As discussed in the Paragraph 7.3, in order to solve the equation that gives the value of the mass flow rate flowing in the process air circuit the air temperatures must be known. However also to estimate the outlet temperature from each component the value of the mass flow rate should be known, therefore there is a creation of an algebraic loop. To solve the whole system with the minimum computational effort, the aeraulic circuit model is disconnected from the thermal model. This disconnection is made with a memory block that gives at the thermal model the value of the mass flow at the previous time step. This leads to errors on the energetic and mass integrity of the system, nevertheless if the integration time step is reduced the issue is minimized.

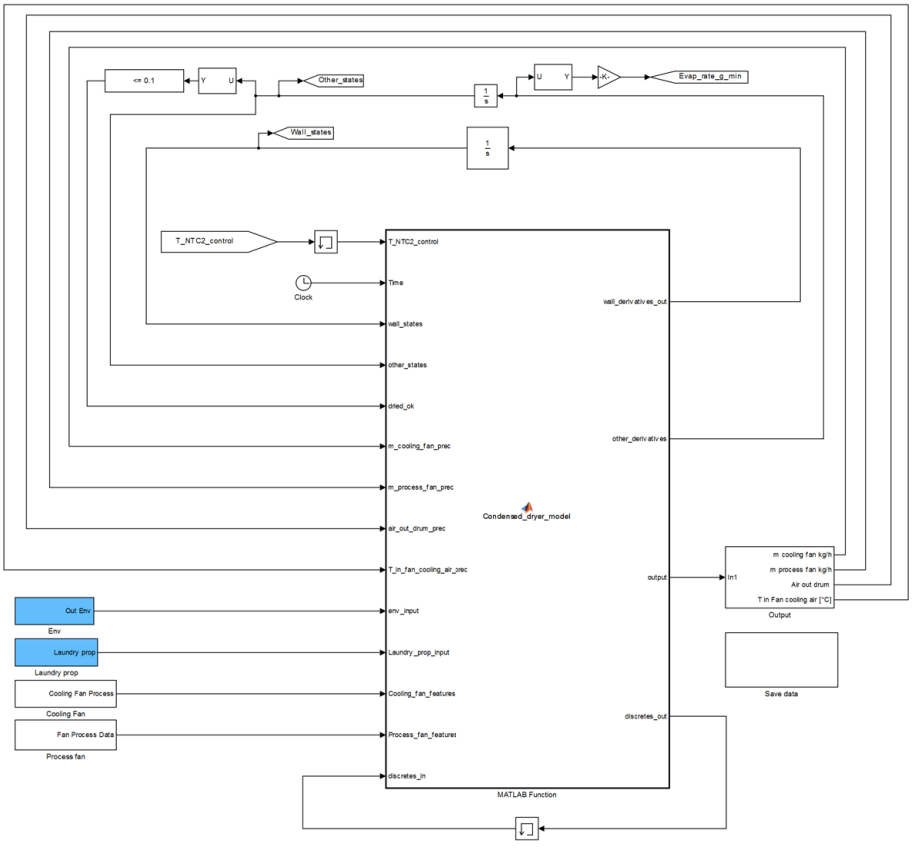

FIGURE 7.16: Condenser tumble dryer Simulink model.

Figure 7.17 compares the difference between the experimental data acquired along a complete drying cycle and the simulated results. The model efficiently predicts the drum and the heat exchanger outlet temperatures. Notice how the heat exchanger outlet temperature is near to the inlet temperature, as occurred in the real cycle. Only in the third phase of the cycle, where the drying process is almost completed (and specific humidity on the air circuit decreases) this difference becomes greater.

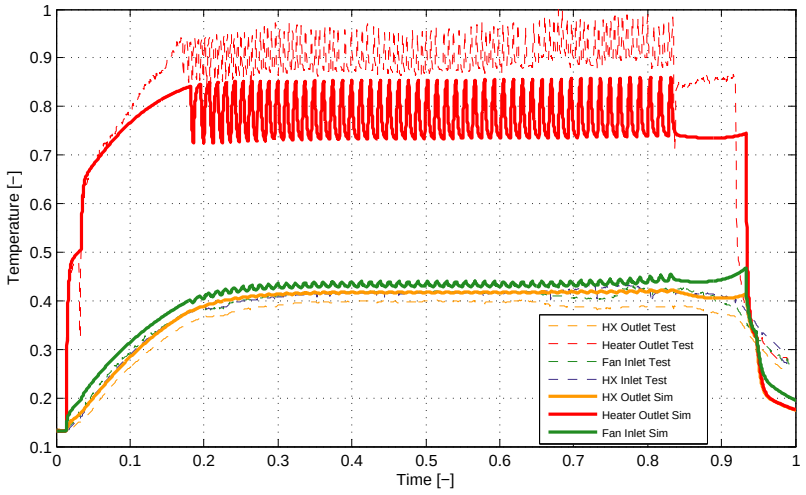

FIGURE 7.17: Comparison between experimental data and model results: air temperatures process side.

Figure 7.18 shows how the relative humidities vary during the drying cycle (the relative humidity measurement is an issue for this kind of tumble dryer since the air is always in saturation conditions). The highest values are reached by the heat exchanger outlet relative humidity with values near to 100%, the lowest values are achieved by the drum inlet relative humidity due to high air temperature value (above 140 ℃). When the electric resistance is shut down in the last phase, for a short period, all the relative humidities reach value near to 100% (temperatures of the aeraulic circuit decrease faster than the specific humidity) and then decrease to a value near to the ambient relative humidity (place where the device is installed).

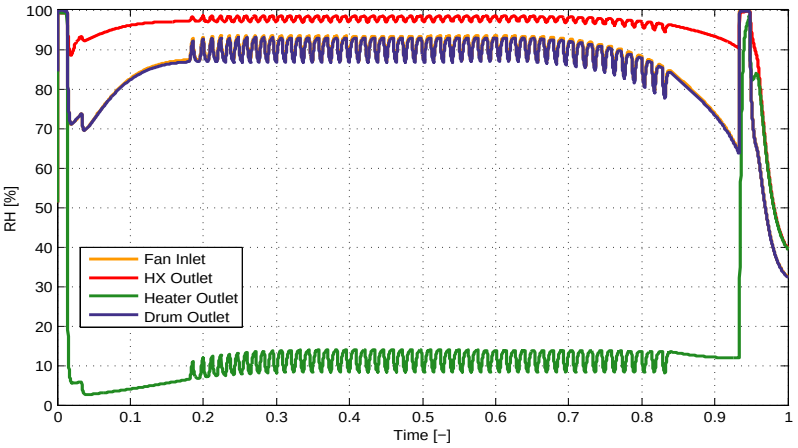

FIGURE 7.18: Process side relative humidities.

Finally, the Figure 7.19 shows how the mass flow rate drawn by the process fan and the mass flow rate blown by the cooling fan vary along the drying cycle. After the device is activated, the mass flow rate drawn by the process fan decreases sharply due to the increment of the fan inlet temperature. The fan pressure rise decreases if the temperature at the its inlet section rises. Along the stationarity phase (where the drum inlet temperature is controlled by a suitable control algorithm) the process mass flow rate remains stable (pressure drop of the laundry does not change significantly due to low air velocity inside the drum). In the cool-down phase the mass flow rates rises rapidly (the fan inlet temperature decreases quickly). The mass flow rate drawn by the cooling fan (purple solid line in the chart) decreases slightly due to the dependency of the heat exchanger crossing mean temperature on the pressure drop correlation (cooling side).

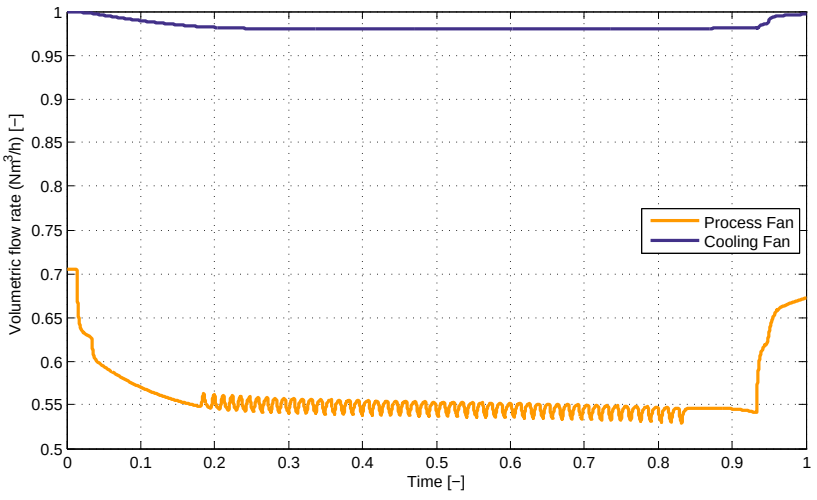

FIGURE 7.19: Condenser tumble dryer mass flow rates.

Chapter 8

Conclusions

8.1 Summary of the dissertation

This dissertation focuses on the dynamic modeling and experimental analysis of different platform of domestic tumble dryers. Three tumble dryer devices were analyzed experimentally and modeled. First, the heat pump tumble dryer was modeled together with the drum and a theoretical model of the drying process, drawn up from energy and mass considerations, was proposed. The model of the drying process is the key element for every platform of tumble dryers and it allowed to develop other two dynamic models: an air vented tumble dryer model and a condenser tumble dryer model. All the proposed models were validated and improved progressively with experimental data.

8.1.1 Dynamic modeling of a heat pump tumble dryer

The model of the heat pump tumble dryer was the most challenging one. First a dynamic model of the vapor compression cycle (VCC) was developed, modeling each components: heat exchangers, capillary tube and compressor. The heat exchanger components were derived using the moving-boundary lumped-parameter modeling approach, and developed with multiple model representations to accommodate the refrigerant phase changes occurring during the drying cycle. As the cycle is strictly non-linear and has dynamic features, the heat pump model needs to describe these dynamics and in order to properly predict the performance of the device it has to change its representation during the phases of the cycle. Therefore, from the VCC modeling methods suggested in the open literature the one most close to achieve these goals is known as the moving boundary, lumped parameter approach and therefore it was chosen. The presented model, if compared to the models available in literature, shows some original features: first an

original choice of the state variables that guarantee mass integrity of the whole model, second the introduction of the pressure drop at the heat exchangers in a static way, in order to reduce the heat exchange between the refrigerant and the air stream without introducing the momentum equation. The evaporator and the condenser models were experimentally validated showing differences from the experimental measurements lower of 5%.

The performance of the capillary tube was evaluated experimentally and the correlation available in literature that better matches the measurements was chosen. Although the analytic correlation chosen shows differences of 15% on the prediction of the measurements, it was preferred to other correlations since it can be generalized and used for different refrigerant fluids.

The compressor model was described dynamically since its capacity affects both the initial transient of the drying cycle and the transient associated to the compressor cooling fan activation (this fan is used for avoiding compressor outlet envelope working conditions). The compressor dynamic behaviour is modeled using two thermal capacities: the first represents the internal body of the compressor (rotor, stator, etc) and the second is the compressor shell, which capacity strongly affects the above described dynamics. The mass flow rate and the compressor power input are described with static relations using the definitions of isentropic and volumetric efficiency, since it is proved that they are not sensitive to the cooling fan activation. The compressor model was validated experimentally with some tests on the calorimetric rig, the result indicates that the simulated results are in agreement with measurements although large deviation can be observed in the first minuets of the cycle due to the low reliability of the efficiencies correlations outside their regression domain.

The aeraulic circuit of the heat pump tumble dryer was experimentally analyzed and modeled. As the mass flow rate affects strongly the performances of the heat pump, the process air circuit was modeled in order to catch two key factors. First, the mass flow rate leakage from the drum, which value determines the thermal load on the evaporator, and hence the performance of the heat pump globally. Second the decrementing of the mass flow rate because of the filter clogging effect due to the production of lint from the laundry. A static model was developed using the electric analogy, since the thermal and mass inertia of the air can be neglected. Every component of the air circuit was characterized experimentally with specific tests for which it was necessary to develop a suitable test rig. The experimental results allowed to develop suitable correlations for the air pressure drop (and pressure raise for the fan) for each component, in this way, in the model, the static pressure balance gives the mass flow rate drawn by the fan and the mass flow rate leakage. Also in this case the whole aeraulic model was validated

using experimental measurements as input data and comparing the results with the other measurements. The comparison shows that the model is in agreement with the experimental data, although the last phase of the cycle is not perfectly described.

A theoretical model of the drying process was built basing on the energy and mass balances. In order to develop the model of the evaporation process some experimental tests were carried out. The analysis allowed to understand the paramount phenomena governing the process. The system laundry-moisture content was divided into two zones: a dry and a wet zone. The extension of the wet zone changes with the load water content of the laundry and an experimental correlation that explains this behaviour was developed using the heat and mass transfer analogy (based on the Lewis number). The correlation, that expresses the ratio between the mass and the heat transfer area, shows a value equal to one until a value of 40% of LWC (load water content) that is recognized as the starting point for the drying zone formation. In addition to the model a correlation is presented, that explains the overall heat transfer coefficient between the air and the laundry. The model was validated through a series of drying tests. The results, comparing the drying cycle time, show deviances lower than 5% (except for a cycle). The presented model has characteristic of originality since any similar model can be found in the open literature.

The merge between the three main parts (heat pump module, aeraulic circuit and laundry-drum) discussed earlier led a complete heat pump tumble dryer model development. The whole model was validated through the comparison between real drying tests. The model shows a great sensitivity to the refrigerant charge and this led to some issues during the tunning procedure. Nevertheless if the degree of superheat and subcooling is matched with the actual values, the model predicts the drying cycle time and the energy consumption with an accuracy lower than 10%. In addition, in some test cases the model showed its capabilities to predict the system performance when the parameters that characterize it vary drastically (compressor displacement, number of fins in the heat exchanger). Therefore, the model can be used as a useful tool to design new heat pump tumble dryers. A final remark is to emphasize that the proposed model represents the first heat pump tumble dryer model with heat exchanger modeled, according to the moving boundary approach, available in literature.

8.1.2 Dynamic modeling of an air vented tumble dryer

The modeling effort on this dryer platform was focused on the understanding of the fluid-dynamic aspects that govern its behaviour. Due to high dimensional and geometric tolerances of its components the total mass flow rate drawn by the fan does not match

the mass flow rate that is heated from the heating element. Experimental measurements showed the presence of two leakage sources where the air can enter into the system: the first is caused by the gap occurring during the drum spin motion between the front and rear gaskets and the front and rear drum flange. This leads to enter an amount of mass flow rate estimated near to 45% of the total mass flow rate. The second source is located at the back flange of the drum due to two reasons: first, three holes on the top of the front panel (used for fire containment) and second, gap in the junction region between the rear drum flange and the back panel. This leads an amount of mass flow rate estimated near to 15% of the total mass flow rate to enter these spaces. As a result, only 40% of the total mass flow rate flows through the heating element. The capabilities of the developed model are able to catch these phenomena designing different aeraulic paths. Great efforts were made in order to develop lumped correlations (derived from experimental measurements) summarizing pressure drop variation for each component of the aeraulic circuit.

The thermal model is focused to describe, in lumped way, the mean temperature of each component that exchanges between them through convective and radiative heat fluxes. The model of the drying process was modified in order to account for the energy losses through the drum since the air temperature at the drum inlet are higher (120-130 ℃) than the heat pump dryer (max 70 ℃). In the model the heat loss is evaluated as proportional to the difference of the mean value of the air temperature crossing the drum and the mean drum temperature.

The comparison with experimental data shows that the simulated results are in excellent agreement with measurements. Both the drying time and energy consumption are predicted correctly. The prediction of the mass flow rate split, between the three main aeraulic circuits, shows small differences in case of aeraulic circuit with discharge cone. Nevertheless, using the same parameters, not negligible differences can be observed when the cone is removed.

8.1.3 Dynamic modeling of a condenser tumble dryer

This kind of tumble dryer can be viewed as an extension of the air vented tumble dryer where the air leaving the drum is recirculated back. Before crossing the heater, the air stream is cooled and dehumidified by an air-to-air heat exchanger with cross flow arrangement. Therefore, in addition to the models developed for the air vented tumble dryer, also a lumped heat exchanger model was developed. The development of the model started from the experimental analysis of the aeraulic circuit that led to develop the empirical correlations for each component both on the cooling and process side.

The comparison with the experimental data shows that the model is able to predict remarkably well (differences lower than 2%) the mass flow rate drawn by the process fan in cases without laundry load, although noticeable differences can be observed in presence of load because of the experimental values are independent from the fan inlet temperature. As the mass flow rate drawn by the process fan must be proportional to the air stream density, the experimental trend was assumed not to be reliable.

The heat exchanger model is based on a 2D finite volume discretization of the metallic plate which properties are considered as lumped. The heat exchanger is characterized by a fast dynamic behavior (since the aluminum plate thickness is lower than 0.2 mm), therefore its dynamic description may be neglected. However, from a numerically point of view, the dynamic approach is useful for reducing the complexity of the numerical problem that has to be solved for a complete description of the heat exchanger. The mean heat transfer coefficient was evaluated experimentally and a correlation expressed in Nusselt number was proposed. In case of mass transfer, the humidity air enthalpy was assumed as the driving potential for total heat transfer. The outlet temperature prediction both for the cooling and process side was checked through experimental data. The greatest difference is lower than 6% and therefore the model can be considered validated.

Furthermore, the model capabilities were checked testing the whole drying cycle against experimental data. First attempts showed noticeable differences on the drying time prediction that can be explained considering the different shape of the rear drum flange compared to the one installed in the heat pump device and the reduced number of the passage holes. This produces a non-uniform distribution of the air inside the drum, that reduces the active portion of the mass flow rate involved in heat and mass transfer exchanges with the laundry load.

8.2 Future work

This work is a staring point for using the developed models to investigate the influence of some parameters on the drying time and energy consumption performance of tumble dryers. Furthermore, many different control strategies can be tested on the models before being implemented on experimental prototype.

8.2.1 VCC model

In order to increase the model reliability and robustness some of the state variables used for describing the heat exchangers could be reconsidered in future works. The goal is

to avoid the inclusion of time derivative terms in the boundary condition vector. These term amplify the signal noise and reduce the reliability and numerical robustness during transient phases. The most promising hypothesis is to substitute the density variable with void fraction. This would also allow to test different void fraction correlations without introducing additional derivative terms.

8.2.2 Drum model

The developed model of the drying process considers only the cotton fabrics. In order to expand the proposed correlations some other fabrics should be tested (wool and other highly porous fabrics, nylon and synthetic fabrics). The drum heat transfer phenomenological correlation should be adjusted accordingly.

Appendix A

Full derivation of the SH-TP-L model

Conservation of refrigerant mass along the superheated region:

the differential equation of the conservation of refrigerant mass must be integrated along the superheated region:

$$\int_0^{L_1(t)} \left[A \cdot \frac{\partial \rho_1}{\partial t} + \frac{\partial \dot{m}}{\partial z} \right] \cdot dz = 0 \tag{A.1}$$

applying the Leibniz's rule for the first term and the fundamental theorem of calculus for the second term, the previous becomes:

$$A \cdot \left[\frac{d}{dt} \int_0^{L_1(t)} \rho_1 \cdot dz - \rho_1(t, z = L_1) \cdot \frac{dL_1}{dt} \right] = \dot{m}_i - \dot{m}_{int-1} \tag{A.2}$$

the term $\rho_1(t, z = L_1)$ could be considered equal to the dry vapor density $\rho_v(p(t))$, additionally $\dot{m}_{int-1}$ is the refrigerant mass flow rate at the boundary between SH and TP zone. Assuming the hypothesis of lumped parameter (ρ_1 is the mean density):

$$A \cdot \left[\frac{d(L_1 \rho_1)}{dt} - \rho_v \cdot \frac{dL_1}{dt} \right] = \dot{m}_i - \dot{m}_{int-1} \tag{A.3}$$

$$A \cdot \left[L_1 \cdot \frac{d\rho_1}{dt} + (\rho_1 - \rho_v) \cdot \frac{dL_1}{dt} \right] = \dot{m}_i - \dot{m}_{int-1} \tag{A.4}$$

the mean density of the superheated zone is function of the pressure, p, and the inlet enthalpy, h_i, since for the monophase refrigerant state is assumed a linear profile ($h_1 = \frac{h_i + h_v}{2}$), therefore the ρ_1 derivative can be obtained through the application of the

chain rule:

$$\frac{d\rho_1}{dt} = \left.\frac{\partial \rho_1}{\partial p}\right|_{h_i} \cdot \frac{dp}{dt} + \left.\frac{\partial \rho_1}{\partial h_i}\right|_{p} \cdot \frac{dh_i}{dt} \tag{A.5}$$

with this definition, rearranging Equation A.4:

$$A \cdot \left[L_1 \cdot \left[\left.\frac{\partial \rho_1}{\partial p}\right|_{h_i} \cdot \frac{dp}{dt} + \left.\frac{\partial \rho_1}{\partial h_i}\right|_{p} \cdot \frac{dh_i}{dt} \right] + (\rho_1 - \rho_v) \cdot \frac{dL_1}{dt} \right] = \dot{m}_i - \dot{m}_{int-1} \tag{A.6}$$

the final form becomes:

$$A \cdot L_1 \cdot \left.\frac{\partial \rho_1}{\partial p}\right|_{h_i} \cdot \frac{dp}{dt} + A \cdot (\rho_1 - \rho_v) \cdot \frac{dL_1}{dt} + \dot{m}_{int-1} = \dot{m}_i - A \cdot \left.\frac{\partial \rho_1}{\partial h_i}\right|_{p} \cdot \frac{dh_i}{dt} \tag{A.7}$$

Conservation of refrigerant energy on the superheated region:

$$\int_0^{L_1(t)} \left[A \cdot \frac{\partial(\rho h)}{\partial t} - A \cdot \frac{\partial p}{\partial t} + \frac{\partial(\dot{m} h)}{\partial z} \right] \cdot dz = \int_0^{L_1(t)} \left[\pi \cdot D_i \cdot \alpha_r \cdot (T_{w1} - T_{r1}) \right] \cdot dz \tag{A.8}$$

assuming the hypothesis of lumped parameters and applying the fundamental theorem of calculus, the equation becomes:

$$A \cdot \int_0^{L_1(t)} \frac{\partial(\rho h)}{\partial t} \cdot dz - A \int_0^{L_1(t)} \frac{\partial p}{\partial t} \cdot dz + \dot{m}_{int-1} \cdot h_v - \dot{m}_i \cdot h_i = \pi \cdot D_i \cdot L_1 \cdot \alpha_r \cdot (T_{w1} - T_{r1}) \tag{A.9}$$

applying the Leibniz's rule at the first term:

$$A \cdot \int_0^{L_1(t)} \frac{\partial(\rho h)}{\partial t} \cdot dz = A \cdot \frac{d}{dt} \cdot \int_0^{L_1(t)} \rho h \cdot dz - (\rho h)_v \cdot \frac{dL_1}{dt} \tag{A.10}$$

$$= A \cdot L_1 \cdot \frac{d(\rho h)_1}{dt} + A \cdot (\rho h)_1 \cdot \frac{dL_1}{dt} - A \cdot (\rho h)_v \cdot \frac{dL_1}{dt} \tag{A.11}$$

$$= A \cdot L_1 \cdot \frac{d(\rho h)_1}{dt} + A \cdot [(\rho h)_1 - (\rho h)_v] \cdot \frac{dL_1}{dt} \tag{A.12}$$

applying the Leibniz's rule at the second term:

$$A \int_0^{L_1(t)} \frac{\partial p}{\partial t} \cdot dz = A \cdot \frac{d}{dt} \int_0^{L_1(t)} p \cdot dz - p \cdot A \cdot \frac{dL_1}{dt} \tag{A.13}$$

$$= A \cdot \frac{dp}{dt} \cdot L_1 + A \cdot p \cdot \frac{dL_1}{dt} - A \cdot p \cdot \frac{dL_1}{dt} \tag{A.14}$$

$$= A \cdot L_1 \cdot \frac{dp}{dt} \tag{A.15}$$

reassembling Equation A.9, it becomes:

$$\begin{aligned} &A \cdot L_1 \cdot \frac{d(\rho h)_1}{dt} + A \cdot [(\rho h)_1 - (\rho h)_v] \cdot \frac{dL_1}{dt} + A \cdot L_1 \cdot \frac{dp}{dt} + \dot{m}_{int-1} \cdot h_v - \dot{m}_i \cdot h_i \\ &= \pi \cdot D_i \cdot L_1 \cdot \alpha_r \cdot (T_{w1} - T_{r1}) \end{aligned} \tag{A.16}$$

noting that $(\rho h)_1 = (\rho h)_1(p, h_i)$, therefore:

$$\frac{d(\rho h)_1}{dt} = \left.\frac{\partial(\rho h)_1}{\partial p}\right|_{h_i} \cdot \frac{dp}{dt} + \left.\frac{\partial(\rho h)_1}{\partial h_i}\right|_{p} \cdot \frac{dh_i}{dt} \tag{A.17}$$

substituting this term in A.16, it becomes:

$$\begin{aligned} &A \cdot L_1 \cdot \left[\left.\frac{\partial(\rho h)_1}{\partial p}\right|_{h_i} - 1 \right] \cdot \frac{dp}{dt} + A \cdot [(\rho h)_1 - (\rho h)_v] \cdot \frac{dL_1}{dt} + \dot{m}_{int-1} \cdot h_v = \\ &= \dot{m}_i \cdot h_i + \pi \cdot D_i \cdot L_1 \cdot \alpha_r \cdot (T_{w1} - T_{r1}) - A \cdot L_1 \cdot \left.\frac{\partial(\rho h)_1}{\partial h_i}\right|_{p} \cdot \frac{dh_i}{dt} \end{aligned} \tag{A.18}$$

Conservation of refrigerant mass along the two-phase region: following the same method discussed for the superheated region, integrating the differential equation on the two phase-zone with the assumption of lumped parameter:

$$\int_{L_1(t)}^{L_1(t)+L_2(t)} A \cdot \frac{\partial \rho_2}{\partial t} \cdot dz = \dot{m}_{int-1} - \dot{m}_{int-2} \tag{A.19}$$

applying the Leibniz's rule at the term on the left side:

$$\begin{aligned} &\int_{L_1(t)}^{L_1(t)+L_2(t)} A \cdot \frac{\partial \rho_2}{\partial t} \cdot dz = A \cdot \left[\frac{d}{dt} \int_{L_1(t)}^{L_1(t)+L_2(t)} \rho \cdot dz + \rho(t, z = L_1(t)) \cdot \frac{dL_1}{dt} - \right. \\ &\left. - \rho(t, z = L_1(t) + L_2(t)) \cdot \left(\frac{dL_1}{dt} + \frac{dL_2}{dt} \right) \right] \end{aligned} \tag{A.20}$$

$$\int_{L_1(t)}^{L_1(t)+L_2(t)} A \cdot \frac{\partial \rho_2}{\partial t} \cdot dz = A \cdot (\rho_2 - \rho_l) \cdot \frac{dL_2}{dt} + A \cdot (\rho_v - \rho_l) \cdot \frac{dL_1}{dt} + A \cdot L_2 \cdot \frac{d\rho_2}{dp} \cdot \frac{dp}{dt} \tag{A.21}$$

in the previous equation some assumptions are made: $\rho(t, z = L_1(t)) = \rho_v$, $\rho(t, z = L_1(t) + L_2(t)) = \rho_l$ and since the Zivi's formulation is depended only by the refrigerant pressure (in this condenser mode the inlet quality is equal to one and the outlet is equal to zero) then also the mean density of the two-phase zone is function only the pressure $\rho_2 = \rho_2(p)$. The final form of the equation of mass conservation for the two-phase zone is:

$$A \cdot L_2 \cdot \frac{d\rho_2}{dp} \cdot \frac{dp}{dt} + A \cdot (\rho_v - \rho_l) \cdot \frac{dL_1}{dt} + A \cdot (\rho_2 - \rho_l) \cdot \frac{dL_2}{dt} - \dot{m}_{int-1} + \dot{m}_{int-2} = 0 \tag{A.22}$$

Conservation of refrigerant energy on the two-phase region:

starting from the differential equation and integrating the term dependent by the pressure:

$$A \cdot \int_{L_1(t)}^{L_1(t)+L_2(t)} \frac{\partial(\rho h)}{\partial t} \cdot dz - A \cdot L_2 \cdot \frac{dp}{dt} + \dot{m}_{int-2} \cdot h_l - \dot{m}_{int-1} \cdot h_v = \pi \cdot D_i \cdot L_2 \cdot \alpha_r \cdot (T_{w2} - T_{r2}) \tag{A.23}$$

applying the Leibniz's rule at the first term:

$$A \cdot \int_{L_1(t)}^{L_1(t)+L_2(t)} \frac{\partial(\rho h)}{\partial t} \cdot dz = A \cdot \left[\frac{d}{dt} \int_{L_1(t)}^{L_1(t)+L_2(t)} (\rho h) \cdot dz + (\rho h)_v \cdot \frac{dL_1}{dt} - (\rho h)_l \cdot \left(\frac{dL_1}{dt} + \frac{dL_2}{dt} \right) \right] \tag{A.24}$$

$$A \cdot \int_{L_1(t)}^{L_1(t)+L_2(t)} \frac{\partial(\rho h)}{\partial t} \cdot dz = A \cdot \left[L_2 \cdot \frac{d(\rho h)_2}{dt} + (\rho h)_2 \cdot \frac{dL_2}{dt} + (\rho h)_v \cdot \frac{dL_1}{dt} - (\rho h)_l \cdot \left(\frac{dL_1}{dt} + \frac{dL_2}{dt} \right) \right] \tag{A.25}$$

the term $d(\rho h)_2/dt$ is dependent only by the refrigerant pressure as discussed earlier:

$$\frac{d(\rho h)_2}{dt} = \frac{d(\rho h)_2}{dp} \cdot \frac{dp}{dt} \tag{A.26}$$

substituting the previous definitions, the final form of the equation of energy conservation is:

$$A \cdot L_2 \cdot \left[\frac{d(\rho h)_2}{dp} - 1 \right] \cdot \frac{dp}{dt} + A \cdot [(\rho h)_v - (\rho h)_l] \cdot \frac{dL_1}{dt} + A \cdot [(\rho h)_2 - (\rho h)_l] \cdot \frac{dL_2}{dt} + \\ + \dot{m}_{int-2} \cdot h_l - \dot{m}_{int-1} \cdot h_v = \pi \cdot D_i \cdot L_2 \cdot \alpha_r \cdot (T_{w2} - T_{r2}) \tag{A.27}$$

Conservation of refrigerant mass along the subcooled zone:

on the same assumptions already done, integrating the differential equation of mass integrity on the subcooled zone, the final expression becomes:

$$A \cdot L_3 \cdot \frac{d\rho_3}{dt} + A \cdot (\rho_l - \rho_3) \cdot \frac{dL_1}{dt} + A \cdot (\rho_l - \rho_3) \cdot \frac{dL_2}{dt} - \dot{m}_{int-2} = \dot{m}_o \tag{A.28}$$

Conservation of refrigerant energy along the subcooled region:

also for the differential equation of the refrigerant energy conservation applying two times the Leibniz's rule assuming the lumped hypothesis, the energy equation becomes:

$$\begin{aligned} &A \cdot \left[((\rho h)_l - (\rho h)_3) \cdot \frac{dL_2}{dt} + L_3 \cdot \frac{d(\rho h)_3}{dt} \right] + A \cdot L_3 \cdot \frac{dp}{dt} - \dot{m}_{int-2} \cdot h_l = \\ &- \dot{m}_o \cdot h_o + \pi \cdot D_i \cdot L_3 \cdot \alpha_r \cdot (T_{w3} - T_{r3}) \end{aligned} \tag{A.29}$$

noting that $h_3 = h(p, \rho_3)$ then the term $\dfrac{d(\rho h)_3}{dt}$ could be expressed as:

$$\frac{d(\rho h)_3}{dt} = \rho_3 \cdot \frac{dh_3}{dt} + h_3 \cdot \frac{d\rho_3}{dt} \tag{A.30}$$

$$= \rho_3 \cdot \left[\left. \frac{\partial h_3}{\partial p} \right|_{\rho_3} \cdot \frac{dp}{dt} + \left. \frac{\partial h_3}{\partial \rho_3} \right|_{p} \cdot \frac{d\rho_3}{dt} \right] + h_3 \cdot \frac{d\rho_3}{dt} \tag{A.31}$$

substituting in A.29 and rearranging:

$$\begin{aligned} &A \cdot L_3 \cdot \left[\rho_3 \left. \frac{\partial h_3}{\partial p} \right|_{\rho_3} - 1 \right] \cdot \frac{dp}{dt} + A \cdot L_3 \left[\rho_3 \cdot \left. \frac{\partial h_3}{\partial \rho_3} \right|_{p} + h_3 \right] \cdot \frac{d\rho_3}{dt} + \\ &+ A \cdot [(\rho h)_l - (\rho h)_3] \cdot \frac{dL_1}{dt} + A \cdot [(\rho h)_l - (\rho h)_3] \cdot \frac{dL_2}{dt} - \dot{m}_{int-2} \cdot h_l = \\ &= -\dot{m}_o \cdot h_o + \pi \cdot D_i \cdot L_3 \cdot \alpha_r \cdot (T_{w3} - T_{r3}) \end{aligned} \tag{A.32}$$

The algebraic system is constituted from Equations: A.7, A.18, A.22, A.27, A.28 and A.32. The complete system results as:

$$\begin{vmatrix} M11 & 0 & M13 & 0 & M15 & 0 \\ M21 & 0 & M23 & 0 & M25 & 0 \\ M31 & 0 & M33 & M34 & M35 & M36 \\ M41 & 0 & M43 & M44 & M45 & M46 \\ 0 & M52 & M53 & M54 & 0 & M56 \\ M61 & M62 & M63 & M64 & 0 & M66 \end{vmatrix} \cdot \begin{vmatrix} dp/dt \\ d\rho_3/dt \\ dL_1/dt \\ dL_2/dt \\ \dot{m}_{int-1} \\ \dot{m}_{int-2} \end{vmatrix} = \begin{vmatrix} N1 \\ N2 \\ N3 \\ N4 \\ N5 \\ N6 \end{vmatrix}$$

where:

$$M11 = A \cdot L_1 \cdot \left. \frac{\partial \rho_1}{\partial p} \right|_{h_i}$$

$$M13 = A \cdot (\rho_1 - \rho_v)$$

$$M15 = 1$$

$$M21 = \left[\left. \frac{\partial (\rho h)_1}{\partial p} \right|_{h_i} - 1 \right]$$

$$M23 = A \cdot [(\rho h)_1 - (\rho h)_v]$$

$$M25 = h_v$$

$$M31 = A \cdot L_2 \cdot \frac{d\rho_2}{dp}$$

$$M33 = A \cdot (\rho_l - \rho_v)$$

$$M34 = A \cdot (\rho_2 - \rho_l)$$

$$M35 = -1$$

$$M36 = 1$$

$$M41 = A \cdot L_2 \cdot \left[\frac{d(\rho h)_2}{dp} - 1\right]$$

$$M43 = A \cdot [(\rho h)_v - (\rho h)_l]$$

$$M44 = A \cdot [(\rho h)_2 - (\rho h)_l]$$

$$M45 = -h_v$$

$$M46 = h_l$$

$$M52 = A \cdot L_3$$

$$M53 = A \cdot (\rho_l - \rho_3)$$

$$M54 = A \cdot (\rho_l - \rho_3)$$

$$M56 = -1$$

$$M61 = A \cdot L_3 \cdot \left[\rho_3 \left.\frac{\partial h_3}{\partial p}\right|_{\rho_3} - 1\right]$$

$$M62 = A \cdot L_3 \left[\rho_3 \cdot \left.\frac{\partial h_3}{\partial \rho_3}\right|_{p} + h_3\right]$$

$$M63 = A \cdot [(\rho h)_l - (\rho h)_3]$$

$$M64 = A \cdot [(\rho h)_l - (\rho h)_3]$$

$$M66 = -h_l$$

and note term:

$$N1 = \dot{m}_i - A \cdot L_1 \cdot \left.\frac{\partial \rho_1}{dh_i}\right|_{p} \cdot \frac{dh_i}{dt}$$

$$N2 = \dot{m}_i \cdot h_i + q_{r,1} - A \cdot L_1 \cdot \left.\frac{\partial (\rho h)_1}{\partial h_i}\right|_{p} \cdot \frac{dh_i}{dt}$$

$$N3 = 0$$

$$N4 = q_{r,2}$$

$$N5 = -\dot{m}_o$$

$$N6 = -\dot{m}_o \cdot h_o + q_{r,3}$$

A.0.3 Partial derivative coefficients

$$\left.\frac{\partial \rho_1}{\partial p}\right|_{h_i} = \frac{\rho_1(p, h_1) - \rho_1(p + dp, h_1(dp))}{dp}$$

where:

$$h_1(dp) = \frac{h_i + h_v(p + dp)}{2}$$

$$\left.\frac{\partial \rho_1}{dh_i}\right|_{p} = \frac{\rho_1(p, h_1) - \rho_1(p, h_1(dh))}{dh}$$

where:

$$h_1(dh) = \frac{h_i + dh + h_v}{2}$$

$$\left.\frac{\partial (\rho h)_1}{\partial p}\right|_{h_i} = \frac{\rho_1(p + dp, h_1(dp)) \cdot h_1(dp) - \rho_1 \cdot h_1}{dp}$$

$$\left.\frac{\partial (\rho h)_1}{\partial h_i}\right|_{p} = \frac{\rho_1(p, h_1(dh)) \cdot h_1(dh) - \rho_1 \cdot h_1}{dh}$$

$$\frac{d(\rho h)_2}{dp} = \frac{\rho_2(p + dp) - \rho_2}{dp}$$

where:

$$\rho_2(p + dp) = \rho_v(p + dp) \cdot \bar{\gamma}(p + dp) + \rho_l(p + dp) \cdot (1 - \bar{\gamma}(p + dp))$$

and

$$\bar{\gamma}(p + dp) = \bar{\gamma}(\rho_g(p + dp), \rho_l(p + dp), x_o = 0, x_i = 1) \quad \text{Zivi's void fraction mean}$$

$$\left.\frac{\partial h_3}{\partial p}\right|_{\rho_3} = \frac{h_3(p + dp, \rho_3) - h_3}{dp}$$

$$\left.\frac{\partial h_3}{\partial \rho_3}\right|_{p} = \frac{h_3(p, \rho_3 + d\rho) - h_3}{d\rho}$$

Terms: dh, $d\rho$, dp are infinitesimal increment arbitrarily chosen.

A.0.4 Wall states

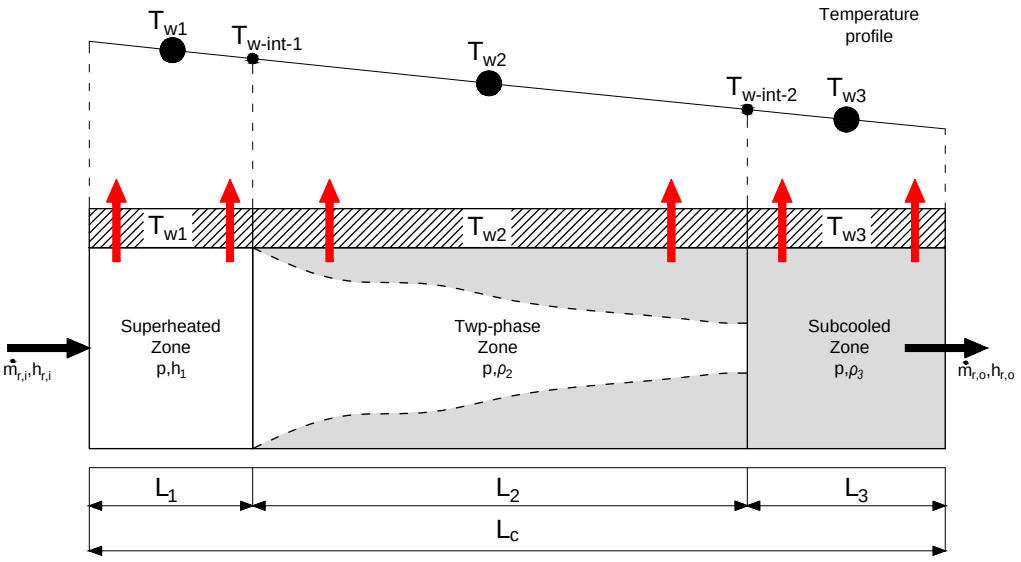

FIGURE A.1: SH-TP-L model wall states.

Knowing the states of the wall (T_{w1}, T_{w2}, T_{w3}), the interface temperatures can be evaluated assuming a linear profile:

$$T_{w-int-1} = T_{w1} \cdot \frac{L_2}{L_1 + L_2} + \frac{L_1}{L_1 + L_2} \cdot T_{w2} \tag{A.33}$$

$$T_{w-int-2} = T_{w2} \cdot \frac{L_3}{L_2 + L_3} + \frac{L_2}{L_2 + L_3} \cdot T_{w3} \tag{A.34}$$

Conservation of wall energy: superheated zone:

the differential equation of the conservation must be integrated spatially over the superheated zone with the assumption of lumped parameter, assuming a constant density and specific heat throughout the wall and constant cross-sectional area:

$$(\rho \cdot cp \cdot S)_w \int_0^{L1(t)} \frac{\partial T_w}{\partial t} \cdot dz = \int_0^{L1(t)} [\pi \cdot D_i \cdot \alpha_r \cdot (T_w - T_r) + \pi \cdot D_i \cdot \alpha_a \cdot (T_a - T_w)] \cdot dz \tag{A.35}$$

the first term must be integrated with the Leibniz's rule:

$$\int_0^{L1(t)} \frac{\partial T_w}{\partial t} \cdot dz = \frac{d}{dt} \int_0^{L1(t)} T_w \cdot dz - T_w(t, z = L_1) \cdot \frac{dL_1}{dt} \tag{A.36}$$

$$= \frac{d(LT_w)_1}{dt} - T_{w-int-1} \cdot \frac{dL_1}{dt}$$

$$= \frac{dL_1}{dt} \cdot T_{w1} + \frac{T_{w1}}{dt} \cdot L_1 - T_{w-int-1} \cdot \frac{dL_1}{dt} \tag{A.37}$$

substituting, in the previous, the definition of $T_{w-int-1}$

$$\int_0^{L1(t)} \frac{\partial T_w}{\partial t} \cdot dz = \frac{dL_1}{dt} \cdot T_{w1} + \frac{T_{w1}}{dt} \cdot L_1 - \left[T_{w1} \cdot \frac{L_2}{L_1 + L_2} + \frac{L_1}{L_1 + L_2} \cdot T_{w2} \right] \cdot \frac{dL_1}{dt} \tag{A.38}$$

$$= L_1 \cdot \frac{T_{w1}}{dt} + \left[(T_{w1} - T_{w2}) \cdot \frac{L_1}{L_1 + L_2} \right] \cdot \frac{dL_1}{dt} \tag{A.39}$$

Equation A.35 becomes:

$$L_1 \cdot \frac{dT_{w1}}{dt} + \left[(T_{w1} - T_{w2}) \cdot \frac{L_1}{L_1 + L_2} \right] \cdot \frac{dL_1}{dt} = \frac{1}{(\rho \cdot cp \cdot S)_{w1}} \cdot [\pi \cdot D_i \cdot L_1 \cdot \alpha_r \cdot (T_w - T_r) + + \pi \cdot D_i \cdot L_1 \cdot \alpha_a \cdot (T_a - T_w)] \tag{A.40}$$

calling $q_{r,1} = \pi \cdot D_i \cdot L_1 \cdot \alpha_r \cdot (T_{w1} - T_{r1})$ and $q_{a,1} = \pi \cdot D_i \cdot L_1 \cdot \alpha_a \cdot (T_a - T_{w1})$, in addition $m_{w1} = (\rho \cdot L_1 \cdot S)_{w1}$, the final expression is:

$$\frac{dT_{w1}}{dt} = \frac{q_{r,1} + q_{a,1}}{(m \cdot cp)_{w1}} - \frac{T_{w1} - T_{w2}}{L_1 + L_2} \cdot \frac{dL_1}{dt} \tag{A.41}$$

Conservation of wall energy: two-phase zone:

with the same procedure developed for the SH wall, the term that needs attention is the partial derivative of the temperature over the time:

$$\int_{L1(t)}^{L1(t)+L2(t)} \frac{\partial T_w}{\partial t} \cdot dz = \frac{d}{dt} \int_{L1(t)}^{L1(t)+L2(t)} T_w \cdot dz - T_w(t, z = L_1 + L_2) \cdot \left[\frac{dL_1}{dt} + \frac{dL_2}{dt} \right] + + T_w(t, z = L_1) \cdot \frac{dL_1}{dt} = \frac{d(LT_w)_2}{dt} - T_{w-int-2} \cdot \left[\frac{dL_1}{dt} + \frac{dL_2}{dt} \right] + T_{w-int-1} \cdot \frac{dL_1}{dt} \tag{A.42}$$

rearranging the previous:

$$\int_{L1(t)}^{L1(t)+L2(t)} \frac{\partial T_w}{\partial t} \cdot dz = L_2 \cdot \frac{dT_2}{dt} + \left[\frac{L_2}{L_1 + L_2} \cdot T_{w1} + \left(\frac{L_1}{L_1 + L_2} - \frac{L_3}{L_2 + L_3} \right) \cdot T_{w2} - \frac{L_2}{L_2 + L_3} \cdot T_{w3} \right] \cdot \frac{dL_1}{dt} + (T_{w2} - T_{w3}) \cdot \frac{L_2}{L_2 + L_3} \cdot \frac{dL_2}{dt} \tag{A.43}$$

and finally:

$$\frac{dT_{w2}}{dt} = \frac{q_{r,2} + q_{a,2}}{(m \cdot cp)_{w2}} - \left[\frac{1}{L_1 + L_2} \cdot T_{w1} + \frac{1}{L_2} \cdot \left(\frac{L_1}{L_1 + L_2} - \frac{L_3}{L_2 + L_3} \right) \cdot T_{w2} - - \frac{1}{L_2 + L_3} \cdot T_{w3} \right] \cdot \frac{dL_1}{dt} - (T_{w2} - T_{w3}) \cdot \frac{1}{L_2 + L_3} \cdot \frac{dL_2}{dt} \tag{A.44}$$

where: $q_{r,2} = \pi \cdot D_i \cdot L_2 \cdot \alpha_r \cdot (T_{w2} - T_{r2})$ and $q_{a,2} = \pi \cdot D_i \cdot L_2 \cdot \alpha_a \cdot (T_a - T_{w2})$

Conservation of wall energy: subcoooled zone:

with the same procedure developed for the SH and TP wall, the term that needs attention is the partial derivative of the temperature over the time:

$$\begin{aligned}\int_{L1(t)+L2(t)}^{L_c} \frac{\partial T_w}{\partial t} \cdot dz &= \frac{d}{dt} \int_{L1(t)+L2(t)}^{L_c} T_w \cdot dz + T_w(t, z = L_1 + L_2) \cdot \left[\frac{dL_1}{dt} + \frac{dL_2}{dt} \right] \\ &= \frac{d(LT_w)_3}{dt} + T_{w-int-2} \cdot \left[\frac{dL_1}{dt} + \frac{dL_2}{dt} \right] \\ &= \frac{dL_3}{dt} \cdot T_{w3} + \frac{T_{w3}}{dt} \cdot L_3 + T_{w-int-2} \cdot \left[\frac{dL_1}{dt} + \frac{dL_2}{dt} \right] \\ &= \frac{dL_3}{dt} \cdot T_{w3} + \frac{T_{w3}}{dt} \cdot L_3 + T_{w-int-2} \cdot \frac{dL_3}{dt} \end{aligned} \tag{A.45}$$

inserting the definition of $T_{w-int-2}$ (given in A.34), as a result the conservation of wall energy equation for the subcooled zone becomes:

$$\frac{dT_{w3}}{dt} = \frac{q_{r,3} + q_{a,3}}{(m \cdot cp)_{w3}} - \frac{T_{w3} - T_{w2}}{L_3 + L_2} \cdot \frac{dL_3}{dt} \tag{A.46}$$

where: $q_{r,3} = \pi \cdot D_i \cdot L_3 \cdot \alpha_r \cdot (T_{w3} - T_{r3})$ and $q_{a,3} = \pi \cdot D_i \cdot L_3 \cdot \alpha_a \cdot (T_a - T_{w3})$.

Appendix B

Full derivation of the TP-L model

The TP-L condenser mode proposed in this work is different from how pointed out in Cervato [24]. Due to the choice of the condenser state variables in this model there is a surplus of information since ρ_c, ρ_3 are already able to completely describe the model. Therefore, expressing one of the state variables as function of the other is required. Here, the length of the two phase zone is made function of: p, ρ_c, ρ_3 and a boundary condition h_i. Following the definition of void fraction mean the density of the two-phase zone can be deduced as:

$$\rho_2 = \rho_g(p) \cdot \bar{\gamma}(p, h_i) + \rho_l(p) \cdot (1 - \bar{\gamma}(p, h_i)) \tag{B.1}$$

$$\rho_c \cdot L_c = \rho_2 \cdot L_2 + \rho_3 \cdot L_3 \tag{B.2}$$

and hence the length of the two-phase zone may be expressed as:

$$L_2 = \frac{\rho_c - \rho_3}{\rho_2(p, h_i) - \rho_3} \cdot L_c \tag{B.3}$$

The time derivative of L_2 could be expressed as:

$$\frac{dL_2}{dt} = \frac{\left(\frac{d\rho_c}{dt} - \frac{d\rho_3}{dt}\right) \cdot (\rho_2 - \rho_3) - (\rho_c - \rho_3) \cdot \left(\frac{d\rho_2}{dt} - \frac{d\rho_3}{dt}\right)}{(\rho_2 - \rho_3)^2} \cdot L_c \tag{B.4}$$

as clear from Equation B.1 the mean density of the two-phase zone is function of the condensation pressure and the inlet enthalpy, therefore its time derivative may be expressed as:

$$\frac{d\rho_2}{dt} = \left.\frac{\partial \rho_2}{\partial p}\right|_{h_i} \cdot \frac{dp}{dt} + \left.\frac{\partial \rho_2}{\partial h_i}\right|_{p} \cdot \frac{dh_i}{dt} \tag{B.5}$$

Rearranging Equation B.4 with the previous definition the time derivative of the two-phase zone becomes:

$$\frac{dL_2}{dt} = \frac{\left(\frac{d\rho_c}{dt} - \frac{d\rho_3}{dt}\right) \cdot (\rho_2 - \rho_3) - (\rho_c - \rho_3) \cdot \left(\left.\frac{\partial \rho_2}{\partial p}\right|_{h_i} \cdot \frac{dp}{dt} + \left.\frac{\partial \rho_2}{\partial h_i}\right|_{p} \cdot \frac{dh_i}{dt} - \frac{d\rho_3}{dt}\right)}{(\rho_2 - \rho_3)^2} \cdot L_c \tag{B.6}$$

and finally, expressing clearly the dependency of the state variables and h_i:

$$\frac{dL_2}{dt} = A_{L_2} \cdot \frac{d\rho_c}{dt} + B_{L_2} \cdot \frac{dp}{dt} + C_{L_2} \cdot \frac{d\rho_3}{dt} + D_{L_2} \cdot \frac{dh_i}{dt} \tag{B.7}$$

where:

$$A_{L_2} = \frac{L_c \cdot (\rho_2 - \rho_3)}{(\rho_2 - \rho_3)^2} \qquad C_{L_2} = \frac{L_c \cdot [(\rho_c - \rho_3) - (\rho_2 - \rho_3)]}{(\rho_2 - \rho_3)^2} \tag{B.8}$$

$$B_{L_2} = -\frac{L_c \cdot (\rho_c - \rho_3)}{(\rho_2 - \rho_3)^2} \cdot \left.\frac{\partial \rho_2}{\partial p}\right|_{h_i} \cdot \frac{dp}{dt} \qquad D_{L_2} = -\frac{L_c \cdot (\rho_c - \rho_3)}{(\rho_2 - \rho_3)^2} \cdot \left.\frac{\partial \rho_2}{\partial h_i}\right|_{p} \cdot \frac{dh_i}{dt} \tag{B.9}$$

Conservation of refrigerant mass along the two-phase region:

the equation of the conservation of refrigerant mass must be integrated along the two-phase region:

$$\int_0^{L_2(t)} \left[A \cdot \frac{\partial \rho_2}{\partial t} + \frac{\partial \dot{m}}{\partial z}\right] \cdot dz = 0 \tag{B.10}$$

applying the Leibniz's rule for the first term and the fundamental theorem of calculus for the second term, the previous becomes:

$$A \cdot \left[\frac{d}{dt}\int_0^{L_2(t)} \rho_2 \cdot dz - \rho_2(t, z = L_2) \cdot \frac{dL_2}{dt}\right] = \dot{m}_i - \dot{m}_{int-2} \tag{B.11}$$

the term $\rho_2(t, z = L_2)$ could be considered equal to the liquid density $\rho_l(p(t))$, additionally $\dot{m}_{int-2}$ is the refrigerant mass flow rate at the boundary between TP and L zone. Assuming the hypothesis of lumped parameter (ρ_2 is the mean density):

$$A \cdot \left[\frac{d(L_2\rho_2)}{dt} - \rho_l \cdot \frac{dL_2}{dt}\right] = \dot{m}_i - \dot{m}_{int-2} \tag{B.12}$$

$$A \cdot \left[L_2 \cdot \frac{d\rho_2}{dt} + (\rho_2 - \rho_l) \cdot \frac{dL_2}{dt}\right] = \dot{m}_i - \dot{m}_{int-2} \tag{B.13}$$

As set out above the mean density of the two-phase zone is function of pressure, p, and inlet enthalpy, h_i, rearranging the previous equation:

$$A \cdot \left[L_2 \cdot \left. \frac{\partial \rho_2}{\partial p} \right|_{h_i} \cdot \frac{dp}{dt} + L_2 \cdot \left. \frac{\partial \rho_2}{\partial h_i} \right|_{p} \cdot \frac{dh_i}{dt} + (\rho_2 - \rho_l) \cdot \frac{dL_2}{dt} \right] = \dot{m}_i - \dot{m}_{int-2} \tag{B.14}$$

with the definition of the time derivative of the two-phase zone and inserting in the previous:

$$\begin{aligned} A \cdot \left[L_2 \cdot \left. \frac{\partial \rho_2}{\partial p} \right|_{h_i} \cdot \frac{dp}{dt} + L_2 \cdot \left. \frac{\partial \rho_2}{\partial h_i} \right|_{p} \cdot \frac{dh_i}{dt} + (\rho_2 - \rho_l) \cdot \left[A_{L_2} \cdot \frac{d\rho_c}{dt} + B_{L_2} \cdot \frac{dp}{dt} \right.\right. \\ \left.\left. + C_{L_2} \cdot \frac{d\rho_3}{dt} + D_{L_2} \cdot \frac{dh_i}{dt} \right] \right] = \dot{m}_i - \dot{m}_{int-2} \end{aligned} \tag{B.15}$$

and grouping the coefficients for describing the derivative of state variables and note term:

$$\begin{aligned} & A \cdot \left[L_2 \cdot \left. \frac{\partial \rho_2}{\partial p} \right|_{h_i} + (\rho_2 - \rho_l) \cdot B_{L_2} \right] \cdot \frac{dp}{dt} + A \cdot (\rho_2 - \rho_l) \cdot C_{L_2} \cdot \frac{d\rho_3}{dt} + \\ & + A \cdot (\rho_2 - \rho_l) \cdot A_{L_2} \cdot \frac{d\rho_c}{dt} + \dot{m}_{int-2} = \dot{m}_i - A \cdot \left[L_2 \cdot \left. \frac{\partial \rho_2}{\partial h_i} \right|_{p} + (\rho_2 - \rho_l) \cdot D_{L_2} \right] \cdot \frac{dh_i}{dt} \end{aligned} \tag{B.16}$$

Conservation of refrigerant energy on the two-phase region:

the equation of the energy conservation must be integrated along the two-phase region:

$$\int_0^{L_2(t)} \left[A \cdot \frac{\partial(\rho h)}{\partial t} - A \cdot \frac{\partial p}{\partial t} + \frac{\partial(\dot{m} h)}{\partial z} \right] \cdot dz = \int_0^{L_2(t)} \left[\pi \cdot D_i \cdot \alpha_r \cdot (T_{w2} - T_{r2}) \right] \cdot dz \tag{B.17}$$

assuming the hypothesis of lumped parameters and applying the fundamental theorem of calculus, the equation becomes:

$$A \cdot \int_0^{L_2(t)} \frac{\partial(\rho h)}{\partial t} \cdot dz - A \int_0^{L_2(t)} \frac{\partial p}{\partial t} \cdot dz + \dot{m}_{int-2} \cdot h_l - \dot{m}_i \cdot h_i = \pi \cdot D_i \cdot L_2 \cdot \alpha_r \cdot (T_{w2} - T_{r2}) \tag{B.18}$$

applying the Leibniz's rule at the first term:

$$A \cdot \int_0^{L_2(t)} \frac{\partial(\rho h)}{\partial t} \cdot dz = A \cdot \frac{d}{dt} \int_0^{L_2(t)} (\rho h) \cdot dz - (\rho h)_l \cdot \frac{dL_2}{dt} \tag{B.19}$$

$$= A \cdot L_2 \cdot \frac{d(\rho h)_2}{dt} + A \cdot (\rho h)_2 \cdot \frac{dL_2}{dt} - A \cdot (\rho h)_l \cdot \frac{dL_2}{dt} \tag{B.20}$$

$$= A \cdot L_2 \cdot \frac{d(\rho h)_2}{dt} + A \cdot [(\rho h)_2 - (\rho h)_l] \cdot \frac{dL_2}{dt} \tag{B.21}$$

applying the Leibniz's rule at the second term:

$$A \int_0^{L_2(t)} \frac{\partial p}{\partial t} \cdot dz = A \cdot \frac{d}{dt} \int_0^{L_2(t)} p \cdot dz - p \cdot A \cdot \frac{dL_2}{dt} \tag{B.22}$$

$$= A \cdot \frac{dp}{dt} \cdot L_2 + A \cdot p \cdot \frac{dL_2}{dt} - A \cdot p \cdot \frac{dL_2}{dt} \tag{B.23}$$

$$= A \cdot L_2 \cdot \frac{dp}{dt} \tag{B.24}$$

reassembling Equation B.18, it becomes:

$$\begin{aligned} &A \cdot L_2 \cdot \frac{d(\rho h)_2}{dt} + A \cdot [(\rho h)_2 - (\rho h)_l] \cdot \frac{dL_2}{dt} + A \cdot L_2 \cdot \frac{dp}{dt} + \dot{m}_{int-2} \cdot h_l - \dot{m}_i \cdot h_i \\ &= \pi \cdot D_i \cdot L_2 \cdot \alpha_r \cdot (T_{w2} - T_{r2}) \end{aligned} \tag{B.25}$$

noting that $(\rho h)_2 = (\rho h)_2(p, h_i)$, therefore:

$$\frac{d(\rho h)_2}{dt} = \left.\frac{\partial(\rho h)_2}{\partial p}\right|_{h_i} \cdot \frac{dp}{dt} + \left.\frac{\partial(\rho h)_2}{\partial h_i}\right|_{p} \cdot \frac{dh_i}{dt} \tag{B.26}$$

substituting this term in Eq. B.25:

$$\begin{aligned} &A \cdot L_2 \cdot \left[\left.\frac{\partial(\rho h)_2}{\partial p}\right|_{h_i} - 1 \right] \cdot \frac{dp}{dt} + A \cdot [(\rho h)_2 - (\rho h)_l] \cdot \frac{dL_2}{dt} + \dot{m}_{int-2} \cdot h_l = \\ &= \dot{m}_i \cdot h_i + \pi \cdot D_i \cdot L_2 \cdot \alpha_r \cdot (T_{w2} - T_{r2}) - A \cdot L_2 \cdot \left.\frac{\partial(\rho h)_2}{\partial h_i}\right|_{p} \cdot \frac{dh_i}{dt} \end{aligned} \tag{B.27}$$

substituting the term dL_2/dt with the definition given in B.7:

$$\begin{aligned} &A \cdot L_2 \cdot \left[\left.\frac{\partial(\rho h)_2}{\partial p}\right|_{h_i} - 1 \right] \cdot \frac{dp}{dt} + A \cdot [(\rho h)_2 - (\rho h)_l] \cdot \left[A_{L_2} \cdot \frac{d\rho_c}{dt} + B_{L_2} \cdot \frac{dp}{dt} + \right. \\ &\left. + C_{L_2} \cdot \frac{d\rho_3}{dt} + D_{L_2} \cdot \frac{dh_i}{dt} \right] + \dot{m}_{int-2} \cdot h_l = \dot{m}_i \cdot h_i + \pi \cdot D_i \cdot L_2 \cdot \alpha_r \cdot (T_{w2} - T_{r2}) - \\ &- A \cdot L_2 \cdot \left.\frac{\partial(\rho h)_2}{\partial h_i}\right|_{p} \cdot \frac{dh_i}{dt} \end{aligned} \tag{B.28}$$

and groping the coefficients for describing the derivative of state variables and note term, calling $q_{r,2} = \pi \cdot D_i \cdot L_2 \cdot \alpha_r \cdot (T_{w2} - T_{r2})$:

$$\begin{aligned} &A \cdot \left[L_2 \cdot \left[\left. \frac{\partial(\rho h)_2}{\partial p} \right|_{h_i} - 1 \right] + [(\rho h)_2 - (\rho h)_l] \cdot B_{L_2} \right] \cdot \frac{dp}{dt} + [(\rho h)_2 - (\rho h)_l] \cdot C_{L_2} \cdot \frac{\rho_3}{dt} + \\ &A \cdot [(\rho h)_2 - (\rho h)_l] \cdot A_{L_2} \cdot \frac{\rho_c}{dt} + \dot{m}_{int-2} \cdot h_l = \dot{m}_i \cdot h_i + q_{r,2} - \\ &\left[A \cdot L_2 \cdot \left. \frac{\partial(\rho h)_2}{\partial h_i} \right|_p + A \cdot [(\rho h)_2 - (\rho h)_l] \cdot D_{L_2} \right] \cdot \frac{dh_i}{dt} \end{aligned} \tag{B.29}$$

Conservation of refrigerant energy along the subcooled zone:

also for the differential equation of the refrigerant energy conservation applying two times the Leibniz's rule assuming the lumped hypothesis, the energy equation becomes:

$$\begin{aligned} &A \cdot \left[((\rho h)_l - (\rho h)_3) \cdot \frac{dL_2}{dt} + L_3 \cdot \frac{d(\rho h)_3}{dt} \right] + A \cdot L_3 \cdot \frac{dp}{dt} - \dot{m}_{int-2} \cdot h_l = \\ &- \dot{m}_o \cdot h_o + \pi \cdot D_i \cdot L_3 \cdot \alpha_r \cdot (T_{w3} - T_{r3}) \end{aligned} \tag{B.30}$$

noting that $h_3 = h(p, \rho_3)$ then the term $\dfrac{d(\rho h)_3}{dt}$: could be expressed as:

$$\frac{d(\rho h)_3}{dt} = \rho_3 \cdot \frac{dh_3}{dt} + h_3 \cdot \frac{d\rho_3}{dt} \tag{B.31}$$

$$= \rho_3 \cdot \left[\left. \frac{\partial h_3}{\partial p} \right|_{\rho_3} \cdot \frac{dp}{dt} + \left. \frac{\partial h_3}{\partial \rho_3} \right|_p \cdot \frac{d\rho_3}{dt} \right] + h_3 \cdot \frac{d\rho_3}{dt} \tag{B.32}$$

substituting in B.30 and rearranging:

$$\begin{aligned} &A \cdot L_3 \cdot \left[\rho_3 \left. \frac{\partial h_3}{\partial h_p} \right|_{\rho_3} - 1 \right] \cdot \frac{dp}{dt} + A \cdot L_3 \left[\rho_3 \cdot \left. \frac{\partial h_3}{\partial \rho_3} \right|_p + h_3 \right] \cdot \frac{d\rho_3}{dt} + \\ &A \cdot [(\rho h)_l - (\rho h)_3] \cdot \frac{dL_2}{dt} - \dot{m}_{int-2} \cdot h_l = -\dot{m}_o \cdot h_o + \pi \cdot D_i \cdot L_3 \cdot \alpha_r \cdot (T_{w3} - T_{r3}) \end{aligned} \tag{B.33}$$

substituting in the previous the definition of dL_2/dt given in B.7 and calling $q_{r,3} = \pi \cdot D_i \cdot L_3 \cdot \alpha_r \cdot (T_{w3} - T_{r3})$

$$\begin{aligned} &A \cdot \left[L_3 \cdot \left[\rho_3 \cdot \left. \frac{\partial h_3}{\partial p} \right|_{\rho_3} - 1 \right] + B_{L_2} \cdot [(\rho h)_l - (\rho h)_3] \right] \cdot \frac{dp}{dt} + A \cdot \left[L_3 \cdot \left[\rho_3 \cdot \left. \frac{\partial h_3}{\partial \rho_3} \right|_p + h_3 \right] \right. \\ &\left. + C_{L_2} \cdot [(\rho h)_l - (\rho h)_3] \right] \cdot \frac{d\rho_3}{dt} + A_{L_2} \cdot [(\rho h)_l - (\rho h)_3] \cdot \frac{d\rho_c}{dt} - \dot{m}_{int-2} \cdot h_l = \\ &= -\dot{m}_o \cdot h_o + q_{r,3} - A \cdot D_{L_2} \cdot [(\rho h)_l - (\rho h)_3] \cdot \frac{dh_i}{dt} \end{aligned} \tag{B.34}$$

The algebraic system is constituted from Equations: B.16, B.29, B.34 and the equation of mass conservation applied on the condenser:

$$\frac{d\rho_c}{dt} = \frac{\dot{m}_i - \dot{m}_o}{A \cdot L_c} \tag{B.35}$$

The complete system results as:

$$\begin{vmatrix} M11 & M12 & M13 & M14 \\ M21 & M22 & M23 & M24 \\ 0 & 0 & M33 & 0 \\ M41 & M42 & M43 & M44 \end{vmatrix} \cdot \begin{vmatrix} dp/dt \\ d\rho_3/dt \\ d\rho_c/dt \\ \dot{m}_{int-2} \end{vmatrix} = \begin{vmatrix} N1 \\ N2 \\ N3 \\ N4 \end{vmatrix}$$

where:

$$M11 = A \cdot \left[L_2 \cdot \left. \frac{\partial \rho_2}{dp} \right|_{h_i} + (\rho_2 - \rho_l) \cdot B_{L_2} \right]$$

$$M12 = A \cdot (\rho_2 - \rho_l) \cdot C_{L_2}$$

$$M13 = A \cdot (\rho_2 - \rho_l) \cdot A_{L_2}$$

$$M14 = 1$$

$$M21 = A \cdot \left[L_2 \cdot \left[\left. \frac{\partial (\rho h)_2}{\partial p} \right|_{h_i} - 1 \right] + [(\rho h)_2 - (\rho h)_l] \cdot B_{L_2} \right]$$

$$M22 = A \cdot [(\rho h)_2 - (\rho h)_l] \cdot C_{L_2}$$

$$M23 = A \cdot [(\rho h)_2 - (\rho h)_l] \cdot A_{L_2}$$

$$M24 = h_l$$

$$M31 = 0$$

$$M32 = 0$$

$$M33 = 1$$

$$M34 = 0$$

$$M41 = A \cdot \left[L_3 \cdot \left[\rho_3 \cdot \left. \frac{\partial h_3}{\partial p} \right|_{\rho_3} - 1 \right] + B_{L_2} \cdot [(\rho h)_l - (\rho h)_3] \right]$$

$$M42 = A \cdot \left[L_3 \cdot \left[\rho_3 \cdot \left. \frac{\partial h_3}{\partial \rho_3} \right|_{p} + h_3 \right] + C_{L_2} \cdot [(\rho h)_l - (\rho h)_3] \right]$$

$$M43 = A_{L_2} \cdot [(\rho h)_l - (\rho h)_3]$$

$$M44 = h_l$$

and note term vector:

$$N1 = \dot{m}_i - A \cdot \left[L_2 \cdot \left. \frac{\partial \rho_2}{\partial h_i} \right|_p + (\rho_2 - \rho_l) \cdot D_{L_2} \right] \cdot \frac{dh_i}{dt}$$

$$N2 = \dot{m}_i \cdot h_i + q_{r,2} - A \cdot \left[L_2 \cdot \left. \frac{\partial (\rho h)_2}{\partial h_i} \right|_p + [(\rho h)_2 - (\rho h)_l] \cdot D_{L_2} \right] \cdot \frac{dh_i}{dt}$$

$$N3 = \frac{\dot{m}_i - \dot{m}_o}{A \cdot L_c}$$

$$N4 = -\dot{m}_o \cdot h_o + q_{r,3} - A \cdot D_{L_2} \cdot [(\rho h)_l - (\rho h)_3] \cdot \frac{dh_i}{dt}$$

One final remark: solved the previous algebraic system then the time derivative of the two-phase zone length can be computed with Equation B.7.

Appendix C

Refrigerant charge migration and initial conditions

In Figure C.1 the evolution of the refrigerant mass flow rate through the capillary tube and the mass flow rate drawn by the compressor during the first minutes of the start-up transient are shown. Initial refrigerant charge inventory on the heat exchanger was established considering the layout and the features of the heat pump module. Different from the refrigerators-freezers where the vertical layout forces the refrigerant charge to fill the evaporator during the shut-down phase, here the horizontal layout (see Figure 3.3) does not guarantee a complete migration of the refrigerant charge from the condenser to the evaporator although a positive pressure gain ($\Delta P = p_{cond.} - p_{evap.}$) occurs for all the shut-down transient ($\approx$ 1 min). Furthermore, experimental evidences (superheat and subcooling degree measurements) show that the condenser refrigerant charge inventory is greater than evaporator one. Björk [49] experimentally investigated the refrigerant mass distribution among the system components during the compressor shut-down and start-up period using the quick-closing valve method and a calculation techniques (*(p-v-T)* relationship) for estimating the refrigerant charge in the components of a domestic refrigerator. The reader is encouraged to refer to [49] and [50] for further details regarding the refrigerant mass measurement method, experimental results and analysis. The ratio between the refrigerant charge in the evaporator and in the condenser is 1/6 as shown in Figure C.1. When the compressor is switched on, it draws an high value of the mass flow rate that leads to decrease the refrigerant charge in the evaporator since the capillary tube needs that the condensation pressure reaches a suitable value before operating. When the capillary tube starts to draw its mass flow rate the refrigerant charge is already migrated to the condenser: see the condenser refrigerant peak near to 20 seconds after the compressor starting. Afterward, a short period (2-3 min), in which the system is unbalanced, occurs. In this phase the evaporator is gradually refelling.

After 3 min, the refrigerant mass flows rate are equal to each other and the charge distribution tends to stabilize in the heat exchangers.

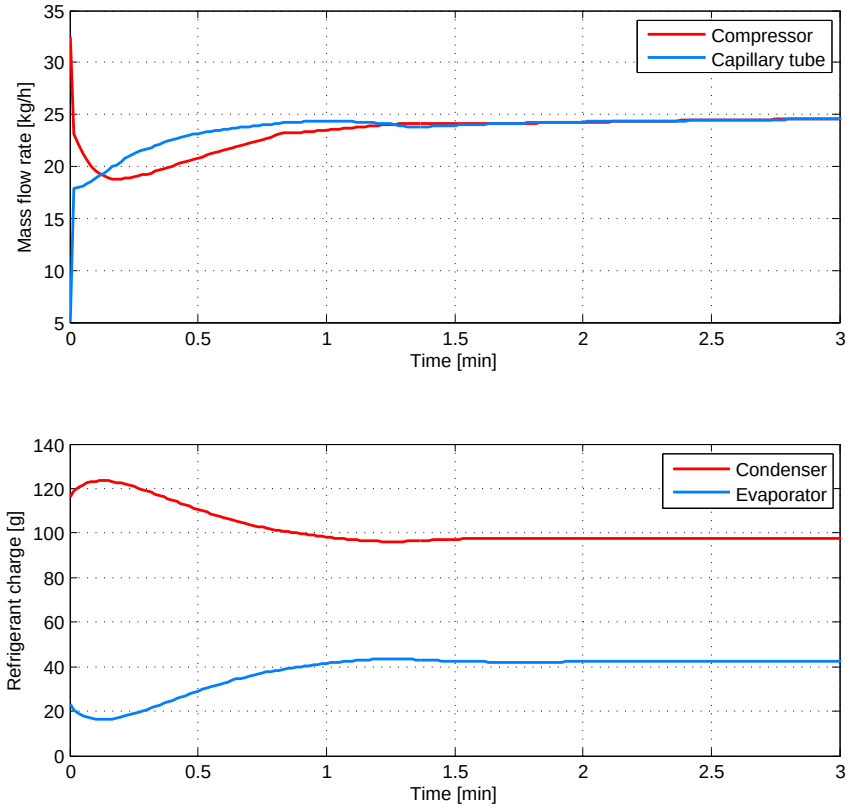

FIGURE C.1: Refrigerant charge migration during the first minutes of the transient.

One final remark is about how the condenser and evaporator initial states are evaluated. Refrigerant charge ($Charge$) is a user parameter and also the initial refrigerant distribution (K_d) is chosen *a-priori*:

$$\rho_c = \frac{Charge \cdot (1 - K_d)}{V_c} \tag{C.1}$$

$$\rho_e = \frac{Charge \cdot K_d}{V_e} \tag{C.2}$$

where $V_{cond.}$ and $V_{evap.}$ are the condenser and evaporator internal volumes. Condensation and evaporation pressure are expressed as follows: theoretically, due to the capillary tube the high and low refrigerant pressure are equalized and their value should be the saturation pressure at the ambient temperature, T_e. Practically, to avoid numerical issues, the condensation pressure is computed at the temperature: $T_{sat,c} = T_e + 1$,

hence:

$$p_c = p(T_{sat,c}) \tag{C.3}$$

$$p_e = p(T_e) \tag{C.4}$$

For the condenser also the initial subcooling is chosen (SC_0) before starting the simulation. With this value is possible to estimate the mean density of the subcooled zone (ρ_3):

$$\rho_3 = \rho(p_c, T_3) \tag{C.5}$$

$$\text{where: } T_3 = \frac{2 \cdot T_l - SC_0}{2} \tag{C.6}$$

in the condenser the mean density of the two-phase zone is calculated assuming an inlet ($x_i = 1$) and outlet ($x_o = 0$) quality and knowing the condensation pressure:

$$\rho_2 = \rho_v \cdot \bar{\gamma}(x_i, x_o, p_c) + \rho_l \cdot (1 - \bar{\gamma}(x_i, x_o, p_c)) \tag{C.7}$$

and hence the length of the two-phase zone is expressed as:

$$L_2 = L_c - \frac{\rho_c - \rho_2}{\rho_l - \rho_2} \cdot L_c \tag{C.8}$$

the previous value is checked with the length of the condenser (L_c). If L_2 is longer than the L_c then L_2 is set to the L_c value and hence the initial condenser mode is TP. The wall states are initialized to:

$$T_{w1} = T_{w2} = T_{w3} = T_{sat,c} - 0.1 \tag{C.9}$$

For the evaporator the initial superheating is chosen (SH_0) and the mean density of the superheated zone is expressed as:

$$\rho_2 = \rho(p_e, T_2) \tag{C.10}$$

$$\text{where: } T_2 = \frac{2 \cdot T_v + SH_0}{2} \tag{C.11}$$

identical as done for the condenser, the mean density for the two-phase zone is expressed as:

$$\rho_1 = \rho_v \cdot \bar{\gamma}(x_i, x_o, p_c) + \rho_l \cdot (1 - \bar{\gamma}(x_i, x_o, p_c)) \tag{C.12}$$

and hence the length of the superheated zone:

$$L_2 = L_e - \frac{\rho_e - \rho_2}{\rho_1 - \rho_2} \cdot L_e \tag{C.13}$$

this length is checked, if it is lower than zero the initial evaporator mode is TP. The wall states are initialized to:

$$T_{w1} = T_v + 1 \tag{C.14}$$

$$T_{w2} = T_v + SH_0 + 1 \tag{C.15}$$

if the initial mode is TP-SH, otherwise:

$$T_{w1} = T_v + 1 \tag{C.16}$$

$$T_{w2} = T_{w1} \tag{C.17}$$

Appendix D

Heat pump tumble dryer Simulink model

As already mentioned, the heat pump tumble dryer was implemented in Simulink. All the blocks were coded using ″User-Defined Functions‟ that allows to write Matlab code for using in Simulink. A series of figures that show the graphical user interface (GUI) of the model are reported in the following figures. The image of the component type is displayed with the component mask. By double clicking the component, the interactive GUI is activated which then allows the user to specify the component physical parameters, operating conditions, and other necessary information, such as gains for the heat transfer coefficient correlations.

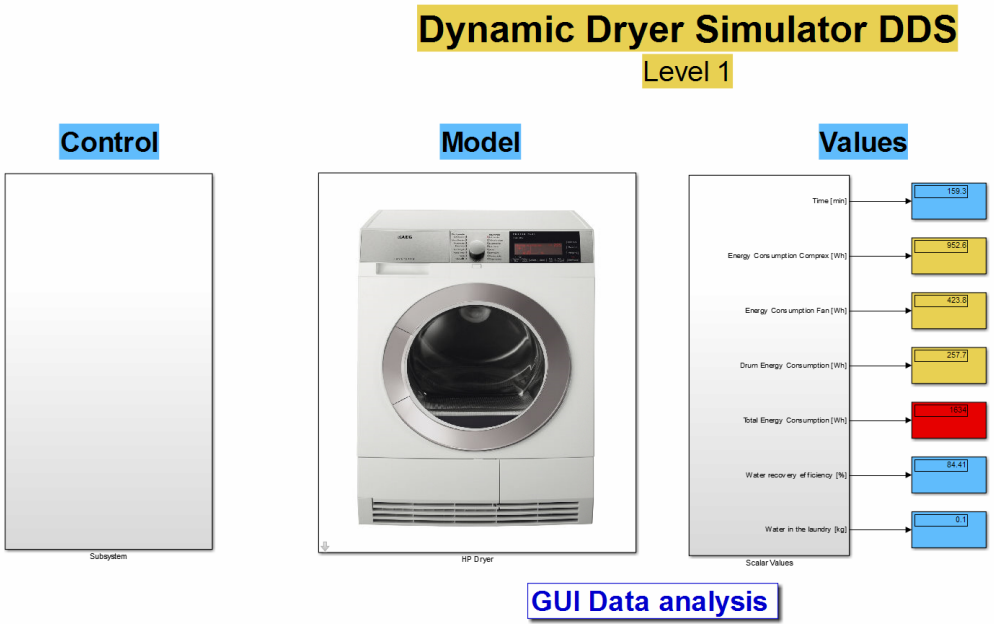

FIGURE D.1: Main window of the heat pump tumble dryer model.

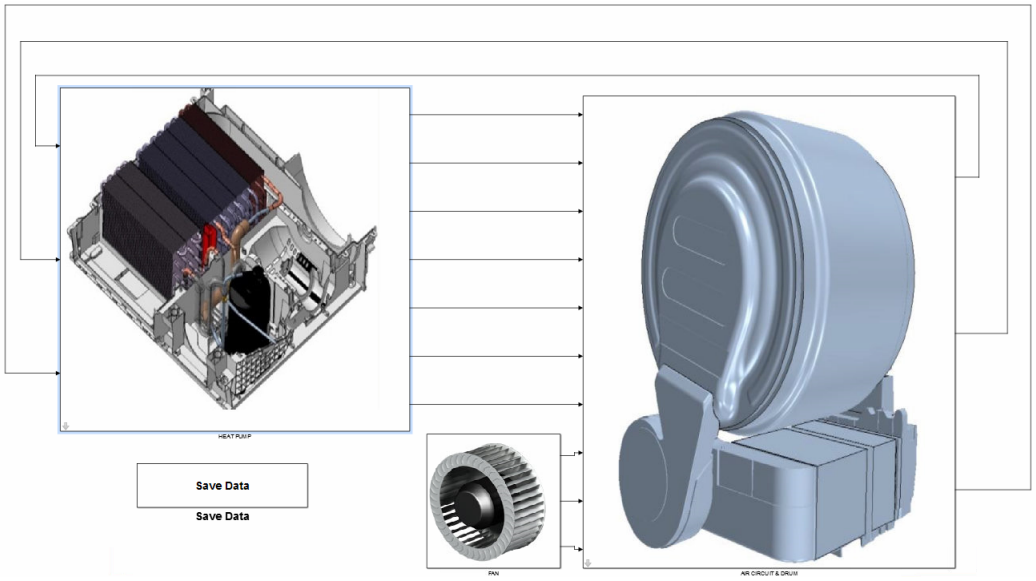

FIGURE D.2: Heat pump and air circuit modules window.

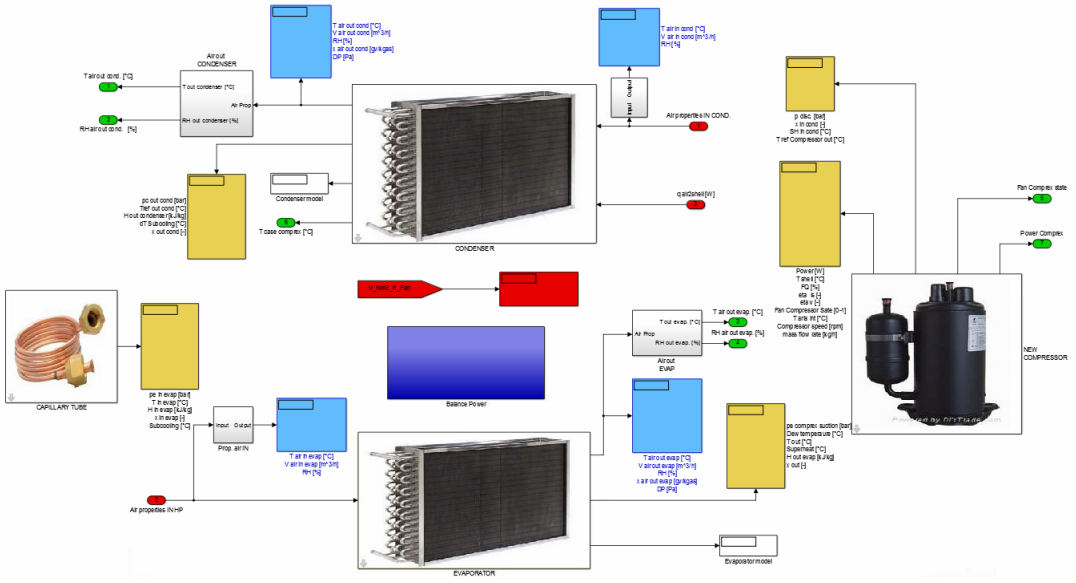

FIGURE D.3: Heat pump module window.

Appendix E

Laundry thermal capacities

As discussed in the Paragraph 4.4.2, the system laundry and water content is model with two zones: a wet zone characterized dynamically and a dry zone modeled in a static way. At an instant of time the equation of the energy conservation applied at the wet zone gives:

$$\frac{du}{dt} = q \tag{E.1}$$

q is the results of the heat fluxes that act on the capacity and the term u is its internal energy, in this case is equal to:

$$u = M_w \cdot c_{p,w} + M_l \cdot R_0 \cdot c_{p,l} \tag{E.2}$$

terms in the previous are described in Chapter 4. Substituting in E.1, it becomes:

$$\frac{d(M_w \cdot c_{p,w} + M_l \cdot R_0 \cdot c_{p,l}) \cdot T_{wet}}{dt} = q \tag{E.3}$$

applying the chain rule and assuming the specifics heat as constants:

$$\frac{dT_{wet}}{dt} \cdot (M_w \cdot c_{p,w} + M_l \cdot R_0 \cdot c_{p,l}) + T_{wet} \cdot \left(\frac{dM_w}{dt} \cdot c_{p,w} + M_l \cdot c_{p,l} \cdot \frac{dR_0}{dt} \right) = q \tag{E.4}$$

hence the time derivative of the laundry:

$$\frac{dT_{wet}}{dt} = \frac{q - T_{wet} \cdot \left(\frac{dM_w}{dt} \cdot c_{p,w} + M_l \cdot c_{p,l} \cdot \frac{dR_0}{dt} \right)}{(M_w \cdot c_{p,w} + M_l \cdot R_0 \cdot c_{p,l})} \tag{E.5}$$

since the term dR_0/dt is depended only by LWC, it may be expressed as:

$$\frac{dR_0}{dt} = \frac{dR_0}{dLWC} \cdot \frac{dLWC}{dt} \tag{E.6}$$

recalling the definition of LWC given in 4.1, the previous becomes:

$$\frac{dR_0}{dt} = \frac{1}{M_w(0)} \cdot \frac{dR_0}{dLWC} \cdot \frac{dM_w(t)}{dt} \cdot 100 \tag{E.7}$$

Substituting in E.5

$$\frac{dT_{wet}}{dt} = \frac{q - T_{wet} \cdot \left(\frac{dM_w}{dt} \cdot c_{p,w} + M_l \cdot c_{p,l} \cdot \frac{1}{M_w(0)} \cdot \frac{dR_0}{dLWC} \cdot \frac{dM_w}{dt} \cdot 100 \right)}{(M_w \cdot c_{p,w} + M_l \cdot R_0 \cdot c_{p,l})} \tag{E.8}$$

In case of modeling the drying zone as dynamic the following definition must be used:

$$\frac{dT_{dry}}{dt} = \frac{q - T_{dry} \cdot \left(M_l \cdot c_{p,l} \cdot \frac{1}{M_w(0)} \cdot \frac{dR_0}{dLWC} \cdot \frac{dM_w}{dt} \cdot 100 \right)}{M_l \cdot (1 - R_0) \cdot c_{p,l}} \tag{E.9}$$

Bibliography

[1] Youn Cheol Park. Transient analysis of a variable speed rotary compressor. *Energy Conversion and Management*, 51(2):277 – 287, 2010.

[2] Lena Stawreberg. *Energy Efficiency Improvements of Tumble Dryers.* PhD thesis, Karlstad University Studies, 2011.

[3] Supplementing Directive 2010/30/eu of the European Parliament and of the Council with regard to energy labelling of household tumble driers. Regulations Regulation No 392/2012, 2012.

[4] PT Tsilingiris. Thermophysical and transport properties of humid air at temperature range between 0 and 100 ℃. *Energy Conversion and Management*, 49(5): 1098–1110, 2008.

[5] THECNICAL COMMEITTEE: Performance of household electrical appliances. International Standard IEC 61121. Technical report, International Electrotechnical Commission, 2010.

[6] Bryan P. Rasmussen. Dynamic modeling for vapor compression systems—Part I: Literature review. *HVAC&R Research*, 18(5):934–955, 2012.

[7] S. Bendapudi, J.E. Braun, Refrigerating American Society of Heating, and Air-Conditioning Engineers. *A Review of Literature on Dynamic Models of Vapor Compression Equipment.* 2002.

[8] Bryan P. Rasmussen and Bhaskar Shenoy. Dynamic modeling for vapor compression systems—Part II: Simulation tutorial. *HVAC&R Research*, 18(5):956–973, 2012.

[9] Bryan Philip Rasmussen. *Dynamic modeling and advanced control of air control of air conditioning and refrigeration systems.* PhD thesis, University of Illinois at Urbana-Champaign, 2011.

[10] Ferdinando Mancini. *Energy Efficiency Improvements of Household Heat Pump Systems.* PhD thesis, Scuola di dottorato di ricerca in ingegneria industriale-Indirizzo Energetica, Università degli Studi di Padova, 2011.

[11] Joseph M Fasl. Modeling and control of hybid vapor compression cycles. Master's thesis, University of Illinois at Urbana-Champaign, 2013.

[12] Thomas L McKinley and Andrew G Alleyne. An advanced nonlinear switched heat exchanger model for vapor compression cycles using the moving-boundary method. *International Journal of Refrigeration*, 31(7):1253–1264, 2008.

[13] Luca Cecchinato and Ferdinando Mancini. An intrinsically mass conservative switched evaporator model adopting the moving-boundary method. *International Journal of Refrigeration*, 35(2):349 – 364, 2012.

[14] Chunlu Zhang and Guoliang Ding. Approximate analytic solutions of adiabatic capillary tube. *International Journal of Refrigeration*, 27(1):17 – 24, 2004.

[15] SM Zivi. Estimation of steady-state steam void-fraction by means of the principle of minimum entropy production. *Journal of Heat Transfer*, 86(2):247–251, 1964.

[16] EnergyEverest. Ref.box. URL `www.energyeverest.com`.

[17] Bin Li and Andrew G. Alleyne. A dynamic model of a vapor compression cycle with shut-down and start-up operations. *International Journal of Refrigeration*, 33 (3):538 – 552, 2010.

[18] Vikrant Aute Hontago, Qiao and Radermacher Reinhard. An improved moving boundary heat exchanger model with pressure drop. 2014.

[19] Dejan Brkić. Review of explicit approximations to the colebrook relation for flow friction. *Journal of Petroleum Science and Engineering*, 77(1):34–48, 2011.

[20] V. Gnielinski. New equations for heat and mass transfer in turbulent pipe and channel flow. *Int. Chem. Eng*, 16(2):359–368, 1976.

[21] A. Cavallini, D. Del Col, L. Doretti, G.A. Longo, and L. Rossetto. Heat transfer and pressure drop during condensation of refrigerants inside horizontal enhanced tubes. *International Journal of Refrigeration*, 23(1):4 – 25, 2000.

[22] A. Cavallini, D. Del Col, L. Doretti, G.A. Longo, and L. Rossetto. Pressure drop during condensation and vaporisation of refrigerants inside enhanced tube. *Heat and Technolog*, 1997.

[23] Alberto Cavallini, Davide Del Col, Luca Doretti, Marko Matkovic, Luisa Rossetto, Claudio Zilio, and Giuseppe Censi. Condensation in horizontal smooth tubes: A new heat transfer model for heat exchanger design. *Heat Transfer Engineering*, 27 (8):31–38, 2006.

[24] Andrea Cervato. Sperimentazione,ottimizzazione e simulazione dinamica di un innovativo refrigeratore di liquido ad ammoniaca. Master's thesis, Università degli studi di Padova, Dipartimento di Fisica Tecnica, 2010.

[25] N.B.O.L. Pettit, M. Willatzen, and L. Ploug-Sørensen. A general dynamic simulation model for evaporators and condensers in refrigeration. Part II: simulation and control of an evaporator: Modèle général dynamique pour évaporateurs et condenseurs frigorifiques. Partie II: Simulation et régulation d'un évaporateur. *International Journal of Refrigeration*, 21(5):404 – 414, 1998.

[26] Frank P. Incropera. *Fundamentals of Heat and Mass Transfer*. John Wiley & Sons, 2006. ISBN 0470088400.

[27] Chi-Chuan Wang, Kuan-Yu Chi, and Chun-Jung Chang. Heat transfer and friction characteristics of plain fin-and-tube heat exchangers, Part II: Correlation. *International Journal of Heat and Mass Transfer*, 43(15):2693 – 2700, 2000.

[28] Chi-Chuan Wang, Young-Ming Hwang, and Yur-Tsai Lin. Empirical correlations for heat transfer and flow friction characteristics of herringbone wavy fin-and-tube heat exchangers. *International Journal of Refrigeration*, 25(5):673–680, 2002.

[29] C-C Wang, C-J Lee, C-T Chang, and S-P Lin. Heat transfer and friction correlation for compact louvered fin-and-tube heat exchangers. *International journal of heat and mass transfer*, 42(11):1945–1956, 1998.

[30] K. E. Gungor and R. H. S. Winterton. Simplified general correlation for saturated flow boiling and comparison of correlation with data. *Chem. Eng. Res. Des.*, 65: 148–156, 1987.

[31] P.K. Bansal and G. Wang. Numerical analysis of choked refrigerant flow in adiabatic capillary tubes. *Applied Thermal Engineering*, 24(5–6):851 – 863, 2004.

[32] Meixia Wang, Cunfang Liu, and Qiangtai Zhou. Simulation on refrigerant flow in adiabatic capillary tube. *Frontiers of Mechanical Engineering in China*, 3(3): 332–336, 2008.

[33] Refrigerating American Society of Heating and Air-Conditioning Engineers. *2002 ASHRAE Handbook: Refrigeration*. ASHRAE HANDBOOK REFRIGERATION SI. American Society of Heating, Refrigeration and Air-Conditioning Engineers, 2002.

[34] Li Yang and Wen Wang. A generalized correlation for the characteristics of adiabatic capillary tubes. *International Journal of Refrigeration*, 31(2):197 – 203, 2008.

[35] Chasik Park, Sunil Lee, Hoon Kang, and Yongchan Kim. Experimentation and modeling of refrigerant flow through coiled capillary tubes. *International Journal of Refrigeration*, 30(7):1168–1175, 2007.

[36] Christian J.L. Hermes, Cláudio Melo, and Fernando T. Knabben. Algebraic solution of capillary tube flows. Part II : Capillary tube suction line heat exchangers. *Applied Thermal Engineering*, 30(6–7):770 – 775, 2010.

[37] Sisir K Padhy. Heat transfer model of a rotary compressor. 1992.

[38] D.P. Sekulić Shah, R.K. *Fundamentals of heat exchanger design, 1st edition.* John Wiley & Sons, 2003.

[39] Satyam Bendapudi, James E Braun, and Eckhard A Groll. A comparison of moving-boundary and finite-volume formulations for transients in centrifugal chillers. *International journal of refrigeration*, 31(8):1437–1452, 2008.

[40] Julian Winkler, Jesse Killion, and Srinivas Garimella. Void fractions for condensing refrigerant flow in small channels. Part II: Void fraction measurement and modeling. *International Journal of Refrigeration*, 35(2):246 – 262, 2012.

[41] Melkamu A Woldesemayat and Afshin J Ghajar. Comparison of void fraction correlations for different flow patterns in horizontal and upward inclined pipes. *International Journal of Multiphase Flow*, 33(4):347–370, 2007.

[42] L. Casarsa and D. Foschiani. TD air circuit assessment and improvment. Task 3 - drum air circuit characterization: pressure losses and leakages. Technical report, Advatech Time S.r.l., Spin-Off University of Udine, 2014.

[43] L. Casarsa and A. Armellini. Rilievo della portata d'aria di processo in una asciugabiancheria. Technical report, Advatech Time S.r.l., Spin-Off University of Udine, 2013.

[44] J Deans. The modelling of a domestic tumbler dryer. *Applied Thermal Engineering*, 21(9):977 – 990, 2001.

[45] V. Yadav and C.G. Moon. Modelling and experimentation for the fabric-drying process in domestic dryers. *Applied Energy*, 85(5):404 – 419, 2008.

[46] A. Armellini and L. Casarsa. Portland dryer characterization. Technical report, Advatech Time S.r.l., Spin-Off University of Udine, 2014.

[47] A. Armellini and L. Casarsa. Measurement of the air flow rate through the heating element. Technical report, Advatech Time S.r.l., Spin-Off University of Udine, 2014.

[48] L. Casarsa and D. Foschiani. Experimental characterization of the aero-thermodynamic behaviour of a condense tumble dryer. Technical report, Advatech Time S.r.l., Spin-Off University of Udine, 2014.

[49] Erik Björk. A simple technique for refrigerant mass measurement. *Applied Thermal Engineering*, 25(8–9):1115 – 1125, 2005.

[50] Erik Björk and Björn Palm. Refrigerant mass charge distribution in a domestic refrigerator, Part I: Transient conditions. *Applied Thermal Engineering*, 26(8–9): 829 – 837, 2006.